
THE UNIVERSITY *of* EDINBURGH

# Controlled nanostructure fabrication using atomic force microscopy

Chaweewan Sapcharoenkun

Degree of Doctor of Philosophy

The University of Edinburgh

2012

## Abstract

Scanning probe microscopy (SPM) nanolithography has been found to be a powerful and low-cost approach for sub-100 nm patterning. In this thesis, the possibility of using a state-of-the-art SPM system to controllably deposit nanoparticles on patterned Si substrates with high positional control has been explored. These nanoparticles have a range of interesting properties and have been characterised by electron microscopy and scanning probe microscopy. The influence of different deposition parameters on the nanoparticle properties was studied.

Contact mode atomic force microscopy (AFM)-based local oxidation nanolithography (LON) was used to oxidise sample surfaces. Two different substrates were studied which were native oxide silicon (Si) and molybdenum (Mo). A number of factors that influence the height and width of the oxide features were investigated in order to achieve the optimal oxidation efficiency. The height and width of the oxide structures were found to be strongly dependent on the applied voltage and scan speed. The tunneling AFM (TUNA) technique was used to measure the ultralow currents flowing between the tip and the sample during the oxidation process. It was found that a threshold voltage for our oxidation experiments was -4.0 ± 1.6 V applied to the tip when fabricating geometric patterns as well as 2.9 ± 1.6 V and 2.8 ± 2.2 V applied to the substrate for nanodot fabrication. In addition, comparisons of nanodot-array patterns produced with different AFM tips were studied. The influence of applied voltage, type of AFM tip and substrate, humidity and ramping time has been studied for dot formation providing a comparison between native oxide Si and Mo surfaces. The nanodot sizes were found to be clearly dependent on the applied voltage, type of substrate, relative humidity and ramping time.

Dip-pen nanolithography (DPN) was used to study a direct deposition strategy for gold (Au) nanodot fabrication on a native oxide Si substrate. In this process, hydrogen tetrachloroaurate ($HAuCl_4$) molecules were deposited onto the substrate via a molecular diffusion process, in the absence of electrochemical reactions. This approach allowed for the generation of Au dots on the $SiO_2$ substrate

without the need for surface modification or additional electrode structures. The dependence of the size of the Au dots on different 'scanning coating' (SC) times of AFM tips was studied. A thermal annealing process was used to decompose the generated $HAuCl_4$ molecular dots to leave Au (0) metal dots. A stereomicroscope has been used for preliminary observation of different steps of Au deposition treatments. A scanning electron microscope (SEM) was used to characterise the SC AFM tips both before and after the DPN process. SEM energy-dispersive X-ray spectroscopy (EDS) has provided information about the elemental content of deposited particles for different annealing temperatures.

Fountain-pen nanolithography (FPN) has also been used to study nanowriting of $HAuCl_4$ salt and a variety of solvents on a native oxide Si surface. In this technique, a nanopipette was mounted within an AFM to deliver appropriate solutions to the silica substrate. We found that an aqueous Au salt solution was the most suitable ink for depositing gold using the FPN technique. In the case of solvents alone, ethanol and toluene were achieved with depositing onto a $SiO_2$ substrate using the FPN technique.

# Declaration

I declare that the work presented in this thesis is my own unless otherwise stated by reference.

Chaweewan Sapcharoenkun, 2012

# Acknowledgements

First of all, I would like to thank my lovely supervisor, *Prof. Eleanor E.B. Campbell*, for all her precious advice and very kind help since the first day in Edinburgh and throughout four years of my PhD life. It is my honour to know her and to have her as my supervisor. I have learnt not only academic but also how to be a good scientist. My PhD life would not have been this far without her. Thank you very much indeed, Eleanor.

I also would like to thank *Dr. Oleg Nerushev* for his advice and very useful help using AFM throughout the years and how to analyse and extract data. Thanks to *Dr. Andrei Gromov* for preparing the samples for AFM measurements, all chemical preparation, giving me a number of useful papers for nanolithography information, and always giving me useful advice. Thanks also to *Dr. Johan Ek Weis* for his advice and very kind assistance every time I asked, every help for SEM measurements and for giving me a number of good papers.

Appreciatively thanks to *Dr. Andrew Gray* for his very kind help to proofread and correct the English correction for my thesis, encouragement and fun during the stressful time. Thanks to *Kirsten Strain* for her kind help throughout the fountain-pen nanolithography experiments and valuable discussion for all details and encouragement for writing the thesis.

Also thanks to the rest of my colleagues, *Dr. Olof Johansson* and *Dr. Gordon Henderson*, for some advice and help though we are using different instruments. Thanks to *Olof* for his optimistic and really good sense of humour. This always makes me happy.

Thanks to *Dr. Nicola Cayzer* for her help with SEM and SEM-EDS analysis and valuable advice throughout SEM experiments.

It is inevitable to thank my lovely family for always providing support and encouragement. Even though, we are so far away, I am always heartened by them.

Thanks also to my Thai friends here and old friends in Thailand who talk with me and cheer me every time I feel discouraged or stressful.

I would like to thank *Krieng Kanchanawatee* for his kind help, friendship, advice, taking care and always being beside me during the hard time throughout my PhD life.

I also would like to thank *Dhassida Sooksawat* for her kind help for proofreading my thesis and always be a nice flatmate.

Last but not least, I have to thank the royal Thai government for the scholarship and giving me a great opportunity to study abroad.

# List of Abbreviations

| | |
|---|---|
| 3-D | Three-dimensional |
| AE | Auger electrons |
| AFM | Atomic force microscopy |
| AFML | Atomic force microscopy nanolithography |
| Al | Aluminium |
| Au | Gold |
| BSE | Backscattered electrons |
| Cr | Chromium |
| DI | Deionised |
| DLC | Diamond-like carbon |
| DPN | Dip-pen nanolithography |
| $e^-$ | Electron |
| EBL | Electron beam lithography |
| E-DPN | Electrochemical DPN |
| EDS | Energy-dispersive X-ray spectroscopy |
| ESEM | Environmental scanning electron microscopy |
| FMO | Ferromagnetic oxide |
| FPN | Fountain-pen nanolithography |
| FWHM | Full-width at half maximum |
| GaAs | Gallium arsenide |
| Ge | Germanium |
| $H^+$ | Protons |
| $H_2$ | Hydrogen gas |
| $HAuCl_4$ | Hydrogen tetrachloroaurate |
| HF | Hydrofluoric acid |
| HW | Half-width |
| LFM | Lateral force microscopy |
| LON | Local oxidation nanolithography |
| MESP | Magnetic etched silicon probes |

| | |
|---|---|
| MHA | 16-mercaptohexadecanoic acid |
| Mo | Molybdenum |
| $MoO_3$ | Molybdenum (VI) oxide |
| Nb | Niobium |
| nc-AFM | Non-contact AFM |
| NFP | Nanofountain probe |
| NMP | *N*-Methyl-2-pyrrolidone |
| NPs | Nanoparticles |
| $O_2$ | Oxygen gas |
| ODT | 1-Octadecanethiol |
| $OH^-$ | Hydroxide ion |
| PE | Primary electrons |
| PMMA | Mo/poly(methylmethacrylate) |
| RH | Relative humidity |
| RTESP | Rotated tapping etched silicon probe |
| SC | Scanning coating |
| SCM-PIC | PtIr-coated Si tip |
| SE | Secondary electrons |
| SEM | Scanning electron microscope |
| SERS | Surface enhanced Raman spectroscopy |
| Si | Silicon |
| $SiO_2$ | Silicon dioxide |
| SPM | Scanning probe microscopy |
| SPML | Scanning probe microscopy nanolithography |
| STM | Scanning tunneling microscope |
| Ta | Tantalum |
| tDPN | Thermal dip-pen nanolithography |
| Ti | Titanium |
| $TiO_2$ | Titanium dioxide |
| TUNA | Tunneling atomic force microscopy |
| X-ray | X-ray radiation |
| XPS | X-ray photoelectron spectroscopy |

| | |
|---|---|
| Zr | Zirconium |
| ZrN | Zirconium nitride |

# Table of Contents

# Chapter 1 Introduction

A possibility of miniaturisation from macroscopic levels to atomic and molecular levels has been discussed for over a half century since a famous talk entitled "There's Plenty of Room at the Bottom" given by Richard Feynman in 1959 and later published as a transcript in 1960 [1]. Feynman presented his vision about miniaturisation, manipulation and controlling of various things on a small scale and detailed some advantages of doing engineering at the atomic and molecular levels. Many ideas, for example, information on a small scale, better electron microscopes, a hundred tiny hands and rearranging the atoms were suggested by Feynman, which seemed to be obscure at that time. However, these ideas have subsequently been developed to be a reality since the invention of the scanning tunneling microscope (STM) in 1981 by Binnig and Rohrer [2]. STM was originally able to image surface topography at the atomic scale with a better resolution than the scanning electron microscope (SEM). This ability of STM paved the good way for subsequent development of other surface characterisation techniques such as atomic force microscopy (AFM) [3]. These techniques have been grouped together and known as scanning probe microscopy (SPM). The development of SPM, the atomic force microscope (AFM) and other scanning probe microscopes (SPMs) has facilitated a deeper understanding of the structure and properties of surfaces. These tools not only can be functional in studying topography but they can also be applied to nanofabrication.

Why was this thesis interested in the study of nanostructures and nanofabrication? This is because when materials are in the nanometre scale (ranging from 1 nm to 100 nm in size), these materials can demonstrate diverse and more interesting properties compared to the larger scale size properties of the same materials. There are two possible reasons for these phenomena, namely an increase in relative surface area per mass unit and the influence of quantum effects [4]. For the former reason, if materials have more surface area, this will lead to an increase in reactivity. For example, nanomaterials are useful for catalytic applications to develop more efficient reactions which can take place with minimum energy consumption

and operate at ambient conditions. For the latter reason, when materials are at the nanometre scale, quantum effects can play a crucial role for modifying optical, magnetic and electronic properties of these nanomaterials. For example, gold nanoparticles can be red, blue or gold colour depending on their sizes.

Nanoscience and nanotechnology now require intensive studies with highly accurate manipulation, positioning, and fabrication of various structures with nanoscale features. In recent years, there has been a dramatic increase of interest in using scanning probe microscopy nanolithography (SPML), especially atomic force microscopy nanolithography (AFML), instead of conventional methods such as photolithography and electron beam lithography [5]. This is due to the many limitations of these conventional approaches, for example, relatively high operating cost in terms of equipment, low throughput, and restricted fabrication on non-planar substrates [5]. SPML could be a powerful and relatively low-cost approach for nanostructure patterning with precise position and location [6]. Compared to conventional techniques, SPM-based nanolithography can achieve higher resolutions up to the order of 1 nm [5]. SPML not only fabricates high resolution nanostructures but can also image in real time and operate at ambient conditions leading to high accuracy fabrication with nanometre resolution [7].

The main aim of this thesis is to focus on the fabrication of nanostructures at desirable locations. The possibility of using a state-of-the-art scanning probe microscopy system to controllably deposit metallic nanoparticles on patterned Si substrates with high positional control is going to be presented. The characterisation of the metallic nanoparticles by using electron microscopy and scanning probe microscopy has been shown.

The thesis is divided into six chapters. Chapter 2 describes the principle of the techniques required for the fabrication and characterisation of nanoparticles, for example, SPM (including STM and AFM), tunneling AFM (TUNA), Raman spectroscopy and scanning electron microscopy (SEM). A detailed description of materials and methods used in this thesis is presented in Chapter 3.

Chapter 4 is focused on the systematic study of a range of parameters which influence the size of oxide features fabricated by contact mode AFM-based local oxidation nanolithography (LON) in order to achieve the optimal oxidation efficiency. A mechanism of the AFM-based LON technique and a review of the literature concerning the dependence of the nanostructures on various parameters are discussed. Two different substrates were studied in this chapter which were native-oxide-layer-coated silicon (Si) and molybdenum (Mo). The tunneling AFM (TUNA) technique was used to measure the ultralow currents flowing between the tip and the sample during the oxidation process.

Chapter 5 is mainly concerned with the deposition of metallic nanoparticles such as gold with two different methods: dip-pen nanolithography (DPN) and fountain-pen nanolithography (FPN). DPN is used to study a direct deposition strategy for gold (Au) nanodot fabrication on a native oxide Si substrate. Hydrogen tetrachloroaurate ($HAuCl_4$) molecules are used as the primary molecular ink to deposit onto the substrate via a molecular diffusion process. The dependence of the size of the Au dots on different 'scanning coating' (SC) times of AFM tips was studied. Different steps of Au deposition treatments have been investigated by a stereomicroscope. SEM was used to characterise the SC AFM tips both before and after the DPN process. SEM energy-dispersive X-ray spectroscopy (EDS) has been used to provide information about the elemental content of deposited particles for different annealing temperatures. Fountain-pen nanolithography (FPN) is also used to study nanowriting of $HAuCl_4$ salt and a variety of solvents on a native oxide Si surface. The influence of aperture size of cantilevered nanopipette used in FPN on the nanowriting is studied. AFM is used to characterise the patterns after nanowriting.

Finally, a conclusion together with an outlook of future experiments is presented in Chapter 6.

# Chapter 2 Experimental Techniques

This chapter introduces the techniques required for the fabrication and analysis of nanoparticles. For instance, scanning probe microscopy (SPM) plays an essential role for deposition of nanoparticles and characterisation. Several different methods including atomic force microscopy (AFM) and scanning electron microscopy (SEM) have been used in this research which will be briefly introduced.

## 2.1 Scanning probe microscopy

SPM encompasses a group of imaging techniques that relate to the measurement of surface properties. SPM can provide three-dimensional (3-D) pictures and structural analyses from the mesoscopic scale to atomic resolution. The basic principle of SPM is based on scanning a surface with a probe/tip. During the scan, the signal received by the probe provides information on topography, electronic structure or force interaction, depending on the technique used. There are two primary types of SPM including scanning tunneling microscopy (STM) and atomic force microscopy (AFM) [8, 9].

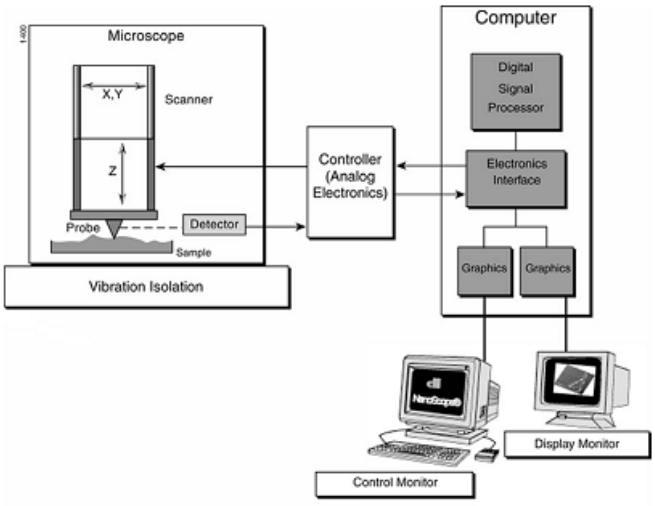


**Figure 2.1** Basic SPM components consist of the microscope system on the left side and the control system composed of two monitors on the right side [10].

Basic components of the SPM consist of a control system and a microscope system. The control system is comprised of a computer, control monitor, display monitor, SPM control electronics and software. The microscope system consists of a sample stage, piezoelectric scanner and SPM detection electronics. All microscope systems are operated by a control system. A controller is connected to the particular microscope that is then operated by the NanoScope control software. There are two main functions of the NanoScope control system. First, it is used for producing drive voltages to control the X-Y scans of the SPM probe. Second, an analogue signal from the microscope detection circuitry is maintained at a constant value.

### 2.1.1 Scanning tunneling microscope

STM relates to electron tunneling, a phenomenon based on a quantum mechanical effect. If two metals or semiconductors are placed close to each other and an electrical bias is applied between them, electrons can travel from one to the other, passing through a potential barrier (Figure 2.2) [11]. This is a quantum mechanical process, known as 'tunneling'. Figure 2.2 shows a one-dimensional electron-tunneling junction between an atomically sharp conducting metal tip and a conducting or semiconducting sample. The tip is brought within a short distance *ca*. 3-10 Å of a sample surface using piezo electric materials. An applied voltage (V) offsets the Fermi levels ($E_F$) of the tip and the substrate. The direction of the electron flow can be determined by the polarity of the bias voltage. As shown in Figure 2.2, if $E_{F,tip}$ is greater than $E_{F,sample}$, this allows electrons tunnel from the occupied states of the tip into the unoccupied states of the sample. For small biases, the quatity of the potential in the barrier and the energy of the tunneling electron can be approximated as the work function ($\Phi$) of the metal (*ca.* 5 eV), consequently, the tunneling current decreases by about an order of magnitude for every 1-Å change in the tip-sample separation (z) [11]. There are two primary modes of STM.

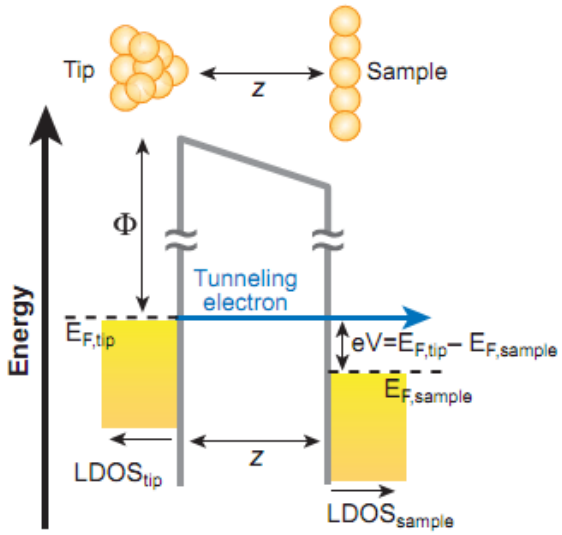


**Figure 2.2** An energy-level diagram for the conduction electron-tunneling junction [11]. An applied bias voltage (V) times the electron charge (e) offset the Fermi energy levels ($E_F$) of the tip and the sample. The distance between the sample and the tip (z) has an exponential influence on the resultant current. LDOS, local density of state; Φ, work function of the metal.

#### 2.1.1.1 Constant current mode

The tunneling current is maintained constant as the tip is scanned across the surface as shown in Figure 2.3 a). The feedback loop maintains the tunnelling current by adjusting the tip-sample separation with a piezo-electric crystal. The topography of the surface is generated by recording the vertical position of the tip. The topography is dependent on the structure geometry and the surface local density of states at the position of the tip [12]. The resolution of the STM using constant current mode can be achieved with atomic resolution or better since the tunneling current is strongly localised and the STM is very sensitive to both lateral and vertical changes in topography. However, the speed of measurement in this mode is relatively slow because of the need for mechanical manipulation of the scanner in the z direction which is controlled through the feedback loop [11]. This mode can be applied to study various types of surfaces such as conductive surfaces or thin nonconductive films and small objects deposited on conductive substrates.


**Figure 2.3** a) Constant current mode of STM and b) Constant height mode of STM [11].

#### 2.1.1.2 Constant height mode

The tunneling current is monitored as the tip is scanned parallel to the surface as shown in Figure 2.3 b). The tip is maintained at a set distance from the sample surface during scanning and the tunneling current is recorded. The topography is represented by the current as a function of lateral position. Constant height mode gives much faster measurements compared to constant current mode. This mode is most appropriate for relatively smooth surfaces since the tip can be easily damaged if the surface is not flat.

### 2.1.2 Atomic force microscopy

AFM involves the detection of van der Waals (or other) forces between the tip and sample surface (see Figure 2.4). The AFM tip is attached to one end of a cantilever, which has a low spring constant. When the cantilever is scanned across the surface, the cantilever is bent up and down. The interactions between the tip and the sample surface are attractive or repulsive forces. These tip-surface interactions can be measured by an atomic force microscope (AFM). There are three different modes in AFM depending on tip and sample separation during scannning.

In order to understand the AFM imaging modes work, it is important to use force-distance curves for simplicity. Figure 2.5 illustrates the force-distance curve which is calculated from a defelction-distance curve [13]. The interaction forces are drawn by monitoring the deflection of the cantilever as the piezo is used to move the

tip towards and contacts the sample. At large separations between the tip and the substrate, there are no net forces and the cantilever is considered to have zero deflection. When the tip approaches the sample surface, it normally begins to pull the probe towards the surface with attractive van der Waals interactions causing a 'snap-in' as the tip becomes unstable and jumps into contact with the sample surface. As the cantilever is continually forced to contact the sample surface, the net interaction becomes repulsive since the tip and the sample apply opposite forces repelling each other. In Figure 2.5, the repulsive forces are shown as being positive and the attractive forces are negative.

Moreover, these attractive and repulsive parts of the force-distance relationship between the tip and the sample can be characterised by modelling the interaction. This relates to the variation of the potential energy of one particle at the apex of the AFM tip which interacts with a particle at the surface of the sample. Figure 2.6 illustrates the variation of the pair-potential energy between two atoms also known as Lennard-Jones potential (solid line) at three different working modes: contact mode, non-contact mode and tapping mode. This potential energy function (U(s)) depends on the separation (s) between the tip and sample surface and is a total potential of the repulsive and attractive interactions. The Lennard-Jones function can be expressed as following:

$$U(s) = 4\varepsilon \left[ \left( \frac{\sigma}{s} \right)^{12} - \left( \frac{\sigma}{s} \right)^{6} \right] \qquad (1)$$

Where s is the tip-sample distance, ε is the depth of the potential well, σ is the finite distance at which the inter-particle potential is zero [14]. ε and σ are normally constants that depend on the material.

The repulsive force at very small tip-sample separations is caused by the Pauli exclusion principle for the overlapping electron clouds of the tip and the sample atoms. The attractive part at relatively large separation of the short-range interaction force is contributed to the van der Waals force domination.

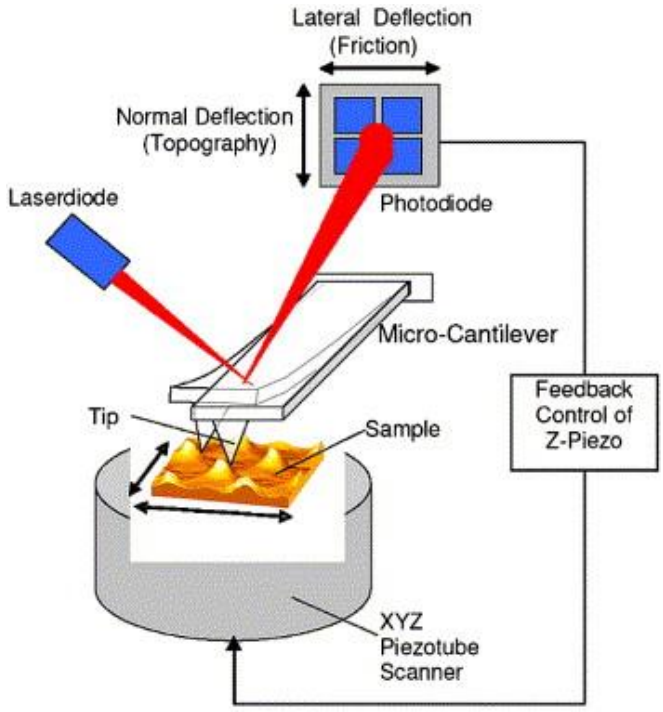


**Figure 2.4** A schematic diagram of an AFM and a beam deflection system [15].

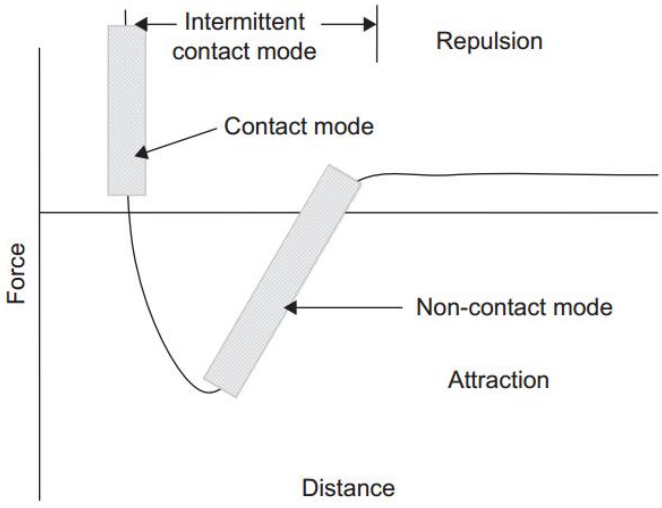


**Figure 2.5** Force-distance curve showing three AFM imaging mode regimes. Contact mode operation is in the repulsive region. Non-contact mode operation can oscillate within the attractive regime only. With intermittent contact or tapping mode, the probe is oscillated colse to the surface with a larger oscillation amplitude compared to non-contact mode and the probe moves through non-interacting, attractive and repulsive regimes [13].

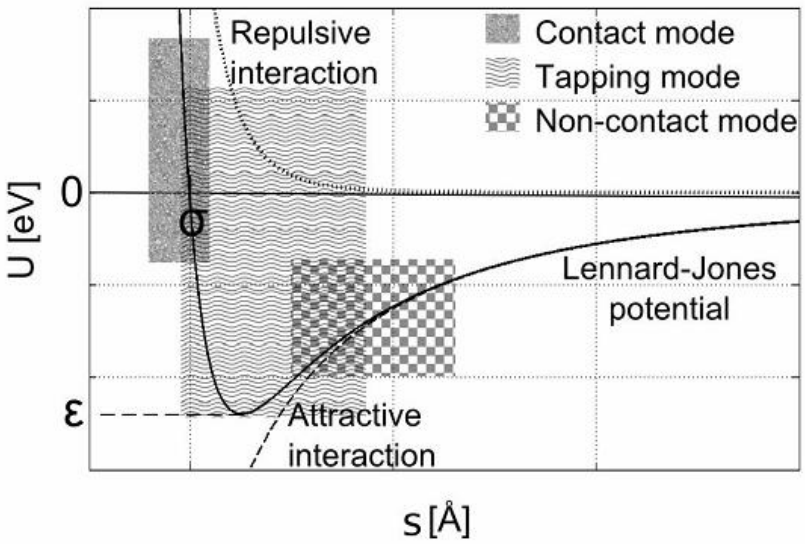


**Figure 2.6** Diagram illustrating the Lennard-Jones interaction potential describing the typical interaction of an AFM tip and the sample surface under three common modes of AFM imaging: contact mode, tapping mode and non-contact mode [14].

#### 2.1.2.1 Contact mode AFM

In contact mode AFM, the AFM tip is always in contact with the sample surface. Consequently, the tip-sample interaction is within the repulsive regime as shown in Figure 2.5. Contact mode AFM was the first mode developed for AFM and is the simplest mode of AFM operation. There are two types for this modes: constant force and variable force. For constant force mode, a constant cantilever deflection between the cantilever and the sample is controlled by a feedback loop that is the z-height is altered as the cantilever is deflected in order to cause a return to the original deflection or set point. A topographic image of the sample surface is built up by the change in z-height as a function of x,y-position. For variable force imaging, the feedback mechanisms are switched off so that the z-position remains constant and the deflection is controlled to produce a topographic image. However, variable force mode can be used only on relatively smooth samples with low lying surface features. This mode can provide a better resolution images than constant force mode.

Contact mode AFM can operate in air, liquid or vacuum environments. Contact mode is very suitable for imaging in liquid. Contact mode can achieve extremely high resolution compared to other modes. Moreover, contact mode AFM

can also work with high speed AFM. However, the disadvantage of contact mode is that the applied normal force leads to a high lateral force applied to the sample. Moreover, contact mode AFM is not suitable for very soft, weakly adsorbed or easily deformed sample surfaces because the samples can be damaged, distorted or otherwise can be removed by the scanning force. In contrast, if contact mode is applied for very hard sample surfaces, the tip can also be easily damaged or changed by the scanning process. In the case of imaging in ambient conditions, since a capillary layer of water is formed between the tip and the substrate, this can lead to the AFM tip being pulled onto the sample surface with a stronger force than the force applied by the operator. Thus, this can cause the damage of either the tip or the sample due to a very large force applied to the surface.

The suitable AFM cantilevers used for contact mode should have force constants that are typically less than 1 N/m and are fabricated from either silicon or silicon nitride.

#### 2.1.2.2 Non-contact mode AFM

During scanning, the probe does not contact the sample surface but oscillates above the adsorbed fluid layer on the sample surface. When the probe approaches the sample surface, long-range interactions, for example, van der Waals and electrostatic forces, happen between atoms in the probe and the sample surface causing a detectable shift in the frequency of the oscillation of the cantilever. To acquire an AC signal from the cantilever, the cantilever is typically oscillated at a frequency a little above the resonant frequency with a small amplitude of less than 10 nm. Non-contact mode AFM is carried out in the attractive regime as shown in Figure 2.5 without passing through the repulsive regime used for contact mode AFM. The AFM tip used should be very stiff and has a high frequency cantilever in the range of 300-400 kHz. The dynamic effects of the attractive force should be monitored in order to maintain the cantilever very close to the surface without jumping to the repulsive regime. The attractive van der Waals forces, extending between 1 nm and 10 nm, are able to reduce the resonant frequency of the cantilever and lead to a decrease in the amplitude of oscillation. Scanning speed used in non-contact mode should be lower

than in contact mode, even though the high resonant frequencies and small amplitudes mean scanning speed usually be greater than in tapping mode.

Either the changes in amplitude or the changes in the phase (which derives from the changes in frequency) are used in the feedback mechanism to maintain the tip to remain out of contact with the sample surface. Since the probe does not contact the surface in the repulsive regime, the interaction's area of the tip and the sample is minimised causing potentially for greater surface resolution. In non-contact mode, phase detection is usually used with small amplitudes since slightly higher sensitivity. Non-contact mode AFM can be used for imaging of almost any sample surface. Non-contact mode sometimes gives better and more consistent results compared to tapping mode AFM due to lower tip wear [16]. However, one of the limiting factors for this mode in air which needs to be taken into consideration is when the sample surface is covered by the contamination layer, this phenomenon leads to an unrepresentative topographic image and can cause low resolution if the sample surface is covered with the contamination layers [16]. To avoid this case, the vibration amplitude during scanning needs to be very small. The AFM tip used should be very stiff. In comparison to other modes, a preferable advantage of non-contact mode is that both the sample surface and the AFM tip suffer less damage and less distortion in the case of very delicate samples such as DNA molecules.

#### 2.1.2.3 Tapping mode AFM

The primary motivation for using tapping mode AFM is to take advantage of the signal-to-noise benefits regarded to modulated signals and the ability to measure images with a small probe-sample force [16]. For tapping mode AFM (sometimes known as intermittant contact mode), the oscillation of the cantilever is close to its resonant frequency. The probe is oscillated with a large amplitude ranging between 20 nm and 100 nm. The probe is oscillated by a piezoelectric element attached to the probe holder. For restricting the amplitude of oscillation, the probe will repeatedly engage and disengage with the surface when its oscillation happen close to a sample surface. For scanning, the probe lightly taps on the sample surface at the bottom of its swing. A feedback mechanism is usually based on amplitude modulation and the

tip-sample interaction passes from the zero-force regime through the attractive force regime and then into the repulsive regime as illustrated in Figure 2.5. These tip-sample interactions through three regimes has various important implications. For example, tip-sample repulsive interaction can cause the possibility of the damage of the tip or the sample. The tip can pass through the contamination layer and tip-sample contact allows some sensing of sample properties.

From the split photodiode detector, a constant signal amplitude is measured and controlled by the feedback loop. A topographic image of the sample surface is obtained in a similar manner as with contact mode AFM. The tapping mode AFM can operate in ambient and liquid environments but is not commonly operated in vacuum due to the limitations in resonant frequency. When imaging in air, the probe is able to contact the sample surface via the adsorbed fluid layer at the typical amplitude of the oscillation without getting stuck. While imaging in liquid, the oscillation need not be at the cantilever resonance. Recently, tapping mode AFM is the most commonly applied technique for imaging in air. The advantage of tapping mode over contact mode AFM is that the problem of lateral forces is almost eliminated due to the movement of the tip perpendicular to the surface as it scans. In comparison with non-contact mode, tapping mode AFM can be better operated in the attractive force and the presence of the capillary layer and give better stability. In liquid, this mode is also widely applied; however, there are still a number of difficulties particularly for the operation. This is because mechanical excitation of the cantilever can also cause excitation of the liquid and liquid cell [17]. Moreover, the understanding of the contrast mechanisms is still unclear.

The suitable AFM cantilevers used for tapping mode should have force constants that are much greater than contact mode AFM (>10 N/m) and higher resonance frequency (normally ranging from 200 kHz to 400 kHz). Tapping mode cantilevers are normally fabricated from silicon.

## 2.2 Tunneling atomic force microscopy

TUNA is a technique that extends from STM and is able to measure high resistance sample surfaces with sub-picoampere tip/sample currents. This method uses contact mode AFM for scanning. The appropriate tip is an electrically conductive tip for example PtIr-coated tips for contact mode scanning capacitance microscopy (SCM-PIC) and CoCr coated (magnetized) Si tips (magnetic etched silicon probes: MESP). The lateral resolution is directly related to the end radius of the tip. A dc bias is applied to the conductive sample and the conductive tip is grounded while the tip is scanning the surface (see Figure 2.7). A linear current amplifier senses the current passing through the sample during scanning detecting from 80 fA to 120 pA. A constant force between tip and sample is maintained so topography and current images of samples can be produced. This advantage facilitates the direct correlation of local topography and electrical properties. TUNA can be applied for dielectric film samples such as silicon dioxide, $SiO_2$, and transistor gate oxides. The tunneling current between the conductive tip and the dielectric film sample strongly depends on film thickness, leakage paths, charge traps and tip geometry [18].

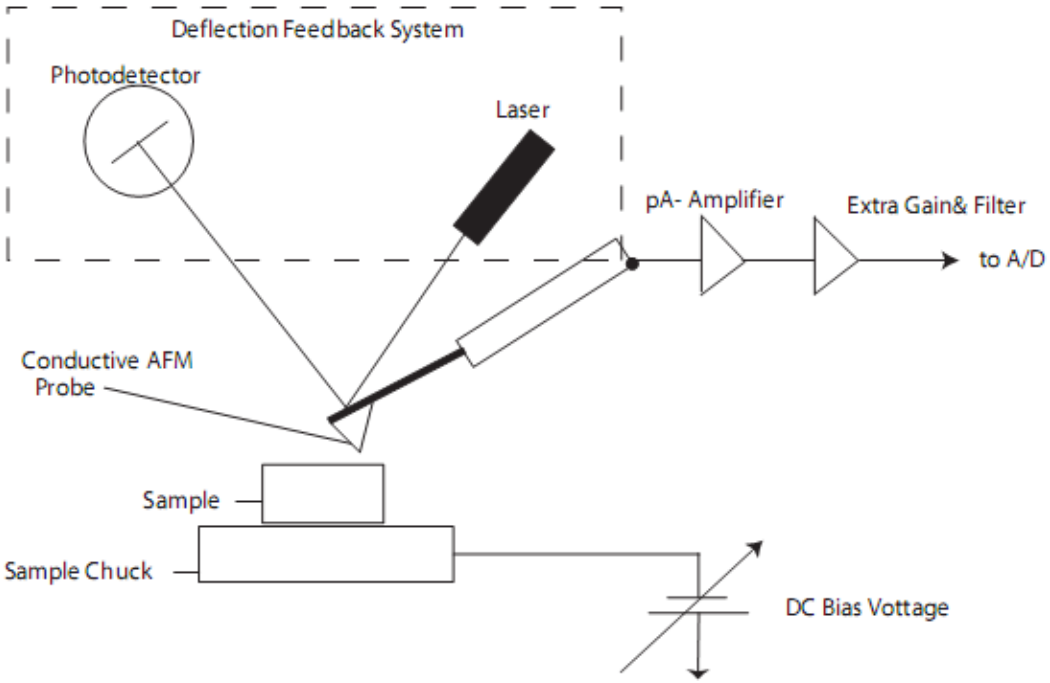


**Figure 2.7** Tunneling AFM (and Conductive AFM) Block Diagram [19].

## 2.3 Scanning electron microscopy

The scanning electron microscope, SEM, was developed soon after a transmission electron microscope, TEM, however SEM took longer to be developed into a practical tool for scientific research. Due to the limitations and complications of using a TEM, nowadays, SEM outnumber TEM. TEM can only examine a very thin sample and requires extensive sample preparation. If the sample is thick, the electrons are mainly scattered within the sample or absorbed instead of being transmitted [20].

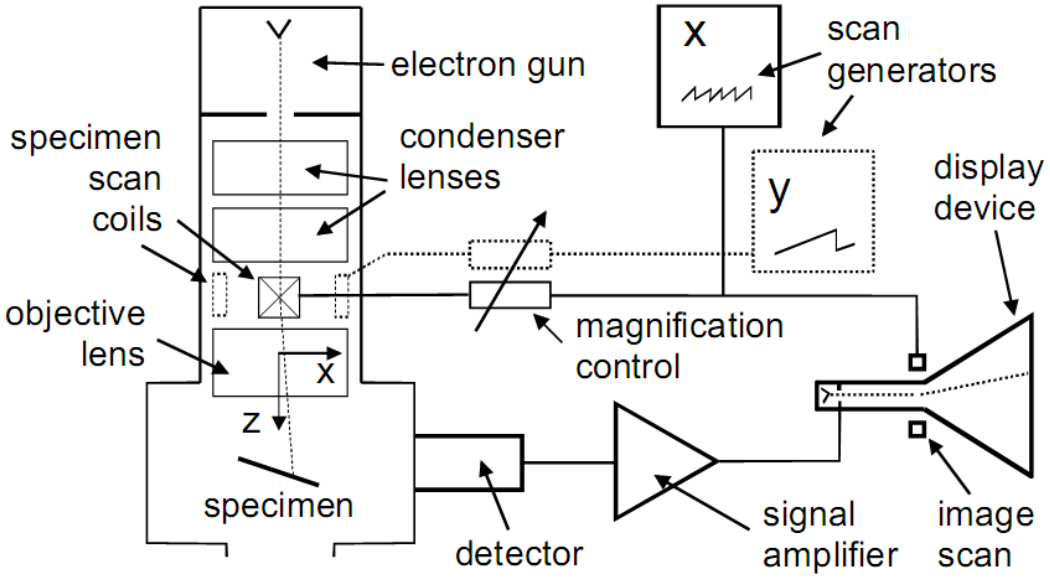


**Figure 2.8** Schematic illustration of a scanning electron microscope [20].

A schematic diagram of a typical SEM is illustrated in Figure 2.8. First, a beam of electrons is generated by an electron gun. There are two typical types of electron gun. The most common type is a thermionic gun which produces electrons from a hot filament. Another type is a field emission gun which uses a strong electric field to generate electrons from a sharp tip. The field-emission guns are able to generate electron beams with a smaller diameter of *ca.* 10-100 nm at the sample thus providing higher resolution. The electrons are accelerated at a voltage of 1-50 keV (typically 30 keV). The electron beam then travels through a few condenser lenses which focus the beam of electrons down toward the specimen. These lenses are electromagnetic in order to bend and focus the electron path. The microscope requires a high vacuum chamber to avoid the scattering of electrons by air molecules. The electron gun is scanned in the x and y directions across the specimen known as raster scanning. When the primary electrons (PE) hit the specimen, they undergo two types of scattering. This can be either elastic or inelastic depending on the energies of the PE and the atomic number of the atoms in the specimen. In elastic scattering, the electron trajectory changes but the kinetic energy and velocity remain constant. This is because the elastic collisions predominantly involve scattering with the atomic nuclei with a corresponding large difference in mass. On the other hand, the inelastic

scattering relates to the interaction of the PE with atomic electrons (from atomic shells). This inelastic interaction produces an atom in an excited state and can lead to various effects such as the production of secondary electrons (SE), backscattered electrons (BSE), Auger electrons (AE) and X-ray radiation (X-ray) as shown in Figure 2.9 [21].

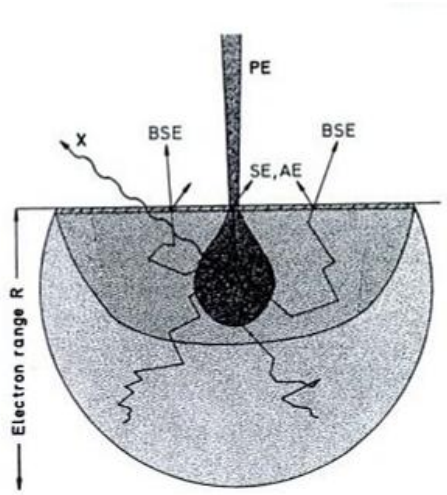


**Figure 2.9** Representation of processes produced by the interaction effects of the primary electron (PE) with a specimen with various depths in the diffusion cloud of the electron range, R. The electrons are emitted predominantly as SE, BSE, X-ray and AE [21].

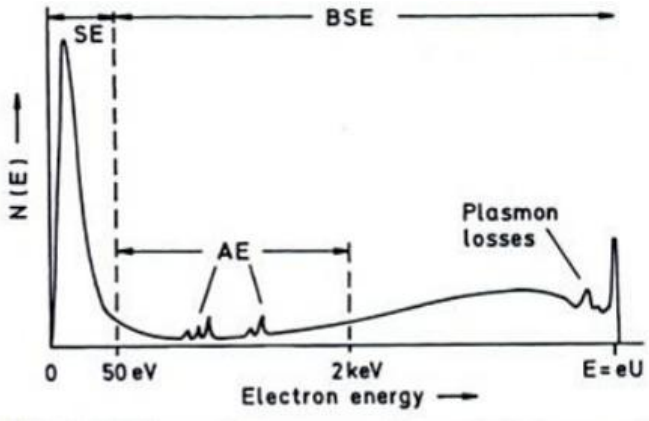


**Figure 2.10** A diagram illustrating the number of electrons emitted from a specimen as a function of the energy of electrons [21].

SE production is the most important mechanism in SEM because the SE signal is used to form a topographic image (a property of the surface structure). This is because SE can be generated with very low energies, less than 50 eV (typically between 2 and 5 eV, see Figure 2.10) and near the surface, within a small depth less than 2 nm, which is easily examined. The detector for SE is an Everhart-Thornley detector (Scintillator-photomultiplier combination) as shown in Figure 2.11.

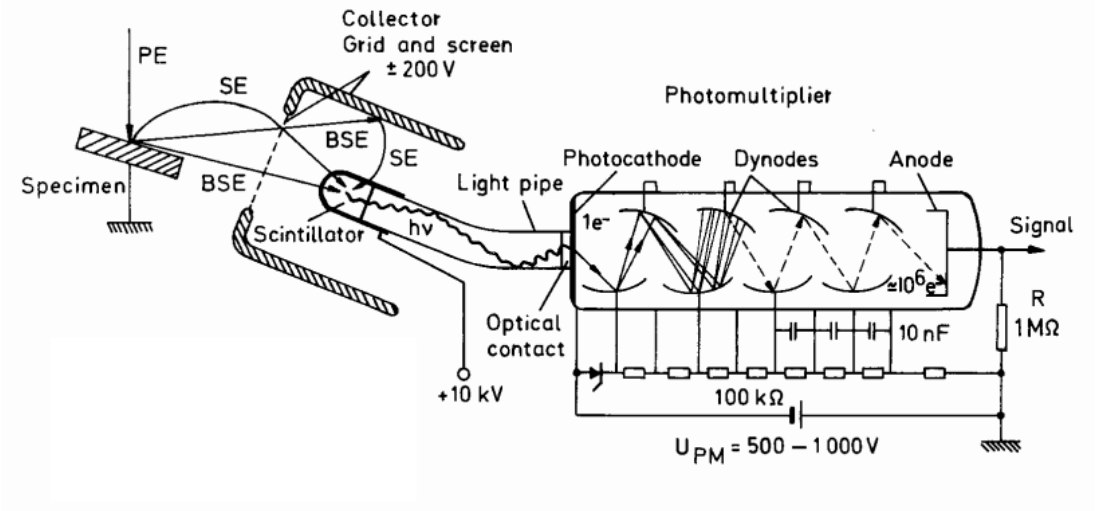


**Figure 2.11** Everhart-Thornley detector (Scintillator-photomultiplier combination) for SE detection [21].

BSE are generated by the ejection of PE with a scattered angle greater than 90 degrees. The intensity of BSE depends directly on the atomic number of the specimen. BSE typically have a broad energy range, with energies greater than 50 eV. BSE images can illustrate the difference between regions with high atomic number (brighter) and regions with low atomic number (darker) and also provide information about the chemical composition of the specimen.

AE and X-rays are produced by the relaxation of the excited atom and the relaxation energy is characteristic for each element. X-rays are ejected when an electron from an occupied higher state decays to fill the hole produced in the inner shell on electron impact. Energy dispersive X-ray spectroscopy (EDS) is a technique which utilises the X-rays emitted from a specimen which has been bombarded by the

electron beam. EDS is employed to identify the elemental composition of the specimen because the X-ray energy is a characteristic of the element.

In the case of AE, the atom excited by the PE beam often undergoes relaxation by an alternative process. It is a process of producing an electron of characteristic energy instead of a characteristic X-ray. Firstly, an inner-shell vacancy is filled and then producing a characteristic X-ray. Subsequently, this X-ray is reabsorbed within the same atom, ejecting a lower-energy electron. Therefore, the original characteristic X-ray is not detected. Instead, a secondary characteristic X-ray is emitted while the outer vacancy is filled. The ejected electron itself possesses energy equal to the difference between the energy of the original characteristic X-ray and the binding energy of the ejected electron. These ejected electrons are known as AE. They are unique among electrons emitted from the sample in that they carry specific chemical information about the atom from which they originated. In addition, in contrast to characteristic X-rays, AE are of very low energy and can travel only a short distance within the sample.

The resolution of an SEM can be influenced by various factors, for example, electron beam diameter, accelerating voltage, scattering volume and SE emission in the specimen and signal/noise ratio. Although SEM has many advantages for example topographic study for a variety of samples and chemical composition determination, there are still some limitations for SEM. For example, the sample must be conductive to avoid charging of the sample. The other constraint is that samples must be stable in a vacuum on the order of $10^{-5}$ – $10^{-6}$ torr. The sample likely to outgas at low pressures is not suitable for examination in conventional SEM. However, low vacuum and environmental SEMs can be other options instead of conventional one, and a greater wide variety of samples can be successfully examined in these specialised instruments.

# Chapter 3 Experimental Section

Chapter 3 will describe the details of the materials and methods used in this work.

## 3.1 Materials

### 3.1.1 Substrate

The primary substrate used in this research was silicon (Si) obtained from the MTI Corporation. Standard Si wafers are commonly used and have a low cost. The orientation of the Si wafers was (100) with a resistivity of 3-6 Ω.cm for *n*-type (a Phosphorus-doped) and covered with approximately a few nm native oxide (silicon dioxide, $SiO_2$) layer for all Si wafers.

In Chapter 4, an additional type of substrate was used for the local oxidation nanolithography experiments. This was a high *n*-doped Si (100) wafer covered with a 100-nm-thick layer of molybdenum (Mo).

### 3.1.2 SPM probes

In Figure 3.1 it can be seen that there are three major parts of AFM probes. First, an AFM cantilever substrate acts as the probe's body in order to make handling simple and this part is handled by pincers to insert the cantilever holder into the probe assembly. The cantilever substrate is sometimes referred to as the AFM holder chip or AFM cantilever holder. Second, an AFM cantilever protrudes from the end of the AFM cantilever substrate. Third, the AFM tip is the portion of the AFM probe that is very close to the sample surface. The AFM tip is mounted at the end of the AFM cantilever. The AFM tip is sometimes referred to as the probe. The AFM tip is square based pyramidal in shape and the radius of the tip end ranges from 5 nm to 50 nm depending on the probe's type.

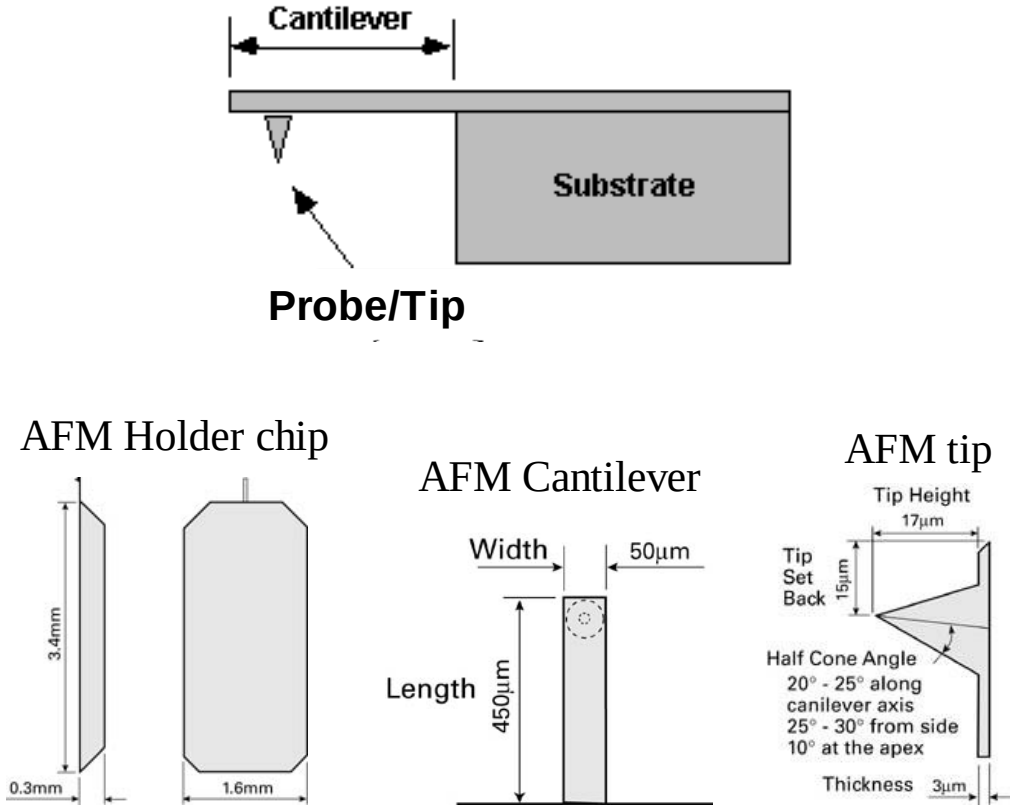


**Figure 3.1** The general model of AFM probes shows the three major components: AFM cantilever substrate/AFM holder chip, AFM cantilever, and AFM tip [22].

For tapping mode AFM imaging, silicon probes with integrated tips and cantilevers are used. The silicon probes are stiff and have large force constants and high resonant frequencies. Two types of AFM tip were used here. One of which is antimony (n) doped Si using a rotated tapping etched silicon probe (RTESP, Veeco Instruments Ltd.) with a tip radius *ca.* 8 nm (maximum *ca.* 10 nm), a force constant of 40 N/m and a resonance frequency 300 kHz [23]. This RTESP tip is now called MPP-11100-10 (Bruker AFM probes). The other is a 30 nm Al-coated, for enhanced reflectivity, rotated monolithic silicon probe (Tap300 Al-G, Budget Sensors) with a tip radius less than 10 nm, a force constant of 40 N/m and a resonance frequency 300 kHz [24]. For contact mode AFM imaging, we employed a super-sharp diamond-like carbon (NSG01-DLC, NT-MDT Co.) tip with typical curvature radius 1-3 nm, a force constant of 5.5 N/m and a resonance frequency 150 kHz [25].

For TUNA and local oxidation nanolithography (see more details in Chapter 4), an appropriate tip is an electrically conductive tip, for example, a Co/Cr coated (magnetized) Si tip (MESP) (see Figure 3.2) or a PtIr-coated Si tip for contact mode (SCM-PIC, Veeco Instruments Ltd.). MESP probes are rectangular silicon cantilevers with an antimony (n) doped-Si tip having an average force constant 2.8 N/m and normal tip apex radius 25 nm (maximum *ca.* 50 nm), according to the manufacturer [26]. SCM-PIC probes are rectangular standard (steep) silicon cantilevers having an average force constant 0.2 N/m and normal tip apex radius 20 nm (maximum *ca.* 25 nm), according to the company. A Cr/Pt-coated tip (ElectricTap300-G, Budget Sensors) has a tip radius less than 25 nm and a force constant of 40 N/m and resonance frequency 300 kHz [27].

For gold deposition using the dip-pen nanolithography technique, an Au-coated tip such as a noncontact probe (NSG01/Au, NT-MDT Co.) with a tip radius *ca.* 35 nm, a normal force constant of 5.1 N/m and a resonance frequency of 150 kHz [28] as shown in Figure 3.3 was used to improve the adhesion of the molecular ink to the tip surface [29] see Chapter 5 section 5.3.1.3 done in more detail.

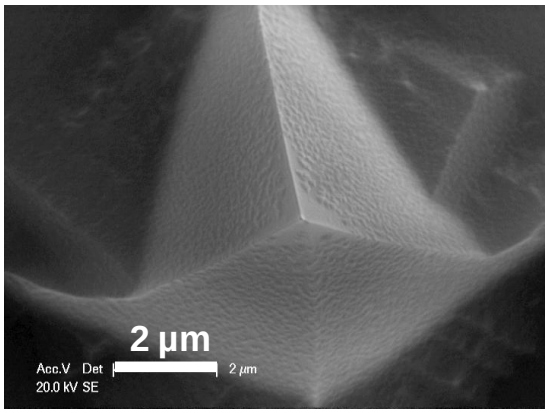


**Figure 3.2** MESP for TUNA and local oxidation nanolithography.

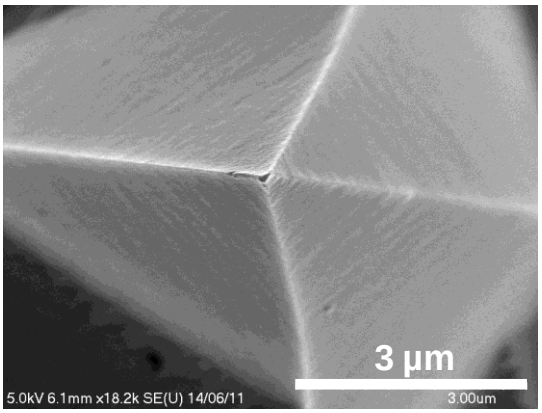


**Figure 3.3** NSG01-Au for gold deposition with dip-pen nanolithography.

### 3.1.3 AFM instrument

The AFM instrument used in this work was a Dimension 3100 AFM (Digital Instruments, Veeco Metrology Group) shown in Figure 3.4. The overall AFM instrument parts are shown in Figure 3.4 b).

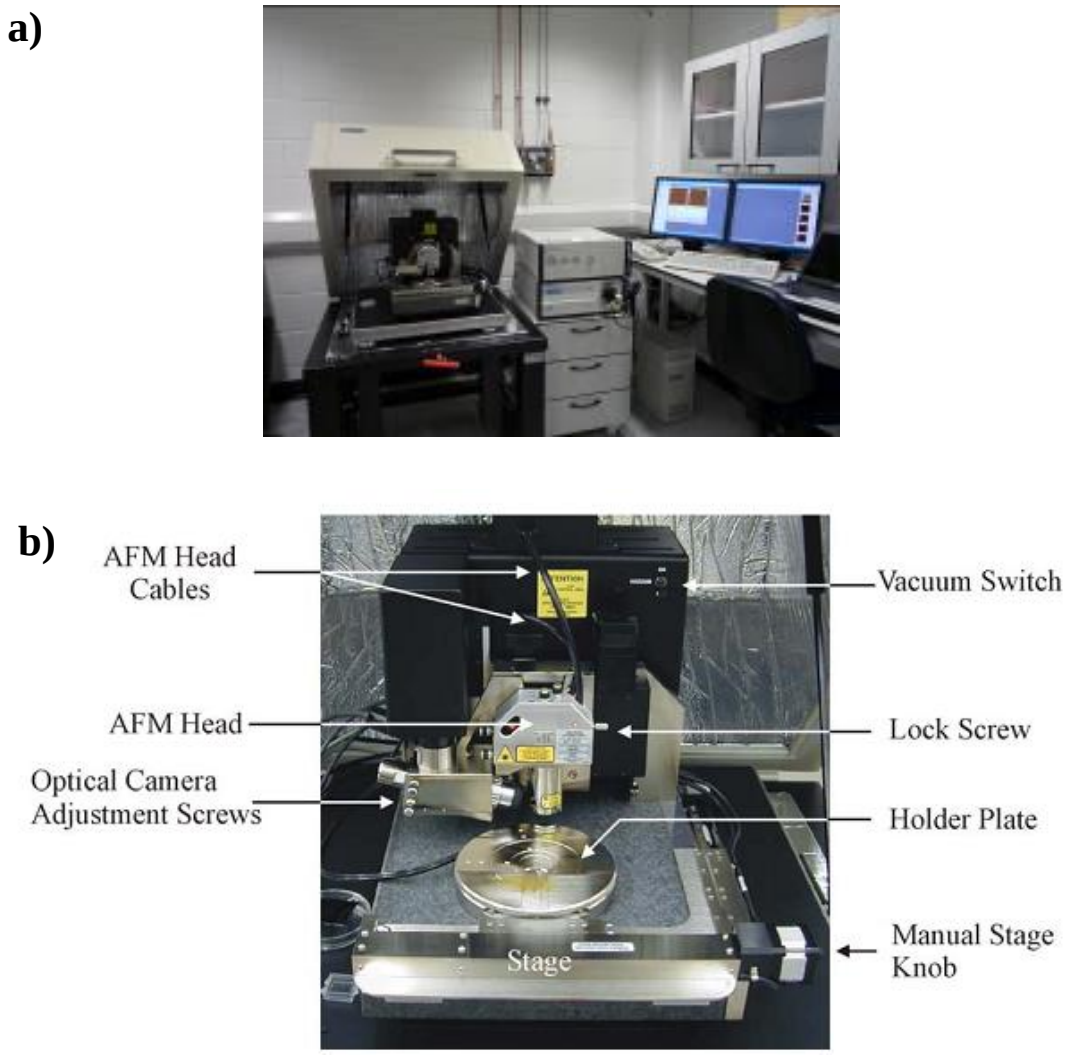


**Figure 3.4** The Veeco NanoMan AFM instrument a) the microscope system on the left side and the control system composed of two monitors on the right side. b) Zoomed in image of the microscope and detailed specification.

## 3.2 Preparation of substrates

A substrate is normally contaminated, for example, by exposure to ambient atmosphere which can cause oxide formation at the surface. For example, the Si wafers used typically have a native oxide coating of *ca.* 2-3 nm thickness [30]. Furthermore, some physical contaminations can take place, such as from dust after cutting the substrate or some grease and oil that has been leftover from touching the surface. All of these contaminants have to be removed by preliminary surface cleaning before an experiment is carried out.

For AFM imaging and nanolithography, *n*-type Si (100) wafers were cut to a size of around 5x5 $mm^2$. They were then treated by a three step process in an ultrasonic bath initially in Decon-90 (~2-5 % V/V) for 30 min to remove any dust on the Si substrate, distilled water for 15 min (3 times) in order to rinse the substrate and finally in ethanol for 30 min. After this, they were blown dry with $N_2$ compressed gas. They were subsequently cleaned by plasma etching using the Plasma Prep III (from Structure Probe, Inc) to remove any residual organic impurities.

For conductive experiments with TUNA and local oxidation nanolithography, the cleaned native-oxide-layer-coated Si substrate was placed on the AFM sample chuck using silver conductive paste to provide a good electrical contact between the silicon chip and the chuck and the Si wafer was left for about 1 hour for the solvent to evaporate (See Figure 3.5).

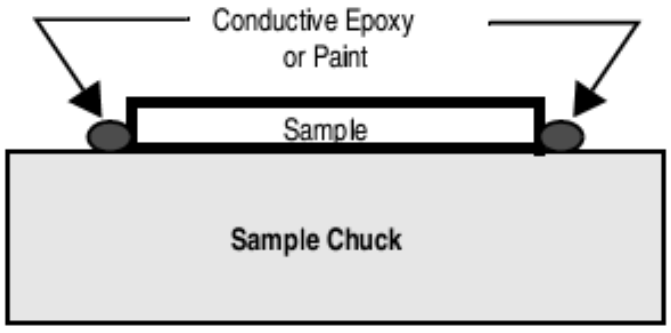


**Figure 3.5** A schematic illustration of electrically connecting a sample to the sample chuck [31].

## 3.3 Tunneling atomic force microscopy

TUNA was operated in contact mode AFM, employing the TUNA microscope mode. The appropriate tip was an electrically conductive tip, for example, SCM-PIC or MESP. A dc bias was applied to the conductive sample ranging from 0 to +10 V and the tip was grounded. A linear current amplifier sensed the current passing through the sample during scanning ranging from 80 fA to 120 pA. A constant force between tip and sample was maintained so topography and current images of samples could be produced.

## 3.4 Local oxidation nanolithography

This technique is not only used for fabricating nanopatterns but can also be applied to mark the substrate which makes it is easy to find small dots or patterns after deposition. We have studied several factors, for example, applied voltage, scan speed, types of AFM probe, types of substrate, relative humidity and ramping time which can influence the oxide dot and line patterns see more details in Chapter 4.

In the case of oxide structures patterned by local oxidation nanolithography, SCM-PIC probes were chosen and NanoMan was employed for writing. The scripts and patterns were performed by employing the NanoMan VS software with the Veeco AFM. Tapping mode AFM was used for imaging and contact mode AFM was exploited for the oxidation on native-oxide-layer-coated Si surfaces. For nanolithography using the NanoMan function, the applied voltage to the tip ranged from -1 V to -10.5 V. The scan speed was varied from 0.1 μm/s to 5.0 μm/s. The feedback was switched off during the local oxidation process. All experiments were conducted at ambient temperature and under relative humidity values of 51 ± 5 %.

In the case of dot patterns, two types of substrates were used for studying the substrate effect. One was an *n*-type Si (100) wafer, covered with a few nm thick layer of native oxide. The other was a high *n*-doped Si (100) wafer covered with a 100-nm-thick layer of Mo prepared as previously described [32]. Dot patterns were generated on the $SiO_2$ and Mo surface at room temperature and pressure. The actual relative humidity will be specifically stated for each result in chapter 4. Various

types of AFM tips were used in this section (see more details in Chapter 4) including MESP, FMG01-Co, ElectriTap300-G and NSG01-Pt. For the study of the effect of AFM tip on oxide pattern, three kinds of AFM tips were used. One of which was a Co/Cr coated AFM with a 20 nm tip radius with a spring constant of 2.8 N/m (MESP from Veeco) [26]. The other of which had about 40 nm tip radius with a spring constant of 3.0 N/m and resonance frequency 60 kHz (FMG01-Co from NT-MDT) [28]. The last one was a Cr/Pt-coated tip (ElectricTap300-G from Budget Sensors) with a tip radius less than 25 nm and a force constant of 40 N/m and resonance frequency 300 kHz [27]. For studying the voltage dependence, we applied a positive bias to the substrate ranging from 0 V to 10 V at a fixed ramping cycle of 0.97 s and relative humidity (RH) of 45 ± 2%. The tip ramping time ranged from 0.23 s to 100 s to investigate the deposition time dependence. The ramping time is the period of one cycle of the AFM tip moving towards and away from the sample. To study the humidity effect on the dot size, we used a commercial humidifier to maintain the desired humidity at 43 ± 2 %RH and 66 ± 2 %RH. This error indicates the overall error in the instrument readings, for relative humidity measurements between 20 % and 80 %.

For most AFM imaging of dot patterns, we employed a super-sharp diamond-like carbon (DLC) tip with typical curvature radius 1-3 nm. The surface was investigated using contact mode AFM. Apart from the study of nanodot arrays in Chapter 4 section 4.3.3, we continued to use the same AFM tip as the nano-patterning process for AFM imaging.

# Chapter 4 Local Oxidation Nanolithography

## 4.1 Introduction

### 4.1.1 Overview

This chapter will focus on studies of local oxidation nanolithography (LON). LON is sometimes known by different names such as local anodic oxidation, nano-oxidation, scanning probe oxidation or scanning probe anodization. However, in this thesis, we will call it local oxidation nanolithography (LON). Local oxidation for surface modification of various materials has attracted a great deal of attention since its development. It was first reported in 1990 when nano-oxidation patterning on hydrogen-passivated *n*-silicon (111) (H-passivated *n*-Si (111)) surfaces was induced by using a scanning tunneling microscope (STM) operating in air [33]. A number of studies concerning the local oxidation of semiconductors such as Si [34-37] and gallium arsenide (GaAs) [34] using STM have subsequently been reported since several research groups have considered the STM-based LON to be a useful nanofabrication technique. Besides semiconductor surfaces, the STM-based LON on metal surfaces has also been studied, this has been done on surfaces such as tantalum (Ta) [38], chromium (Cr) [39] and titanium (Ti) [40, 41].

Although the STM-based LON is a very attractive technique for nanoscale fabrication, it does have some disadvantages, for example, it is only suitable for conducting materials while atomic force microscope (AFM) based LON can be operated on any kind of substrates. As mentioned earlier in Chapter 2 section 2.1, STM has two modes of operation: constant-height and constant current mode. The constant current mode is adopted more often since the tunneling current is normally used as a lithographic source. In contrast, AFM operates by measuring attractive or repulsive forces between the tip and sample. To elucidate the limit of STM, Figure 4.1 a) and b) show the investigation by STM imaging compared to AFM imaging of oxide stripes generated by STM-based LON on a H-passivated Si (111) substrate as reported by Fontaine and co-workers [35]. The STM operation is controlled by a

constant current mode and is sensitive to the conductivity of the sample surface. When the oxide stripes, which have a higher resistance compared to H-passivated Si surface (non-oxidised regions), are imaged by STM in the constant tunneling current mode, these regions appear as indentations as shown in Figure 4.1 a) and c). The indentations appeared since the feedback loop was controlled by decreasing the tip-sample distance until an occurrence of electron tunneling and/or an electric field to maintain a constant current. The STM image does not show the actual surface topography of the sample. In contrast, the tapping mode AFM image clearly showed the actual height of the oxide stripes (Figure 4.1 b) and c)). Moreover, tip-sample contact can damage the tip if the STM tip is brought down far enough to crash into the insulating oxide surface [42]. Consequently, the drawbacks of STM-based imaging are an unreliable oxide height measurement and tip damage during nanolithography. To overcome this, the AFM-based LON offers advantages over STM-based LON with independent writing and imaging processes. AFM can first operate LON and then subsequently image the surface with the same tip without further current exposure [35, 43].

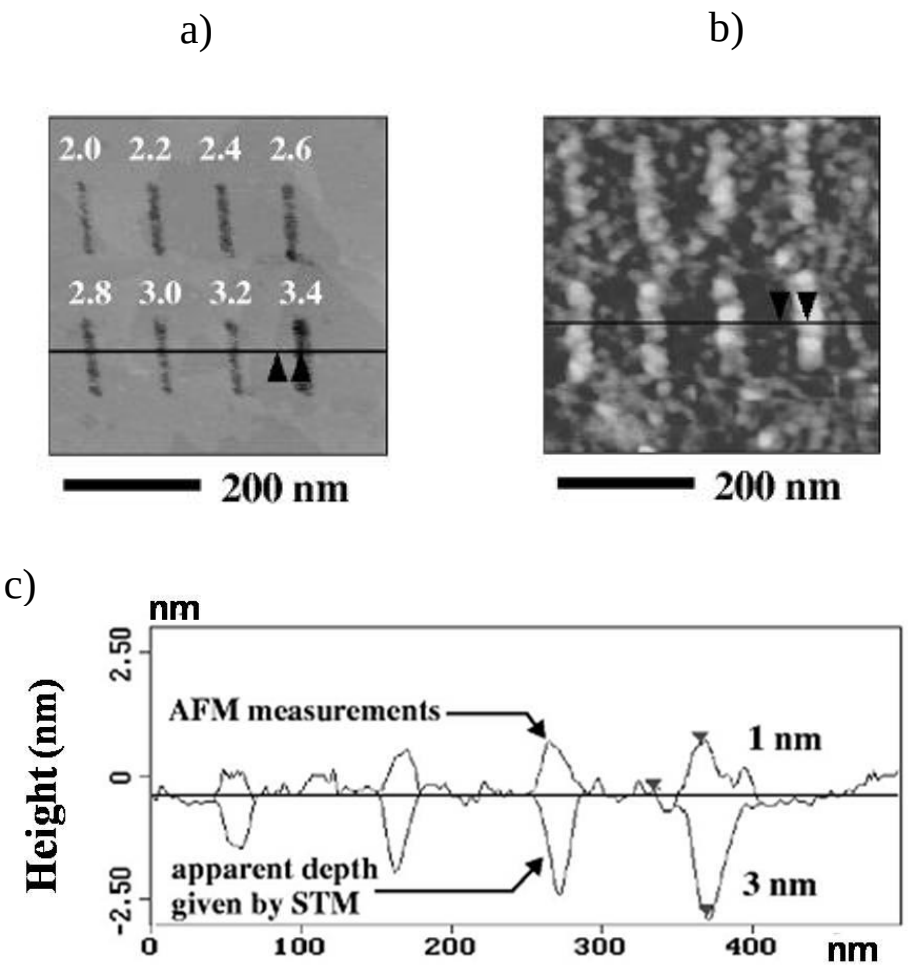


**Figure 4.1** a) STM image of oxide stripes produced by STM on H-passivated *n*-type Si (111) at different applied voltages (indicated above each stripe) with current of 100 *p*A, b) Tapping mode AFM image showing the same stripes as in part a), and c) cross sections from both STM and tapping mode AFM imaging [35].

Compared to STM-based LON, AFM-based LON has become a more powerful tool for nanoscale fabrication since the surface modification and the feedback control for imaging are independent. Another important advantage of AFM-based LON is its applicability to materials with low electrical conductivity. However, in order to write on an insulator surface, it should be a very thin film of insulator on an underlying conductive substrate and not on a bulk insulator. The first report by Day and Allee in 1993 [42] demonstrated AFM-based LON on a $p^+$-Si substrate by applying a positive bias to the substrate. They could achieve sub-100 nm

resolution oxide structures. Yasutake and co-workers [44] later illustrated AFM–based LON with an applied negative bias to the conductive AFM tip on a native-oxide-coated *n*-Si (100) substrate. The authors found that the oxidation of Si was enhanced by an electric field. After that, AFM-based LON has been extensively studied on a variety of materials, for example, native-oxide Si substrates [30, 42, 44-48], H-passivated Si substrates [49-54], and metals (e.g. aluminium (Al) [55], chromium (Cr) [56], molybdenum (Mo) [56-58], niobium (Nb) [57, 58] and titanium (Ti) [59-62] ).

### 4.1.2 Principle of AFM-based local oxidation nanolithography

LON is an electrochemical technique where a negative tip bias is applied as shown in Figure 4.2 a). In AFM-based LON under ambient conditions, the water meniscus formed by capillary force between the tip and the sample surface acts as an electrolyte, while using the conductive AFM tip as a cathode and the metallic or semiconducting substrate as an anode. This forms a two-electrode nanoelectrochemical cell as shown in Figure 4.2 b), sometimes referred to as a 'nanocell' [63]. When a negative tip bias is applied, the water meniscus is ionised and the field induces ion migration (mainly $H^+$ and $OH^-$ ions) within the water meniscus generated between the tip and substrate, where the electrochemical reaction occurs. As a consequence, localised oxide nanostructures are fabricated by the reaction between the ions and substrate.

A number of studies have suggested possible mechanisms of LON for oxide growth which can be related to various factors, such as the electrical field strength, the presence of the water meniscus and the diffusion of oxidative anions ($O^-$ or mainly $OH^-$) to the surface [45, 63-65].

For AFM-based LON on a Si substrate, the electrochemical reactions and charge transfer processes in the nanocell have been proposed by Bloeß *et al.* [63] for *p*-type Si substrate. Furthermore, Sugimura *et al.* [66] proposed an oxidation mechanism for the STM-based LON on an *n*-type H-passivated Si surface using a

positive sample bias. Since in our study an *n*-type Si substrate was primarily used, the possible mechanism is proposed as follows:

I. Reactions at the Si surface (anode):

$$Si + 2H_2O \rightarrow SiO_2 + 4H^+ + 4e^- \quad (1)$$

$$2H_2O \rightarrow O_2\uparrow + 4H^+ + 4e^- \quad (2)$$

II. Reaction at the tip (cathode):

$$4H_2O + 4e^- \rightarrow 2H_2\uparrow + 4OH^- \quad (3)$$

III. Reaction in water:

$$4H^+ + 4OH^- \rightarrow 2H_2O \quad (4)$$

Reactions 1-4 clearly show that the oxide growth involves significant consumption of water and electrons ($e^-$) as well as the electron generation. Figure 4.2 b) depicts the specific schematic of the nanocell for a Si surface and shows the two major parts: water supply and water consumption. Bloe*ß et al.* [63] also suggested that the high electric field strength (E) between the AFM tip and substrate can induce the water condensation as shown in reaction 3. $H_2O$ molecules are decomposed into protons ($H^+$) and oxygen gas ($O_2$) as shown in reaction 2. Electron ($e^-$) tunneling from water molecules to the conduction band of the oxide is related to hydrogen gas ($H_2$) and oxyanion ($OH^-$) generation as shown in reaction 3. In the nanocell, the $H^+$ and $OH^-$ ions generated from reaction 1-3 can recombine spontaneously as shown in reaction 4 since there is a very small gap between the AFM tip (cathode) and the Si (anode) substrate. The same authors also demonstrated that an increase of relative humidity and the amount of water in the nanocell can lead to an increase in the diameter of the oxide structures. In addition, during the initial stages of nano-oxidation, direct electron tunneling (reaction 5) has also to be taken into account due to the small distance between the tip and the Si surface.

$$e^- (Tip) \rightarrow e^- (Si) \quad (5)$$

Gordon *et al*. proposed a mechanism based on native-oxide formation followed by a proximal probe anodization process [65]. As already mentioned in Chapter 3 section 3.2, a Si wafer is normally covered with a native-oxide layer since the Si surface undergoes various water cleaning and rinsing steps and also is exposed to atmosphere at ambient humidity. After the initial native-oxide layer has been created, Figure 4.3 shows the electric field set-up and the electron tunneling created by the voltage difference between the conductive AFM tip and the native-oxide surface [65]. This creates negatively charged hydroxide ions and extends the native-oxide thickness. However, the electric field which assists the oxide growth has to exceed the diffusion limit on the order of 1 x $10^7$ V/cm with a tip bias of 7-8 V needed to grow oxides about 80 Å thick.

Moreover, Dagata *et.al*. [64], Avouris et al. [67], and Gwo [68] proposed the same oxidation mechanism taking place in the nanocell at the Si surface.

$$Si + 4h^+ \text{ (hole)} + 2(OH^-) \rightarrow SiO_2 + 2H^+ \qquad (6)$$

The hydroxide ions ($OH^-$) are produced by the hydrolysis of the water in the meniscus. The hydroxide ions are driven by the electric field to the $Si/SiO_2$ interface and then react with positively charged holes, $h^+$, on the Si surface in order to fabricate silicon dioxide, $SiO_2$.

a)

b)

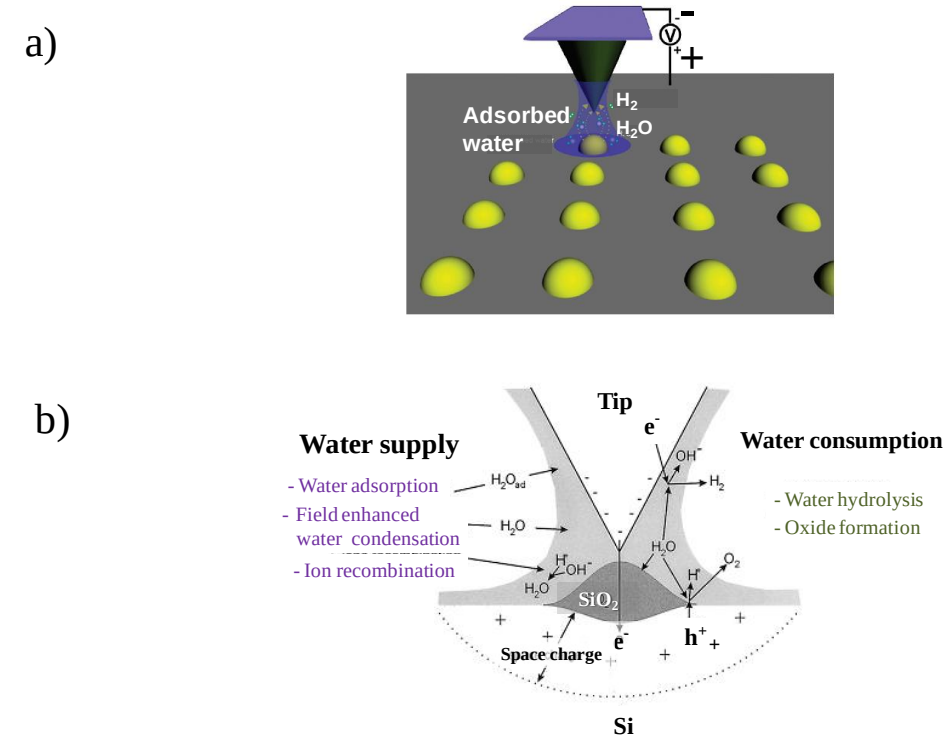


**Figure 4.2** a) Schematic diagram of AFM-based local oxidation nanolithography (AFM-based LON) [69] and b) the model shows specific features with relevant species of the nanocell for oxide growth on a Si surface by AFM-based LON [63].

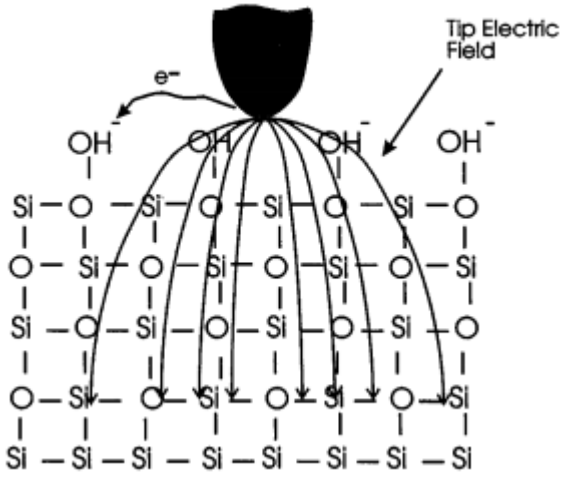


**Figure 4.3** Schematic representation of the electric field and electron tunneling applied from the conductive AFM tip to create additional oxide on a native-oxide-coated Si substrate [65].

### 4.1.3 Influence of humidity

One interesting aspect of LON is that this technique can be operated in air. Consequently, the environment during the LON process has to be controlled in order to guarantee high reproducibility and controllability of nanostructures. Among various environmental factors, relative humidity is a crucial factor affecting LON. As already mentioned above when describing the mechanism of LON, relative humidity influences the formation of the water layer, which is the primary source of oxidative anions in the nanocell. There have been a number of good studies of the relative humidity effect on the oxide structure using AFM-based LON [48, 54, 67, 70].

#### 4.1.3.1 Influence of humidity on Si or native-oxide-coated Si surface

The role of ambient humidity was investigated with respect to the electrolyte behaviour in the LON process by Avouris *et al*. in 1997 [67]. They applied -10 V to the conductive AFM tip and induced oxidation on a H-passivated *n*-type Si (100) substrate in different humidity conditions. Figure 4.4 a) and b) are AFM images of the oxide patterns written with a speed of 0.3 μm/s and the relative humidity (RH) at 61 % and 14 %, respectively. As a result of reducing the RH from 61 % to 14 %, the line width decreased from ~90 nm to ~22.5 nm, which was about a factor of 4 reduction. The authors explained that the ambient humidity considerably affected the lateral resolution.

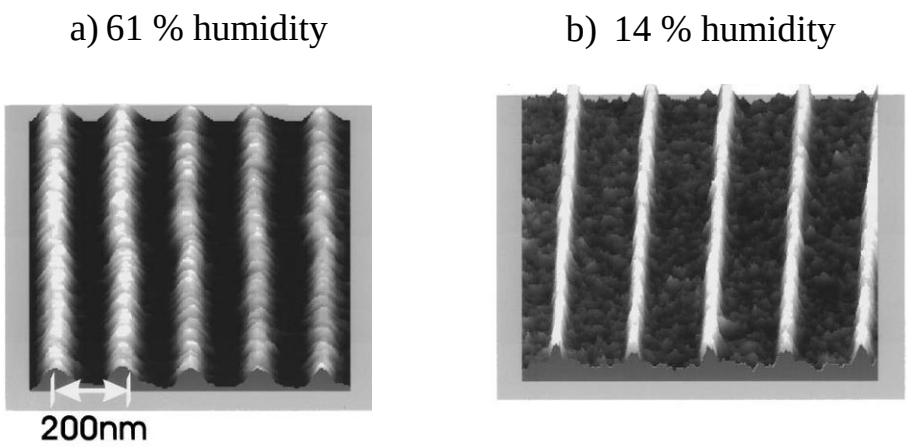


**Figure 4.4** Two AFM images of the tip-induced Si oxide lines deposited on the *n*-type Si (100) surfaces written with a -10 V tip bias and 0.3 μm/s speed: a) induced at 61 % RH obtained ~90 nm line width and b) induced at 14 % RH obtained ~22.5 nm line width [67].

In 2003, Kuramochi and co-workers [48, 54] published two papers concerning the effect of the RH on AFM-based LON. The first publication reported a systematic study of RH ranging from 40 % to 80 % using contact mode AFM [48]. Examples of AFM images and line profiles of fabricated oxide dots deposited on a native-oxide-coated *p*-type Si (001) surface for different oxidation conditions are shown in Figure 4.5. When an oxide dot was created by applying a sample bias of 8 V for an exposure time (*t*) of 100 s with low RH of 50 %, a dome shape dot was formed with a diameter of about 300 nm and a height of 3.8 nm as shown in Figure 4.5 a). However, when the RH was increased to 80 % with constant voltage and exposure time, a two-storied shape was obtained with a narrow upper half and a broad base as shown in Figure 4.5 b). They suggested that these results were affected by the space charge effect and ionic diffusion during the fabrication. Since the fabricated silicon oxides are insulators, a negative surface potential was produced at the centre and surrounded by a positive potential [45], this could prevent the current flow and decreased the ionic concentration in the core region of the growing oxide. The oxide could, however, continue to grow horizontally because the current flowed along the adsorbed water layer. The authors also showed the dependence of the height and diameter of the oxide dots as a function of the applied voltage (ranging

between 2 V and 10 V) at various RH values (40 % - 70 %) and the same exposure time (200 s) as shown in Figure 4.6 a) and b). The height and diameter of the fabricated oxide dots increased with both applied voltage and RH values.

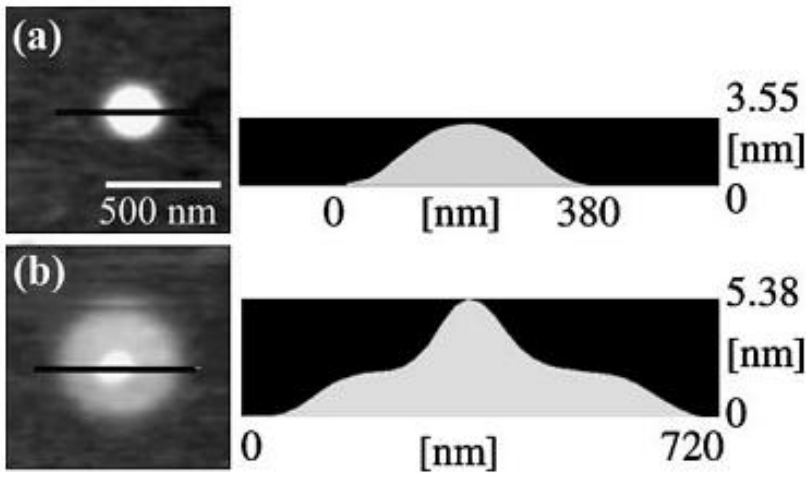


**Figure 4.5** Two AFM images and line profiles of the fabricated oxide dots deposited on a native-oxide covering on a *p*-type Si (001) surface using contact mode AFM LON with the same sample bias voltage ($V_s$) of 8 V and the exposure time (*t*) of 100 s. a) A dome-shaped dot fabricated at RH = 50 % and b) A two-storied shape dot fabricated at RH = 80 % [48].

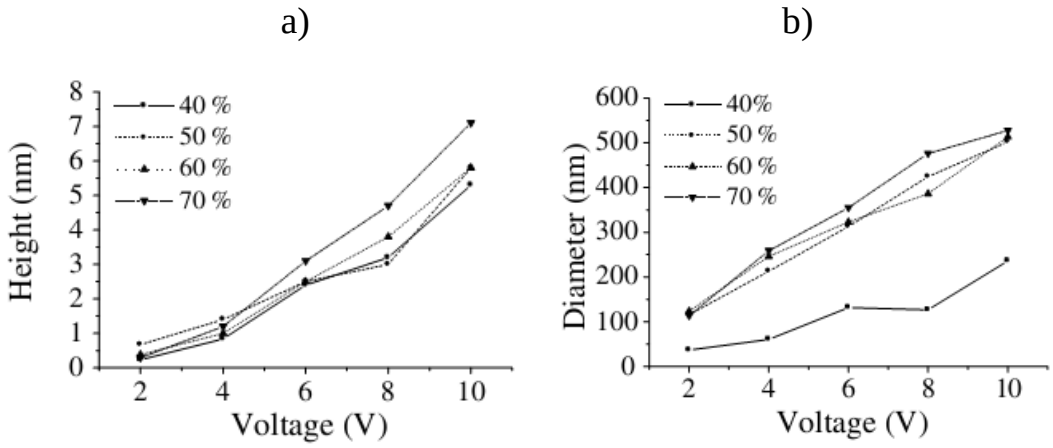


**Figure 4.6** Two graphs showing the dependence of a) the height and b) the diameter of the fabricated oxide dots as a function of the sample bias voltage at various RH values (40 % - 70 %) at the exposure time of 200 s. The lines in the plot a) and b) are only visual guides [48].

The second study of Kuramochi and co-workers [54] revealed the results of *in situ* current monitoring during LON at various RH values between 40 % and 70 % using contact mode AFM. Figure 4.7 a) shows a topographic image of four dome-shape oxide dots fabricated on a H-passivated *p*-Si (001) surface by applying a 7.5 V sample bias ($V_s$) for an exposure time ($t$) of 10 s and RH of 45 %. When increasing the applied bias and RH to 9.5 V and 70 % respectively (Figure 4.7 b)), the fabricated dot appeared as a two-storied shape with a broadening of the base and much broader ring compared to the four dome-shape dots. These results were in good agreement with the above report [48]. To provide further evidence that the size of the fabricated oxide dots clearly depends on applied voltage and RH, Figure 4.8 a) and b) show the diameter and the height of oxide dots as a function of voltage with different RH values ranging from 40 % to 70 %. These graphs clearly show that an increase of the voltage and RH lead to an increase in the size of the oxide dots in the same manner as in their previous work [48]. Moreover, Figure 4.8 c) and d) also revealed the expected faradaic current[1] ($I_{exp}$, expected charge) and the total integrated current[2] ($I_{int}$, integrated charge) as a function of applied voltage, respectively for various values of RH (40 % - 70 %). These two plots show that $I_{int}$ and $I_{exp}$ depend similarly on applied voltage and RH. They also found that when the relative humidity exceeds 55 % the total integrated current involves ionic (in the form of $O^-$ and $OH^-$) diffusion phenomena.

[1] The expected faradaic current is estimated from the volume of the fabricated oxide dots in Figure 4.7 a) and b).

[2] The total integrated current or the detected faradaic current was obtained by integration of an *I versus t* curve.

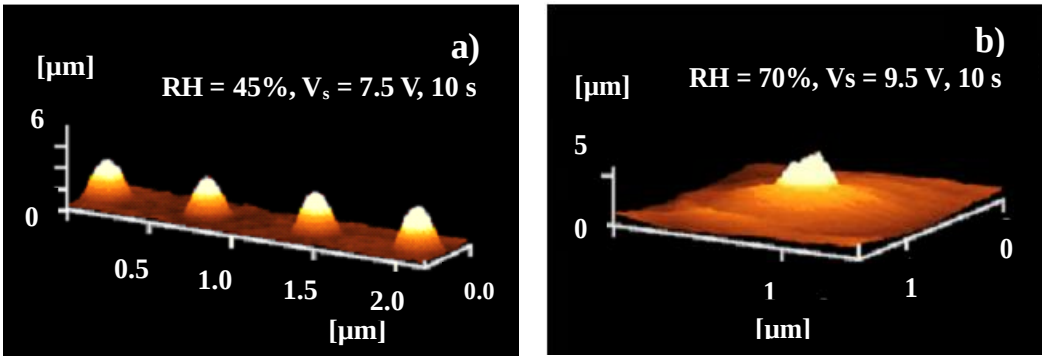


**Figure 4.7** Two AFM images of the fabricated oxide dots deposited on a H-passivated *p*-type Si (001) surface using contact mode AFM LON. a) Dome-shaped dots fabricated at RH = 45 %, $V_s$ = 7.5 V applied to a sample for *t* = 10 s. b) A two-storied shape dot fabricated RH = 70 %, $V_s$ = 9.5 V applied to a sample for *t* = 10 s [54].

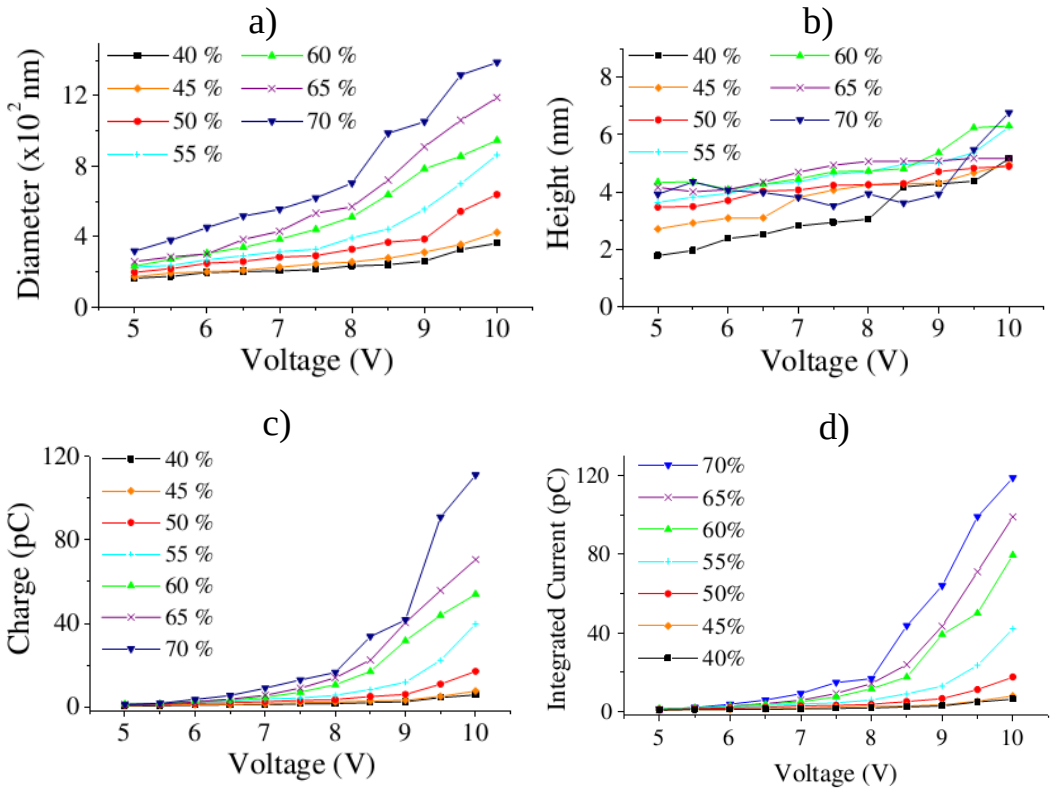


**Figure 4.8** The relationship of a) diameter and b) height of fabricated oxide dots as a function of voltage for the RH range from 40 % to 70 %. c) The expected faradaic current ($I_{exp}$) obtained from the volume of oxide dots. d) The total integrated current ($I_{int}$) during 10 s of exposure time at various values of RH. The lines in the plot c) and d) are only eye guides [54].

#### 4.1.3.2 Influence of humidity on metallic surface

The study of humidity effect on the width of titanium dioxide ($TiO_2$) line fabricated by AFM-based LON on a Ti thin film on a GaAs substrate was introduced by Held *et al.* [71] in 1998. Figure 4.9 shows a linear dependence of the full-width at half maximum (FWHM) of $TiO_2$ lines on relative humidity, with values ranging from 30 % to 65 %. The authors also explained that if the relative humidity was lower than 25 %, oxidation did not take place. In addition, they could achieve the smallest homogeneous $TiO_2$ line width with a humidity of 30 %, a scan rate of 10 µm/s and a tip bias of -4 V. In addition, Farkas *et al.* [72] reported AFM-based LON on zirconium (Zr) and zirconium nitride (ZrN) films. They found that the height of the oxide dots depended on the film composition and thickness (see Figure 4.10 a)), while the width of oxide dots was independent of material and thickness (see Figure 4.10 b)). The authors explained that different substrate compositions cause variations in wetting behaviour, different contact angles of the meniscus with the sample surface leading to different meniscus shapes. Changing the meniscus shape, therefore, results in a different electric field distribution since the meniscus is the medium in which the electric field propagates. This leads to variations in the height of oxide dots. Consequently, Figure 4.10 b) showed that the width of the oxide dots depends linearly on the relative humidity but does not depend on the film materials or thickness. Considering the height dependence, the authors also found that the oxide height increases linearly with humidity at long exposure times greater than 200 s. Furthermore, the height of the oxide dots grown on ZrN films was greater than those on Zr films by a factor of *ca.* 2.

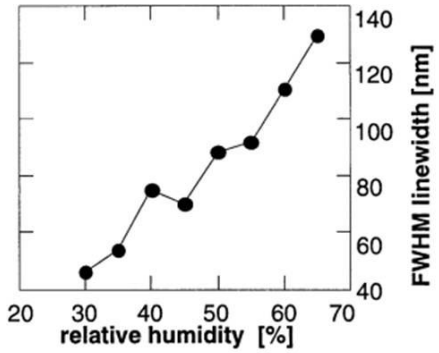


**Figure 4.9** Relationship between the relative humidity and the full-width at half-maximum (FWHM) of $TiO_2$ lines fabricated by AFM-based LON on a Ti thin-film on a GaAs substrate for a tip bias of -5.5 V, scan rate was not given [71].

a)

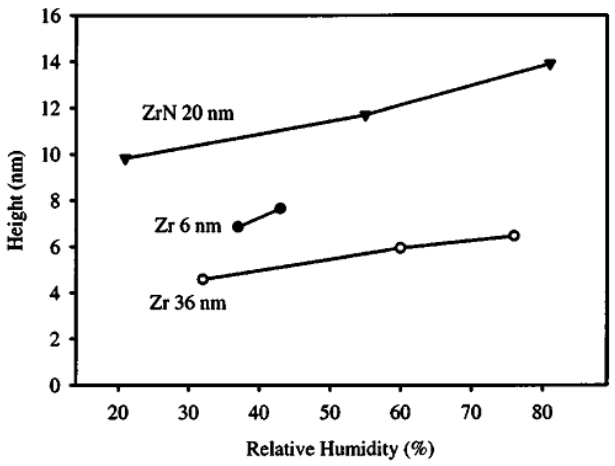


b)

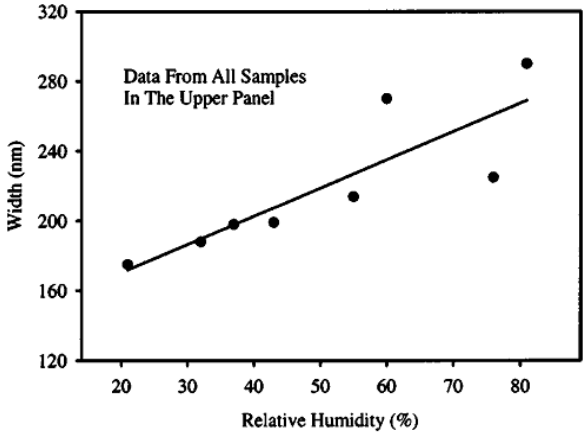


**Figure 4.10** The dependence of a) height and b) width on relative humidity for Zr and ZrN films. The applied sample voltage was 8 V and relative humidity values were studied from 21 % to 81 %. The legend in a) also indicates the film thickness in each case [72].

### 4.1.4 Influence of applied voltage

In AFM-based LON, not only is the control of the humidity in the ambient environment necessary for the oxidation process but an applied voltage or applied electrode potential is also a crucial parameter affecting the oxidation results. This is because the applied potential produces the ions and influences their transport to the surface.

#### 4.1.4.1 Influence of applied voltage on Si or native-oxide-coated Si surface

A number of studies have investigated the effect of the applied voltage [35, 73-75] on the size of the fabricated $SiO_2$ structures. One such study was performed by Tseng and Notargiacomo [73]. Figure 4.11 a) and b) are examples of AFM images showing $SiO_2$ structures in line and dot formation, respectively. The authors employed contact-mode AFM and varied the tip bias from -3 V to -9 V at a writing speed of 1 µm/s with 60 % RH. The results confirmed that the height and width of the $SiO_2$ was linearly dependent on the magnitude of the applied voltage. For example, the lateral width of the line and dot patterns, as shown in Figure 4.11 a) and b), increased from approximately 10 nm to 40 nm while the applied voltages increased from -3 V to -9 V.

The study of Pérez-Murano and co-workers [74] also demonstrated the nanoscale oxidation of Si surfaces with tapping mode AFM. They investigated the influence of the threshold voltage[3] ($V_{th}$) necessary to fabricate the modifications with respect to the tip-to-sample distance. Figure 4.12 a)-d) show the AFM images of modified Si surfaces with four different tip-surface distances (5.3, 4.4, 3.5, and 2.6 nm, respectively). They found that the $V_{th}$ was linearly affected by the average tip-to-sample distance. However, when the applied voltage was higher than $V_{th}$, the lateral dimension of the modification did not depend on the average tip-to-sample distance. In contrast, the modification dimension depended on the bias voltage. Moreover, Pérez-Murano *et al.* [74] also explained that in tapping mode the maximum value of

[3] A minimum voltage difference between tip and substrate must be applied for starting the oxidation.

the electric field is equal for the same bias voltage independently of the average tip-to-sample distance.

In the work of Ma *et al.* [75], the $V_{th}$ for the AFM-based LON on a native $SiO_2$ layer of *n*-type Si (111) wafer was *ca.* 4 V applied to the sample. The relative humidity was maintained between ~60 % and ~68 %. It was also shown that the height of the fabricated large area oxide bumps on the native $SiO_2$ layer depended linearly on the sample pulsed bias (see Figure 4.13). The linear line was fitted with the errors bar of 0.2 nm for all data from the oxide heights. A study of Fontaine *et al.* [35] showed a linear dependence on the height of $SiO_2$ stripes as a function of sample voltage as shown in Figure 4.14. These oxide stripes were fabricated by contact mode AFM LON on a H-passivated *p*-type Si (100) wafer at different scan speeds of 1, 4 and 16 µm/s. Furthermore, the results clearly showed that the slope of the graph depended on the scan speed.

The dependence of the oxide width on the applied voltage was studied by Fontaine *et al.* [35] using a simple estimation of the electric field around the AFM probe, calculated by the charge imaged method. They revealed from their estimation when the electric field was below a critical electric field value ($E_c$) as shown in Figure 4.15, the oxide strip did not grow. It was evident that the applied electric field between the tip and the surface is an important parameter for the oxidation process.

In addition, as already shown in section 4.1.3.1 of influence of humidity, the studies of Kuramochi *et al.* [48, 54] revealed that the height and diameter of the oxide dots increased with an increase of applied sample voltages (see Figure 4.6 and Figure 4.8 a) and b)).

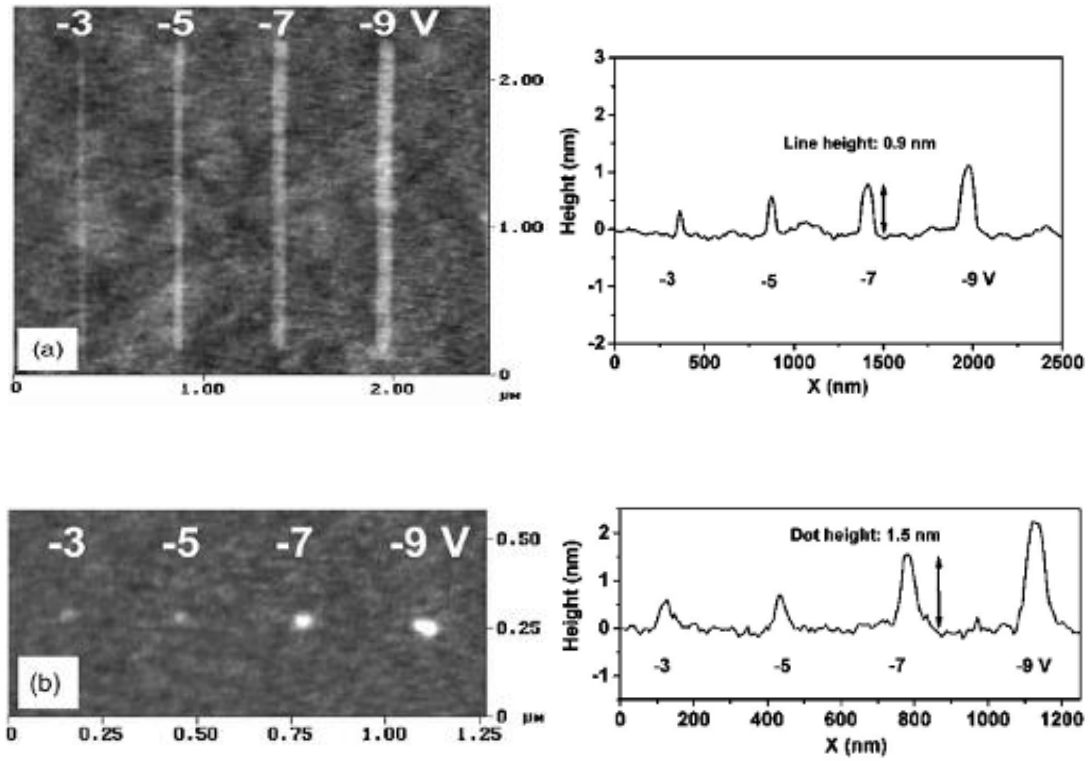


**Figure 4.11** The line and dot patterns of $SiO_2$ written by varying the bias from -3 V to -9 V with a pulse duration of 500 ms and with a 1 µm/s scanning speed with 60 % RH: a) the line patterns and b) the dot pattern of the AFM image (left) and the matching height profile (right) [73].

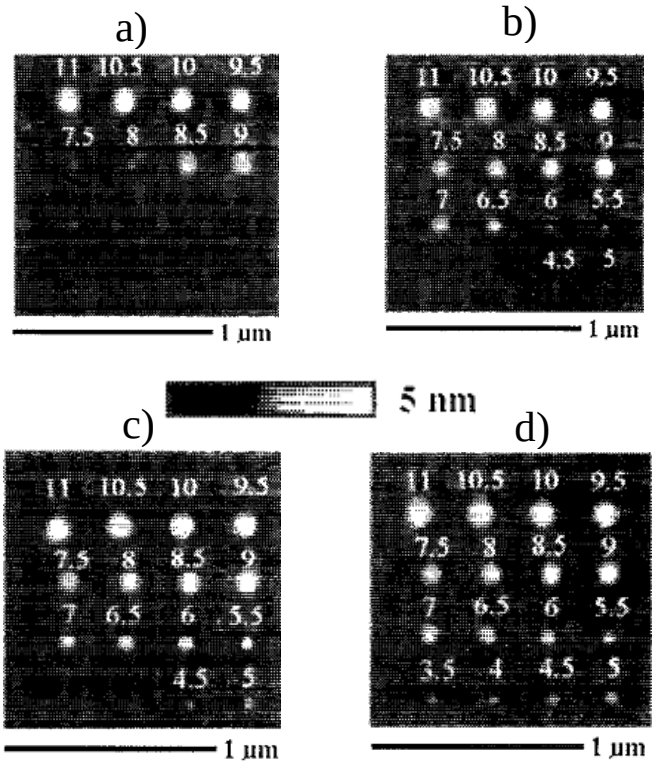


**Figure 4.12** Tapping mode AFM images of the modifications on Si surfaces with four different tip-to-sample distances: a) 5.3, b) 4.4, c) 3.5, d) 2.6 nm. The number above each dot is the positive sample bias (ranging from 3.5 V to 11 V) with pulses of 1 s [74]**.**

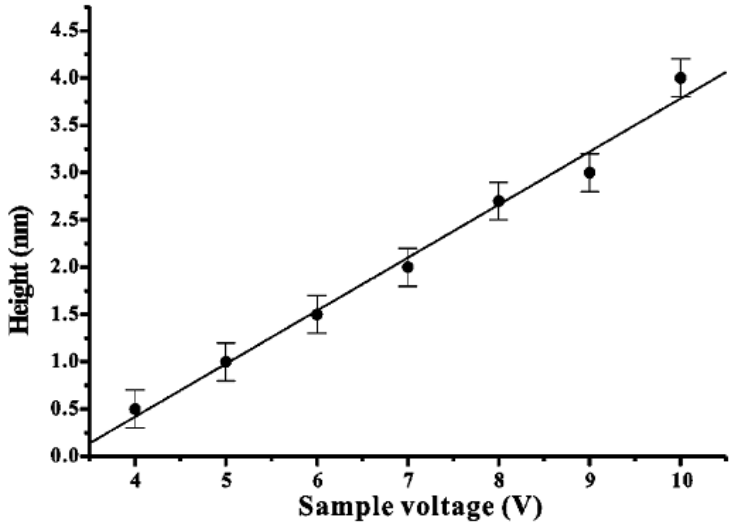


**Figure 4.13** Relationship between the sample bias and height of the fabricated large area oxide bumps on a native $SiO_2$ layer of *n*-type Si (111) wafer obtained by AFM-based LON. The relative humidity was controlled between ~60 % and ~68 % [75].

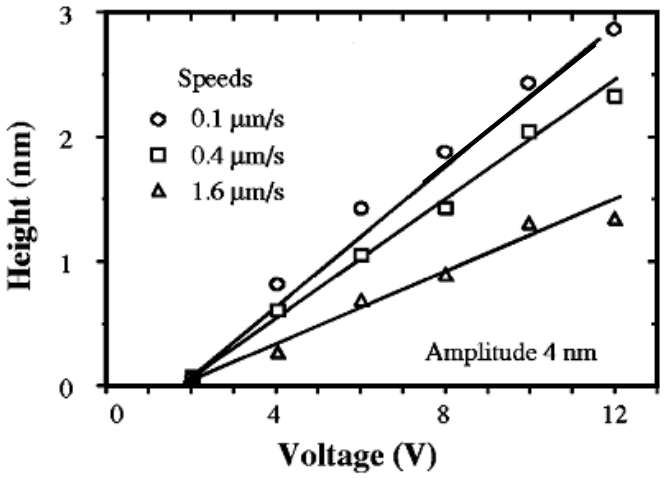


**Figure 4.14** a) Relationship between the sample bias voltage and height of the oxide stripes obtained by contact mode AFM-based LON on a H-passivated *p*-type Si (100) wafer at different scan speeds [35].

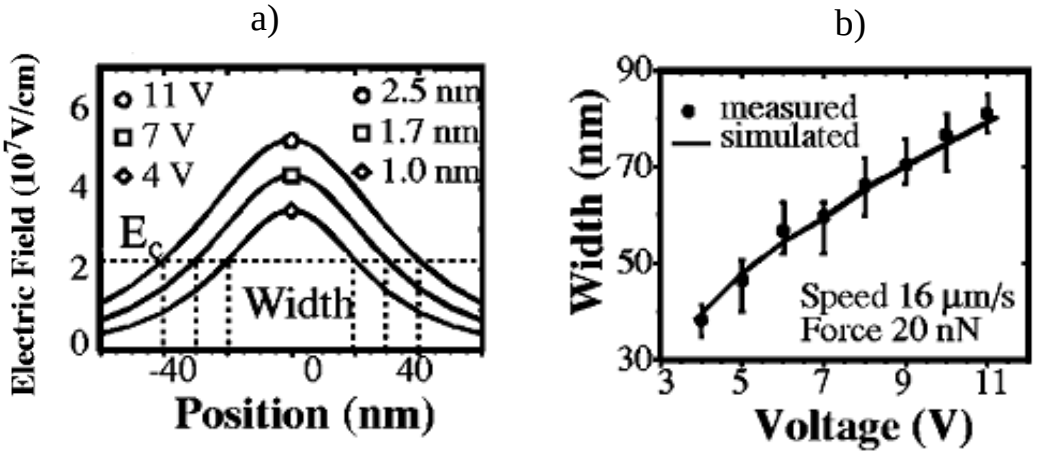


**Figure 4.15** a) Profile of the electric field at the sample surface underneath the conductive probe. b) The estimated and measured width of oxide strip fabricated by contact mode AFM on H-passivated *p*-type Si (100) at the same speed for different voltages [35].

#### 4.1.4.2 Influence of applied voltage on metallic surface

Lopour and co-workers [61] used their home-built AFM instrument to study the effect of voltage alteration on titanium oxide patterns. Figure 4.16 a) and b) show a topographic image and a corresponding profile, respectively, of fabricated $TiO_x$[4] lines on a Ti film (50 nm thickness) obtained by contact mode AFM LON with different sample voltages from 6 V to 9 V at a constant writing speed of 100 nm/s. The humidity conditions were not given in their report. The applied voltage dependence of height and half-width at a constant scan speed of 100 nm/s is shown in Figure 4.16 c). It is clear that the height ($h$) depended linearly on the applied voltage (V) with a linear equation of $h = -3.80 + 1.44$ V. This result correlated well with the study by Vullers *et al.* [62] who also showed a linear dependence of the height of the written titanium oxide lines on the applied voltage for uncoated tips and diamond coated tips. Lopour *et al.* [61] also calculated the theoretical threshold voltage from the above equation which was 2.6 V. This was too low compared to the actual threshold voltage (5 V). Therefore, they suggested that the LON process was not linear in the vicinity of its threshold value. In contrast to the height, the half-width did not show a linear dependence on the applied voltage. On the other hand, Vuller *et al.* [62] reported that they obtained a linear dependence of the width of the $TiO_x$ lines on the applied voltage without showing the data.

[4] The authors reported that the titanium oxide structures formed were a mixture of TiO and $TiO_2$.

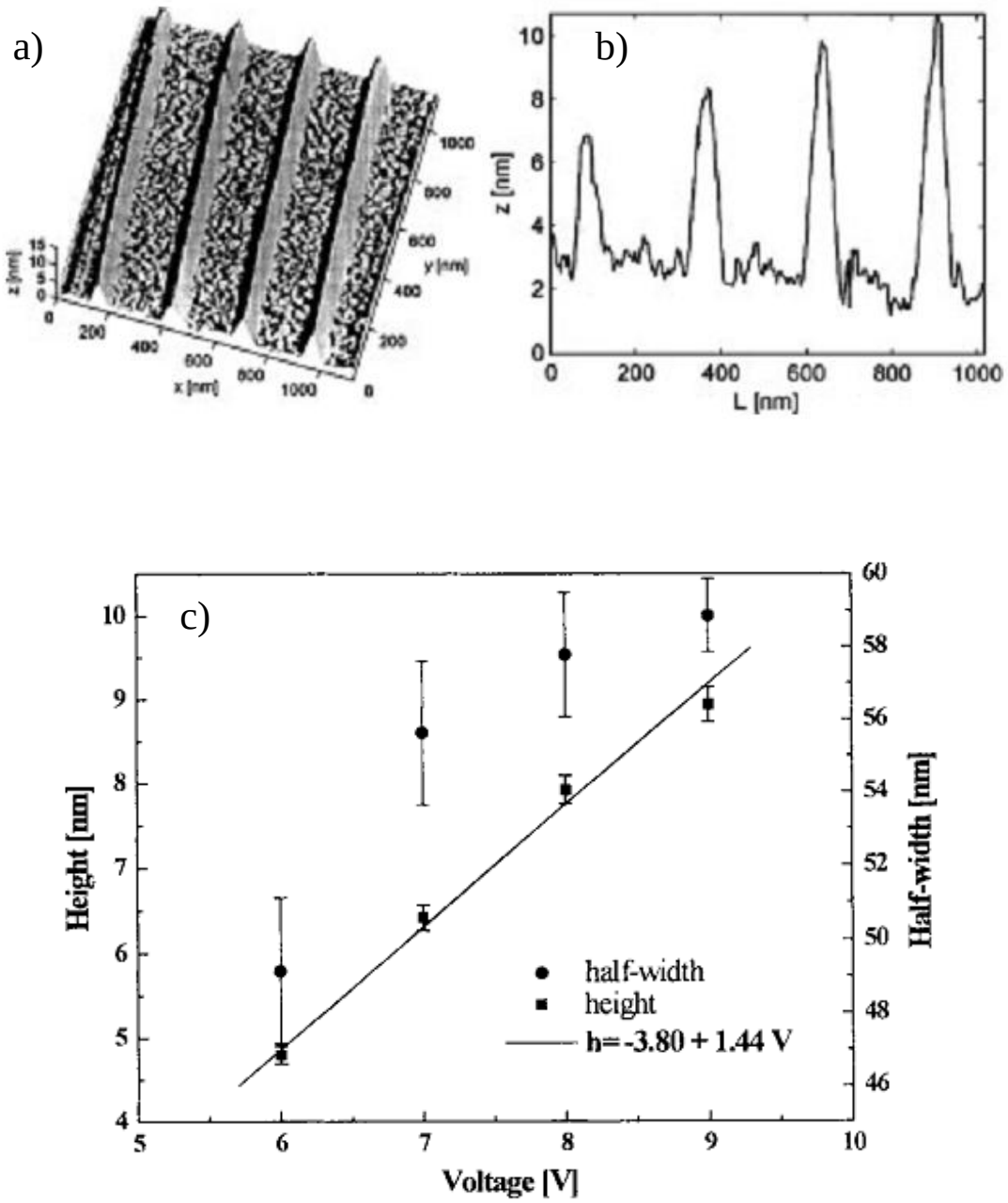


**Figure 4.16** a) AFM image and b) corresponding profile of $TiO_x$ nanowires fabricated on a 50-nm-thick Ti film with various applied sample voltages from 6 V to 9 V at a constant writing speed of 100 nm/s. c) Relationship between sample bias voltage and height (left side of the graph) and half-width (right side of the graph) of the oxide lines from a) [61].

### 4.1.5 Influence of oxidation time

#### 4.1.5.1 Influence of oxidation time on Si or native-oxide-coated Si surface

Tello and García presented a comparison of LON working in non-contact and contact mode AFM [76]. They demonstrated that non-contact AFM can produce smaller dots than contact AFM. Figure 4.17 a) and b) are the AFM images of the nano-oxide dots acquired from contact AFM and non-contact AFM respectively. They applied a pulsed voltage (-20 V) with pulse durations from 0.001 s to 3 s. The results apparently showed that the dot width depended on the pulse durations and smaller widths were obtained in non-contact AFM oxidation. The authors also illustrated other results where the dot height and aspect ratio (height/width) were dependent on pulse durations as shown in Figure 4.18 a) and b). Figure 4.18 a) shows the logarithmic dependence of the dot's height on the pulse duration time for both contact and non-contact AFM LON. In addition, for fixed pulse duration times, the dot height difference decreases with a decrease of the applied voltage. They found that non-contact AFM was able to fabricate oxide dots which were greater in both height and aspect ratio. They discussed two possible reasons for these observations. The first suggestion was the controllability of the lateral size of the water meniscus in non-contact AFM. Another potential cause was related to the higher mechanical energy required by contact AFM in order to deflect the cantilever, leading to the smaller vertical growth rate in contact AFM.

A study of kinetic measurements by Avouris *et al.* [77] is displayed in Figure 4.19. The height of the oxide dots fabricated by AFM-based LON on *n*-type Si (100) wafer for different tip voltages of -5 V, -10 V and -20 V at about 50% ambient humidity was plotted as a function of the voltage pulse duration ($t$). The oxide growth rate decreases rapidly with time, as $1/t$, as seen from the fits of the data. The authors reported that no clear bias threshold was observed.

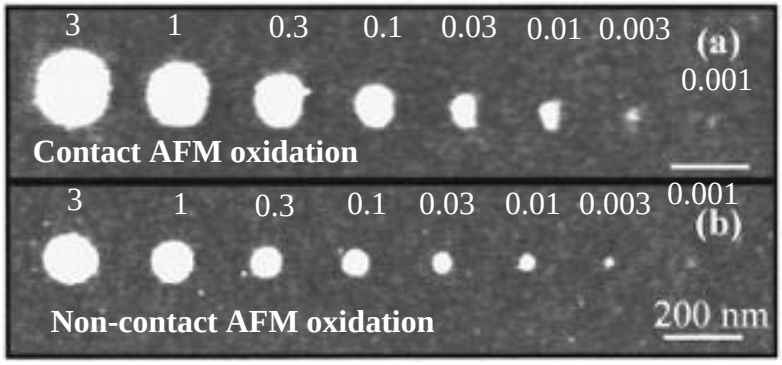


**Figure 4.17** AFM images of nano-oxide dots produced with different pulse durations: 3, 1, 0.3, 0.1, 0.03, 0.01, 0.003, and 0.001 s, with a constant voltage bias of 20 V (negative tip) and a relative humidity of 36 %. a) contact AFM LON and b) non-contact AFM LON [76].

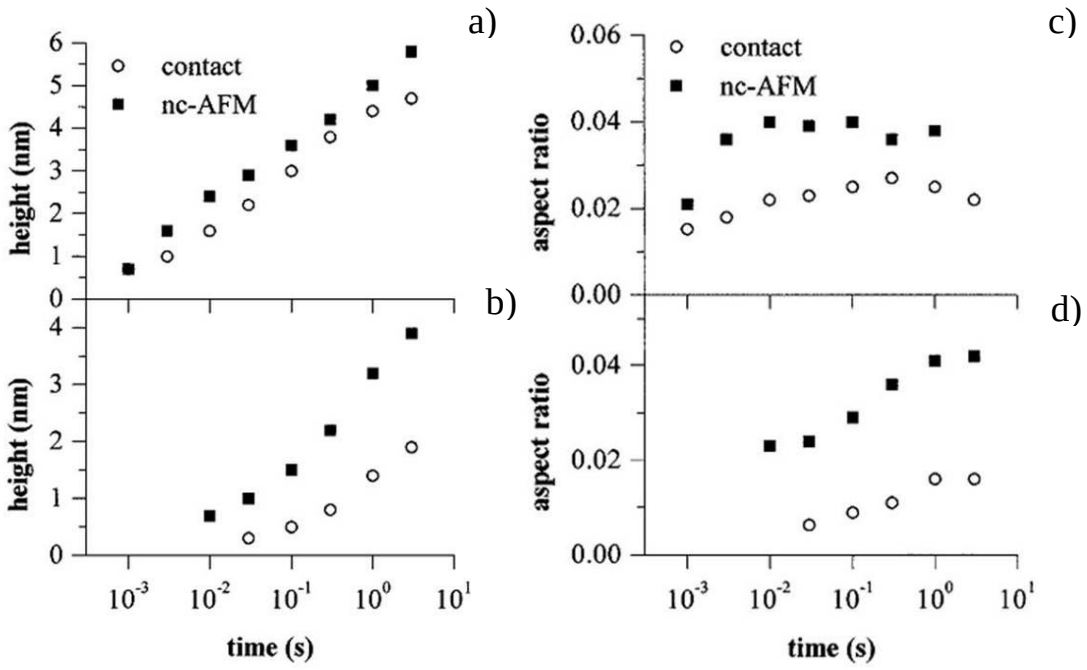


**Figure 4.18** (Left) Relationship of pulse duration time and oxide dot height obtained by contact AFM and non-contact AFM (nc-AFM) LON with a negative tip voltage of a) 20 V and b) 14 V and a relative humidity of 36 %. (Right) Relationship of pulse duration time and aspect ratio (height/width) produced by contact AFM and non-contact AFM LON with a negative tip voltage of c) 20 V and d) 14 V and a relative humidity of 36 % [76].

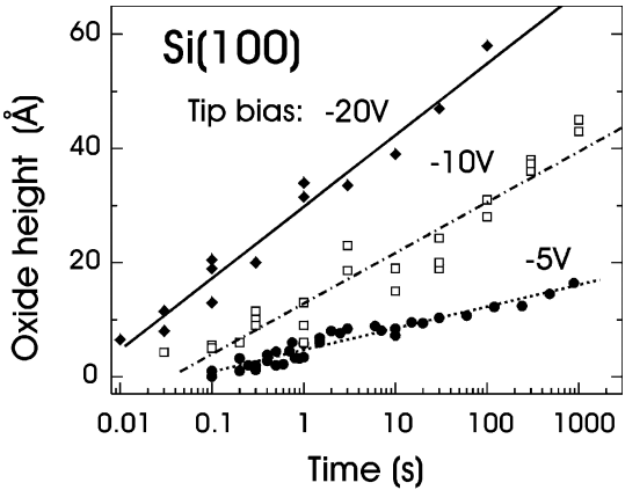


**Figure 4.19** a) Relationship between the voltage pulse duration (time) and height of the oxide dots fabricated by AFM-based LON on *n*-type Si (100) wafer for different tip voltages of -5 V, -10 V and -20 V at about 50 % ambient humidity [77].

#### 4.1.5.2 Influence of oxidation time on metallic surface

Fang *et al.* [78] studied the effect of oxidation (anodization) time on the height and width of fabricated $TiO_2$ nanodots. Figure 4.20 a) shows an AFM image of $TiO_2$ dots obtained by non-contact AFM based LON on 50-nm-thick Ti films coated on a *p*-type Si (100) substrate for various applied static sample voltages of 7, 8, 9, and 10 V with different anodization times of 0.5, 1, 2, 5, and 10 s at a relative humidity of 65 %. The authors noted that a longer anodization time and a larger anodization voltage resulted in larger and taller oxide dots (see Figure 4.20 a)). Figure 4.20 b) and c) illustrate the oxide height and oxide width at different static sample voltages ranging from 7 V to 10 V as a function of the anodization time, respectively. It can be seen that both oxide height and width depend logarithmically on anodization time and also increase with increasing applied voltage. Fang and co-workers [78] suggested that the observed relationship between the $TiO_2$ height and the anodization time involved field-assisted oxidation of very thin films as described by Kim *et al*. [79].

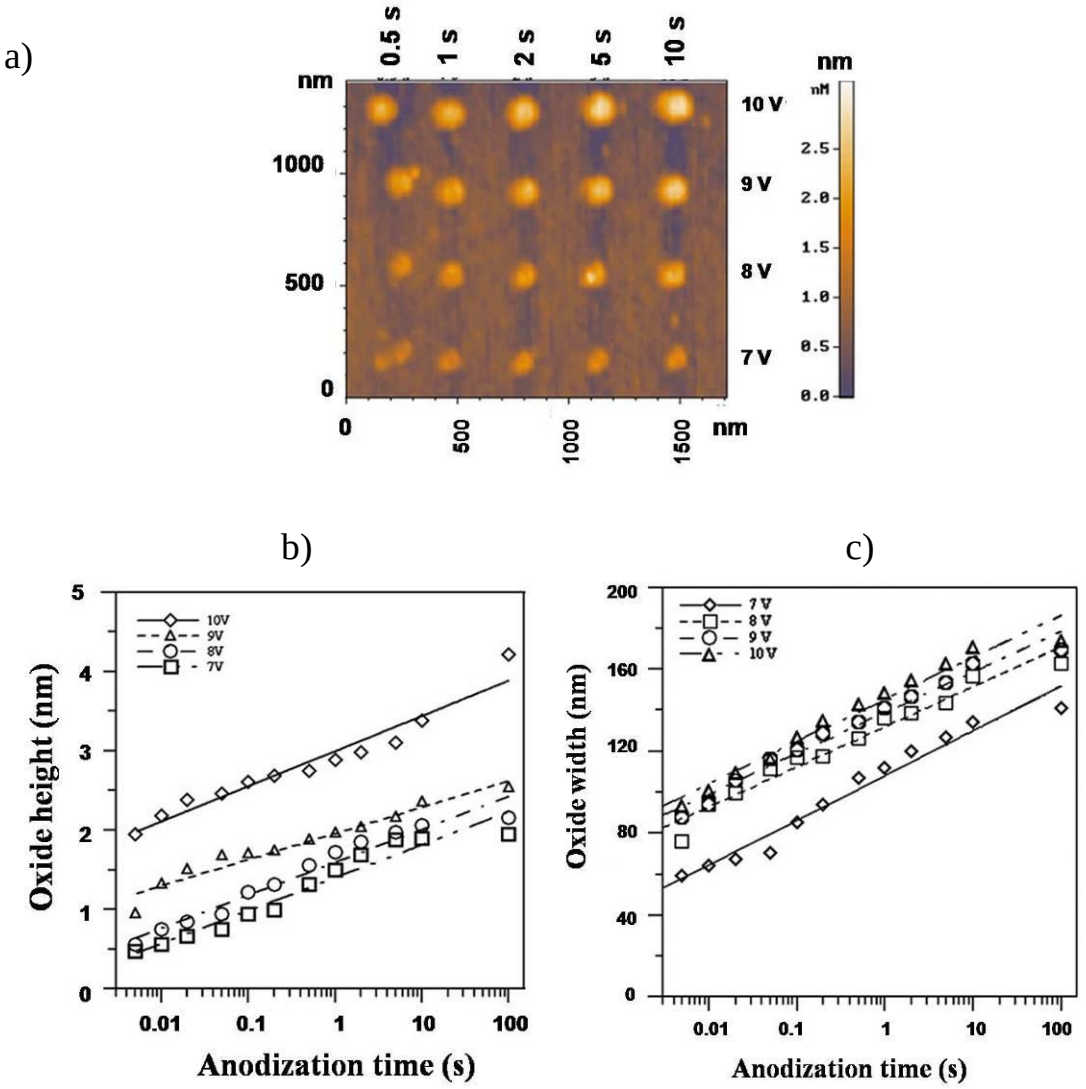


**Figure 4.20** a) AFM image of a sequence of $TiO_2$ nanodots fabricated by AFM based LON on 50-nm-thick Ti films coated on a *p*-type Si (100) wafer for various applied static sample voltages of 7, 8, 9, and 10 V under different anodization times of 0.5, 1, 2, 5, and 10 s at a relative humidity of 65 %. b) Relationship between anodization times and the height of the $TiO_2$ dots during the oxidation process. c) Relationship between anodization times and the widths of the $TiO_2$ dots during the oxidation process [78].

### 4.1.6 Influence of scan speed

For line or structure formation, the scan speed of the tip plays a key role in the LON. Consequently, an appropriate study of scan speed to achieve the optimal oxidation of structures is required.

#### 4.1.6.1 Influence of scan speed on Si or native-oxide-coated Si surface

Fontaine *et al.* [35] studied the effect of the AFM tip scan speed on the height of fabricated oxide stripes generated by contact mode AFM LON on a H-passivated *p*-type Si (100) at various sample bias values ranging between 4 V and 12 V as shown in Figure 4.21. The oxide height shows a logarithmic decrease with an increase of writing speed for each sample voltage. The authors also observed that an average slope was approximately 0.5 nm per decade for each voltage. They also calculated that a threshold speed which is the minimum speed to initiate the oxide growth ranged from 200 μm/s for 4 V up to 0.1 m/s for 12 V for a threshold height of 0.3 nm.

Kuramochi *et al.* [48] also showed the dependence of the height of the oxide lines as a function of the tip speed ranging between 125 nm/s and 1250 nm/s as shown in Figure 4.22. The oxide lines were fabricated by applying a constant sample bias of 6 V with different relative humidity values ranging from 40 % to 80 % on a native-oxide layer on a *p*-type Si (001). Kuramochi and co-workers [48] found that the oxide line height decreased with increasing the tip speed.

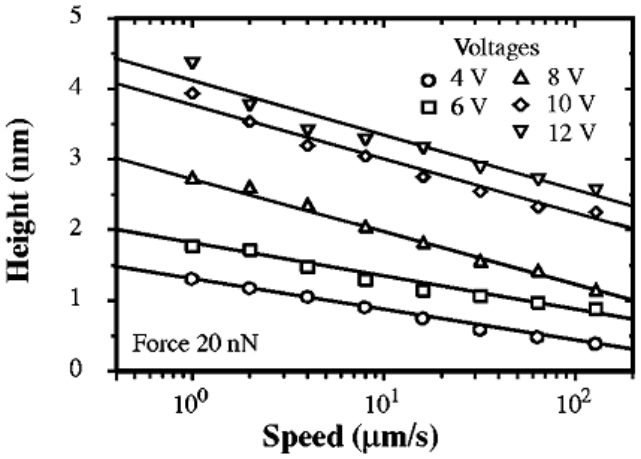


**Figure 4.21** a) Relationship between the tip scan speed and height of the oxide stripes fabricated by contact mode AFM-based LON on a H-passivated *p*-type Si (100) wafer at different sample voltages ranging from 4 V to 12 V [35].

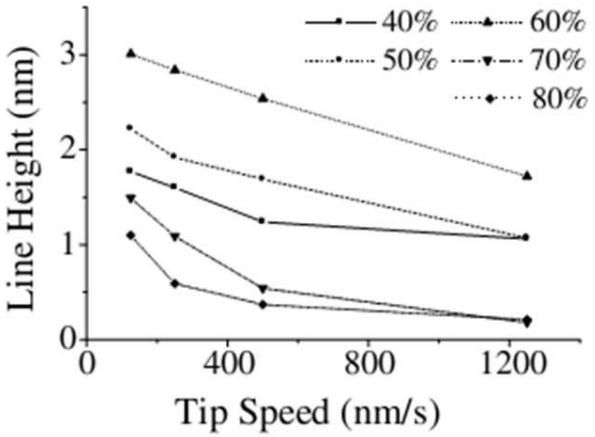


**Figure 4.22** a) Relationship between the tip scan speed and height of the oxide lines fabricated by contact mode AFM-based LON on a native-oxide layer on a *p*-type Si (001) at different relative humidity ranging from 40 % to 80 %. The sample voltage was maintained at 6 V [48].

#### 4.1.6.2 Influence of scan speed on metallic surface

Lopour *et al.* [61] showed the dependence of height and half-width of the titanium oxide (a mixture of TiO and $TiO_2$) lines obtained by contact mode AFM LON at a constant voltage of 6 V on writing speed as shown in Figure 4.23. Lopour *et al.* [61] reported that the height ($h$) of $TiO_x$ lines linearly decreased with the

writing speed ($v$) which could be expressed by this equation: $h = 4.41 - 1.51v$. However, we found that the graph is in the logarithmic scale which means that the height show the logarithmic dependence on the scan speed. Their results were similar to the results of Vullers *et al.* [62]. Figure 4.24 shows the logarithmic dependence of the height of the titanium oxide lines fabricated by contact mode AFM LON with different scan speed values at a constant applied sample voltage on the writing speed reported by Vuller *et al.* [62]. However, the half-width as shown in Figure 4.23 did not show a linear decrease on a linear-logarithmic scale when the writing speed was increased.

Another study of scan rate influence on the width of titanium oxide lines fabricated by AFM-based LON on a Ti thin film on a GaAs substrate was observed by Held et *al.* [71]. The full-width at half maximum (FWHM) of titanium oxide lines significantly decreased with an increase of a scan rate from 1 μm/s to 3 μm/s as shown in Figure 4.25. FWHM of titanium oxide lines was then found to reach a plateau with an increase of a scan rate above 3 μm/s.

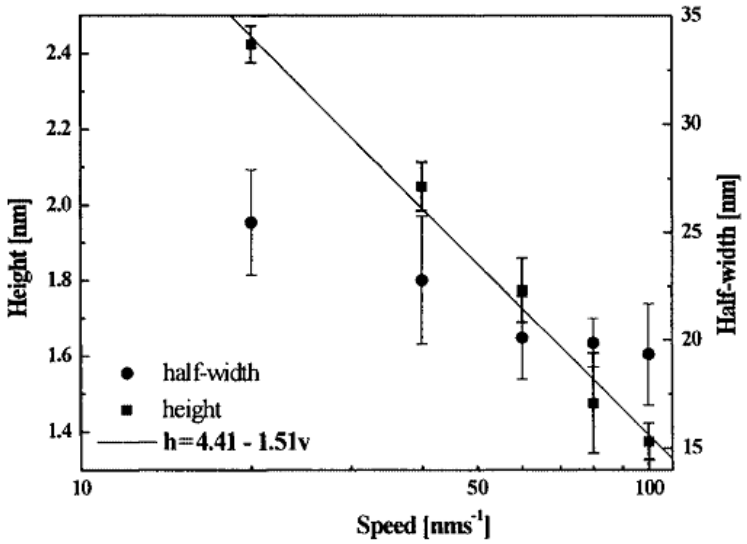


**Figure 4.23** Relationship between the scan speed and height (left side of the graph) and half-width (right side of the graph) of $TiO_x$ lines fabricated on a 8-nm thick Ti film by contact mode AFM LON with various writing speed values at a constant sample voltage of 6 V [61].

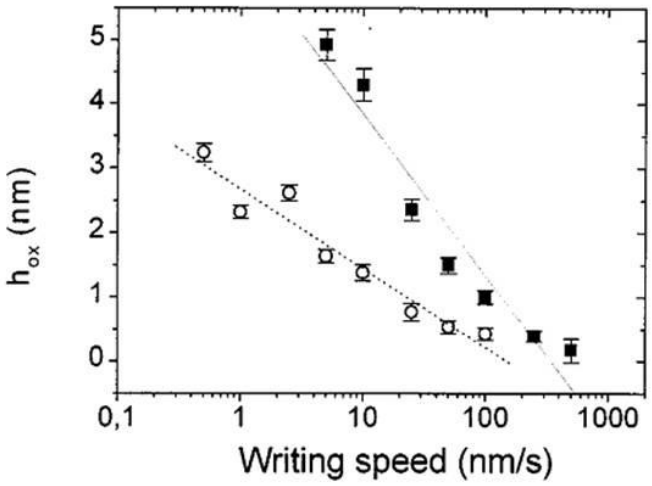


**Figure 4.24** Relationship between the writing speed and height of $TiO_x$ lines fabricated on a Ti film by contact mode AFM LON with various writing speed values at a constant sample voltage. No value for the bias voltage was given. The relative humidity was roughly stated that their experiments took place under a relative humidity between 40 % and 60 %. Data are shown for uncoated tips (■) and for diamond coated tips (○) [62].

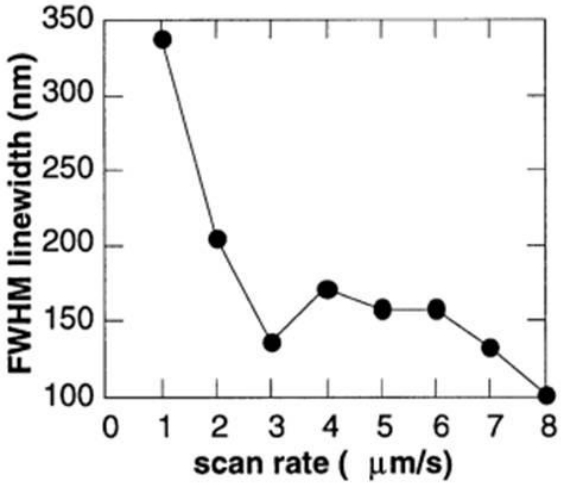


**Figure 4.25** Relationship between the scan rate and full-width at half maximum (FWHM) of titanium oxide lines fabricated on a Ti film on a GaAs substrate by contact mode AFM LON with various scan rate values at a constant tip bias of -5.5 V. The relative humidity was not stated [71].

### 4.1.7 Local oxidation nanolithography of Mo

Relatively few studies have been published on the AFM-based LON on molybdenum (Mo) layers. Since this is a main topic of the thesis, the prior work on Mo is discussed below although there have been no systematic studies of using parameter. The first report of the AFM-based LON of Mo was given in 2002 by Rolandi *et al*. [80]. They showed the fabrication of a molybdenum (VI) oxide ($MoO_3$) pattern obtained by tapping mode AFM LON of a Mo thin-film on a *p*-type Si (100) substrate and subsequently performed etching of the nano-oxide of $MoO_3$ by water dissolution. The molybdenum oxide structures were found to be of the $MoO_3$ form since the authors described that only this form can be dissolved in water while $MoO_2$ and $Mo_2O_5$ forms are insoluble in water. The solubility of $MoO_3$ can be found from the *CRC* Handbook of Chemistry and Physics [81].

Figure 4.26 a) shows an AFM image of 35 nm wide and 8 nm high of $MoO_3$ stripes (the bright lines) obtained by tapping mode AFM LON with a scan speed of 1 µm/s and a positive sample bias of 10.5 V on 4 nm thick Mo on *p*-type Si (100) substrate. These authors also showed Mo LON on a Mo/poly(methylmethacrylate) (PMMA) on top of a $SiO_2$ surface. Figure 4.26 b) illustrates an AFM image of ~ 30 nm wide $MoO_3$ lines written with tapping-mode AFM LON with a scan speed of 0.7 µm/s and a positive sample bias of 9.5 V on Mo/PMMA on an insulating $SiO_2$ substrate. These results demonstrated the versatility of the AFM-based LON method on either Mo thin films or Mo/polymer bilayer nanomasks for further chemical etching and lift-off processes on Si and $SiO_2$ substrates. However, in their report, they only suggested the suitable conditions for LON process with a scan rate ranging between 0.4 µm/s and 1 µm/s and an applied sample bias varying from 7 V to 11 V without showing a systematic study of these parameters.

Goto *et al.* [82] later exploited LON on a Mo surface to obtain Mo-oxide as a nanomask for further fabrication of $Fe_{2.5}Mn_{0.5}O_4$ (FMO) ferromagnetic oxide nanostructures. In the report of Pellegrino *et al.* [83], a $MoO_3$ pattern fabricated by AFM based LON on Mo/PMMA bilayer was also used as resist nanomask patterning of $(Fe,Mn)_3O_4$ (FMO) thin films.

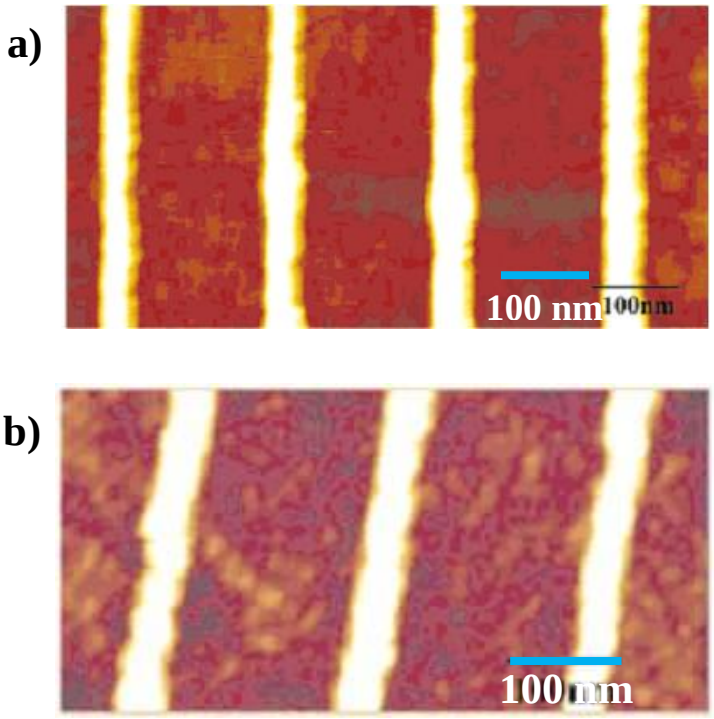


**Figure 4.26** a) AFM image of *ca.* 35-nm-wide $MoO_3$ lines fabricated by tapping-mode AFM LON on a 4 nm thick Mo film on *p*-type Si (100) substrate with a scan speed of 1 µm/s and a positive sample bias of 10.5 V. b) AFM image of *ca.* 30-nm-wide $MoO_3$ lines obtained by tapping-mode AFM LON of a 4 nm thick Mo/PMMA bilayer resist on insulating $SiO_2$ substrate with a scan speed of 0.7 µm/s and a positive sample bias of 9.5 V [80].

## 4.2 Motivation

As already discussed above, AFM-based LON has successfully been shown to create nanoscale structures with high resolution on various material surfaces especially on native-oxide-coated Si and Mo substrates. Moreover, nanoscale features can be achieved with optimal resolution with a cost effective technique compared to electron beam lithography (EBL). In addition, the oxide features fabricated by AFM-based LON can be used as markings for further experiments. To begin with the study of the AFM-based LON on materials, one option would be Si substrates since Si substrates have been intensively used in nanoelectronic and microelectronic applications with the patterning surface for a certain purpose. Moreover, a number of publications of the AFM-based LON on Si substrates have been well studied and they would not be difficult to understand the mechanism and effects of using parameters for nanooxidation. However, only the small numbers of publications have been shown concerning systematic studies of the parameters for AFM-based LON on native-oxide-coated Si substrates without surface modification and functionalisation. Therefore, a systematic study of the parameters for AFM-based LON on native-oxide-layer Si substrates would be beneficial for fundamental understanding of the mechanism.

Another option would be Mo substrates since the AFM-based LON of Mo can be used as nanomasks for the patterning of structures on Si or $SiO_2$ substrate. Up to now, there have been no systematic and mechanism studies about the effects of using parameter on Mo substrates. Even though, the study of Rolandi *et al*. suggested the suitable conditions for AFM-based LON process but they did not show a systematic study of parameters such as scan rate, relative humidity and applied voltage. Furthermore, until now, there have been no examples of direct current detection during AFM-based LON on Mo substrates presented, due to the difficulty of detecting the low current on the order of *p*A-nA. TUNA measurement is used to study the current passing through the substrate to the conductive AFM tip during the oxidation process.

The aim of the following sections of this chapter is to investigate the factors which influence the height and width of the oxide features, for example, the applied voltage, scan speed, type of AFM tip, ramping time[5] and humidity in order to achieve the optimal oxidation efficiency. For the initial investigation, comparisons of different tip voltages and different scan speeds were studied on nanoscale line features on a native-oxide-coated Si surface. Then the study moves onto a comparison of arrays of nanodots with different AFM tip effects. After that, the influence of applied voltage, humidity and ramping time was studied for dot formation making a comparison between native-oxide-coated Si and Mo surfaces.

[5] The ramping time is the period of one cycle of the AFM tip moving towards and away from the sample.

## 4.3 Results and discussion

### 4.3.1 Influence of voltage

#### 4.3.1.1 Oxide pattern as a function of voltage

In order to study the effect of the applied voltage on the oxidation process, pattern geometry was studied as a function of the voltage applied to the tip. Figure 4.27 shows a series of different oxide patterns obtained by contact mode AFM LON. The nanopatterns were fabricated using a PtIr-coated Si tip (SCM-PIC, see Table 4.1) with a normal tip radius of about 20 nm and a force constant of 0.2 N/m [23] with a tip speed of 1 μm/s. Additionally, the applied tip voltage was varied from -1 V to -9 V as depicted in the values above each pattern with a relative humidity of 51 ± 5 % on the native-oxide layer on top of an *n*-type Si (100) substrate. We can see immediately that with a negative bias applied to the tip of less than -4 V the oxide patterns were not obtained. Consequently, in this observation, -4 V is the threshold voltage ($V_{th}$) for oxidation.

With an applied negative bias above -4 V, oxide features were clearly generated and imaged as protrusions on the native $SiO_2$ surface. Some of the oxide patterns exhibited defects during the oxidation process as shown in the 3-D image (Figure 4.27 a)). Figure 4.27 b) and c) present the AFM image and the corresponding profile (the height and width) of the oxide features in a horizontal direction, respectively. Considering the height, when the negative bias applied to the tip was increased from -4 V to -9 V, the height also gradually increased from approximately 0.23 nm to 1.90 nm. The half-width also increased steadily from *ca.* 150 nm to 300 nm. From this preliminary investigation, it is clear that the height and the width of the oxide structure depend on the value of the applied voltage. This was well correlated with a previous report of Hattori *et al.*[84] who showed that both oxide strip height and width (FWHM) increased with the applied voltage. Such oxide strips were fabricated by AFM-based LON with a positive bias applied to a native-oxide-coated *n*-type Si (111) substrate.

In order to gain a deeper understanding about factors influencing the oxide height and oxide width for the oxidation process, several strips were produced by contact mode AFM LON on the native-oxide-layer-coated *n*-type Si (100) surface. Such strips were created using a PtIr-coated Si tip (SCM-PIC, see Table 4.1) with a normal tip radius about 20 nm and a force constant of 0.2 N/m [23]. A constant tip velocity of 1 μm/s was used with varying applied voltages to the tip, the value of which is shown above each strip (increased from -5 V to -10.5 V) in Figure 4.28. This measurement was performed with a relative humidity of 51 ± 5 %. The dependence of the height and half-width of the oxide strips as a function of voltage corresponding to Figure 4.28 is demonstrated in Figure 4.29 a) and b), respectively. The half-width measurement is shown in Figure 4.29 c). The right hand side of the oxide structure appeared broader than the left hand side because of too fast scan speed (the tip scanned from left to right). The width of the left hand side was taken as being a more accurate value. We can see that the heights (h) of the oxide patterns increase linearly when greater negative bias (V) is applied to the tip, which is expressed by equation (7) (see Figure 4.29 a)):

$$h = (-0.16 \pm 0.01)\ V - (0.64 \pm 0.08) \qquad (7)$$

$$\text{For;} \quad V = -5, -5.5, -6, \ldots, -10.5$$

From equation (7), the slope was equal to -0.16 ± 0.01 which means the height increased by 0.16 nm/V with increasing negative bias applied to the tip. Furthermore, the theoretical threshold voltage obtained from the equation (7) was -4.0 ± 1.6 V in good agreement with the above result in Figure 4.27. Our threshold voltage result was in good agreement with the report by Ma *et al.* [75] who also found that a $V_{th}$ value was approximately +4 V applied to the substrate, for AFM-based LON on the native $SiO_2$ layer on a Si (111) wafer. However, the difference was that they used a pulsed voltage, whereas a dc voltage was used here. Nevertheless, in the case of considering some studies with different sample surfaces but similar doping (*n*-type) Si substrate, our threshold voltage value was not consistent with the study of Fontaine *et al.* [35] who found that the typical threshold voltage on H-passivated *n*-type Si (100) was *ca.* 0.0 V using a silicon nitride AFM

cantilever. Fontaine *et al.* [35] reported that for the experiments of *n*-type substrates, no clear difference of the threshold voltage (below 1 V) on the doping level was found. As a result of this consideration, different surfaces were assumed to have an influence on the values of the threshold voltage.

Considering the height dependence on the voltage, our result was in good agreement with the study of Ma *et al*. [75] as already discussed in section 4.1.4.1. As illustrated in Figure 4.13, Ma *et al.* [75] also showed a linear dependence of the height of the fabricated large area oxide bumps on the sample pulsed bias. These oxide bumps were fabricated on the native-oxide-layer-coated *n*-type Si (111) at the relative humidity values ranging from 60 % to 68 %. In comparison to the oxide height obtained by the study of Ma *et al.* [75] at the same applied voltage, the heights of oxide strips obtained by our experiment were much smaller than that of Ma *et al.* for all voltage values. The possible reasons for this could be affected by many factors. For example, first, the different types of applied voltage used were dc voltage in our case and ac modulation for the study of Ma and co-worker [75]. Several studies have suggested that increasing oxide thickness could decrease the electric field by this relation $E = V/x$ and this resulted in the significant reduction of the oxide height when using the dc voltage. Moreover, it can be further explained by the influence of the space charge effect as reported by Dagata *et al.* [64], Pérez-Murano *et al.* [85], and Park *et al*.[86] that applying ac modulation to the substrate could change in the electrical properties of the oxidation process. Furthermore, the space charge that was built up within the growing oxide was reduced and the spatial extent of the water meniscus was also reduced when using the ac modulation. This led to the effective increase in the oxide height when applying ac modulation compared to applying the dc voltage. Another factor that could be affected was the relative humidity. In our experiment, the relative humidity was maintained at $51 \pm 5$ %. In contrast, Ma *et al.* [75] studied at a relative humidity of 60 – 68 %. This also caused a smaller of the oxide heights in our results. For the humidity effect, this will be discussed in more details in section 4.3.4.

Our result was also similar to a study by Stiévenard *et al.* [87] who showed a linear dependence of the height as a function of the voltage applied to the sample.

They performed AFM-based LON with various sample bias ranging from 4 V to 10 V with a relative humidity of 70 % and studied oxidation on H-passivated *p*-type Si (100) wafers. Additionally, Fontaine *et al.* [35] also reported a linear dependence of the oxide height on the voltage range from 2 V to 12 V applied to the sample with respect to the grounded tip, with various tip speeds. They also showed that the tip speed can influence the slope of the linear fit. As a consequence, taking our result and several relevant studies into consideration, it can be established that the oxide height is linearly dependent on the applied bias.

Considering the half-widths (HW) of the oxide structures, they were also found to depend linearly on the tip voltage according to the following equation as shown in Figure 4.29 b):

$$HW = (-0.016 \pm 0.003)\ V + (0.093 \pm 0.027) \quad (8)$$

For; V= -5, -5.5, -6, -6.5, …, -10.5

Our observation was well correlated with the study of Fontaine *et al.* [35]. As already discussed earlier in Section 4.1.4.1 (see Figure 4.15 b)), Fontaine and colleague [35] also showed the linear dependence of the oxide width on the applied voltage using a simple estimation of the electric field around the AFM probe. They revealed from their estimation when the electric field was below a critical electric field value ($E_c$) as shown in Figure 4.15 a), the oxide strip did not grow. It was evident that the applied electric field between the tip and the surface is an important parameter for the oxidation process and considerably influence the oxide width.

a)

b)

c)

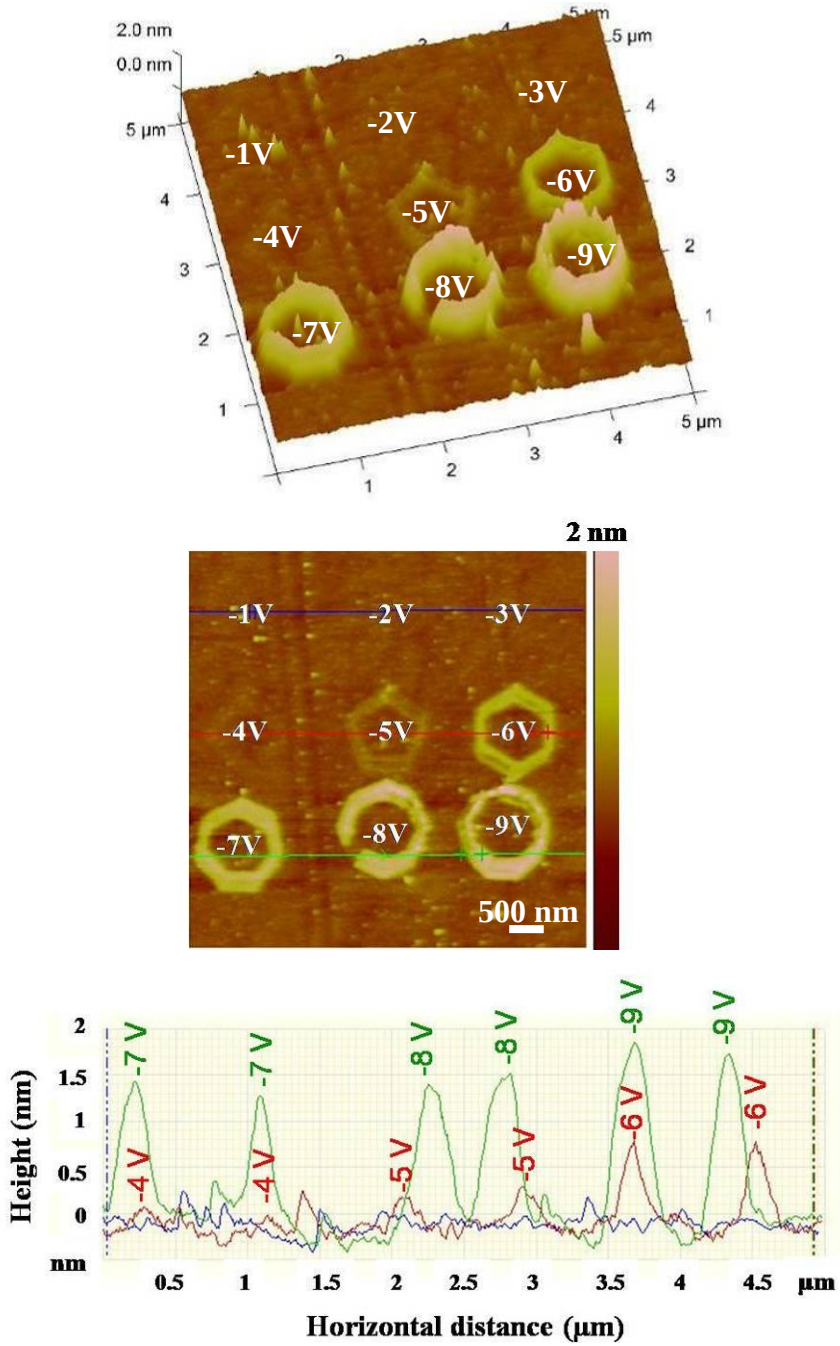


**Figure 4.27** AFM images of a sequence of local oxidation patterns fabricated by contact mode AFM LON using a PtIr-coated Si tip (SCM-PIC). A normal tip radius about 20 nm and a force constant of 0.2 N/m was used with different applied tip voltages ranging from -1 V to -9 V at a constant scan speed of 1 µm/s and a relative humidity of 51 ± 5 % on a native-oxide layer covered on the *n*-type Si (100) wafer: a) the 3-D AFM image, b) the topographic image and c) the corresponding height and width profiles of the oxide patterns.

**Table 4.1:** Typical properties of different AFM tips used for investigation in this chapter.

| *Type* | *Coating* | *Tip radius (nm)* | *Force constant (N/m)* | *Resonance frequency (kHz)* |
|---|---|---|---|---|
| SCM-PIC | Pt/Ir | 20 (max ~ 25) | 0.2 (0.1 – 0.4) [(a)] | 13 ± 3 |
| ElectriTap300-G | Cr/Pt | <25 | 40 (20 - 75) | 300 ± 100 |
| MESP | Co/Cr | 25 (max ~ 50 ) | 2.8 (1.0 - 5.0) | 75 ± 25 |
| FMG01-Co | Co/Cr | 40 | 3.0 (1.0 - 5.0) | 60 ± 10 |
| NSG01-Co | Co/Cr | 6 (guaranteed 10 ) | 5.1 (1.45 - 15.1) | 150 ± 72 |
| NSG01-Pt | Pt | 6 | 0.6 (0.13 - 2.0) | 48 (26 – 76) |

**[(a)] The value in a bracket represents the range between the minimum and maximum value.

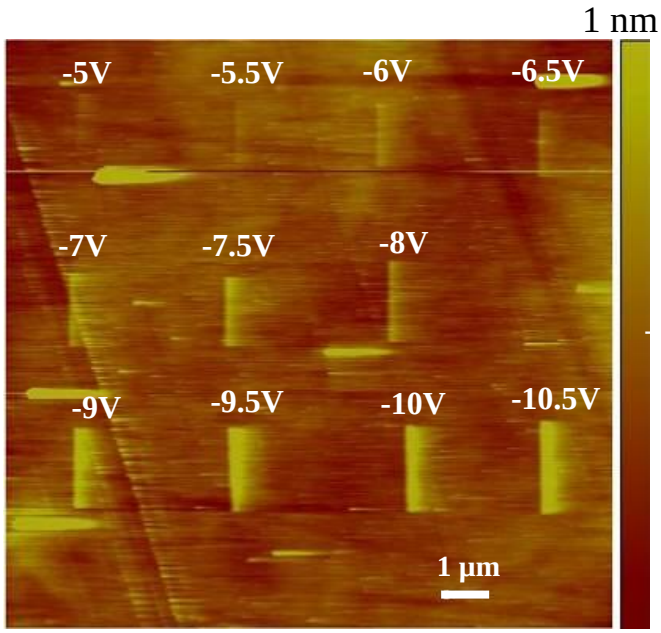


**Figure 4.28** AFM image of oxide strips obtained by contact mode AFM LON on a native-oxide-layer-coated *n*-type Si (100) using a PtIr-coated Si tip (SCM-PIC). A normal tip radius of about 20 nm and a force constant of 0.2 N/m were used with different applied tip voltages ranging from -5 V to -10.5 V (the values depicted above each strip) at a constant scan speed of 1 µm/s with a 51 ± 5 % RH.

a)

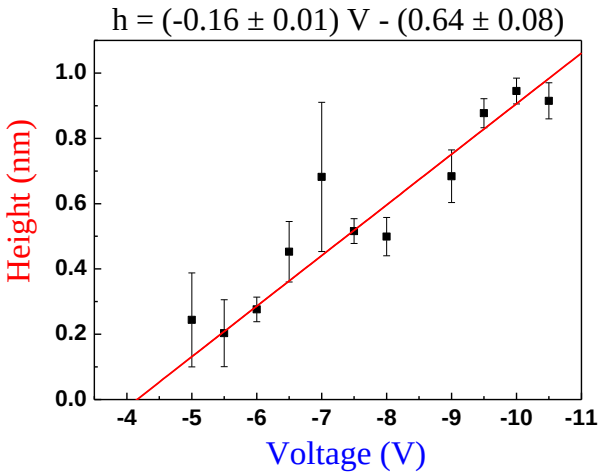


b)

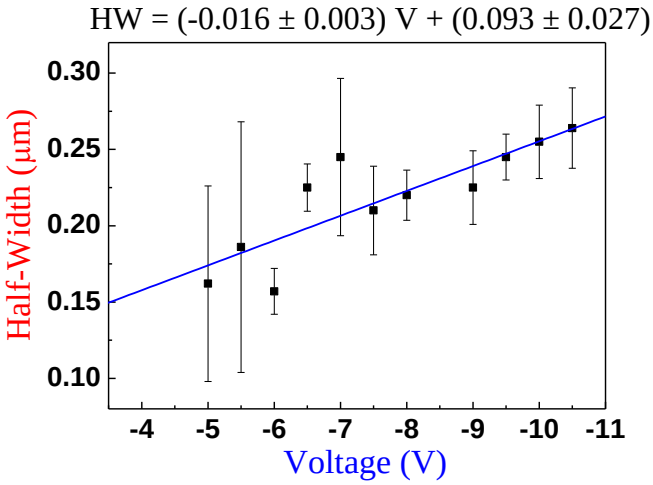


c)


**Figure 4.29** The dependence of the height (a) and half-width (b) of the oxide lines as a function of the tip voltage. The data were measured from Figure 4.28 by means of an average of six measured data points for each strip. The error bar represents one standard deviation from the mean value of each strip. a) The average height of oxide strips at different tip voltages and the corresponding linear fitting equation. b) The average half-width of oxide strips at different tip voltages and the corresponding linear fitting equation. c) Due to scanning artifacts (scanning with too fast scan speed), the right hand side of the structure in Figure 4.28 appeared broader than the left hand side (the tip scanned from left to right). The width of the left hand side was taken to be a more accurate value.

#### 4.3.1.2 Dot size as a function of voltage

From previous results in section 4.3.1.1, we found that a tip bias below -4 V did not create any nanofeatures on the substrate because -4 V is the threshold voltage. In order to study in more detail the threshold voltage of nanodot fabrication, a Co/Cr-coated tip (MESP, see Table 4.1) with a tip radius about 25 nm (maximum *ca.* 50 nm) and a spring constant of 2.8 N/m [26] was held above the native-oxide ($SiO_2$) surface maintaining a ramping time of 0.97 s and a relative humidity of 45 ± 2 %. The oxide nanodots were fabricated by contact mode AFM LON on a native-oxide layer on an *n*-type Si (100) substrate with various applied substrate bias values ranging from 1 V to 10 V as illustrated in Figure 4.30 a). Even though, a different type of AFM tip was used, this result further confirmed that the threshold voltage was found to be +4 V applied to the substrate for initiating the oxidation process. Consequently, we assumed that the threshold voltage does not depend on the type of AFM tip specifically in terms of coating material of the tip. Figure 4.30 b) shows an example of half-width measurement of the oxide dot for our works. Due to an elongate dot result obtained and in order to avoid the tip convolution artifacts, we take the vertical direction as a main direction for the half-width measurement. However, additional unknown error, such as the free amplitude and the setpoint of the tapping mode AFM cantilever is possible to affect the measurements of topography [88, 89]. The most half-width measurements of nanodots below sections were measured by this manner.

Figure 4.31 shows two series of nanodots obtained by applying different sample voltages ranging from 4 V to 10 V on a native-oxide-layer-coated *n*-type Si (100) substrate. The patterning experiment was repeated eleven times at seven different voltages. The size of nanodots increased with increasing sample bias. The data from Figure 4.31 a) and b) were used to create plots of dot height and half-width as a function of substrate bias in Figure 4.32 and 4.33. As can be seen from Figure 4.32, the height of the nanodots linearly increases with substrate bias voltage for both experiments. In the plot of average height as a function of voltage in Figure 4.32 test 1, the nanodots average height increases from ~ 0.5 nm to 5 nm as the applied bias increases from 4 V to 10 V relative to the substrate. Considering the plot of test 2 in

Figure 4.32, the nanodots have an average height increasing from 0.6 nm to 3.4 nm as the applied bias increased from 4 V to 10 V relative to the sample. Our results were similar to the study of Fontaine *et al.* [35] who found the linear dependence of oxide dot height as a function of the applied voltage. However, there were some differences that they used tapping mode AFM LON and pulse voltages ranging from 4 V to 11.5 V applied to the sample for 100 ms. Additional work which was similar to our observation was the study of Kuramochi *et al.* [48] who also observed a linear dependence of oxide dot height as a function of applied sample voltages (2 V - 10 V) with various humidity values ranging from 40 % to 70 %. Kuramochi *et al.* [48] studied the fabrication of oxide nanodots using contact mode AFM LON on a *p*-type Si (001) wafer with a rhodium-coated Si tip.

Considering the slopes of the linear fits obtained from nanodot height measurements (see Figure 4.32), their values were found a slight difference namely 0.40 ± 0.05 nm/V in test 1 (blue line) and 0.45 ± 0.08 nm/V in test 2 (red line). However, they still were in good agreement if we also considered the errors. It can be seen from the Figure 4.32 that in the low voltage region (from 4 V to 7 V) the average height values were very similar, whereas in the high voltage region (from 8 V to 10 V) the difference in the average height values of the oxide dots slightly increased. The threshold voltage value obtained from the linear fit equation of Figure 4.32 test 1 was found to be 2.9 ± 1.6 V, while the threshold voltage value obtained from the linear fit equation of Figure 4.32 test 2 was found to be 2.8 ± 2.2 V. These two values were in excellent agreement. Although, the mean values of the threshold voltage were a slight lower than the threshold voltage from section 4.3.1.1 (-4.0 ± 1.6 V), if we considered the error value, our results were still consistent.

Considering the slopes from above investigation of nanodot heights measurements (see Figure 4.32), these results were different from earlier results in section 4.3.1.1 for the slope of the heights of the nanostrip fabrication (see Figure 4.29 a)). A plausible reason could be due to the different speed of the tip used. As the study of Fontaine *et al.* [35] (see Figure 4.14) showed that the slopes of the graph strongly depended on the scan speeds and increased with decreasing scan speed. It could be assumed from our results that the speed of the nanodot fabrication with the

ramping time of 0.97 s which is equal to 1.03 Hz was probably faster than the scan speed of 1 µm/s used in the nanostrip fabrication. Considering the height values, the heights of the oxide nanodots were greater than that of oxide nanostrip fabrication at the same voltage value. In AFM-based LON, the value of negative tip bias is identical to the value of the positive substrate bias. For example, -4 V tip bias is equal to +4 V substrate bias. Our results were in good agreement with the study of Tseng and Notargiacomo [73] who also showed that the heights obtained with oxide nanodots fabrication were greater than that of oxide nanostrip fabrication as already shown in Figure 4.11.

Considering the half-width (Figure 4.33), the results were found the difference in both experiments. In Figure 4.33 test 1, the applied voltage dependence of the half-width of nanodots was fluctuating slightly but with a growing trend. When the applied sample bias was increased from 4 V to 10 V, the half-width oscillated between approximately 55 nm to 73 nm. However, it was possible to fit a linear dependence with a gradient of 1.53 ± 0.80 nm/V. Considering the half-width of Figure 4.33 test 2, it was found that the half-width of the nanodots depends on the applied voltage. When the applied positive bias to the substrate was increased from 4 V to 10 V, the half-width gradually increased from approximately 78 nm to 145 nm, however there is a small fluctuation. A linear fit provides a gradient of 12.4 ± 3.3 nm/V. Taking values of the gradients into account, the oxide widths from both experiments were different and could not be achieved with repeatable results. Although, the experimental parameters such as relative humidity and ramping time were maintained and controlled as consistent as possible for these two experiments, but the most possible reason for this phenomenon could be related to the tip artifact. This is due to the fact that the results in test 2 were imaged with the same AFM tip after imaging the results of test 1. Consequently, the tip convolution or tip wear could cause the elongation of the width in the horizontal direction. As a result, we could only conclude from our investigation that the width seemed to depend on the applied voltage and close to the linear dependence.

Considering the half-width dependence on the voltage, since the applied voltage plays a major role for the meniscus size as the study of Calleja *et al.* [90]

found that the meniscus diameter linearly increased with applied voltage as shown in Figure 4.34. They explained that the water meniscus formation involves the interplay of van der Waals force, condensation energy, surface tension and electrostatic interaction. In this case, increasing the applied voltage leads to an increase of electrostatic interaction. Since LON was confined within the water meniscus, an oxide lateral size was directly related to the water bridge size. However, there were some differences between their experiments and those presented here such as they were performed by non-contact mode AFM LON on a native-oxide-coated *p*-type Si (100) substrate at 45 % RH and various pulse durations (0.3 ms, 30 ms and 3 s).

From these plots, it can be assumed that high voltages tend to give high aspect ratio features. For the effect of voltage on the oxidation process, Avouris *et al.* [67, 77] explained that the voltage dependence directly involves the electric field which plays a crucial role in the oxidation process. This is because the initial growth takes place at very high electric field strength near the tip apex of up to ~ $10^8$ V/cm. A field-induced oxidation mechanism for very thin oxide films was first proposed by Cabrera and Mott [91]. In their model, the function of the electric field is to decrease the activation energy to facilitate the motion of ionic species across the oxide films. Gordon *et al.* [65] explained that after the first oxide layer forms, additional oxide thickness can be grown with electric field assistance (Cabrera-Mott mechanism [91]). The electric field enhances the ion diffusion ($OH^-$ or $O^-$) through the growing oxide film due to the contact potential $V_0$ (Mott potential) difference between the initial oxidized silicon and the adsorbed oxygen layer. These lead to the continued oxide growth from combination of the ions with holes in the silicon substrate. However, when the oxide thickness increases, the electric field is decreased until the electric field is insufficient for ionic diffusion (< $10^7$ V/cm [65, 67, 77]). This can cease the oxide growth. In the experiment of Gordon *et al.* [65], the oxide thickness could be grown to *ca.* 80 Å with the tip bias of 7-8 V.

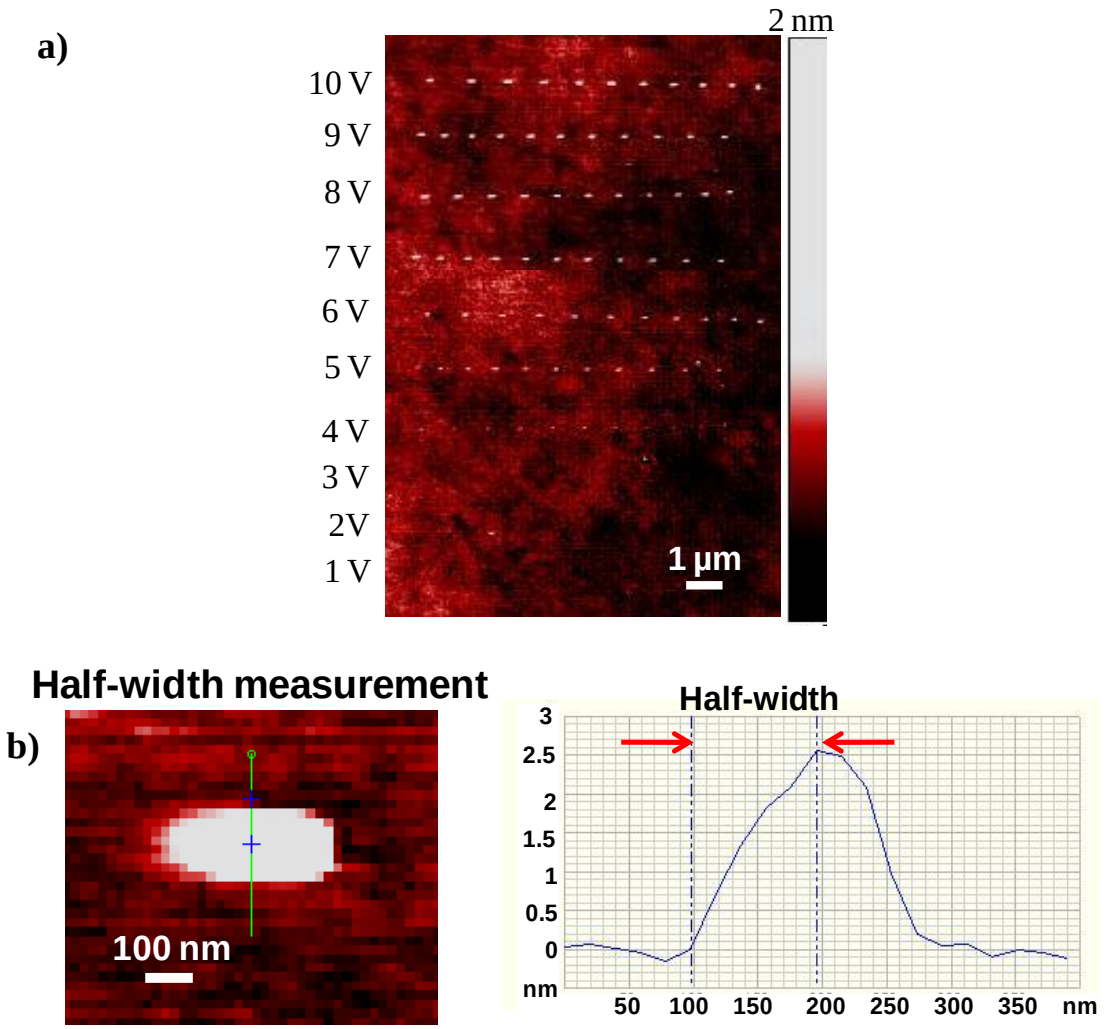


**Figure 4.30** AFM image of a series of nano-oxide dots deposited on a native $SiO_2$ surface with different applied voltages ranging from 1 V to 10 V to the substrate using a Co/Cr-coated tip (MESP) with a tip radius about 25 nm (maximum *ca.* 50 nm) and a spring constant of 2.8 N/m at a ramping time of 0.97 s with a relative humidity of 45 ± 2 %. b) Showing an example of half-width measurement of the oxide dot and corresponding half-width profile. Due to an elongate dot result obtained from the tip convolution effect, we take the vertical direction as a main direction for the half-width measurement. This will be the same for all half-width measurements of nanodots.

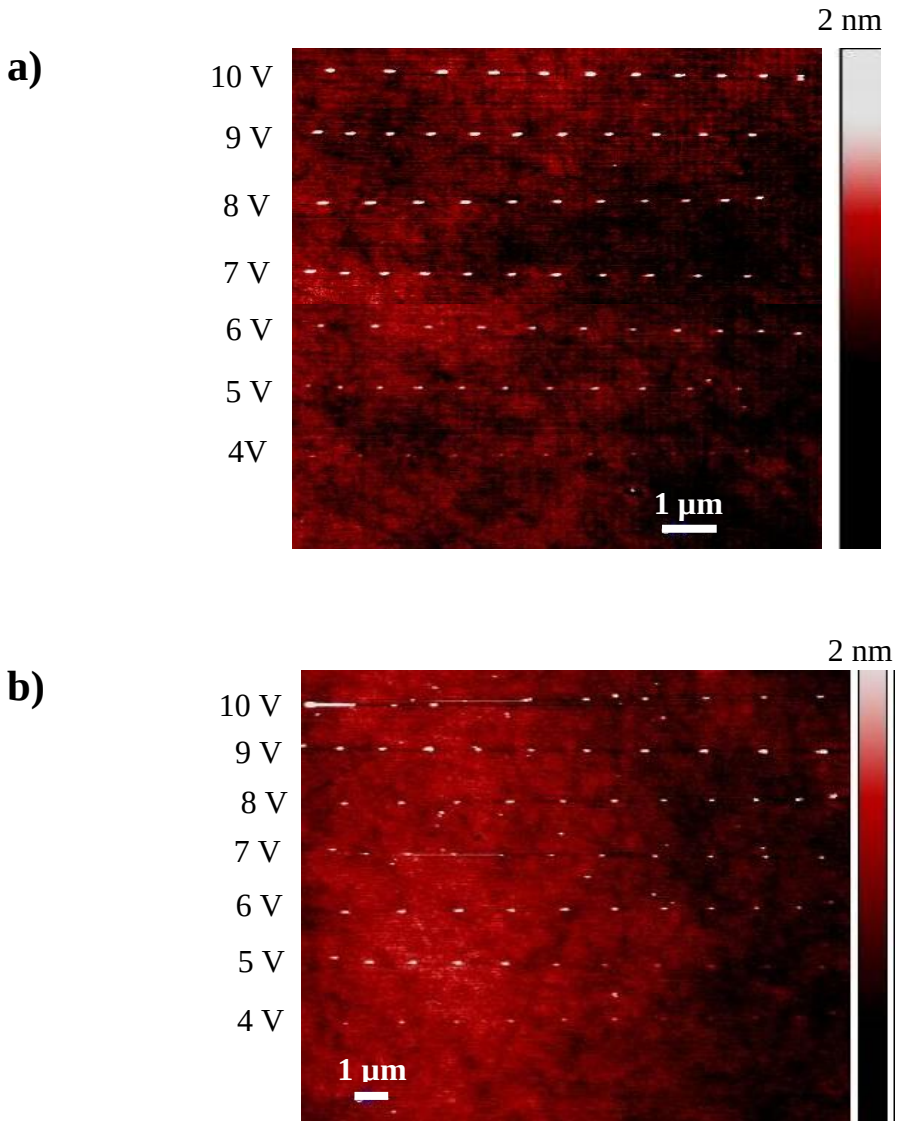


**Figure 4.31** Two AFM images show a series of nano-oxide dots deposited on a native $SiO_2$ surface with different applied voltages ranging from 4 V to 10 V to the substrate using the same MESP tip and same conditions at a ramping time of 0.97 s and a relative humidity of 45 ± 2 %.

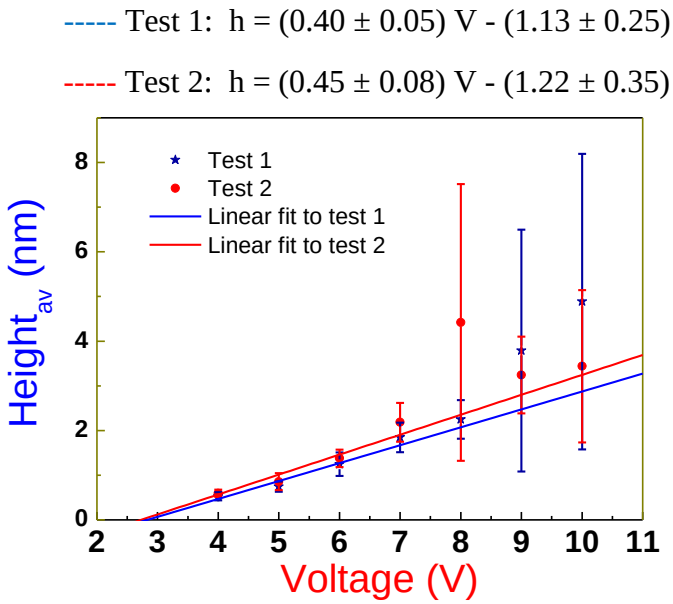


**Figure 4.32** Dependence of the height of oxide dots as a function of the substrate voltage extracted from the data in Figure 4.31 a) and b) labelled as test 1 and test 2, respectively. The data were measured by means of an average of measured data for 11 dots. The error bars represent the standard deviations of the mean of each figure.

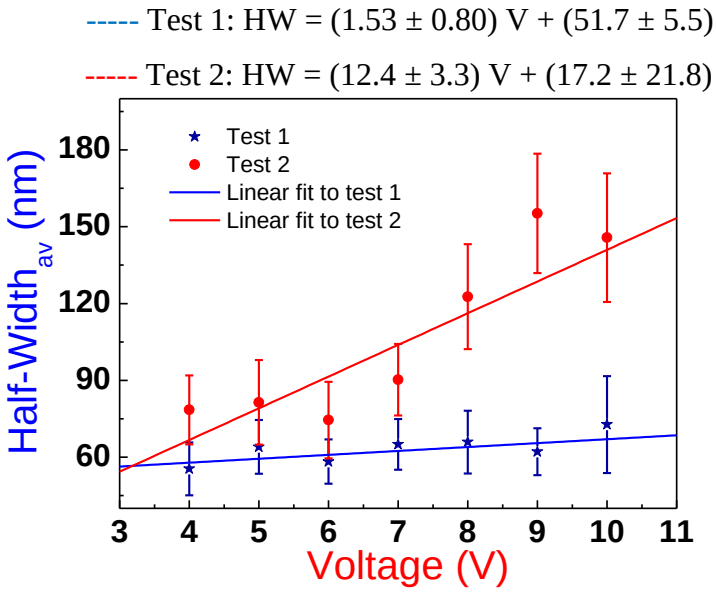


**Figure 4.33** Dependence of the half-width of the oxide dots as a function of the substrate voltage extracted from the data in Figure 4.31 a) and b) labelled as test 1 and test 2, respectively. The data were measured by means of an average of measured data for 11 dots. The error bars represent the standard deviations of the mean of each figure.

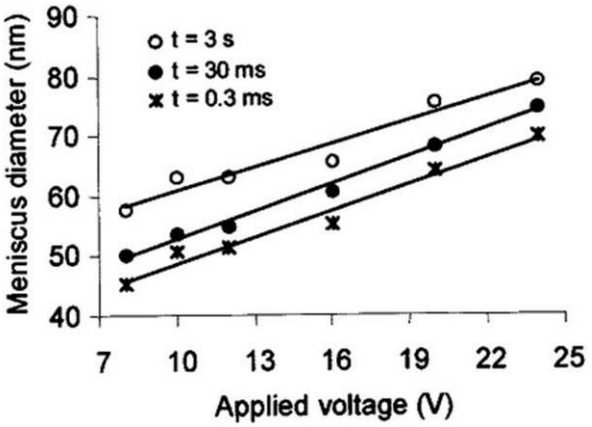


**Figure 4.34** The dependence of the water meniscus on the applied voltage at the relative humidity of 45 % for three different pulse durations of 0.3 ms, 30 ms and 3 s [90].

### 4.3.2 Oxide pattern as a function of scan speed

The focus moved onto the study of how the oxide features depend on the scan speed. Figure 4.35 a) and b) display a series of different oxide features fabricated by contact mode AFM on the native-oxide-layer-coated *n*-type Si (100) substrate using a PtIr-coated Si tip (SCM-PIC, see Table 4.1) with a tip radius of about 20 nm and a force constant of 0.2 N/m [23] with a constant applied substrate voltage of 6 V and variable scan speeds (5, 4, 3, 2, 1, 0.5, 0.1, 0.05, 0.04, 0.03, 0.02, and 0.01 µm/s). The values of the scan speed are shown above each pattern. The relative humidity was 60 ± 5 %. The results showed that when the scan speed was reduced, the height of the oxide pattern was observably increased. In other words, the slower scan speed resulted in larger oxide size.

Figure 4.36 a) and b) depict the height profiles of the oxide features corresponding to Figure 4.35. Figure 4.36 a) shows the exponential dependence of the dot's height on the scan speed. The data changes significantly for low scan speeds. The range from 0.01 µm/s to 0.10 µm/s is replotted in Figure 4.36 b). However, the decrease in height (h) for low scan speeds ($v$) can be well fitted with a straight line which is expressed by equation (9) (see Figure 4.36 a)).

$$h = (-4.8 \pm 1.5)\, v + (1.7 \pm 0.1) \quad (9)$$

For; $v = 0.01, 0.02, \ldots, 0.10$

The oxide heights decrease with increasing the scan speed ranging from 0.01 µm/s to 1 µm/s. However, the behaviour seems to have a slight decrease for speeds above 1 µm/s. Our results are relatively consistent with the previous study of Kuramochi *et al.* [48] as shown earlier in Figure 4.22. They found that the oxide line height decreased with increasing the tip speed. The tip speed was varied from 125 nm/s to 1250 nm/s (this range was equal to from 0.125 µm/s to 1.25 µm/s). Considering their results at higher tip speed ranged from ~500 nm/s to 1250 nm/s, the oxide height seemed to have a smaller decrease and seemed to saturate compared to that at lower tip speed. However, Kuramochi *et al.* [48] did not show the data at the higher tip speed (> 1250 nm/s). Compared to the study of Fontaine *et al.* [35] as already shown in Figure 4.21, our results were in contradiction with their results since they found that the oxide height of fabricated oxide stripes shows a logarithmic decrease with an increase of writing speed for each sample voltage, whereas we found the linear dependence at the low scan speed. Taking these into consideration, it was supposed that from our investigation when the scan speed was increased at the low scan speed, this gave a significant decrease of the oxide height until it reached the slight decrease at the high scan speed.

Figure 4.37 a) and b) depict the half-width profiles of the oxide features corresponding to Figure 4.35. In Figure 4.37 a), it can be seen that the width decreases with increasing scan speed. In Figure 4.37 b), the high scan speed region is plotted (ranging from 1 µm/s to 5 µm/s) where it can be seen that a significant decrease occurs only for speeds greater than *ca.*1 µm/s. The dependence of the line half-width (HW) on the high range of the writing speed ($v$) (see Figure 4.37 b)) can be appropriately fitted with this equation:

$$HW = (-0.022 \pm 0.009)\, v + (0.25 \pm 0.03) \quad (10)$$

For; $v = 1, 2, \ldots, 5$

It can be seen that an increase in the lateral dimension depends almost linearly on a decrease of the tip velocity. However, the line half-width does not increase linearly after the writing speed goes below 1 μm/s, it seems to be constant. This can be explained by a two-step growth process proposed by Kuramochi *et al.* [48] taking place at a long oxidation time. This process consists of the initial high growth stage in the centre part of the meniscus right underneath the tip followed by the effect of the ionic diffusion through the adsorbed water layer occurring when the current flow under the tip is prevented by the oxide growth at the centre. Kuramochi *et al.* [48] assumed that principally the ionic diffusion was the rate limiting factor for long exposure times. Consequently, compared to our results at the fast scan speed (short exposure time), the initial oxidation takes place at the central part under the AFM tip until this growing oxide prevents the current flow at the central region. Subsequently, at the slower scan speed or longer oxidation time, the oxide is grown in the lateral dimension because of the ionic diffusion along the lateral dimension. This leads to an increase in the oxide width with decreasing the scan speed or increasing the oxidation time. However, the oxide growth in the lateral dimension was also limited by the water meniscus size as the study of Bloeß *et al.* [63]. As discussed earlier in the introduction section, the relative humidity and electric field are crucial parameters which play an essential role for the formation of the meniscus generated between the tip and sample surface [48, 63]. Consequently, from our results, the slower tip velocity generated wider oxide lines determined by the ionic diffusion until the width of the written oxide line was limited by the size of the meniscus.

As a result of these considerations between the height and width dependencies, it can be supposed that for the fast scan speed the oxidation takes place in the lateral dimension due to the ionic diffusion until it reaches the limitation of the water meniscus diameter determined by the humidity and the applied electric field. Subsequently, the oxidation was able to grow only in the vertical direction. As a consequence, the oxide height depends on the scan speed but only after the width is saturated.

a)

b)

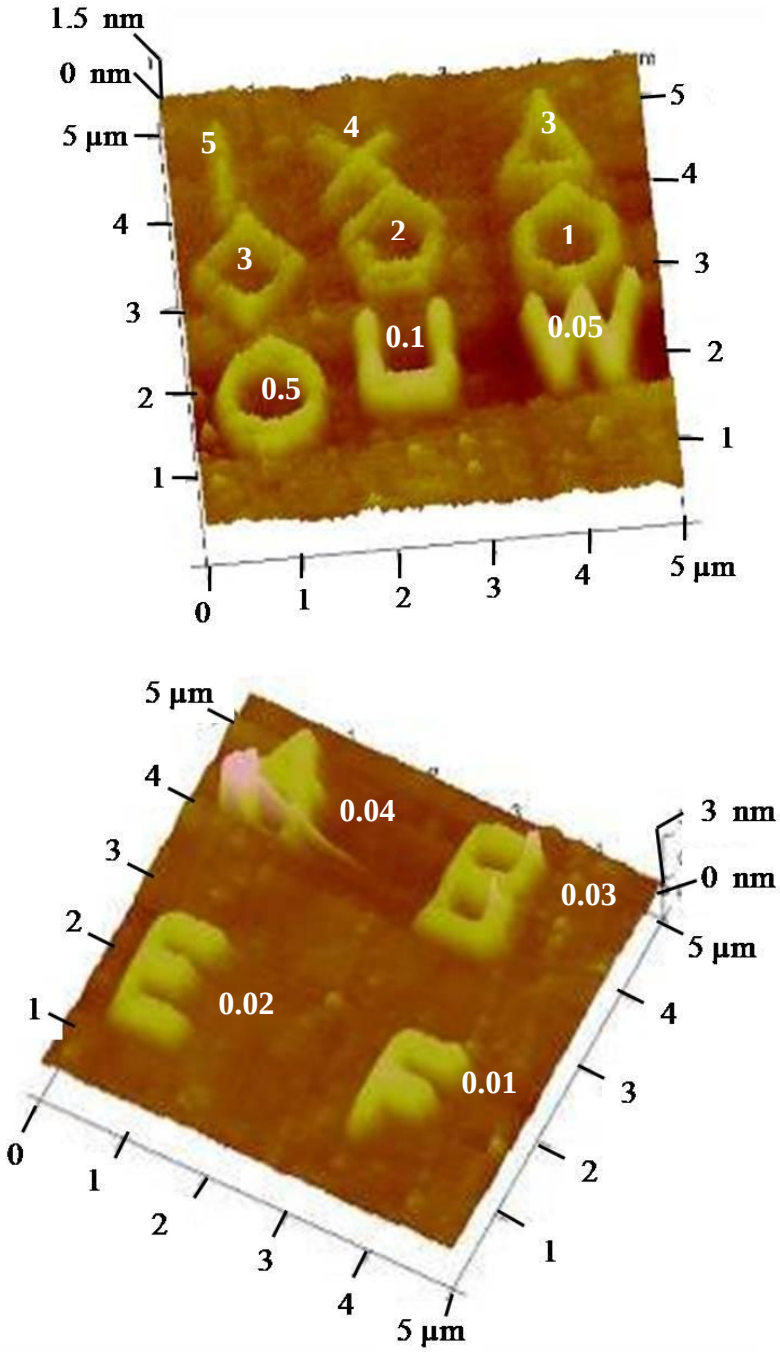


**Figure 4.35** Two 3-D AFM images of a series of oxide patterns fabricated on the native-oxide layer on *n*-type Si (100) substrates using a PtIr-coated Si tip (SCM-PIC) with a normal tip radius about 20 nm and a force constant of 0.2 N/m. A constant substrate positive voltage of 6 V was applied with 60 ± 5 % RH with different scan speeds (the values as depicted above the patterns): a) 5, 4, 3, 2, 1, 0.5, 0.1 and 0.05 µm/s, b) 0.04, 0.03, 0.02 and 0.01 µm/s.

**a)**

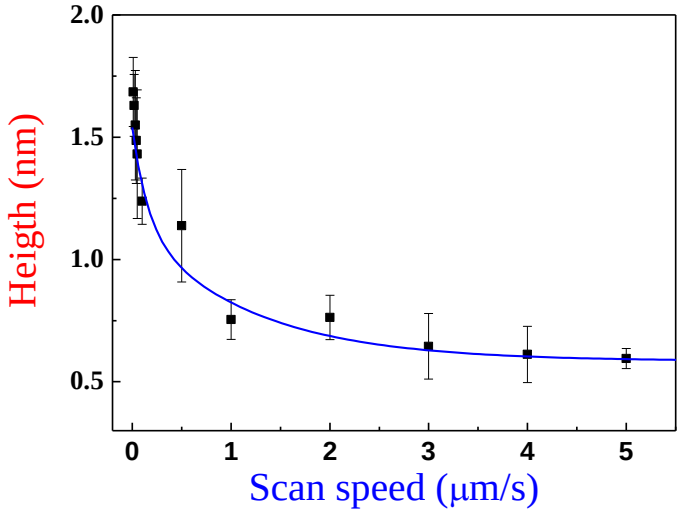


**b)**

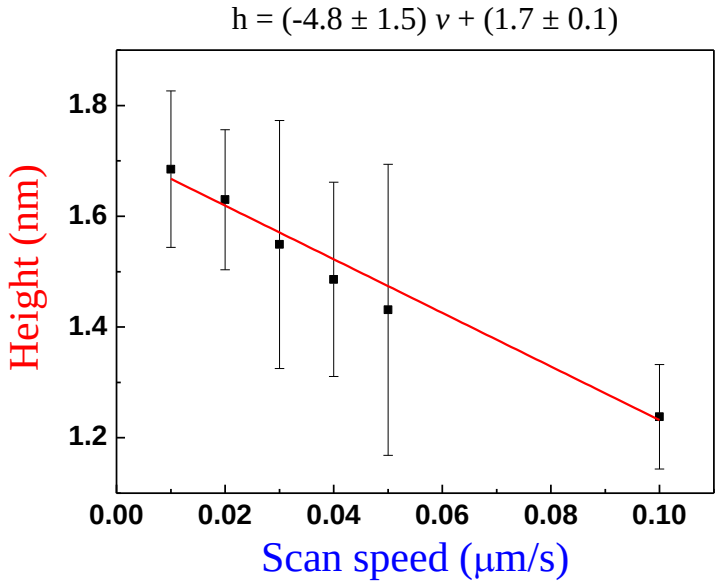


**Figure 4.36** The dependence of the height of the oxide patterns as a function of the scan speed for a constant substrate positive voltage (6 V). The experimental data were measured from Figure 4.35 a) and b) by means of an average of six measured data for each feature. The error bar represents one standard deviation of the mean of each figure. a) The graph shows the linear-linear plot of the average height of each oxide feature at different scan speeds from 0.01 μm/s to 5 μm/s. b) The graph shows linear-linear plot of the average height of each oxide pattern at different scan speeds for the low scan speed range (from 0.01 μm/s to 0.1 μm/s) and the corresponding curve fitting equation.

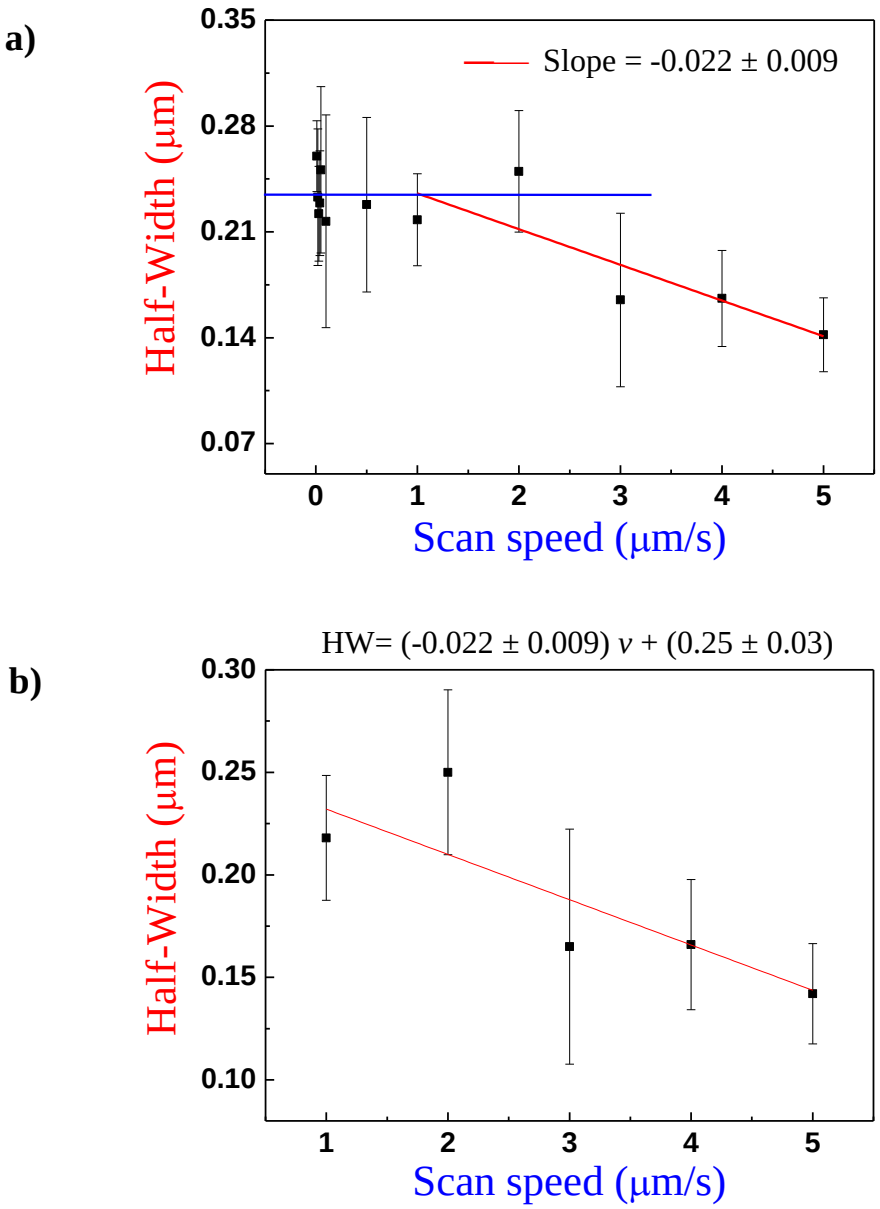


**Figure 4.37** The dependence of the half-width of the oxide patterns as a function of the scan speed for constant substrate positive voltage (6 V). The experimental data were measured from Figure 4.35 a) and b) by means of an average of six measured data for each feature. The error bar represents the standard deviation of the mean of each feature. a) Linear-linear plot of the average half-width of each oxide feature at different scan speeds from 0.01 μm/s to 5 μm/s. b) Linear-linear plot of the average half-width of each oxide pattern at different scan speed from the high scan speed range (from 1 μm/s to 5 μm/s) and the corresponding curve fitting equation.

### 4.3.3 Influence of the AFM tip

#### 4.3.3.1 Effect of the AFM tip on oxide pattern as an array

In this section, we investigate the LON process on a native-oxide-layer-coated Si surface using two different AFM tips to reveal the effect of the type of AFM tip for nanoarray fabrication.

Figure 4.38 and 4.40 present AFM images of oxide nanodot arrays on a native-oxide layer on an *n*-type Si (100) surface obtained by LON in contact mode AFM. These dots were fabricated using conductive AFM tips one of which is a Cr/Pt-coated tip (ElectriTap300-G, see Table 4.1) with a tip radius less than 25 nm and a force constant of 40 N/m [27] with the results shown in Figure 4.38 and the other is a Co/Cr-coated tip (MESP, see Table 4.1) with a tip radius about 25 nm (maximum *ca.* 50 nm) and a spring constant of 2.8 N/m [26] with the resulting dots shown in Figure 4.40. The dots were formed using the same conditions of an applied substrate bias of 5 V and ramping time of 0.97 s with relative humidity of 45 ± 2 %. After each oxidation process, the same AFM tip was subsequently used for imaging. Figure 4.39 demonstrates a size distribution of nanoarrays (array 1, 2 and 3) fabricated using Cr/Pt-coated tip (ElectriTap300-G). Additionally, Table 4.2 summarises the data of all three arrays including the average height and the average half-width of the oxide dots and the mean standard deviation. All size distributions of array 1, 2 and 3 were well fitted with log-normal distribution with an average height of 1.06 ± 0.12 (11%), 0.87 ± 0.11 (13%) and 1.01 ± 0.11 (11%) nm along with an average half-width of 70.0 ± 10.5 (15%), 78.0 ± 9.0 (12%) and 69.8 ± 7.5 (11%) nm. The height and half-width of dots in array 1 and 3 are nearly identical about 1 nm and 70 nm, respectively. In the case of array 2, although, the mean values of the height and the half-width were a slight difference from array 1 and 3, but if we also considered the standard deviation, it was found that array 2 was in good agreement with array 1 and 3.

Figure 4.41 (left panel) also shows a log-normal size distribution of two arrays (array 4 and 5) with average heights of 1.52 ± 0.13 (9%) and 1.15 ± 0.12

(10%) nm. In addition, Table 4.3 summarises the data of array 4 and 5 including the average height and the average half-width of the oxide dots and the mean standard deviation. However, an average half-width distribution illustrates different forms of curve fittings which were a log-normal distribution for array 4 and a bimodal distribution for array 5 (see Figure 4.41 right panel). An average half-width of array 4 falls into 62.5 ± 2.4 (4%) nm which is similar to an average half-width of the first peak of array 5 (62.5 ± 2.8 (5%) nm), which is the position maximum (see Figure 4.41 in the top and bottom row of right panel). The second highest peak of array 5 is 93.0 ± 3.3 (4%) nm as illustrated in Figure 4.41 (a bottom row and right panel). Taking these results into consideration, it was found a slight difference of the mean values of the height of array 4 and 5 even considering the error values which they should be identical while in the case of the half-width the mean values were in good agreement, although all of the relevant parameters during the experiments such as applied voltage, ramping time and relative humidity were maintained and controlled as consistent as possible. However, a plausible reason could be due to the imaging artifact from the tip convolution. This is due to the fact that the same AFM tip used from the oxidation process was subsequently used to image the patterning results. This might be a critical effect for the deviation of imaging results. Moreover, it could be observed that all oxide dots looked elongated.

For comparison between two types of AFM tips when using contact mode AFM, it was found that the Cr/Pt-coated tip with smaller tip radius (< 25 nm) results in oxide dots with smaller heights compared to the Co/Cr-coated tip with larger tip radius ($25 \leq R_{tip}$[6] $\leq 50$). This result was in contradiction with the study of Djurkovic *et al.* [92] who showed that increasing the AFM tip radius leads to a decrease of the oxide dot height. Moreover, the half-width of oxide dots in array 1-3 of Cr/Pt-coated tip (a smaller tip radius) are larger than that in array 4 and 5 of Co/Cr-coated tip (a larger tip radius). This also was in contradiction with the study of Djurkovic *et al.* [92] who showed that increasing the AFM tip radius leads to an increase of the oxide dot width.. The smallest height and half-width achieved by Cr/Pt-coated tip were *ca.* 0.63 nm and 40 nm, respectively. In the case of Co/Cr-coated tip, very fine oxide

[6] $R_{tip}$ is the tip radius.

dots with 0.45 nm in height and 52.5 nm in half-width were obtained. Furthermore, the largest size of fabricated oxide dots obtained from Cr/Pt-coated tip were *ca.* 1.8 nm in height and 100 nm in half-width. On the other hand, the Co/Cr-coated tip (a larger tip radius) produced a larger oxide size with a 3.5 nm oxide height and 100 nm oxide half-width. Our results were not correlated with the study of Kremmer *et al.* [93] concerning the relationship between the electric field distribution during the oxidation process and the AFM tip radius. Their simulation results revealed that the electric field strength on the $SiO_2$ surface increased with decreasing tip radius as illustrated in Figure 4.42 due to the non-planar geometry of the tip. Considering the oxide thickness, in our case the thickness of the native-oxide layer was about a few nm and in the simulation of Kremmer *et al.* [93] the oxide thickness was 5 nm covered by a 3 nm water film. Moreover, Takemura and colleagues [94] also showed the theoretical analysis of the electric field strength at the film surface of CoFe using different curvature radius of the cantilever at the applied bias of 2 V as shown in Figure 4.43. They found that the size of the nanostructures strongly depended on the curvature radius of the cantilever and the diameter of the nanodot increases with increasing the tip radius. This could be well correlated with our results and could be deduced that the smaller tip radius fabricated a smaller oxide width than the greater tip radius.

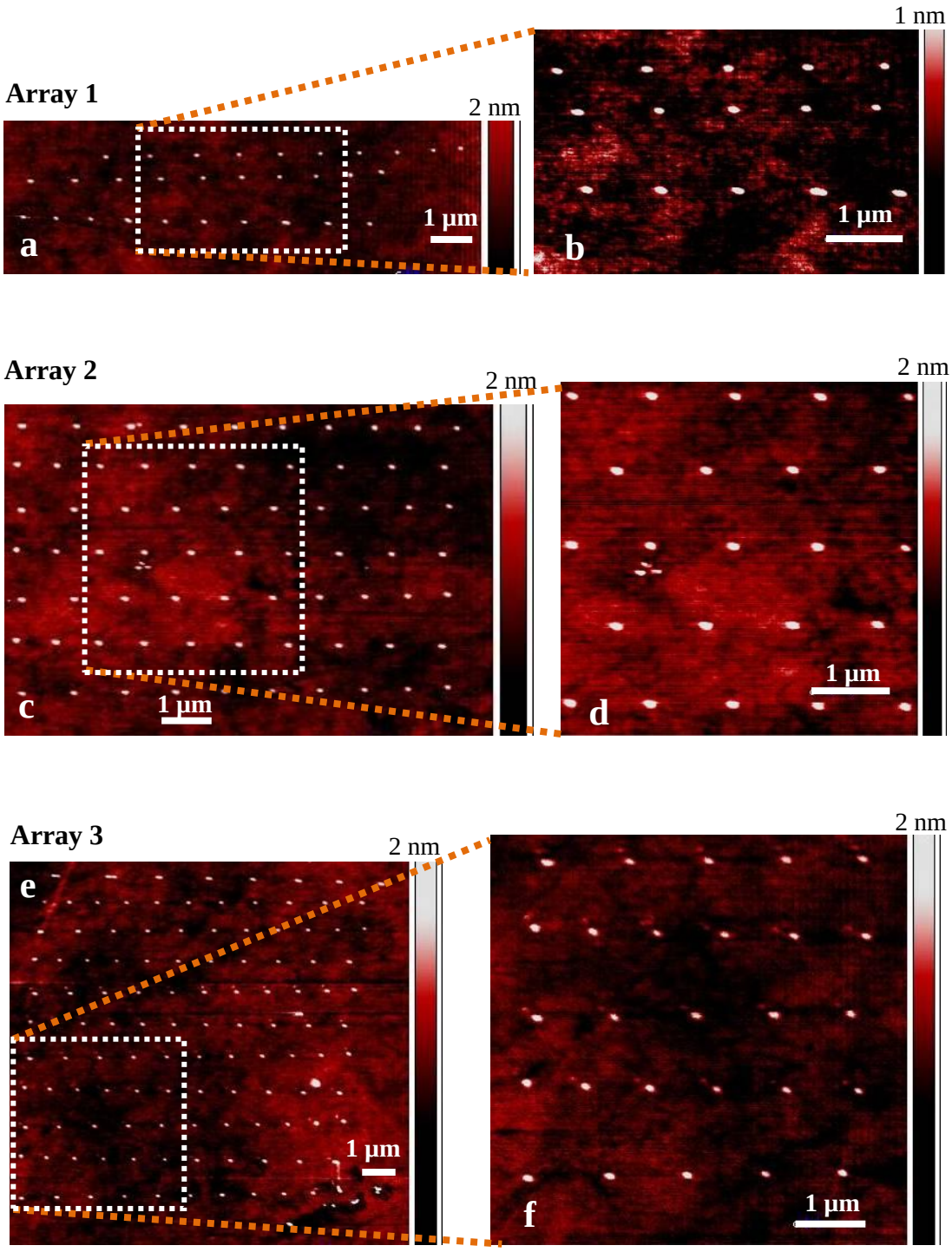


**Figure 4.38** AFM images show three arrays of oxide dots on a native $SiO_2$ surface generated by local anodic oxidation with the same AFM tip type (ElectriTap300-G: a Cr/Pt-coated tip with tip radius less than 25 nm) and same conditions of an applied substrate positive bias of 5 V and ramping time of 0.97 s under relative humidity of 45 ± 2 %.

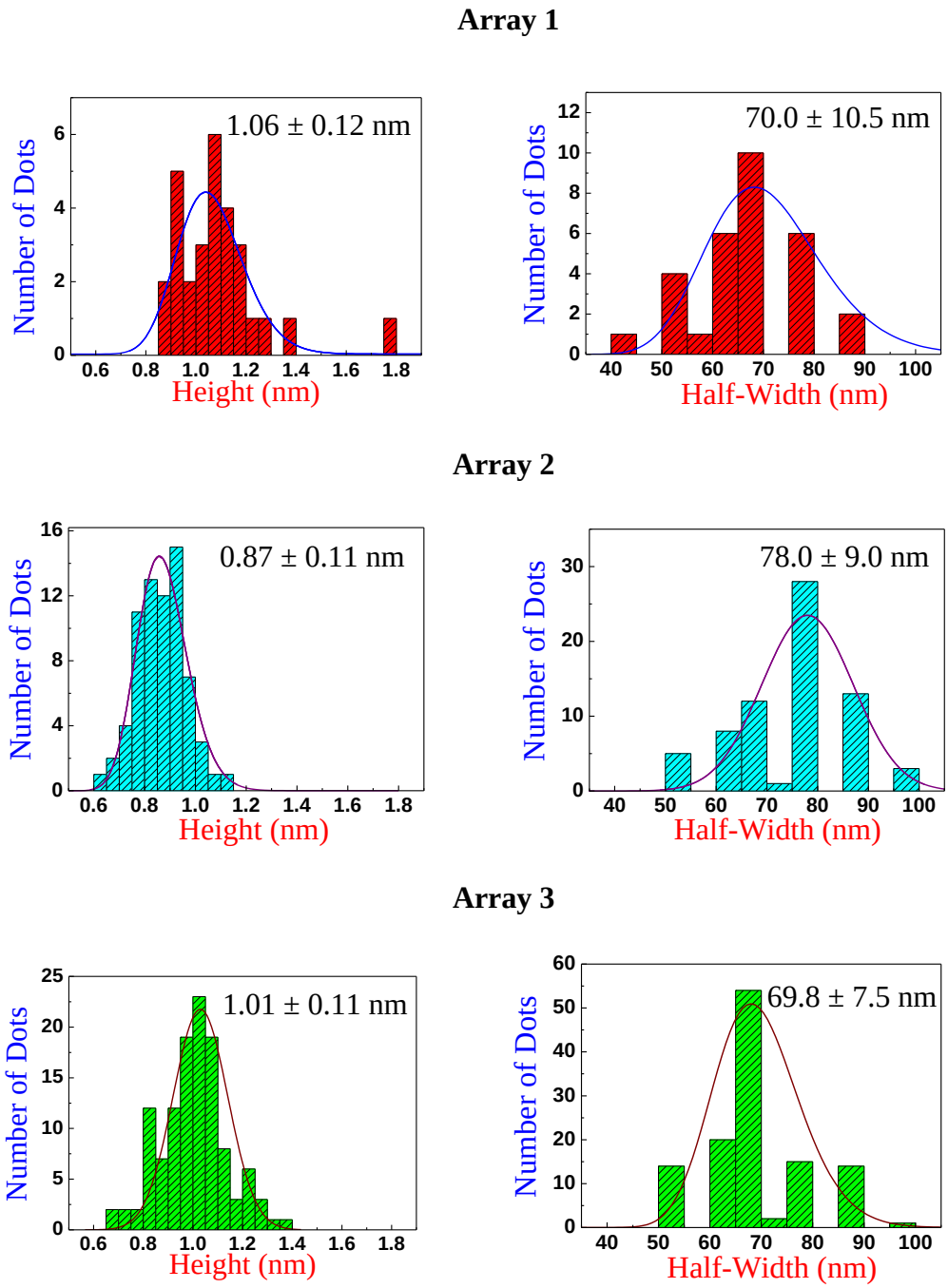


**Figure 4.39** The graphs show the height (left panel) and half-width (right panel) distributions from AFM images in Figure 4.38 of three arrays obtained with a Cr/Pt-coated tip.

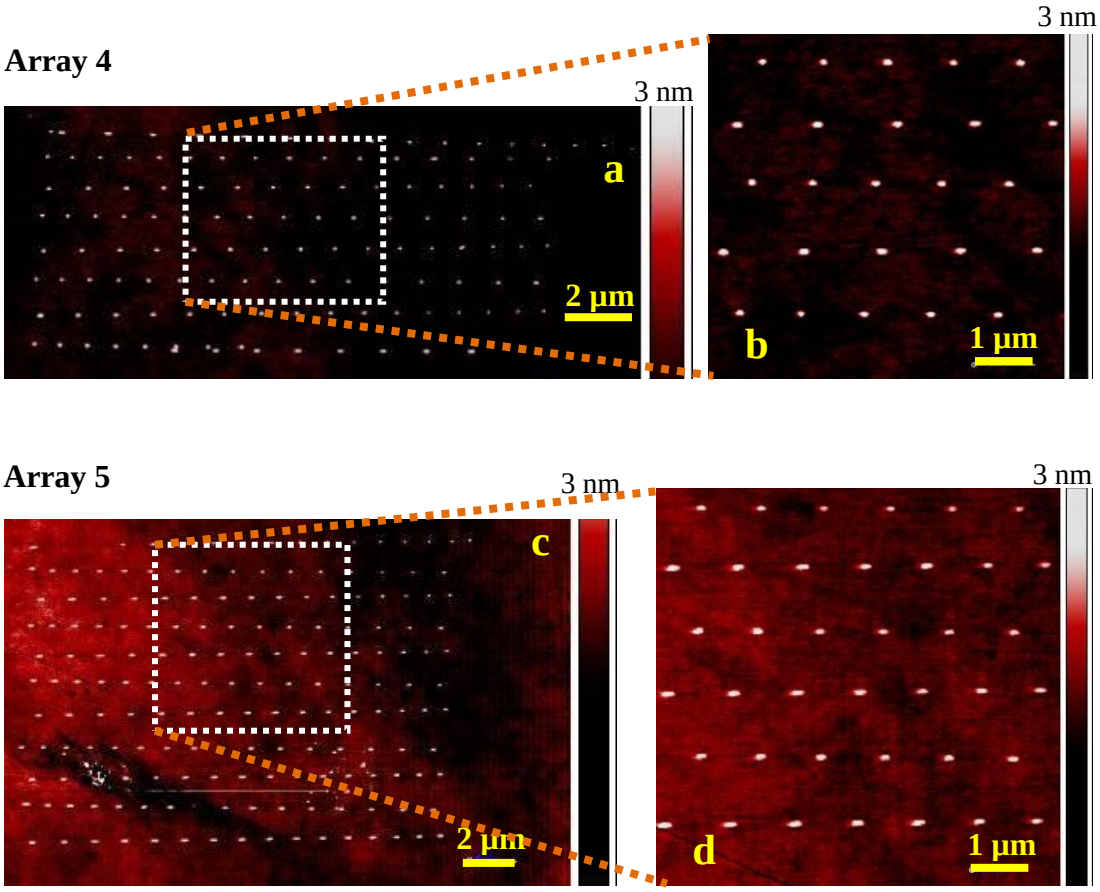


**Figure 4.40** AFM images show arrays of oxide dots on a native $SiO_2$ surface fabricated by local anodic oxidation with the same AFM tip type (MESP: a Co/Cr-coated tip with tip radius about 25 nm (maximum *ca.* 50 nm)) and the same conditions of an applied substrate positive bias of 5 V and ramping time of 0.97 s under relative humidity of 45 ± 2 %.

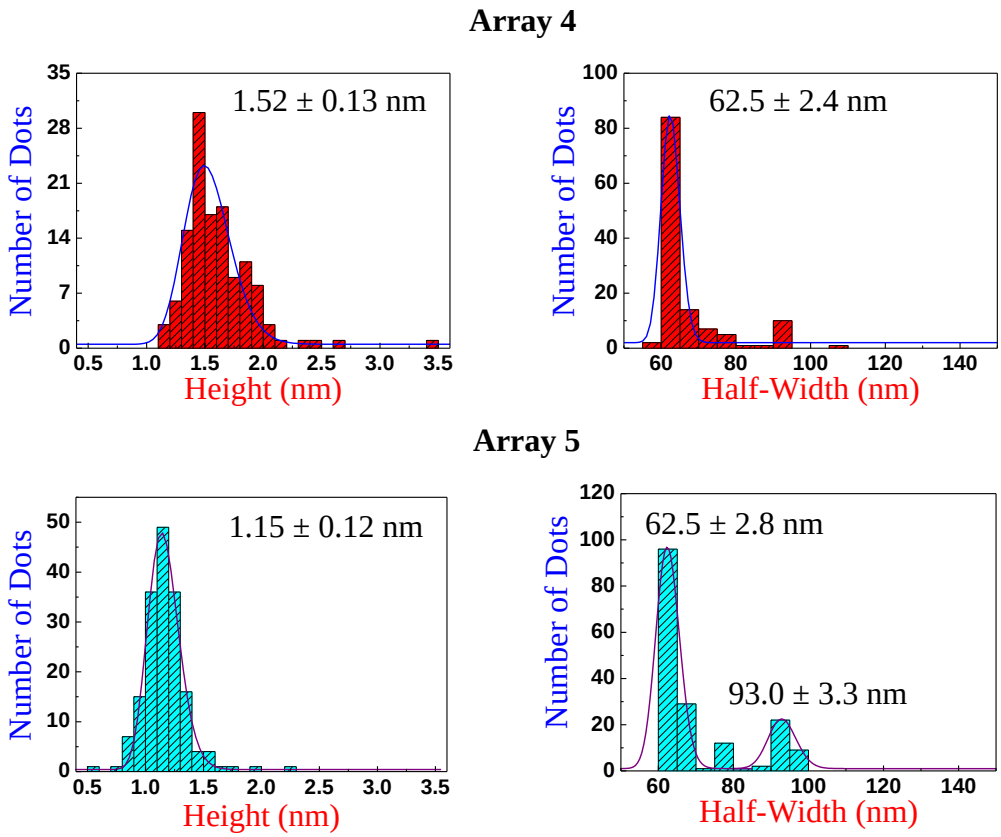


**Figure 4.41** The graphs show the height and half-width distributions from AFM images in Figure 4.40 of two arrays obtained with a Co/Cr-coated tip.

**Table 4.2**: Summary of the size and size distribution of the oxide nanodots using a Cr/Pt coated tip (ElectriTap300-G).

| ***Array*** | ***Height*** *(nm)* | ***mean standard deviation*** | | ***Half-width*** *(nm)* | ***mean standard deviation*** | |
|---|---|---|---|---|---|---|
| | | nm | % | | nm | % |
| 1 | 1.06 | 0.12 | 11 | 70.0 | 10.5 | 15 |
| 2 | 0.87 | 0.11 | 13 | 78.0 | 9.0 | 12 |
| 3 | 1.01 | 0.11 | 11 | 69.8 | 7.5 | 11 |

**Table 4.3**: Summary of the size and size distribution of the oxide nanodots using a Co/Cr coated tip (MESP).

| ***Array*** | ***Height*** *(nm)* | ***mean standard deviation*** | | ***Half-width*** *(nm)* | ***mean standard deviation*** | |
|---|---|---|---|---|---|---|
| | | nm | % | | nm | % |
| 4 | 1.52 | 0.13 | 9 | 62.5 | 2.4 | 4 |
| 5 | 1.15 | 0.12 | 10 | 62.5 (peak 1) | 2.8 | 5 |
| | | | | 93.0 (peak 2) | 3.3 | 4 |

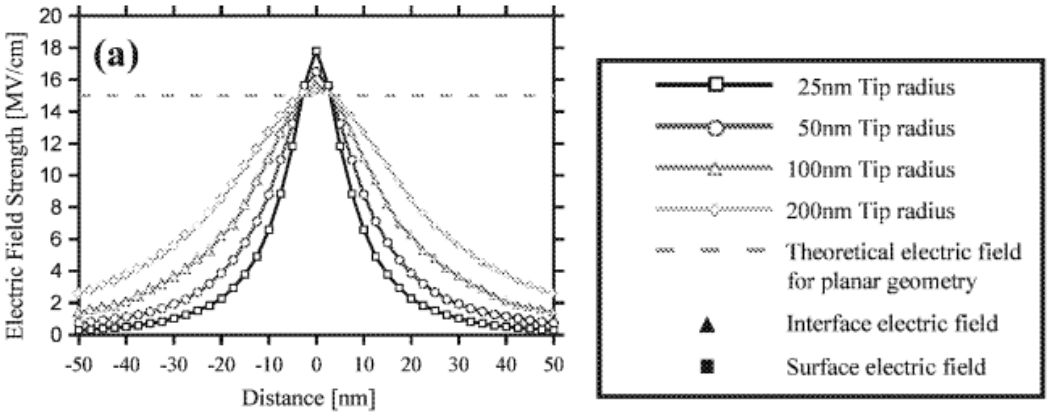


**Figure 4.42** Distribution of the electric field as a function of tip radius ranging from 25 nm to 200 nm on the $SiO_2$ surface. The oxide thickness is 5 nm and it is covered by a 3 nm water film. Distance marked 0 nm is at the centre of the tip. The horizontal dashed line represents the theoretical electric field for a planar geometry instead of the non-planar geometry of the tip [93].

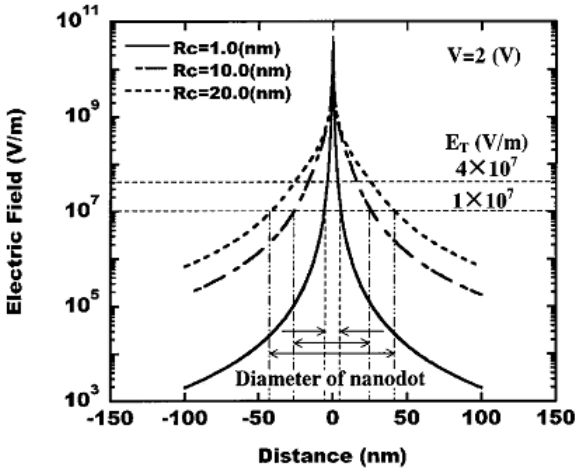


**Figure 4.43** Distribution of electric field strength at the film surface calculated for various curvature radii of the cantilever under an applied voltage of 2 V [94].

#### 4.3.3.2 Effect of the AFM tip and substrate on oxide dot

As already described in many places, the dots sizes are affected by voltage, but the voltage is not the only factor that influences the deposition. In fact, the AFM tip radius and substrate may also affect the dot sizes. As discussed earlier in section 4.3.3.1, the type of AFM tip with different radius affects the size of nanodots. Consequently, the influence of the type of AFM tip and substrate on the size of nanodots will be studied in more detail below to gain better understanding.

Dot sizes were studied as a function of voltage for a fixed substrate but different tip (Figure 4.44 a) and 4.45 a)) or with a fixed AFM tip with different substrate (Figure 4.44 b) and 4.45 b)). Figure 4.44 demonstrates the nanodot height dependence on the tip voltage for two different types of AFM tips: MESP and FMG01-Co (Figure 4.44 a)); as well as two different types of substrates: native $SiO_2$ and Mo (figure 4.45 b)). MESP (see Table 4.1) is a Co/Cr-coated tip with a tip radius about 25 nm (maximum *ca.* 50 nm), a typical force constant of 2.8 N/m and a resonance frequency of 75 kHz [26]. FMG01-Co (see Table 4.1) is a Co/Cr-coated tip with a tip radius 40 nm, a normal force constant of 3.0 N/m and a resonance frequency of 60 kHz [28].

In each experiment, the substrate voltage was increased from 6 V to 10 V. The behaviour of the nanodeposition seems dependent on the type of tip and substrate. For the same voltage and wafer, the height of nanodots grown by the smaller tip radius (MESP tip) is higher compared to the larger tip radius (FMG01-Co tip). This was in contradiction to the previous observation in section 4.3.3.1 which showed the results in the opposite way. However, the results were in good agreement with the studies of Djurkovic *et al.* [92] and Kremmer *et al.* [93] who showed that increasing the AFM tip radius leads to a decrease of the oxide dot height. It should be noted that the results in this experiment might be affected by the relative humidity difference since the RH during experiments of MESP (45 ± 2 %) on native oxide substrate was higher than that of FMG01-Co (40 ± 2 %) on native oxide substrate resulting in the higher oxide dots obtained in the case of MESP. Taking these into consideration, in this experiment, it could be concluded that the tip radius has a strong influence on the height of oxide dots.

The plots in Figure 4.45 show the dot half-width of oxide nanodots as a function of voltage at a fixed ramping time. It is found that the half-width of the nanodots does not strongly depend on the applied voltage in the case of FMG01-Co on both native-oxide layer and 100-nm-thick Mo surface. This is because the half-width of nanodots was fluctuating when the applied substrate bias voltages was increased. On the native $SiO_2$ surface, the dot width deposited with the MESP tip (with normal tip radius about 25 nm) is considerably narrower than that from the FMG01-Co tip in Figure 4.45 a). This is due to the smaller tip apex of MESP compared to that of FMG01-Co (about 40 nm tip radius) which causes the smaller size of the meniscus between the tip and sample. These results can be explained by the theoretical analysis of Lin *et al.* [95] who confirmed that the radius of the water bridge strongly depended on the radius of the probe tip.

Considering the influence of the type of substrate on the size of oxide dots, the oxide nanodots were fabricated by contact mode AFM LON with FMG01-Co tip on a native-oxide $SiO_2$ and Mo surface. During the oxidation process, the relative humidity was controlled at 40 ± 2 % and a ramping time of 0.97 s. As already discussed in section 4.1.7, the molybdenum oxide stoichiometry fabricated by AFM-

based LON proposed by Rolandi *et al.* [80], Pellegrino *et al.* [83] and Goto *et al.* [82] was $MoO_3$. Consequently, the fabricated oxide dots on Mo surface in this thesis were also assumed to be $MoO_3$. Possible oxidation mechanisms for Mo substrate could be expressed as these reactions:

IV. Reactions at the Mo surface (anode):

$$Mo + 3H_2O \rightarrow MoO_3 + 6H^+ + 6e^- \quad (11)$$

$$2H_2O \rightarrow O_2\uparrow + 4H^+ + 4e^- \quad (12)$$

V. Reaction at the tip (cathode):

$$6\,H_2O + 6e^- \rightarrow 3H_2\uparrow + 6OH^- \quad (13)$$

VI. Reaction in water:

$$6H^+ + 6OH^- \rightarrow 6H_2O \quad (14)$$

For the same conditions (voltage and tip), the height and width of oxide dots on native $SiO_2$ surface are less than those on the Mo surface as illustrated in Figure 4.44 b) and Figure 4.45 b), respectively. The results could be implied that the type of substrate can influence the size of oxide nanodots. This behaviour can be explained by the wettability of the substrate and the sample conductivity [96].

The wettability or the wetting[7] property with water of a surface can be classified as hydrophilicity and hydrophobicity. If water can spread over the surface without the formation of droplets, this is called a hydrophilic surface. On the other hand, if the surface cannot be wetted by water but forms water droplets instead, it is a hydrophobic surface. Schenk *et al.* [97] pointed out that the hydrophilic and hydrophobic nature of the tip and the substrate had an effect on the vertical and lateral capillary forces between the tip and substrate. In the present case, the $SiO_2$ surface is hydrophilic while the Mo surface is relatively hydrophobic [98]. The

[7] Wetting is determined by the equilibrium contact angle, θ, and can be classified as three different states. The first state is a complete or perfect wetting, in which the water can spread completely over the surface, if $\theta = 0$. The second state is a partial wetting on the solid, if $\theta < 90$. If $\theta > 90°$ ($\cos\theta < 0$), the liquid does not wet the solid and forms a droplet on the surface.

Co/Cr-coated tip (FMG01-Co) used in our experiment is also somewhat hydrophobic. Kaibara *et al.* [99] presented schematic models of the effect of tip and surface wettability on the adhesion force as demonstrated in Figure 4.46. They used a gold-coated AFM tip which is relatively hydrophobic. They explained that the adhesion force between hydrophobic tip and hydrophilic surface (Figure 4.46 a)) is weaker than that between hydrophobic tip and hydrophobic surface (Figure 4.46 b)). This is because of the strong attractive interaction of the latter in comparison to the repulsive force of the former exerted by the water absorption on the hydrophilic surface. However, a consideration of the adhesion force alone is not adequate to explain why the oxidation on Mo created a greater oxide size than that on $SiO_2$. There are various relevant interactions taking place during the formation of the water bridge, for example, the electrostatic interaction, the van der Waals interaction, the interaction of water molecules with the surface and the interaction with the external field due to polarization of the water molecules [100].

Cambel and Šoltýs [96] found that the sample conductivity has an effect on the electric field distribution. They showed that lowering the conductivity of the upper layer of the substrate leads to a drastically decrease of the electric field. Moreover, they found a general feature of LON that the upper-layer conductivity basically controls the width of oxide features [96]. Consequently, in our results, the conductivity of the native $SiO_2$ surface is lower than that of the Mo surface. This can cause the lower electric field between the tip and sample and lead to smaller size of oxide nanodots in the case of the native $SiO_2$ substrate.

a)

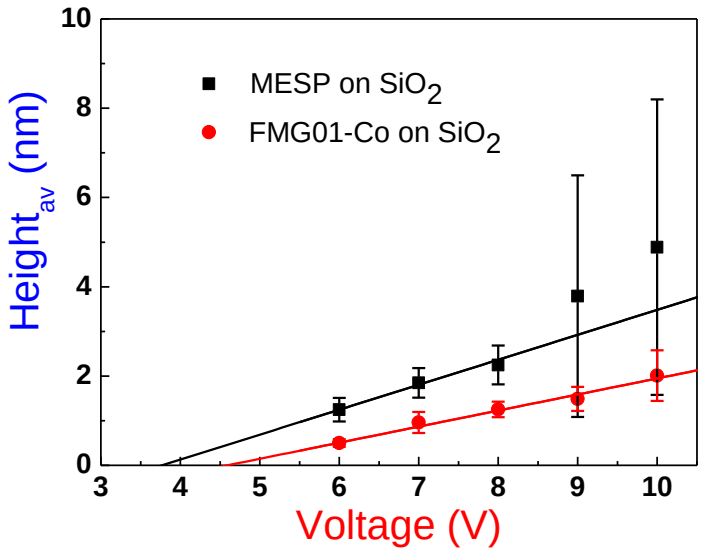


b)

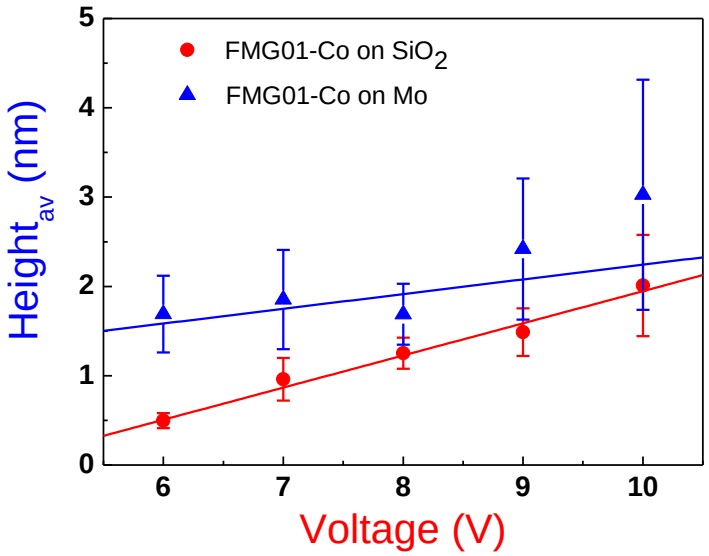


**Figure 4.44** Dependence of the nanodot height as a function of the substrate voltage. The data were measured by means of an average of 5 or more nanodots deposited with different applied substrate voltages ranging from 6 V to 10 V at a ramping time of 0.97 s and a relative humidity of 45 ± 2 % (MESP on native $SiO_2$) and 40 ± 2 % (FMG01-Co on native $SiO_2$ and Mo). The error bars represent the standard deviation of the mean of each figure. (a) Comparison of the dot height with different types of AFM tip on native $SiO_2$. (b) Comparison of the dot height on different types of substrate with the same AFM tip, FMG01-Co.

a)

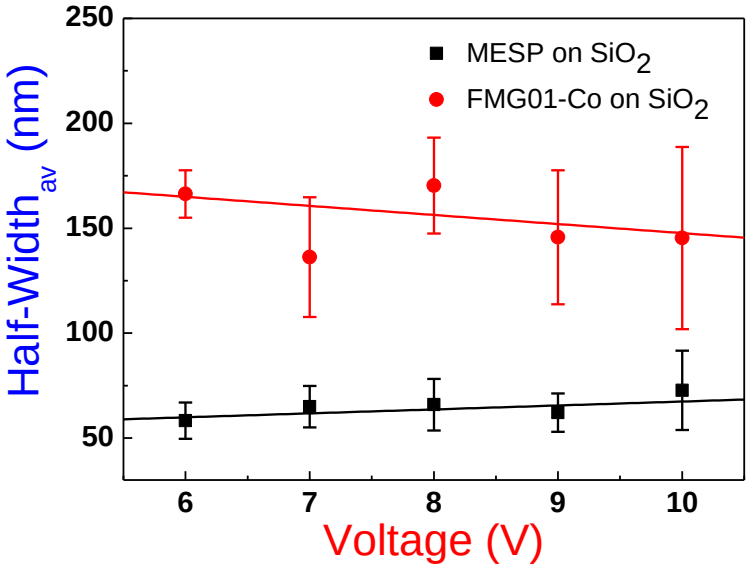


b)

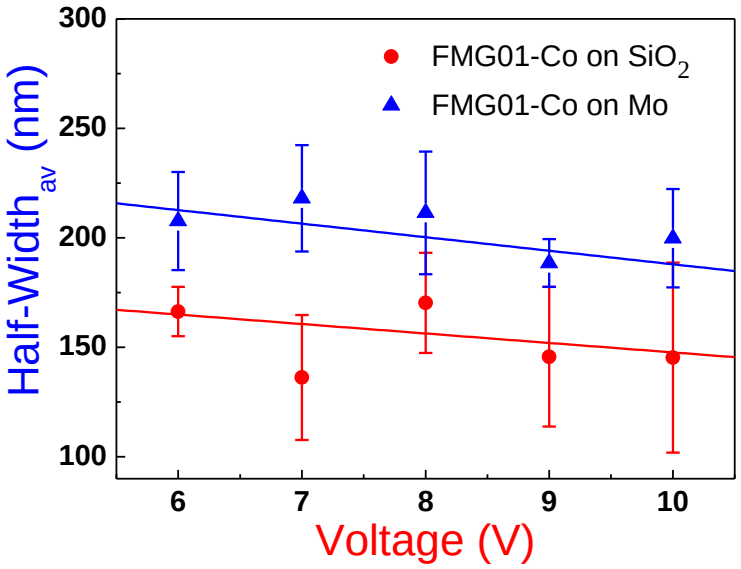


**Figure 4.45** Dependence of the nanodot half-width as a function of the substrate voltage based on 5 or more oxide nanodots deposited with different applied substrate voltages ranging from 6 V to 10 V at a ramping time of 0.97 s and a relative humidity of 45 ± 2 % (with MESP on native $SiO_2$) and 40 ± 2 % (with FMG01-Co on native $SiO_2$ and Mo). The error bars represent the standard deviation of the mean value of each figure. (a) Comparison of the dot half-width with different types of AFM tip on $SiO_2$. (b) Comparison of the dot half-width on different types of substrate with the same type of AFM tip, FMG01-Co.

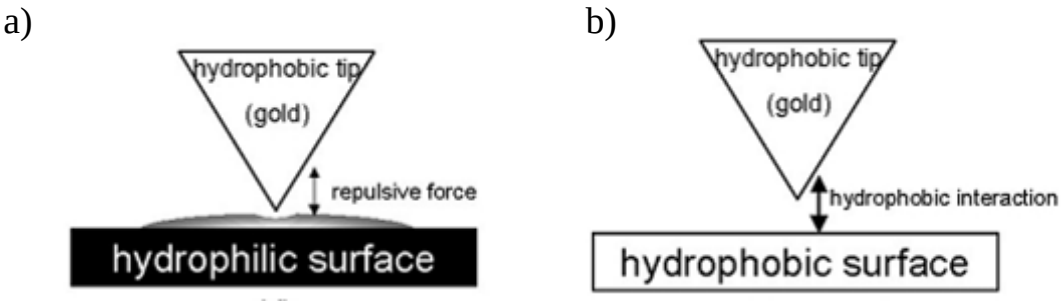


**Figure 4.46** Schematic illustrations of the effect of wettability of the tip and substrate on adhesion force. The hydrophobic (gold-coated) tip interacts with a) the hydrophilic surface with a repulsive force and b) the hydrophobic surface with an attractive interaction [99].

### 4.3.4 Dot size as a function of humidity

One of the key factors for AFM-based LON is the relative humidity of the environment. This is because AFM-based LON involves an adsorbed water layer on the surface and water bridge formation, where the electrolyte ($OH^-$ and $O^{2-}$) under ambient conditions is necessary to initiate the oxidation mechanism. To explore the role of humidity on surface modification in the LON experiment, oxide dot patterns were fabricated on a 100-nm-thick Mo layer covering an *n*-type Si substrate with a ramping time of 0.2 s using 5 V substrate bias voltage. A Co/Cr-coated tip (FMG01-Co) with a tip radius 40 nm, a force constant of 3.0 N/m and a resonance frequency of 60 kHz [28] was used. The relative humidity was kept at either a lower state of 43 ± 2 % or higher state of 66 ± 2 % using a commercial humidifier. The high humidity was adjusted by introducing water vapour into the chamber. Fifty to sixty dot patterns of oxide dots were deposited at both fixed humidities. Figure 4.47 a) and b) show that the nanodot size varied for different humidities. A visual inspection reveals that the size of oxide dots at fixed applied bias and tip ramping time considerably increased with increasing humidity. The bar graphs in Figure 4.48 a) and b) show the dot height and half-width as a function of relative humidity (as measured from Figure 4.47 a) and b)). These graphs were created on the basis of averaging 50-60 experiments performed under the same conditions. The graphs

clearly show that the height at high humidity was larger by a factor of 2.3 compared to that at low humidity (Figure 4.48 a)). In Figure 4.48 b), the half-width was around 0.27 μm when the relative humidity was 66 ± 2 % but lowering the humidity to 43 ± 2 % reduced the width by a factor of 1.48. This result confirms that the relative humidity significantly influences the size of the oxide dots.

As already mentioned in section 4.1.3, there have been many published papers which studied the effect of humidity on the AFM-based LON on various surfaces, such as, Si [48, 54, 67], thin film Ti [71], Zr and ZrN [72]. Some papers mentioned the effect of humidity mainly on the width but hardly observed an influence on the height. For example, the Avouris group [67] investigated the role of ambient humidity on oxide lines created by AFM-based LON on H-passivated *n*-type Si (100) as illustrated in Figure 4.4. A scan speed of 0.3 μm/s and a tip bias of -10 V were used for the oxidation. They found an increase in humidity from 14 % to 61 % leads to an increase of the line width by a factor of *ca.* 4. However, the oxide height only showed a small change. In addition, Bloe*β et al*. [63] performed the oxidation on H-passivated *p*-type Si (111) at a sample bias of 10 V for 1 s under different humidity conditions. Bloe*β* and co-workers also found that an increase of the humidity only affects the oxide width but does not lead to an increase of oxide height (see Figure 4.49). Additional work by Kuramochi *et al.* [48] revealed that an increase of the relative humidity from 40 % to 70 % significantly affected the diameter of either the oxide dots or the oxide lines. They experimented on a native-oxide layer on a *p*-type Si (001) wafer. However, taking into account the height difference, there was only a slight increase when the humidity was increased. Therefore, they were primarily interested in the investigation of the oxide volume differences. For instance, they showed that the oxide volume differences were equal to 1.2 $nm^3$ with the ΔRH of 10 % (70 % - 60 %) and 1.4 $nm^3$ with the ΔRH of 20 % (60 % - 40 %) at a sample bias of 10 V. After consideration of these previous reports on Si wafers, our results provided contrasting behaviour on a Mo surface especially in the case of height dependence. This is because other works found only a slight change in oxide height when the humidity increased but our results showed an increase by a factor of 2.3 when the humidity increased by about 23 %.

Consequently, the focus moved to the reports on the metal surface. The study of Held *et al.* [71] on a Ti thin film surface using a -5.5 V tip bias clearly showed a linear relationship between the width of oxide lines and relative humidity as already illustrated in Figure 4.9. Comparison of their data at the comparable humidity values with our data between ~45 % RH and ~65 % RH, the FWHM oxide line width increases from *ca.* 70 nm to *ca.* 130 nm which is approximately a factor of 2. However, in our case, the half-width was less increased by a factor of 1.48. Though, the height dependence was not shown in their report. Furthermore, Farkas *et al.* [72] also reported a linear dependence of the height and width of oxide dots as a function of humidity on Zr and ZrN surface as shown earlier in Figure 4.10 a) and b), respectively. The authors also showed that the oxide height increases linearly with humidity but only at long oxidation times (t > 200 s) as depicted in Figure 4.10 a). Taking into consideration their data, when the humidity increased from ~ 30 % to ~ 60 %, the height of oxide dots on a 36 nm thick Zr surface also increased from *ca.* 4.5 to *ca.* 6 nm which is about a factor of 1.3. Additionally, the height of the oxide dots grown on ZrN films was consistently greater than those on Zr films approximately by a factor of 2. This means that the film composition and film thickness play an important role in the height of oxide dots. Figure 4.10 b) showed that the width of the oxide dots depended linearly on the relative humidity but did not depend on the film materials and thickness. However, at the humidity above 60 %, the width seemed to be somewhat scattered with a large deviation from the linear fit leading to a difficulty in estimating the increase of the oxide width. Nevertheless, if we take into account an increase of humidity from about 43 % to 60 %, the width increased approximately by a factor of 1.4 for the data of Farkas *et al.* [72]. Their results therefore seem to be in good agreement with ours.

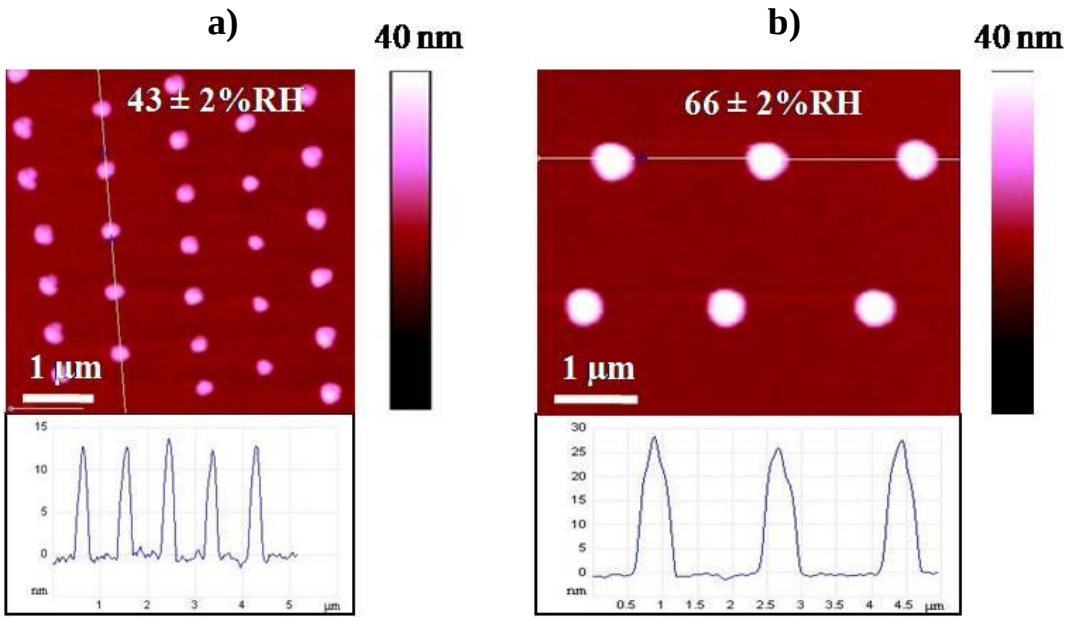


**Figure 4.47** AFM images and height profile of oxide nanodots deposited on a 100-nm-thick Mo layer covering an *n*-type Si wafer produced with different humidity values (a) 43 ± 2 % RH and (b) 66 ± 2 % RH at a substrate bias of 5 V and a ramping time of 0.2 s.

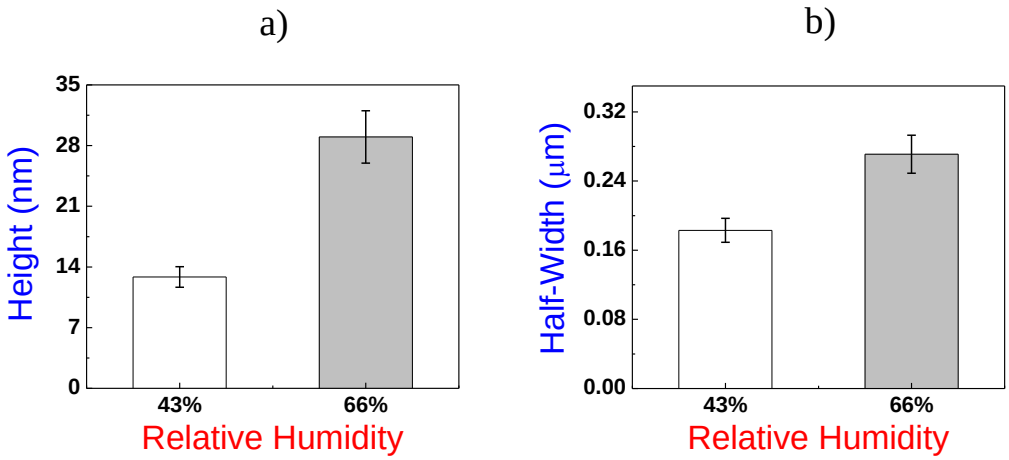


**Figure 4.48** Two graphs display the dependence of the height and half-width of the nanodots as a function of the relative humidity. The data were measured from Figure 4.47 taking an average of 50-60 dots. (a) The average height of nanodots at different relative humidity values. (b) The average half-width of nanodots at different relative humidity values.

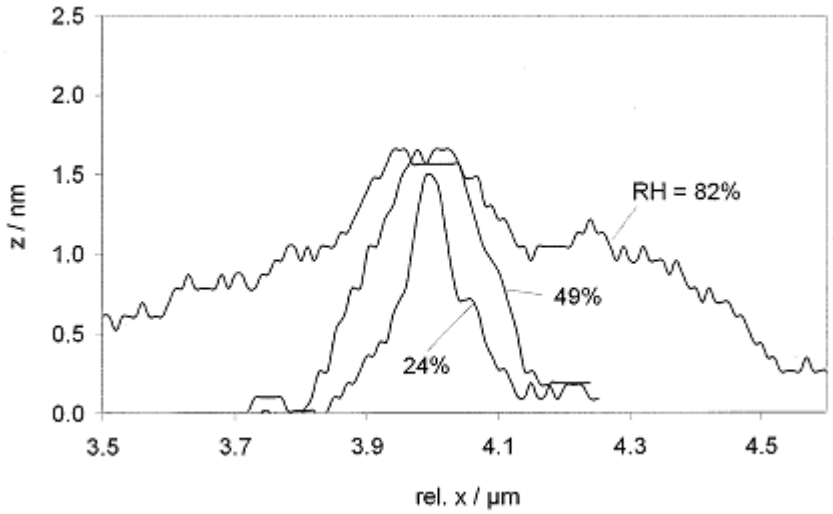


**Figure 4.49** Cross-sections of oxide dots fabricated by AFM-based LON with the applied sample bias of 10 V and exposure time of 1 s under various humidity conditions (RH= 24 %, 49 % and 82 %) [63].

### 4.3.5 Tunneling atomic force microscopy

A measurement of the Faradaic current has been shown to be an important method to gain more understanding during the LON process, since the transport of oxyanions between the tip and substrate plays an essential role for the oxidation mechanism [54, 67, 77]. Tunnelling AFM (TUNA) was used to measure the current and investigate the influence of various parameters on the LON process. This is due to the ability of the TUNA technique to measure ultralow currents (measurement range up to 120 *p*A) flowing from the sample to the tip at a fixed DC bias during the oxidation process. In addition, TUNA can record an AFM image and TUNA current simultaneously resulting in the direct correlation of a sample location with its electrical properties. The native-oxide $SiO_2$ wafer was observed by TUNA with various applied biases. Figure 4.50 shows TUNA current images taken at various DC sample voltages ranging from 5 V to 10 V applied to the substrate and the AFM tip was grounded as the tip was scanning the sample in contact mode. A Pt-coated conductive tip (NSG01-Pt, see Table 4.1) with 6 nm tip radius, force constant of 0.6 N/m and resonance frequency of 48 kHz was used. The substrate was kept under a relative humidity of 58 ± 2 %. We can clearly observe increases of TUNA current

and the number of conductive spots with increasing applied voltage from 5 V to 10 V in Figure 4.50 a) and b). By increasing the positive substrate bias from 5 V to 10 V, the current maximum increases from ~0.5 nA to ~6 nA. Moreover, the current profile shows a variation in the lateral dimension. The possible reason for this can be explained by changing the contact area of the AFM tip with the sample surface during scanning. Furthermore, some examples of TUNA measurement during oxide dot fabrication on a Mo surface as a function of oxidation time is illustrated in Figure 4.51. A Co/Cr coated AFM tip (FMG01-Co, see Table 4.1) with 40 nm tip radius, force constant of 3.0 N/m and resonance frequency of 60 kHz was used for this study. In order to analyse the influence of the voltage effects, the TUNA currents as a function of time with various substrate bias voltages ranging from 1 V to 10 V and 0 V to -10 V were respectively plotted in Figure 4.51 a) and b). The relative humidity was kept constant at 40 ± 2 %. In Figure 4.51 a), the waveform of the TUNA current shows that the current gradually increases as the AFM tip slightly approaches the substrate and then the TUNA current sharply increases to the maximum position due to the contact of the AFM tip to the substrate which leads to the high initial oxidation process. Subsequently, the TUNA current suddenly drops since the growing of the oxide dot which is an insulator. After that, the TUNA current slightly decreases since the AFM tip is retracted from the substrate. It can be seen that the maximum positions of the TUNA current ($I_{peak}$) increased with increasing more positive substrate bias (V) see Figure 4.51 a). It can be drawn a common model between the $I_{peak}$ and V as following: $I_{peak} = aV$. Where, a is a constant and V is the substrate bias ranging between 1 V and 10 V. Additionally, it is worth to note that with applied substrate bias voltages between 0 V and -3 V the TUNA current can also be observed as demonstrated in Figure 4.51 b), however, this behaviour was supposed that the TUNA current passes through the sample but it is not attributed to the oxidation process. While applying the substrate voltages between -4 V to -10 V (see Figure 4.51 b)), it can be seen that no TUNA current could be detected. After this section, the TUNA current will be further investigated during the oxide dot fabrication for a more complete understanding of the oxide growth kinetics.

**a)**

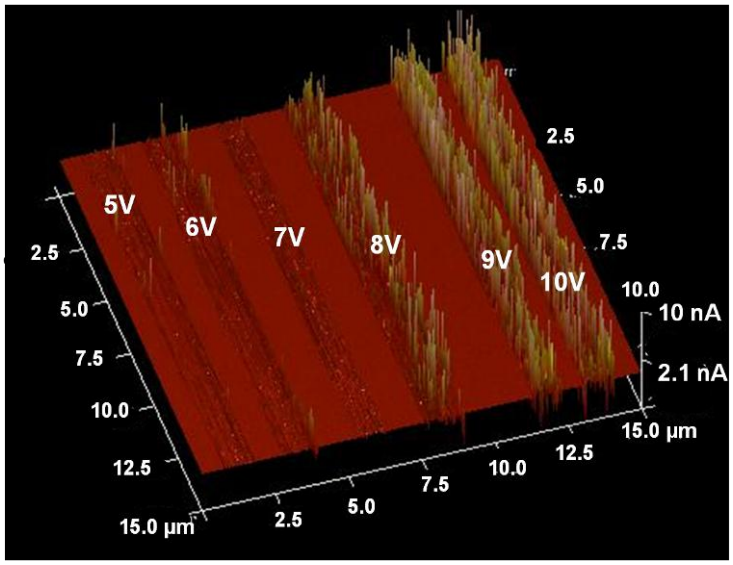


**b)**

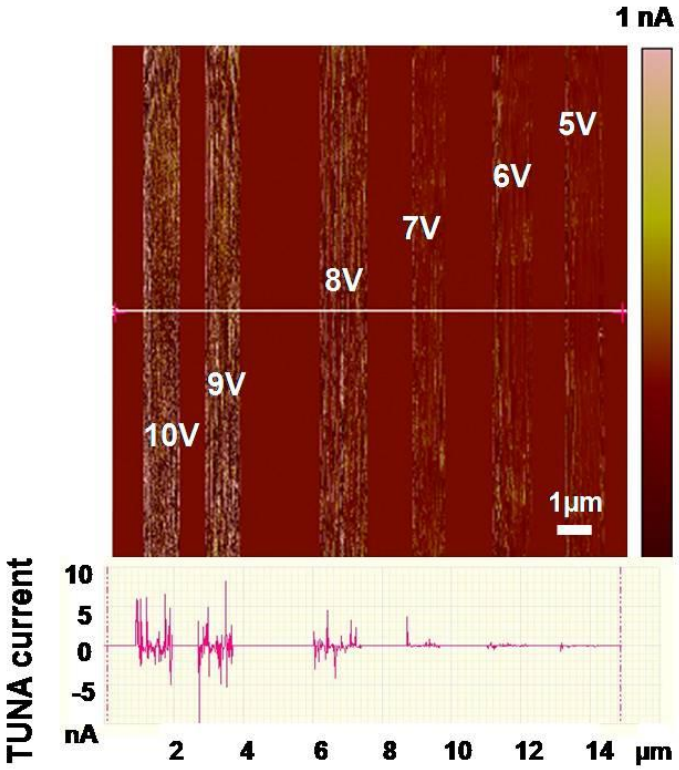


**Figure 4.50** a) TUNA 3-D image and b) TUNA current image with corresponding profile taken on a native-oxide-layer-coated *n*-type Si (100) substrate at a wide range of substrate bias voltages ranging from 5 V to 10 V (the precise values are depicted above each strip) with a Pt-coated AFM tip (NSG01-Pt) with 6 nm tip radius, force constant of 0.6 N/m and resonance frequency of 48 kHz under a relative humidity of 58 ± 2 %. The tip was grounded for the TUNA measurements.

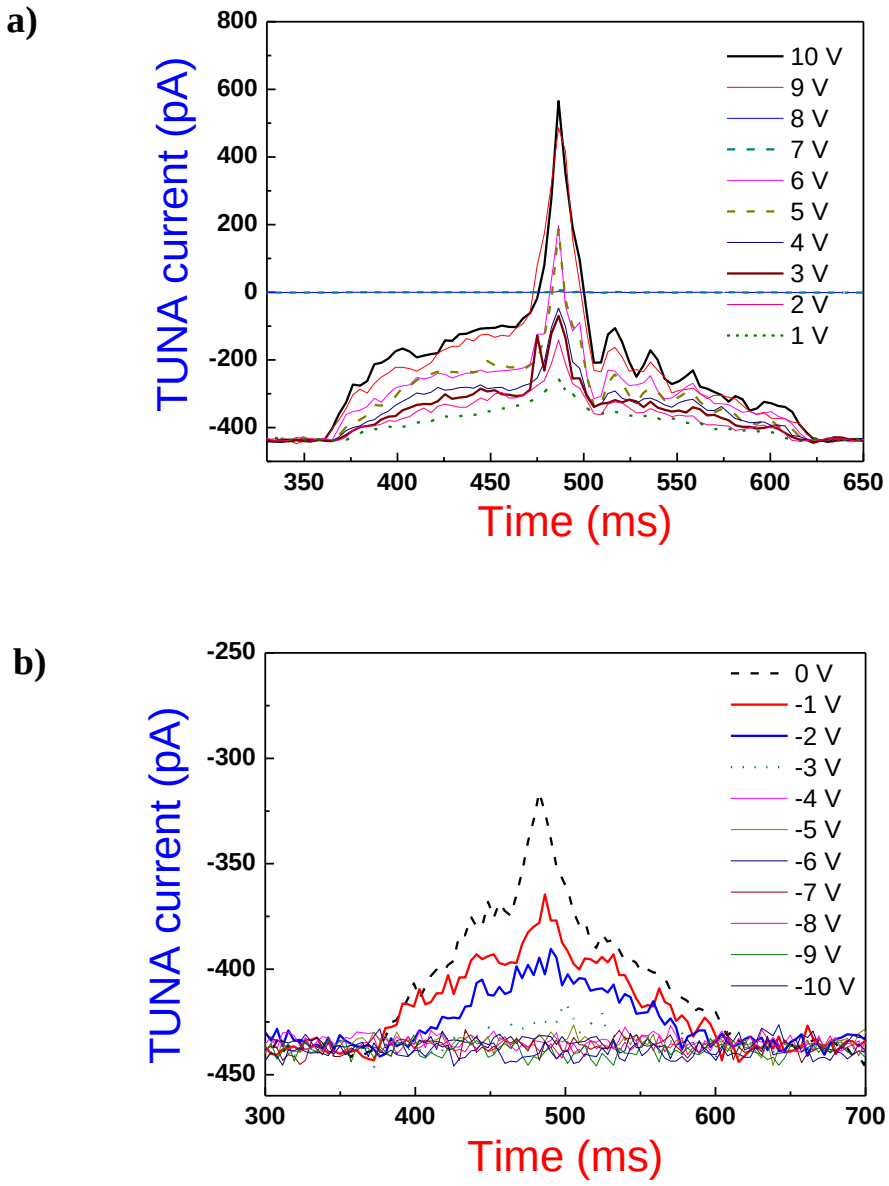


**Figure 4.51** The dependence of TUNA current as a function of time taken on Mo surface at various substrate bias voltages ranging from 0 V to 10 V in a) and from 0 V to -10 V in b) with a Co/Cr-coated AFM tip (FMG01-Co) with 40 nm tip radius, force constant of 3.0 N/m and resonance frequency of 60 kHz under a relative humidity of 40 ± 2 %. The tip was grounded for the TUNA measurements.

### 4.3.6 TUNA measurement and relative humidity effect on dot size

To further understanding the influence of the relative humidity on the oxide dot formation, measurement of the faradaic current supplied from the substrate to the AFM probe contact point is critical as it is related to the ionic diffusion [54]. Figure 4.52 a) and c) show some examples of the detected TUNA currents during the oxidation process at low humidity (43 ± 2 %) and high humidity (66 ± 2 %). In Figure 4.52 a) at low humidity, the current intensity detected during the oxidation varied between 10 *p*A and 120 *p*A with different waveforms for each oxide dot fabrication. Figure 4.52 b) shows the expanded graph of the TUNA current at low humidity. By contrast, with the high humidity in Figure 4.52 c), the waveform of the detected current of each oxidation dot behaved rather uniformity under the same conditions. The waveform of the current indicates that the current sharply increases to about 18 *p*A and decayed with time for ~25-30 ms. Therefore, a comparison between low and high humidity did not find any correlation with the current intensity. Recently, Takemura and colleagues [101] reported the measurement of faradaic current during AFM-based LON on various types of substrates, such as a Si substrate with native-oxide layer and H-passivated on the surface, NiFe thin film and NiFe thin film capped by $Al_2O_3$. They found that nearly half of the detected current was used for the oxidation process on native-oxide-layer-coated *p*-type Si.

The study by Kuramochi *et al.* [54] showed that the total oxidative charges in the form of $O^-$ and $OH^-$ passed into the oxide can be obtained by the integration of *I-t* curves. Consequently, we measured the amount of charge, which was obtained by the integration of the TUNA current versus time curve as illustrated in Figure 4.52. Figure 4.53 exhibits the relationship between the relative humidity and the integrated charge. We found a significant increase of the average integrated charge from *ca.* 405 *p*C to *ca.* 457 *p*C with increasing relative humidity. This is in contrast with the study of Kuramochi and co-workers [54] as already shown in Figure 4.8 d). They also demonstrated the relationship between the integrated current and the sample bias for various values of relative humidity but their studies used a H-passivated *p*-type Si (001) wafer. From their results, if the sample voltage was below 8 V, the integrated charge ($I_{int}$) had only a small increase ($\Delta I_{int} < 10$ *p*C) with increasing humidity from

40 % to 70 %; however, in our experiments, it was found a considerably increase about 50 *p*C from 43 ± 2 % to 66 ± 2 %. This can be explained by the different substrates used. As the study of Shimada *et al.* [102] reported that the current level when oxidising the Si substrate (lower conductive substrate) was lower than that when oxidising the NiFe thin films (higher conductive substrate). In our case, the Mo surface is more conductive than the H-passivated *p*-type Si (001) substrate of the study of Kuramochi *et al.* [54]. As a result, the currents observed in our case were much larger compared to that in the study of Kuramochi and co-workers [54].

To verify if the oxide dot was efficiently fabricated by the current (total integrated charge) generated between the AFM tip and substrate during AFM-based LON, a comparison of the volumes of the nanodots obtained with different methods was illustrated in Figure 4.54. There were three different means of calculating the oxide volumes. Firstly, the theoretical volume ($V_{int}$) was calculated from the integrated charge ($Q_{int}$) of the data from Figure 4.53. This method assumed that the behaviour of $V_{int} \propto Q_{int}$. Therefore, $V_{int}$ was presented by the following equation:

$$V_{int} = (Q_{int} / 6q_e)*(m_{Mo}/\rho_{Mo}) \quad (11)$$

Where $Q_{int}$ is the integrated charge; $q_e$ is the elementary charge; $m_{Mo}$ is the mass of Mo and $\rho_{Mo}$ is the density of Mo. $6q_e$ is due to the electron being involved in the oxidation reaction of Mo (0) to Mo (VI) in $MoO_3$.

Secondly, the volume of oxide dot above the surface ($V_{surf}$) was calculated from measurement of the height and the half-width data from Figure 4.48. From the AFM image results in Figure 4.47 and the size measurement in Figure 4.48, we assumed that the geometry of an oxide dot is close to a cylindrical shape. The volume was then calculated by the following equation:

$$V_{surf} = \pi(HW)^2 h \quad (12)$$

Where HW is the half-width and h is the height of an oxide dot. Lastly, since it is well-known that the LON also takes place under the surface [67, 70, 77], the total dot volume ($V_{total}$) is obtained by assuming that the oxide dot consists of the

volume of oxide above and below the surface. This can be estimated by using the oxide thickness (D) instead of the oxide height (h). As the studies of Fontaine *et al.* [35] and Bloeß *et al.* [63] reported a similar ratio of the height ($h_{ox}$) to the total oxide thickness ($D_{ox}$) of oxide dot equal to 0.6. Thus, the oxide thickness can be determined as h/0.6. The total volume is then obtained by this equation:

$$V_{total} = \pi(HW)^2(h/0.6) \quad (13)$$

Figure 4.54 a) and b) exhibit the comparison of three different volumes including $V_{int}$, $V_{surf}$ and $V_{total}$ at a low humidity (43 ± 2 %) and high humidity value (66 ± 2 %). All volumes at higher state humidity clearly show greater values than that at lower state humidity. To examine this correspondence quantitatively, $V_{total}$ should be equivalent to $V_{int}$ in the case that all of the integrated charge is used for the oxidation process. However, Figure 4.54 a) indicates that less than a half of the detected charge at low humidity is actually used for the oxidation process, since both $V_{total}$ and $V_{surf}$ values are less than 50 % of $V_{int}$ value. On the other hand, in the case of high humidity as illustrated in Figure 4.54 b), both $V_{total}$ and $V_{surf}$ values are greater than 50 % of $V_{int}$ value. Even though, $V_{total}$ at high RH is a slight greater than $V_{int}$. This phenomenon can be related to the estimation of the total volume by using the ratio of oxide height to oxide thickness from previous published papers [35, 63] which may not correctly represent the real thickness of oxide dots due to the different substrate used. Another possible reason could be the inaccurate size measurement from the tip artifact which leads to the overestimated volume of both $V_{surf}$ and $V_{total}$. However, the AFM tip used for imaging has very small tip radius about 1-3 nm (NSG01-DLC, NT-MDT Co.), the effect of the tip convolution could be, therefore, ignored. Consequently, this observation revealed that a 23 % difference in humidity leads to a significant difference in the final volumes of the oxide dots when other parameters are controlled, such as voltage and ramping time. The important role of the relative humidity on the oxidation process on Mo surface is clearly shown through the above comparisons, since the increase in humidity leads to a higher efficiency of the charge in generating the larger oxide volume.

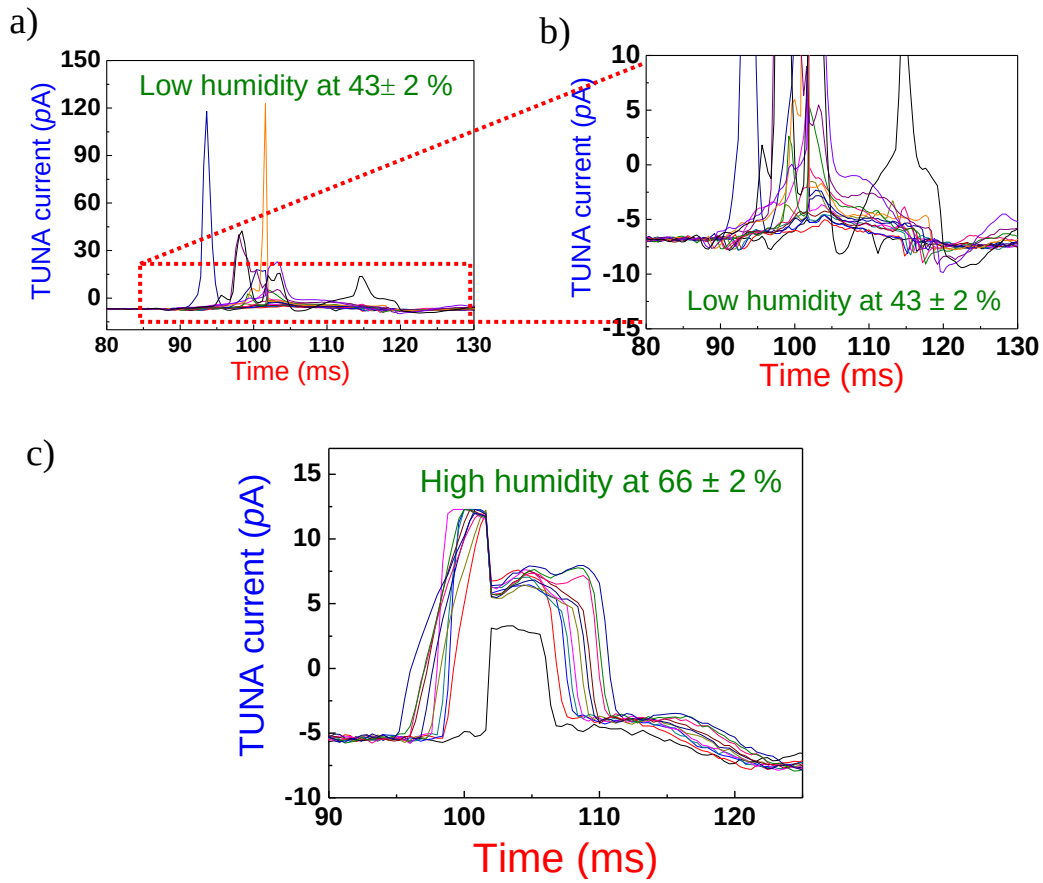


**Figure 4.52** The TUNA currents passed through the probe-substrate during nano oxidation on Mo surface obtained from Figure 4.47 with different relative humidity a) 43 ± 2 %, b) expanded scale in a) and c) 66 ± 2 % at 5 V substrate bias and a ramping time of 0.2 s.

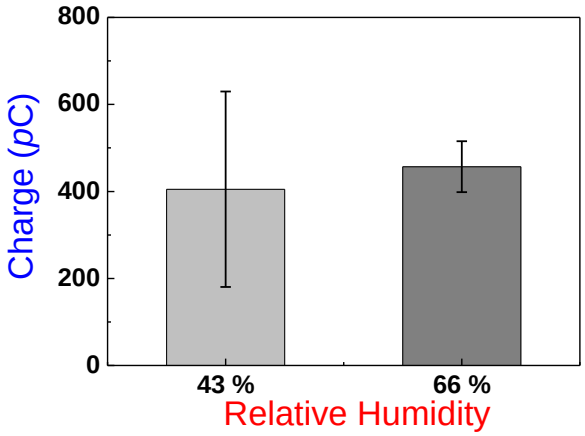


**Figure 4.53** The correlation between the relative humidity and the total amount of detected charges from integration of TUNA current *vs* time curves in Figure 4.52.

a)

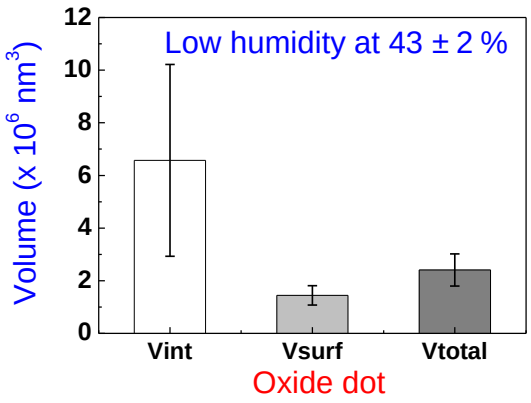


b)

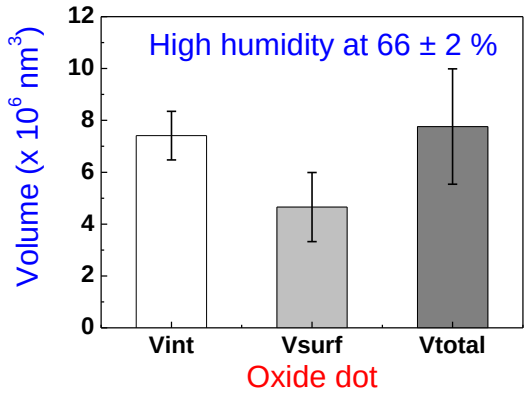


**Figure 4.54** Two graphs display a comparison of the volume of the nanodots obtained with different methods (a) at low humidity of 43 ± 2 % and (b) at high humidity of 66 ± 2 %. The first left column represents the theoretical volume ($V_{int}$) obtained from the integrated charge of the data in Figure 4.53 and calculated by assuming the behaviour $V_{int} \propto Q_{exp}$ of the oxidation process. The middle column represents the volume of oxide dot above the sample surface ($V_{surf}$) which is calculated from the height (h) and the half-width (HW) of oxide dots from the data in Figure 4.48. The geometry of oxide dots is assumed to be a cylinder [$V_{surf} = \pi(HW)^2h$], where HW and h are the half-width and height of the oxide dots, respectively. The last column on the right hand side represents the total dot volume ($V_{total}$) which is obtained by using the ratio of the oxide height (h) to the oxide thickness[8] (D) equal to 0.6 [35, 63] so the oxide thickness (D) is equal to h/0.6. The total volume is calculated by this equation: $V_{total} = \pi(HW)^2(h/0.6)$.

[8] The oxide thickness is the total height of the oxide dot obtained by summing of the height above the surface and below the surface.

### 4.3.7 Dot size as a function of deposition time

One more important factor is the deposition time or the duration of the oxidation process. To obtain a deeper understanding of AFM-based LON on a metal surface and to assess the faradaic current, the modification on a 100-nm-thick Mo layer on top of an *n*-type Si substrate was investigated by varying the ramping time. Figure 4.55 shows a series of oxide dots that were prepared with different ramping times which corresponds to the deposition times of the tip. The ramping time was increased from 0.23 s to 100 s with the probe moving to a new position before each pulse. The ramping time is depicted beside each row of oxide dots. The applied substrate bias voltage and relative humidity were maintained at 10 V and 47 ± 2 %, respectively. A Co/Cr-coated tip (FMG01-Co, see Table 4.1) with a tip radius of 40 nm, a force constant of 3.0 N/m and a resonance frequency of 60 kHz [28] was used. The dot sizes significantly increased with increasing ramping time (increasing the deposition time).

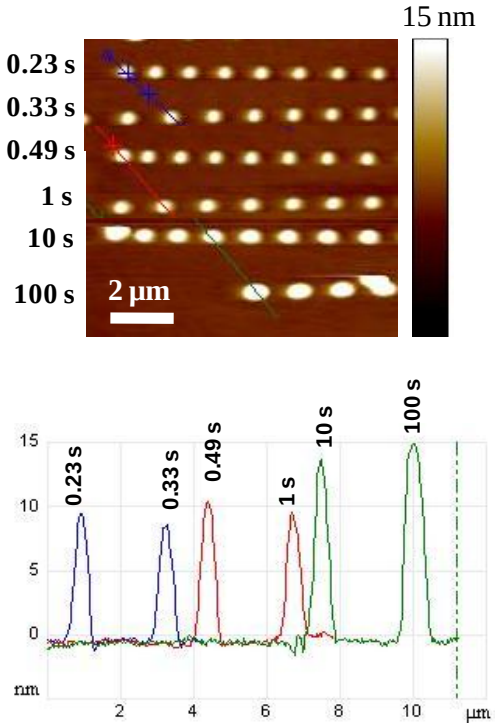


**Figure 4.55** AFM image and height profile of oxide nanodots deposited on the 100-nm-thick Mo layer covering of the *n*-type Si substrate with different ramping times ranging from 0.23 s to 100 s at a substrate bias of 10 V and a relative humidity of 47 ± 2 %.

Figure 4.56 shows the measured TUNA current during the oxidation process. The current intensity varied from 600 *p*A to 12 nA, becoming smaller with increasing ramping time from 0.23 s to 100 s as shown in Figure 4.56 a) - f). It was found that the current was saturated at 12 nA for the slow ramping times of 0.23, 0.33 and 0.49 s as can be seen from Figure 4.56 a) - c). In Figure 4.56 a) – d), the waveform of the current indicates that the current during the pulse gradually increased with time, for the ramping time between 0.23 s and 1 s, and then the current suddenly dropped during the constant applied substrate bias voltage at 10 V and 47 ± 2 % RH. For the ramping time of 10 s and 100 s in Figure 4.56 e) and f), the full range of the current seemed to behave in an opposite way under the same conditions. The current sharply increased and then decayed with time. However, when it was considered in more detail by expanding the range as shown in Figure 4.56 g) and h) for the ramping time of 10 s and 100 s, it was found that the current was gradually increased with time in the start region, although, the data points were relatively rough. This was consistent with the ramping time between 0.23 s and 1 s. After considering this observation, the correlation between the ramping time and the current waveform was in good agreement in the start region; however, the decaying behaviour seemed to be the influence of increase of the oxide thickness.

To analyse the dot formation, the amount of charge was calculated by the integral of the current versus time data plot from Figure 4.56, supplied from the substrate to the probe contact point. Then, Figure 4.57 shows the relationship between the ramping time and the integrated charge. A linear dependence was found for the charge with increasing the ramping time. The small region of the ramping time ranging from 0.23 s to 1 s was replotted in Figure 4.57 b). The graph in Figure 4.57 a) shows linear fit with a gradient of 87.6 ± 5.7 *p*C/s while the graph at a low ramping region in Figure 4.57 b) shows a power-law dependence. Graphs of charge *vs* height and charge *vs* half-width are presented in Figure 4.58 a) and b). These graphs show the exponential behaviour of the height and width of the oxide dots as a function of the total charge. It is clear from Figure 4.58 that first the height and width considerably increase with increasing total charge and then stay constant for charges above 3000 *p*C. This was probably because the charges above 3000 *p*C were the over

currents which were considered not to contribute to the oxidation reaction as the studies of Takemura *et al.* [94] and Shimada *et al.* [102].

The current efficiency of the oxidation process can be evaluated by comparing the volume from the integrated charge ($V_{int}$) and the volume of the fabricated oxide dot which is $V_{surf}$ and $V_{total}$. Figure 4.59 and 4.60 show a comparison of the volumes obtained with different methods as discussed earlier in section 4.3.6 as a function of the charge and the ramping time, respectively. Firstly, the theoretical volume ($V_{int}$) was calculated using equation (11) and the data were obtained from the integrated charge ($Q_{int}$) of the data from Figure 4.57. Secondly, the volume of oxide dot above the surface ($V_{surf}$) was calculated using equation (12) and the height and the half-width data from Figure 4.58 were used. The total volume ($V_{total}$) is then obtained using equation (13).

From both Figure 4.59 and 4.60, the graphs show very similar trends for the correlation of the volumes versus the charges as well as the volume versus the ramping time. It was found that with applying a small number of charges below ~160 *p*C (see Figure 4.59) and at a low ramping time of 0.23 s and 0.33 s (see Figure 4.60), the values of both $V_{surf}$ and $V_{total}$ are greater than that of $V_{int}$. This can be due to the saturated current at low ramping time where the exact current used for oxidation process could not be detected as already discussed above. After a charge above ~180 *p*C and a ramping time approximately above 0.40 s, it can be seen that only $V_{total}$ is higher than $V_{int}$ as shown in Figure 4.59 b) and 4.60 b). However, when the charge and the ramping time was increased to above ~1000 *p*C and ~10 s, $V_{int}$ seem to be considerably increased, whereas $V_{total}$ and $V_{surf}$ stay constant as illustrated in Figure 4.59 a) and Figure 4.60 a). It is explainable that with a high ramping time (or long exposure time) the excess charge from the tip seems to be no longer used for the oxidation process. Shimada *et al.* [102] explained that after the conductive sample surface is oxidised the current is considered as excess current when this current passing through the substrate does not contribute to the oxidation process. From our investigation on the Mo surface, the current efficiency decreased with an increase in the ramping time. As a result, the oxidation process on the Mo surface depends on the ramping time but only for short ramping times.

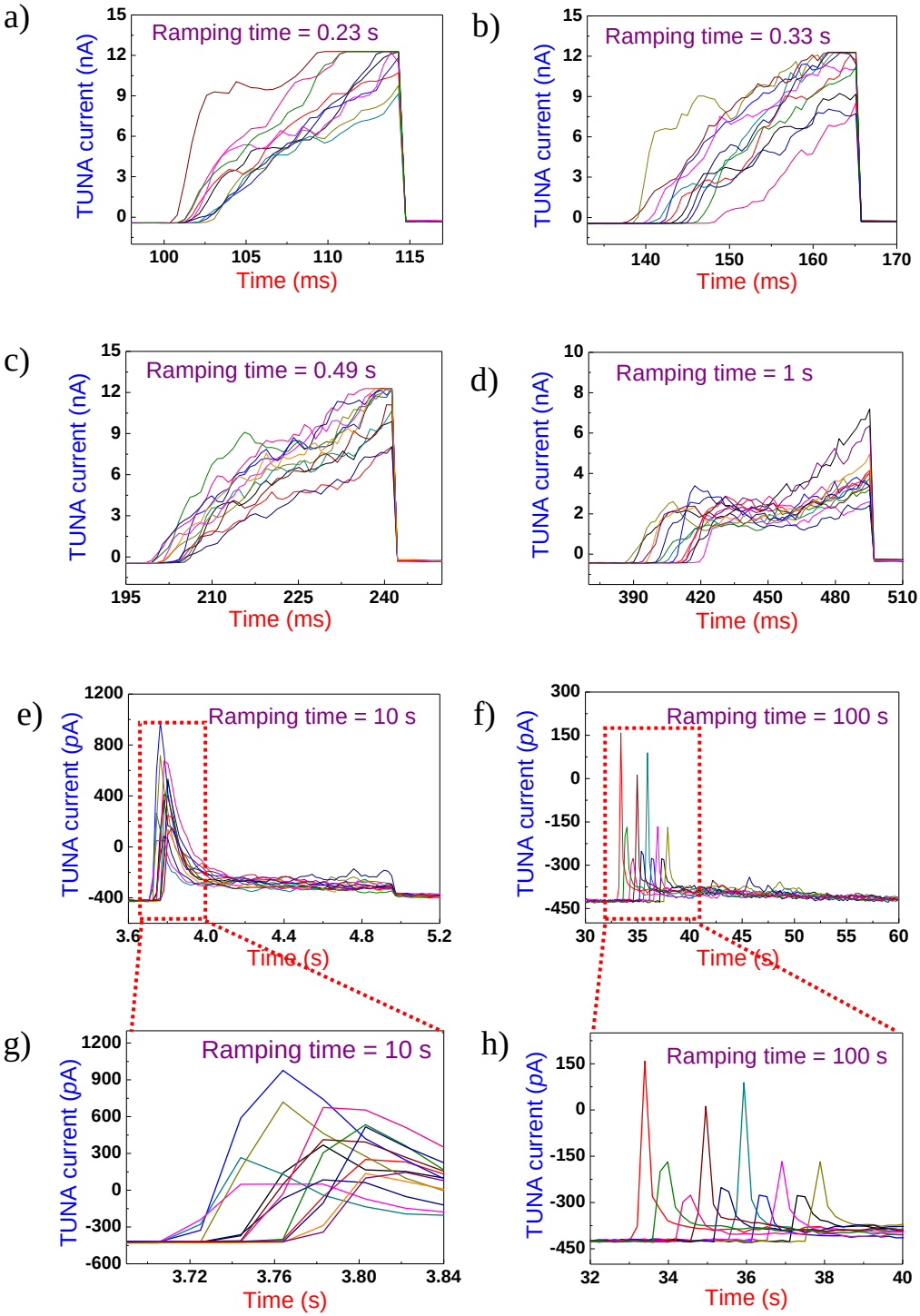


**Figure 4.56** The detected TUNA currents passed through the probe-substrate during nano-oxidation process for various values of ramping time of a) 0.23 s, b) 0.33 s, c) 0.49 s, d) 1 s, e) 10 s and f) 100 s at 10 V substrate bias and a relative humidity of 47 ± 2 %. g) and h) are the expanded ramping time regions of e) 10 s and f) 100 s, respectively.

a)

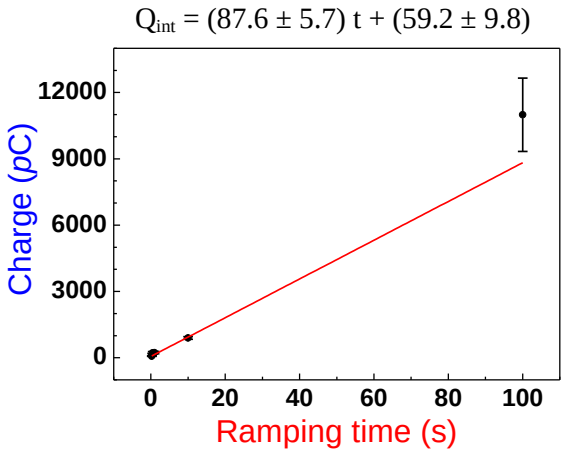


b)

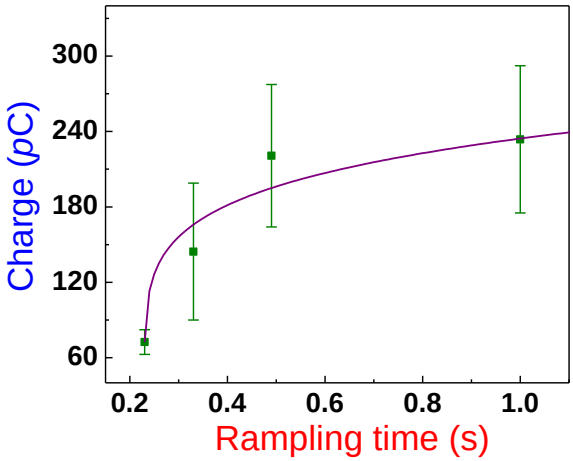


**Figure 4.57** The correlation between the ramping time (t) and calculated charges (Q) from integrated TUNA current *vs* time in Figure 4.56. a) The graph shows the linear-linear plot of the average integrated charge of each oxide dot at different ramping time from 0.23 s to 100 s and the corresponding linear fitting equation. b) The graph shows the linear-linear plot of the average integrated charge of each oxide dot at different ramping time from the low ramping time range (from 0.23 s to 1 s) with power dependence.

a)

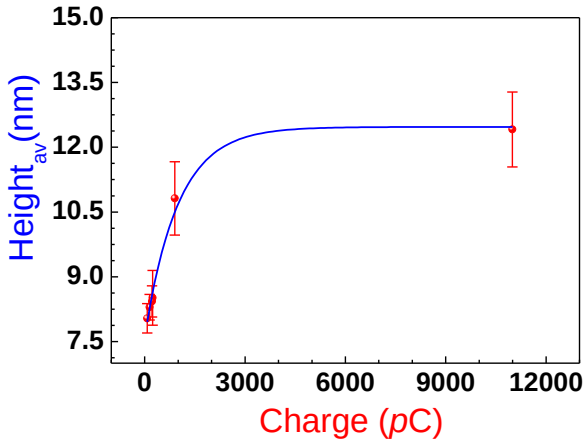


b)

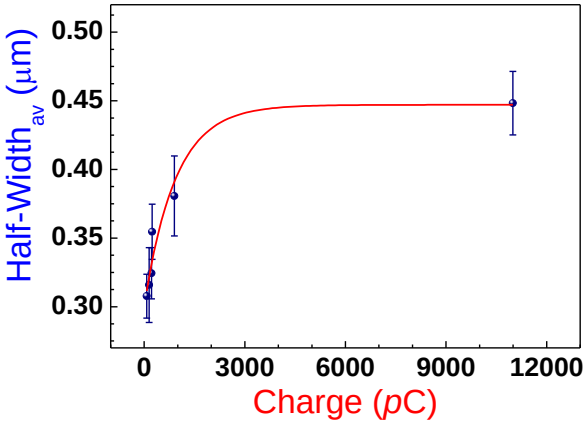


**Figure 4.58** Two graphs display the dependence of the height and half-width of the nanodots as a function of the charge from the substrate. The data were measured from Figure 4.55 by means of an average of 10 dots. The error bars represent the standard deviation of the mean of each data set. (a) The average height of nanodots at different charges. (b) The average half-width of nanodots at different charges.

a)

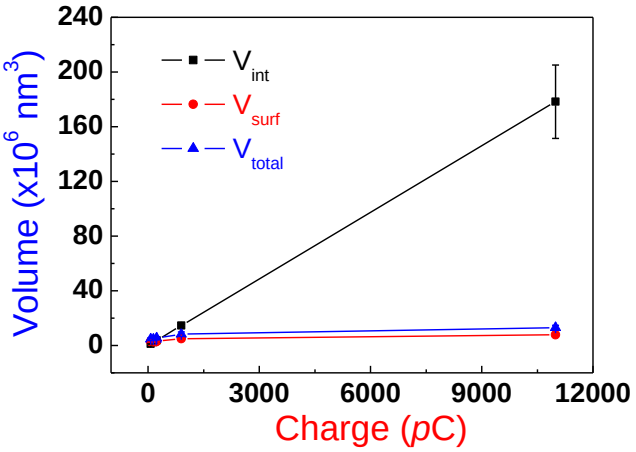


b)

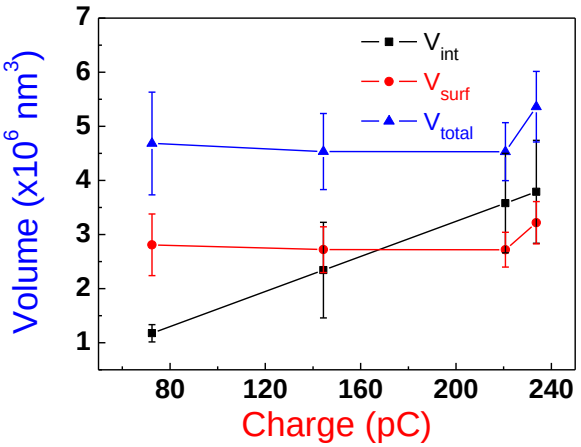


**Figure 4.59** Comparison of the volumes of the nanodots obtained with different methods which are $V_{int}$, $V_{surf}$ and $V_{total}$ as already discussed in section 4.3.6 as a function of the charge from the substrate. The theoretical volume ($V_{int}$) is obtained from the integrated charge of the data in Figure 4.57 and calculated by assuming the behaviour $V_{int} \propto Q_{exp}$ of the oxidation process. The volume of oxide dot above the sample surface ($V_{surf}$) is calculated from the height (h) and the half-width (HW) of oxide dots from the data in Figure 4.58. The geometry of oxide dots is assumed as a cylinder [$V_{surf} = \pi(HW)^2h$], where HW and h are the half-width and height of the oxide dots, respectively. The total dot volume ($V_{total}$) is calculated by following equation: $V_{total} = \pi(HW)^2(h/0.6)$. a) The graph shows the plot at different ramping times from 0.23 s to 100 s. b) The graph shows the plot at different ramping times from the low region of ramping time range (from 0.23 s to 1 s). A fitting line in the graphs is only a guide for the eyes.

a)

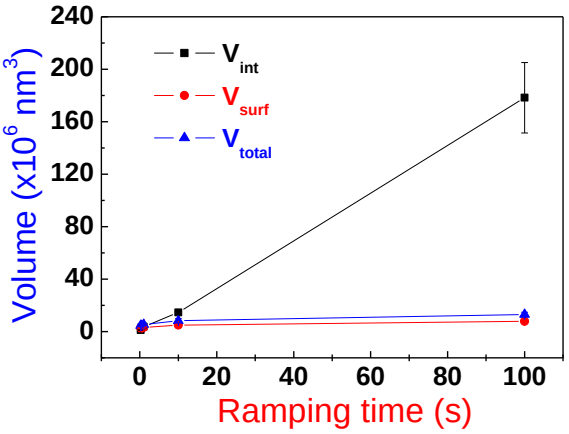


b)

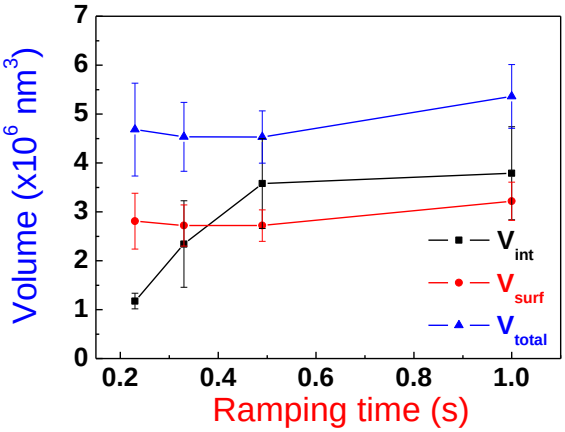


**Figure 4.60** Comparison of the volumes of the nanodots obtained with different methods which are $V_{int}$, $V_{surf}$ and $V_{total}$ as already discussed in Figure 4.59 as a function of ramping time. a) The graph shows the plot at different ramping times from 0.23 s to 100 s. b) The graph shows the plot at different ramping times from the low region of ramping time range (from 0.23 s to 1 s). A fitting line in the graphs is only a guide for the eyes.

## 4.4 Conclusions

This chapter was devoted to the study of AFM-based LON in contact mode. AFM-based LON was used to oxidise substrates under the apex of an AFM tip biased with a negative voltage with respect to the sample. If such a tip was being scanned over the surface in the presence of adsorbed water, a nanometre-scale oxidised pattern could be formed. The main purpose of this chapter was to understand the AFM-based LON mechanism, to optimise the parameters and to scale up the resolution of the technique for routine fabrication. The main central interest was on the Si substrate due to its importance for microelectronics. Another one was the Mo substrate since the AFM-based LON of Mo can be used as nanomasks for the patterning of structures on Si or $SiO_2$ substrate. A number of parameters which can influence the AFM-based LON process were investigated on either a native-oxide-layer-coated Si substrate or a Mo substrate. This chapter yielded the following results:

1. The height and width of the oxide geometric and line structure fabricated on the native-oxide layer covered on the *n*-type Si (100) substrate strongly depended on the applied voltage and scan speed. It was found that the height and the width of the oxide structure depend on the value of the applied voltage. This was in good agreement with a previous report of Hattori *et al.*[84] who also showed that both oxide strip height and width (FWHM) increased with the applied voltage.

2. The height grew linearly as a function of applied tip voltage. Our result was in good conformity with the study of Ma *et al*. [75]. In comparison to the oxide height at the same applied voltage, the heights of oxide strips obtained by our experiment were much smaller than those of Ma *et al.* [75] for all voltage values. The potential reasons for this could be affected by many factors, for example, the different types of applied voltage used (dc voltage in our case and ac modulation for the study of Ma and co-worker [75]), the reduction of space charge effect as reported by Dagata *et al.* [64], Pérez-Murano *et al.* [85], and Park *et al.*[86] when applying ac modulation to the substrate and the different values of relative humidity used (51 ± 5 % in our experiment but 60 – 68 % in the study of Ma

*et al.* [75]). Our result was also similar to the studies by Stiévenard *et al.* [87] and Fontaine *et al.* [35] who showed a linear dependence of the height as a function of the voltage applied to the sample. Additionally, Fontaine *et al.* [35] also reported that the tip speed can influence the slope of the linear fit. As a consequence, taking our result and several relevant studies into consideration, it can be established that the oxide height is linearly dependent on the applied bias.

3. The width also grew linearly as a function of applied tip voltage. Our observation was well correlated with the study of Fontaine *et al.* [35]. They revealed from their estimation when the electric field was below a critical electric field value ($E_c$) the oxide strip did not grow. It was evident that the applied electric field between the tip and the substrate is a key parameter for the oxidation process and considerably influence the oxide width.

4. The nanodots clearly depend on the applied voltage, type of AFM tip and sample, relative humidity and ramping time. The height of nanodots generated on the native-oxide layer of the *n*-type Si (100) wafer linearly increased with the substrate bias voltage. Our results were comparable to the study of Fontaine *et al.* [35]. However, there were some variations that they used tapping mode AFM LON and pulse voltages applied to the sample. Additional work which was similar to our observation was the study of Kuramochi *et al.* [48]. Taking into account at the same voltage value, the heights of the oxide nanodots were greater than that of oxide nanostrip fabrication. Our results were in good agreement with the study of Tseng and Notargiacomo [73].

5. It was found that the half-width of the nanodots generated on the native-oxide-layer-coated *n*-type Si (100) wafer depends on the applied voltage. However, the applied voltage dependence of the half-width of nanodots was slightly fluctuating but with a growing trend. We could conclude from our investigation that the width seemed to depend on the applied voltage and close to the linear dependence. It was learnt from the study of Calleja *et al.* [90] that the applied voltage plays a major role for the meniscus size and the meniscus diameter linearly increased with applied voltage. Since AFM-based LON was confined

within the water meniscus, an oxide lateral size was directly related to the water bridge size.

6. For the effect of voltage on the oxidation process, it was gained knowledge from the study of Avouris *et al.* [67, 77] that the voltage dependence directly involves the electric field which plays a crucial role in the oxidation process. The electric field enhances the ion diffusion ($OH^-$ or $O^-$) through the growing oxide film due to the contact potential $V_0$ (Mott potential) difference between the initial oxidised silicon and the adsorbed oxygen layer. These lead to the continued oxide growth from combination of the ions with holes in the silicon substrate. However, when the oxide thickness increases, the electric field is decreased until the electric field is insufficient for ionic diffusion ($< 10^7$ V/cm [65, 67, 77]). This can cease the oxide growth.

7. It was found that -4.0 ± 1.6 V applied to the tip was a threshold voltage for our experiments when fabricating geometric patterns. This was in good agreement with the report by Ma *et al.* [75] who also found that a $V_{th}$ value was approximately +4 V applied to the native oxide Si (111) substrate. However, the difference was that they used a pulsed voltage, while a dc voltage was used in our study. However, in the case of different sample surfaces but similar doping (*n*-type) Si substrate, our threshold voltage value was not consistent with the study of Fontaine *et al.* [35] who found that the typical threshold voltage on H-passivated *n*-type Si (100) was ~0.0 V. As a result of this consideration, it was assumed that different surfaces have an influence on the values of the threshold voltage.

8. In the case of nanodot fabrication, the threshold voltage value obtained from the linear fit equation was found to be 2.9 ± 1.6 V and 2.8 ± 2.2 V from two experiments. These two values were in excellent agreement. It was deduced that the threshold voltage does not depend on the type of AFM tip specifically in terms of coating material of the tip.

9. The dependence of the height and the width on the scan speed was found. When the scan speed was reduced, the height of the oxide pattern was noticeably

increased. The slower scan speed resulted in larger oxide size. The oxide heights exponentially decrease with increasing the scan speed ranging from 0.01 µm/s to 5 µm/s . Our results are consistent with the previous study of Kuramochi *et al.* [48]. However, our results were in contradiction with the study of Fontaine *et al.* [35] since they found that the oxide height of fabricated oxide stripes showed a logarithmic decrease with an increase of writing speed for each sample voltage. However, it was assumed from our investigation that when the scan speed was increased at the low scan speed, this gave a significant decrease of the oxide height then it slightly decrease at the high scan speed.

10. It was found that an increase in the lateral dimension depends almost linearly on a decrease of the tip velocity. However, after the writing speed goes below 1 µm/s, the line half-width does not increase linearly, it seems to be constant. This can be explained by a two-step growth process proposed by Kuramochi *et al.* [48] consisting of the initial high growth stage in the centre part of the meniscus right underneath the tip followed by the effect of the ionic diffusion through the adsorbed water layer. The ionic diffusion was the rate limiting factor for long exposure times. Consequently, compared to our results at the fast scan speed (short exposure time), the initial oxidation took place at the central part under the AFM tip until this growing oxide prevented the current flow at the central region. Subsequently, at the slower scan speed, the oxide was grown in the lateral dimension because of the ionic diffusion along the lateral dimension. This led to an increase in the oxide width with decreasing the scan speed. However, the oxide growth in the lateral dimension was also limited by the water meniscus size as the study of Bloe*ß et al.* [63]. The relative humidity and electric field are also crucial parameters for the formation of the meniscus [48, 63]. Consequently, from our results, the slower tip velocity generated wider oxide lines determined by the ionic diffusion until the width of the written oxide line was limited by the size of the meniscus.

11. As a result of the studies of the height and width dependencies on the scan speed, for fast scan speeds oxidation occurred in the lateral dimension due to the ionic diffusion until it reached the limitation of the water meniscus diameter caused by

the humidity effect and the applied electric field. Then, the oxidation was able to grow only in the vertical direction at the slower scan speed. Consequently, after the width was saturated, the oxide height linearly depended on the scan speed.

12. The study of the effect of the AFM tip on oxide array pattern, all size distributions of 3 arrays obtained by the smaller tip radius were well fitted with log-normal distribution. The height and half-width of dots in 2 arrays are nearly identical about 1 nm and 70 nm. However, if considering the mean values of the height and the half-width together with the standard deviation, it was found that the size of 3 arrays were in excellent agreement. For the larger tip radius, it was found a slight difference of the mean values even including the error values which they should be identical It was found that the smaller tip radius results in oxide dots with smaller heights compared to the larger tip radius. This result was in contradiction with the study of Djurkovic *et al.* [92] who showed that increasing the AFM tip radius leads to a decrease of the oxide dot height. The half-width of oxide dots of the smaller tip radius are larger than that of the larger tip radius. This also was in contradiction with the study of Djurkovic *et al.* [92] who showed that increasing the AFM tip radius leads to an increase of the oxide dot width. It was found that the AFM tip radius may play a critical role for the difference of the width measurement. The smallest height and half-width achieved by the smaller tip radius were *ca.* 0.63 nm and 40 nm, respectively. In the case of the larger tip radius, very fine oxide dots with 0.45 nm in height and 52.5 nm in half-width were obtained. Furthermore, the largest size of fabricated oxide dots obtained from the smaller tip radius were *ca.* 1.8 nm in height and 100 nm in half-width. On the other hand, the larger tip radius produced a larger oxide size with a 3.5 nm oxide height and 100 nm oxide half-width. These results was in contradiction with the simulation of Kremmer *et al.* [93] relating to the electric field on the $SiO_2$ surface increased with decreasing tip radius. Our results could be confirmed by the study of Takemura and colleagues [94].

13. The study of the effect of the AFM tip on oxide dot was found that the height of nanodots grown by the smaller tip radius was higher than the larger tip radius. This was in contradiction to the above observation in nanoarray fabrication which

showed the results in the opposite way. However, the results were in good agreement with the studies of Djurkovic *et al.* [92] and Kremmer *et al.* [93] who showed that increasing the AFM tip radius leads to a decrease of the oxide dot height.

14. It was found that the half-width of the nanodots does not strongly depend on the applied voltage in the case of the larger tip radius on both native-oxide layer and Mo surface. This is because the half-width of nanodots was fluctuating when the applied substrate bias voltages was increased. On the native $SiO_2$ surface, the dot width deposited with the smaller tip radius was considerably narrower than that with the larger tip radius. This is due to the smaller tip apex causing the smaller size of the meniscus between the tip and sample compared to that of the larger tip radius. The theoretical analysis of Lin *et al.* [95] could confirmed our investigation.

15. Considering the influence of the type of substrate on the size of oxide dots, the fabricated oxide nanodots were studied on a native-oxide $SiO_2$ and Mo surface. It was assumed that the molybdenum oxide stoichiometry was $MoO_3$ as proposed by Rolandi *et al.* [80], Pellegrino *et al.* [83] and Goto *et al.* [82]. For the same voltage and tip, the height and width of oxide dots on native $SiO_2$ surface were smaller than those on the Mo surface. The results were explained by the wettability and the sample conductivity of the substrate. In our case, the $SiO_2$ surface is hydrophilic while the Mo surface is hydrophobic and the hydrophobic tip was used. The study of Kaibara *et al.* [99] could be one possibility to explain our investigation that the adhesion force between hydrophobic tip and hydrophilic $SiO_2$ surface is weaker than that between hydrophobic tip and hydrophobic Mo surface. This is because of the strong attractive interaction of the latter in comparison to the repulsive force of the former exerted by the water absorption on the hydrophilic surface. However, it was found that the consideration of the adhesion force alone was not adequate to explain why the oxidation on Mo created a greater oxide size than that on $SiO_2$ due to various relevant interactions taking place during the formation of the water bridge, for example, the electrostatic interaction, the van der Waals interaction, the

interaction of water molecules with the surface and the interaction with the external field due to polarization of the water molecules [100]. Consequently, considering the sample conductivity effect on the oxide size as the study of Cambel and Šoltýs [96] could be explained our results that the conductivity of the native $SiO_2$ surface is lower than that of the Mo surface. This can cause the lower electric field between the tip and sample and lead to smaller size of oxide nanodots in the case of the native $SiO_2$ substrate.

16. The fabricated oxide dots on the Mo surface increased in size with increasing relative humidity. The height at high humidity was larger by a factor of 2.3 compared to that at low humidity. The half-width was around 0.27 μm when the relative humidity was 66 ± 2 % but lowering the humidity to 43 ± 2 % reduced the width by a factor of 1.48. This result confirms that the relative humidity significantly influences the size of the oxide dots. Following consideration of the previous reports of Avouris *et al.* [67], Bloe*β et al*. [63] and Kuramochi *et al.* [48] on Si wafers, they mentioned the effect of humidity mainly on the width but hardly observed an influence on the height. Our results provided contrasting behaviour on a Mo surface especially in the case of height dependence. This is because other works found only a slight change in oxide height when the humidity increased but our results showed an increase by a factor of 2.3 when the humidity increased by about 23 % (from 43 ± 2 % to 66 ± 2 %). Consequently, the reports on the metal surface were considered. The results of Farkas *et al.* [72] seem to be in good agreement with ours since the width increased approximately by a factor of 1.4 with an increase of humidity from ~43 % to 60 %. However, the increase of the height by a factor of 2.3 of our result was much larger than that by about a factor of 1.3 of the study of Farkas *et al.* [72]. Our results was found a smaller increase in the half-width (by a factor of 1.48) compared to the study of Held *et al.* [71] who found an increase of approximately a factor of 2 between ~45 % and ~65 % RH on a Ti thin film surface. However, the height dependence was not shown in Held *et al.* [71] report.

17. The TUNA technique provided the ability to measure the ultralow currents flowing through the sample to the tip during the oxidation process. It was found that the TUNA current increased with increasing more positive substrate bias.

18. The TUNA measurement of the faradaic current supplied from the substrate to the AFM probe contact point was studied to further understanding the influence of the relative humidity on the oxide dot formation. However, a comparison between low and high humidity did not find any correlation with the current intensity. It was found a significant increase of the average integrated charge from *ca.* 405 *p*C to *ca.* 457 *p*C with increasing relative humidity from 43 ± 2 % to 66 ± 2 %. The currents observed in our case (about 50 *p*C) were much larger than that in the study of Kuramochi and co-workers [54] (less than 10 *p*C) on a H-passivated *p*-type Si (001) wafer. This can be explained that the Mo surface used in our case is more conductive than the H-passivated *p*-type Si substrate used in the study of Kuramochi *et al.* [54].

19. The comparison of the volumes of the nanodots obtained with different methods including $V_{int}$, $V_{surf}$ and $V_{total}$ was studied. All volumes at higher state humidity (66 ± 2 %) clearly show greater values than that at lower state humidity (43 ± 2 %). However, it was found that less than a half of the detected charge at low humidity is actually used for the oxidation process, since both $V_{total}$ and $V_{surf}$ values are less than 50 % of $V_{int}$ value. On the other hand, in the case of high humidity, both $V_{total}$ and $V_{surf}$ values are greater than 50 % of $V_{int}$ value. Even though, $V_{total}$ at high RH is a slight greater than $V_{int}$. This phenomenon can be affected by a number of factors, for example, the incorrect estimation of the total volume and the inaccurate size measurement from the tip convolution effect leading to the overestimated volume of both $V_{surf}$ and $V_{total}$. Consequently, our observation revealed that a 23 % difference in humidity leads to a significant difference in the final volumes of the oxide dots when other parameters are controlled. In addition, the increase in humidity leaded to the higher efficiency of the charge to fabricate the larger oxide volume.

20. The effect of ramping time was investigated on the Mo surface. It was found that the dot sizes significantly increased with increasing ramping time. The current intensity becoming smaller with increasing ramping time from 0.23 s to 100 s. The correlation between the ramping time and the current waveform was in good agreement in the start region for all of the ramping time; however, the decaying behaviour seemed to be the influence of increase of the oxide thickness. A linear dependence was found for the charge with increasing the ramping time. It was found that the height and the width considerably increase with increasing total charge and then stay constant for charges above 3000 *p*C. This was possibly because the charges above 3000 *p*C were the over currents considering not to contribute to the oxidation reaction which was in consistency with the studies of Takemura *et al.* [94] and Shimada *et al.* [102]. It was found that with applying a small number of charges below ~160 *p*C and at a low ramping time below 0.33 s, the values of both $V_{surf}$ and $V_{total}$ are greater than that of $V_{int}$. This can be due to the saturated current at low ramping time where the exact current used for oxidation process could not be detected. After a charge above ~180 *p*C and a ramping time approximately above 0.40 s, it was found that only $V_{total}$ was higher than $V_{int}$. However, when the charge and the ramping time were increased to above ~1000 *p*C and ~10 s, $V_{int}$ seemed to be considerably increased, whereas $V_{total}$ and $V_{surf}$ stay constant. It is reasonable that with a high ramping time the excess charge from the tip seems to be no longer used for the oxidation process as the study of Shimada *et al.* [102]. The results showed that the oxidation efficiency decreased with increasing the ramping time. The oxidation process on the Mo surface depends on the ramping time but only for short ramping times.

# Chapter 5 Metallic Nanoparticle Deposition

## 5.1 Introduction

This chapter will mainly discuss the deposition of metallic nanoparticles such as gold with two different methods: dip-pen nanolithography (DPN) and fountain-pen nanolithography (FPN).

### 5.1.1 Overview of dip-pen nanolithography

Since the initial development of the DPN technique in 1999 by Mirkin's group [103], DPN has been the focus of a great deal of research owing to its simplicity and usefulness for nanoscale patterning. In recent years, DPN has been successfully applied to pattern a variety of ink and substrate combinations. A range of inks, such as organic molecules [103-106], inorganic molecules, biological molecules (e.g., DNA [107] or proteins [108]), polymers [109-111], colloidal particles [112, 113], sols [114, 115] and metal ions [114-116] have been used to pattern various hard and soft surfaces, including metals, insulators or functional monolayers adsorbed on a variety of surfaces.

### 5.1.2 Principle of dip-pen nanolithography

DPN has demonstrated the ability to fabricate a one molecule thick layer with sub-100 nm resolution through the controllable movement of an ink-coated AFM tip on a desired substrate. As shown in Figure 5.1, DPN is a 'direct-write' method that uses an AFM tip as a pen. The tip is coated with ink molecules, namely any materials which can be deposited on a substrate with a water meniscus acting as a transfer medium [117]. The transport of ink molecules from the AFM tip to the substrate is related to a capillary force [118].

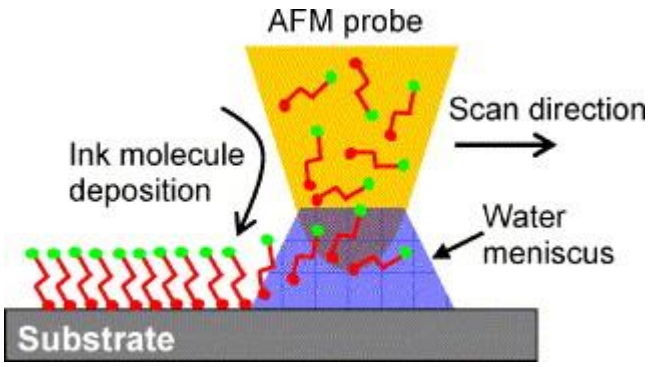


**Figure 5.1** A schematic diagram of dip-pen nanolithography showing the AFM tip coated with ink molecules which are transported from the AFM tip to the substrate via the water meniscus [117].

The general mechanism for the transfer of ink molecules to the surface can be divided into three main steps as discussed by Basnar and Willner [119]. The first step relates to a meniscus behaving as a bridge for ink transport. An increase in humidity and decrease in the tip-sample separation can cause an increase of the meniscus size as studied theoretically by Jang *et al*. [120]. In 2005, Weeks *et al.* [121] studied the dependence of the meniscus formation on various relative humidity values using environmental scanning electron microscopy (ESEM) as shown in Figure 5.2. The ESEM images in Figure 5.2 were taken at a constant temperature (5 ºC) with different relative humidity values controlled by varying the water vapour pressure. Three sample images were given at 40 % RH, 2 Torr (Figure 5.2 a)); 60 % RH, 3.2 Torr (Figure 5.2 b)); 99 % RH, 6.4 Torr (Figure 5.2 c)). These images clearly showed that an increase in relative humidity caused a significantly increased meniscus size in both height and width. In addition, Weeks and co-workers [121] also showed that the relative humidity influenced the meniscus height as determined by measuring the distance from the substrate surface to the cone contact line[9] as shown in Figure 5.3. A SiN cantilever tip was used. The SiN tip was in contact with a Si substrate for growth (0 % - 99 % RH) followed by retreat (99 % - 0 % RH) of the meniscus. It can be seen from Figure 5.3 that the growth of the meniscus has an exponential dependence on the relative humidity whereas the decrease of the meniscus

[9] The contact line is where the change in angle between the meniscus and the cantilever tip is observed as shown in Figure 5.2 c).

demonstrated a linear dependence on the humidity. Weeks *et al.* [121] noted that a decrease of the meniscus was clearly observable until 40 % RH for the retreat measurement, however, for the growth measurement, a stable meniscus could not be observed until 70 % RH. The authors explained that although they could not observe the meniscus formation below 70 % RH, they could not definitely determine whether the meniscus existed or not. This is because of the limitation of the ESEM resolution under their imaging conditions which is approximately 50 nm, thus a very small meniscus would not be observable. Subsequently, in 2006, Weeks and De Yoreo [122] further studied the dependence of the meniscus growth as a function of time. The authors showed the ESEM images of meniscus formation between a tip and a gold-coated Si substrate at different times during the growth with 98 % RH (see Figure 5.4). These images show that an increase of the meniscus size strongly depended on the time. The authors observed that the meniscus was very stable after reaching equilibrium. Additionally, Weeks and De Yoreo [122] suggested that the temperature, relative humidity, meniscus's curvature, and surface roughness influenced the condensation times.

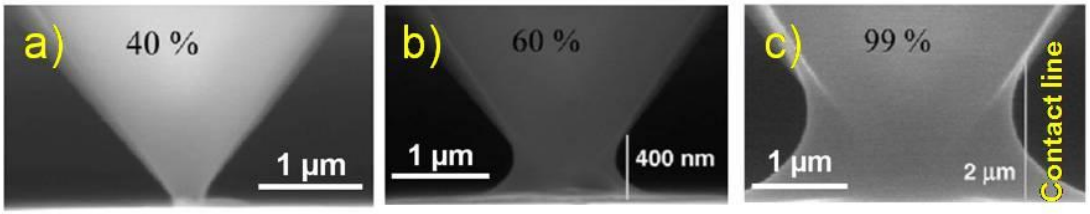


**Figure 5.2** A series of ESEM images of the growth of a meniscus between the tip-substrate separations at various relative humidity values as controlled by varying the water vapour pressures : a) 40 % RH, 2 Torr; b) 60 % RH, 3.2 Torr; c) 99 % RH, 6.4 Torr. All images were collected at 5 ºC, 15.0 kV accelerating voltage, at 35000x [121].

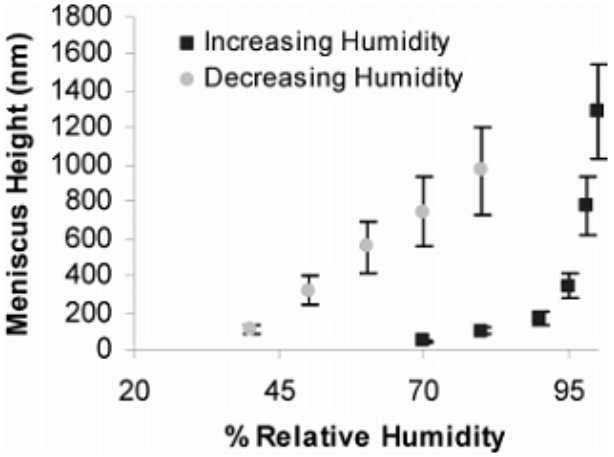


**Figure 5.3** Dependence of the meniscus height on the relative humidity of the forward (0 % - 99 % RH) and retreat (99 % - 0 % RH) for a SiN AFM tip in contact with a Si substrate. The meniscus height was determined by measuring the perpendicular distance from the substrate surface to the condensate/cone contact line as illustrated in Figure 5.2 [121].

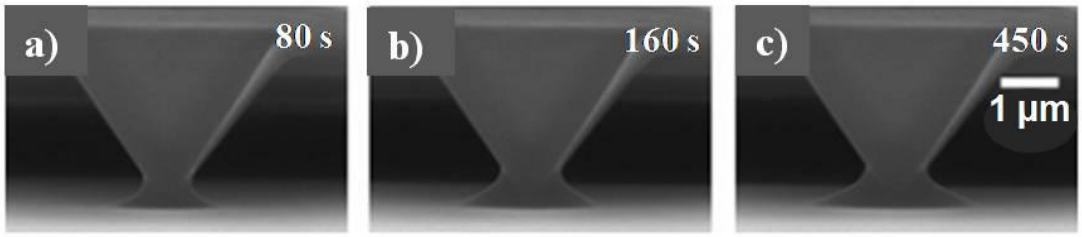


**Figure 5.4** A series of ESEM images of the growth of a meniscus between the tip-substrate separation at 98 % RH: a) at t= ~80 s, b) at t= ~160 s and c) at t= ~ 450 s. A Au-coated Si substrate was used [122].

The second step involves the deposition rate determining step, which is the ink removal from the tip and transfer to the substrate. The deposition rate can be increased by increasing the temperature [123] or humidity [124] or using an ink with a higher hydrophilicity [125]. Chung *et al*. [123] studied the dependence of ink transport on tip temperature during thermal DPN (tDPN). Figure 5.5 shows a lateral force microscopy (LFM) image of 16-mercaptohexadecanoic acid (MHA) dot arrays fabricated on a Au substrate using a tip-substrate contact time of 3 s for each dot. The relative humidity was maintained at 46 %. When the tip temperature was increased

from 25 ºC to 45 ºC, the diameter of the MHA dots increased from 250 nm to 2750 nm. The average line width of MHA arrays increased from 74 nm to 580 nm as the tip temperature was increased from 24 ºC to 34 ºC. Note that the line pattern data were not given by Chung *et al.* [123]. Chung and colleagues [123] explained that the dissolution of MHA into the meniscus plays an important role in determining feature sizes and is directly dependent on the temperature. One more important effect of ink diffusion is the hydrophilicity of surfaces. Hampton *et al.* [125] proposed a mechanism for the transport of double-ink molecules including 1-octadecanethiol (ODT) and MHA as illustrated in Figure 5.6. The solubility of MHA in water is over 100 times larger than that of ODT since MHA consists of the carboxylic acid terminal group [126]. ODT is naturally more hydrophobic than MHA. Figure 5.6 a) shows the ODT patterned on top of MHA and Figure 5.6 b) shows the MHA patterned on top of ODT. Hampton *et al*. [125] elucidated from their experiment with double-ink deposition that the deposition rate of ODT (hydrophobic molecule) on a MHA (hydrophilic molecule) pattern (Figure 5.6 a)) was higher than that of MHA on an ODT pattern (Figure 5.6 b)). This is because a broader spreading of the water meniscus can facilitate the transport of ODT on the MHA surface as can be seen from Figure 5.6 a).

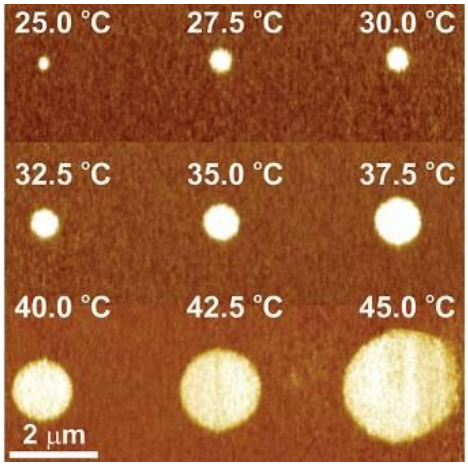


**Figure 5.5** LFM images of MHA dot patterns generated by thermal DPN (tDPN) on a gold substrate. The tip-substrate contact time was 3 s for all depositions and the relative humidity was controlled at 46% with different tip temperatures ranging from 25.0 ºC to 45.0 ºC as showing above each dot [123].

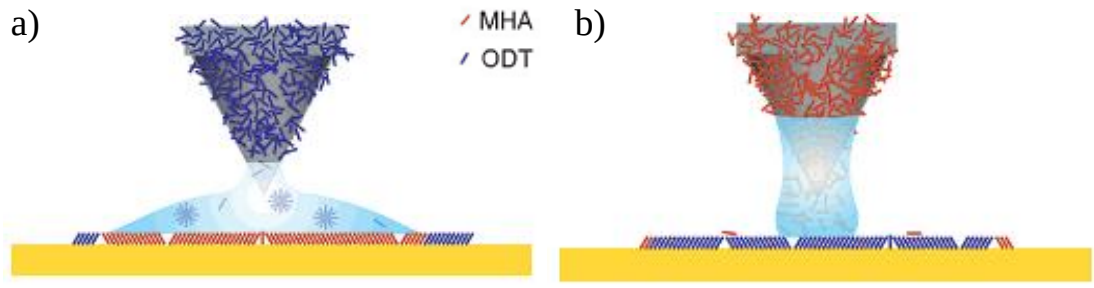


**Figure 5.6** Two schematic diagrams of meniscus formation on a hydrophilic MHA and a hydrophobic ODT layer: a) ODT formed on top of MHA. b) MHA formed on top of ODT [125].

The last step depends on the diffusion of the ink on the substrate. The number and strength of the binding sites on the surface play a crucial role in this step. Jang *et al*. [127] proposed a transport mechanism for the molecular inks from the tip to the substrate by a random walk simulation model as a three-step process including molecular deposition, lateral diffusion on a previous molecular monolayer, and termination of diffusion by chemical substrate binding (See Figure 5.7). Jang *et al.* [127] considered the simplest case of the diffusion of ink molecules on a two-dimensional lattice with strong trapping sites. The ink molecules are trapped and immobile if they reach the chemisorbing sites on the surface. The molecules which are deposited faster will be adsorbed sooner compared to the slower deposited molecules. The slower molecules, thus, need to find previously unoccupied trapping sites. The authors noted that the highest density region should be around the tip due to the finite mobility of the ink molecules. Jang and co-workers [127] pointed out that the relative time scale of diffusion with respect to that of deposition is considered to be a key parameter. If diffusion is much faster than deposition, adsorption might proceed in a one-molecule-at-a-time fashion. But if the opposite case is true, the simultaneous diffusion of many molecules might be involved the transport.

Jang and co-workers [127] showed that, in the case of a fixed tip, circular patterns were generated and depended on the deposition rate as shown in Figure 5.8. The eight snapshots of circles are shown in Figure 5.8 a) and b) for slow and fast deposition cases, respectively. The total time taken for all the molecules to be trapped by lattice sites has been divided into eight equally speed time intervals. For the case of slow deposition in Figure 5.8 a), the circular growth is produced step by step with new molecules added at the outer rim of the circle. In contrast, for the fast deposition case in Figure 5.8 b), the periphery is defined to one quarter of the total time. This causes a negligible growth at later times.

In the case of a moving tip, the pattern resolution was strongly dependent on the tip speed and deposition rate. The binding sites' strength on the surface can influence the diffusion which was experimentally studied by Manandhar *et al.* [128] and theoretically considered by Lee and Hong [129]. Manandhar *et al*. [128] demonstrated that a weak binding of the organic molecules on the surface was generally possible in DPN, causing either circular or fractal-like formations. Lee and Hong [129] investigated weak binding surface molecules and found that strong intermolecular interactions and non-uniform substrate-molecule interactions can create differently shaped patterns as well as fractal-like structures.

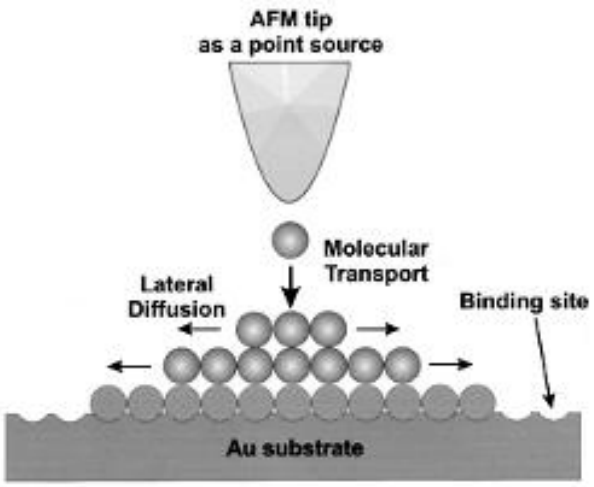


**Figure 5.7** A schematic model of a transport mechanism of ink molecules during the pattern formation [127].

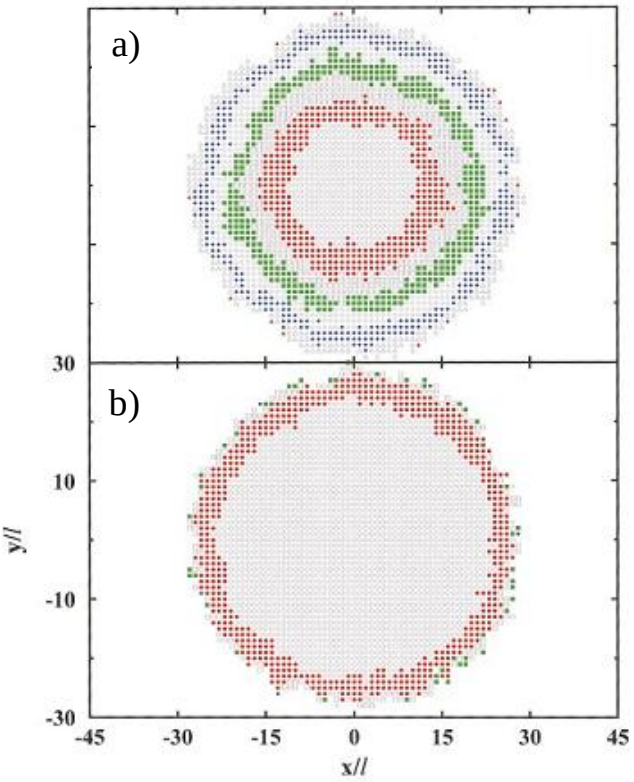


**Figure 5.8** Simulated formation of circular patterns generated by a tip in a fixed position. The different colours of the rings mark molecules deposited at different times and the deposited molecules started at the centre and end at the rim of the circle. a) Slow and b) fast deposition cases are plotted for deposition of 2500 ink molecules [127].

### 5.1.3 Dip-pen nanolithography of metal

The deposition of solutions containing metal nanoparticles as inks for the patterning process [112, 130-134] or metal ion ink-solutions for the *in-situ* fabrication of particles during the writing step [114-116, 135] on various surfaces using DPN technique has attracted intensive research efforts.

The number of attempts to deposit noble nanoparticles especially gold (Au) on various surfaces have increased dramatically over the past decade due to its interesting properties. Using hydrogen tetrachloroaurate ($HAuCl_4$) as the ink for AFM DPN, Maynor *et al*. [114] were able to fabricate Au nanostructures on Si

surfaces pre-treated with hydrofluoric acid to remove the oxide layer. The authors supposed that the reaction involved the Si surface-induced reductive mechanism without the application of voltages. Figure 5.9 a) presents the schematic model of a DPN process where Au (III) ink was dissolved in the water meniscus and subsequently reacted with the Si surface before being reduced from Au (III) to Au (0). Maynor and colleagues revealed through various investigations that the deposited nanostructures were composed of metallic Au (0). Firstly, the nanostructures were not dissolved in either aqueous or non-aqueous solvents. This indicated that they were not composed of soluble Au complexes. Secondly, there was no change when the structures were heated to 300 ºC in air, indicating that they did not consist of organic material. In addition, when heating up to 500 ºC in inert gas, they showed an aggregation changing from lines to a series of dots since they underwent a phase transition. Lastly, in comparison with $SiO_2$ structures fabricated by the AFM-based LON process (see Chapter 4), the Au structures were not etched away by hydrofluoric acid (HF), whereas the $SiO_2$ structures were completely removed. Additionally, Maynor *et al.* also compared the deposited structures on thermal oxide Si and H-terminated Si wafers using X-ray photoelectron spectroscopy (XPS) as illustrated in Figure 5.10. Both wafers were immersed into a $2 \times 10^{-4}$ M aqueous solution of $HAuCl_4$ for 9 h followed by washing with ethanol to remove the Au (III) complex. The XPS spectra revealed that only the H-passivated Si wafer was suitable for Au (0) deposition while no Au deposition occurred on the thermal oxide Si wafer. Figure 5.9 b) illustrates the sub-100-nm resolution of Au nanostructures, "DU" pattern, produced by employing DPN. Approximately 1-3 layers of Au atoms were deposited with a height of 4-10 Å. The authors discussed that the tip geometry, scan speed, and relative humidity can influence the deposition, size, and dimension of the nanostructures.

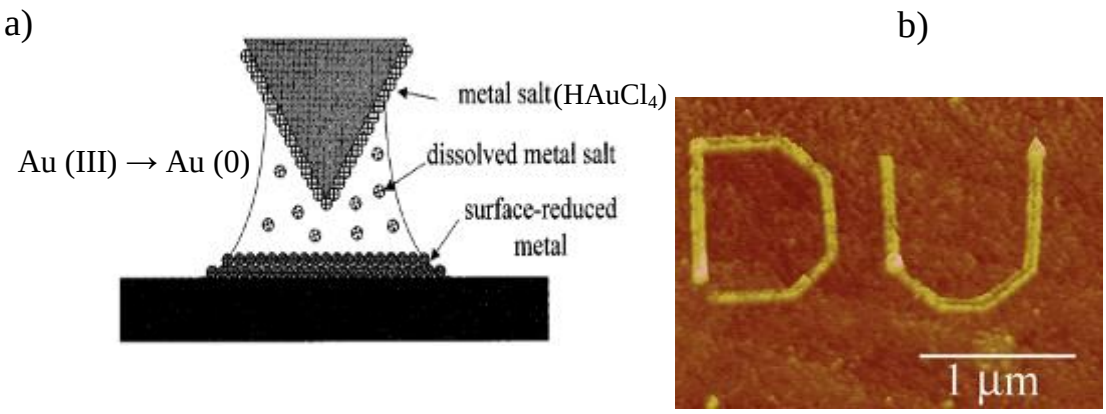


**Figure 5.9** a) A schematic diagram of a DPN method using Au ionic ink and b) A Au pattern generated by DPN with speed of 10 nm/s and 40 %RH [114].

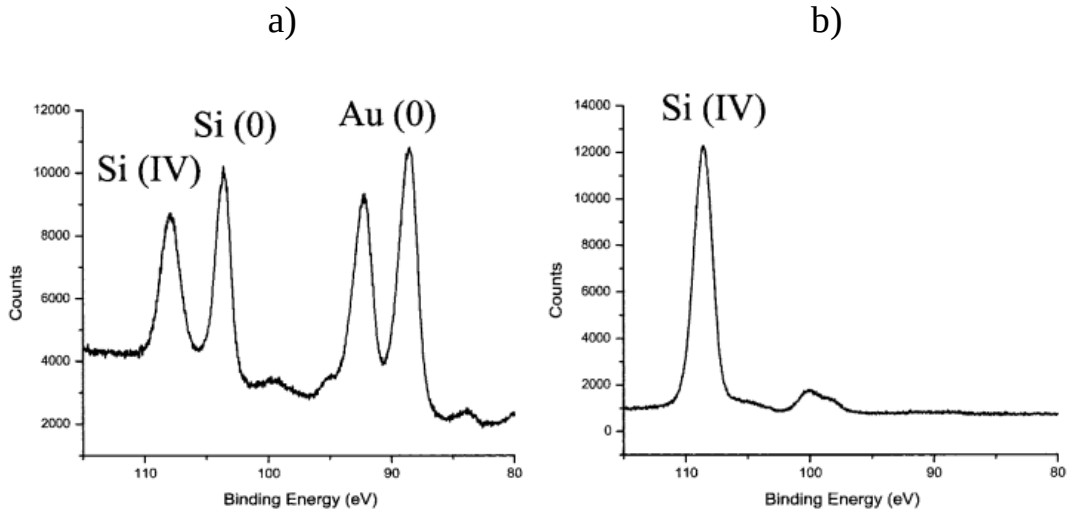


**Figure 5.10** X-ray photoelectron spectra of a) H-terminated Si and b) thermal oxide Si surfaces immersed in an aqueous 2 x $10^{-4}$ M $HAuCl_4$ for 9 h followed by washing in ethanol. The XPS spectrum of the Si wafer clearly shows Au (0) deposition, while the XPS spectrum of $SiO_2$ wafer shows no evidence of Au deposition [114].

The study of Porter and co-workers [116] used three methods including photolithography, microcontact printing and DPN for the nanoparticle film deposition of noble metals (e.g., Au, Pd and Pt) on germanium surfaces. Considering only the DPN method, Porter *et al*. used a Si tip dipped into an aqueous 20 mM $AuCl_4^-$ ink solution, diluted with acetonitrile (1:10 v/v) in order to reduce surface

tension and dried for 5 min. The writing speed was successful at a rate of 0.2 μm/s with a relative humidity of 50 %. Figure 5.11 a) shows a schematic diagram of the DPN of Au salt on a Ge (100) substrate. Figure 5.11 b) demonstrates an AFM image of a Au line with a length of 550 nm, width of 30 nm and height of 10 nm drawn in air via the DPN process on a native-oxide-coated Ge (100) surface. These authors also reported that they could achieve similar results with $PdCl_4^-$ ink solution patterning.

a)

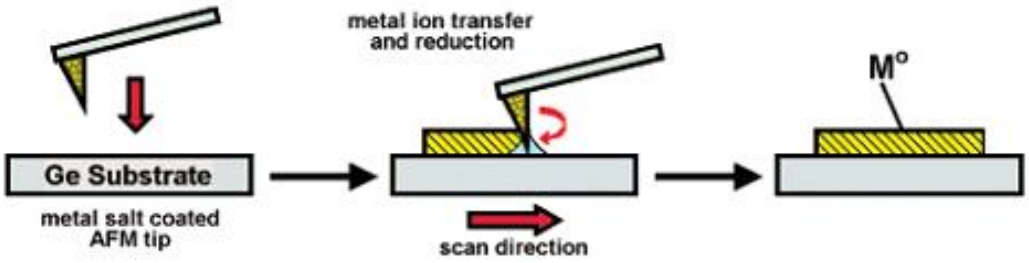


b)

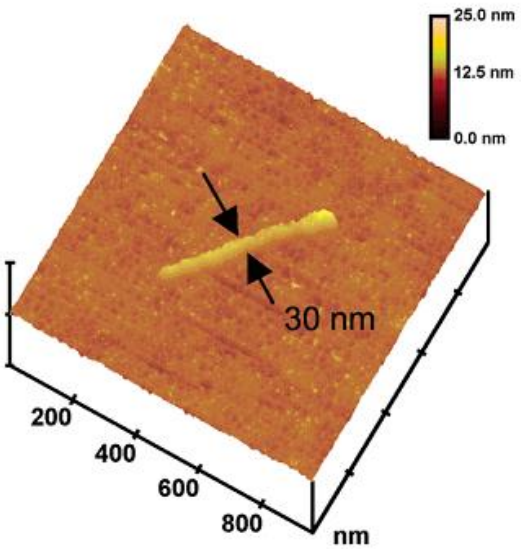


**Figure 5.11** a) A schematic diagram of DPN on germanium (Ge) substrate. b) AFM image of a Au line (550 nm long, 30 nm wide and 10 nm high) fabricated on a native-oxide-coated Ge (100) surface [116].

Subsequently, the study of Sung *et al.* [29] showed direct deposition of Au nanodot arrays with sub-50-nm scale features fabricated using the DPN technique on various insulating substrates, for example, $SiO_2$, $Al_2O_3$ and polyimide. In their process, $HAuCl_4$ ink was deposited onto insulating substrates while maintaining a tip temperature of 35-39 ºC, a chamber temperature of 20-25 ºC and chamber humidity of 20-35 %. Subsequently, the generated molecular ink patterns were annealed to decompose the $HAuCl_4$ molecule to leave only the Au metal on the substrates. Figure 5.12 a) shows an AFM image of Au nanodots deposited on a $SiO_2$ surface after annealing at 270 ºC for 10 s in vacuum. The diameters (FWHM) of the Au dots from Figure 5.12 a) show a Gaussian distribution with a mean diameter of 47.9 ± 3.1 nm as illustrated in Figure 5.12 b). This result clearly showed that they could achieve uniform sub-50-nm Au dot patterns using the DPN method.

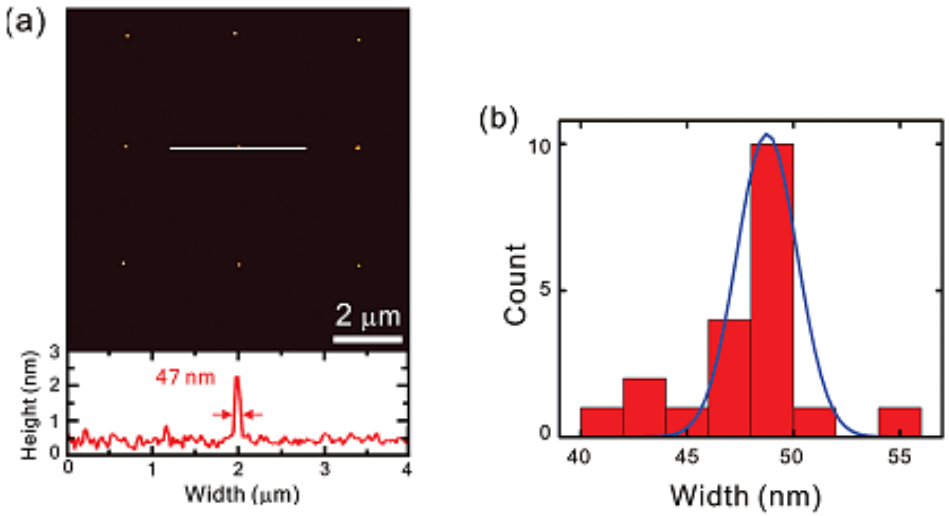


**Figure 5.12 a)** AFM image of a uniform Au dot array fabricated on a $SiO_2$ surface after an annealing process. The corresponding height profile of a Au dot structure is shown below the image. b) A Gaussian distribution of the diameter of Au dot patterns with a mean diameter (FWHM) of 47.9 ± 3.1 nm [29].

Li *et al*. [136] showed that Electrochemical DPN (E-DPN) could be used to deposit both metal and semiconductor nanoparticles on surfaces. The difference between DPN and E-DPN is the function of the water meniscus. For the latter technique, the water meniscus is used as a medium (for an electrochemical cell) to dissolve metal salts and reduce these salts to metals, which can be deposited on a solid-substrate. In the study by Li and co-workers, Pt metal was deposited on a hydrofluoric acid washed Si surface using the E-DPN technique as shown in Figure 5.13 a). Pt (IV) was electrochemically reduced to Pt (0) using the tiny water meniscus as a transfer medium and also by applying a positive DC bias to the tip. Then the Pt metal was deposited on a *p*-type Si surface. The Pt line achieved was around 0.4 nm in height and 30 nm in width. The important factors for this study were humidity, scan rate, and applied voltage for the control of height and width of Pt metal by employing such a technique. Figure 5.13 b) displays the Pt line on the left created by E-DPN and $SiO_2$ on the right produced by AFM-based LON. After exposure to an ethylene atmosphere in argon at 500 $^{\circ}$C for an hour, the Pt line changed as carbon depositions occurred, whereas the $SiO_2$ line was unaltered (See Figure 5.13 c)).

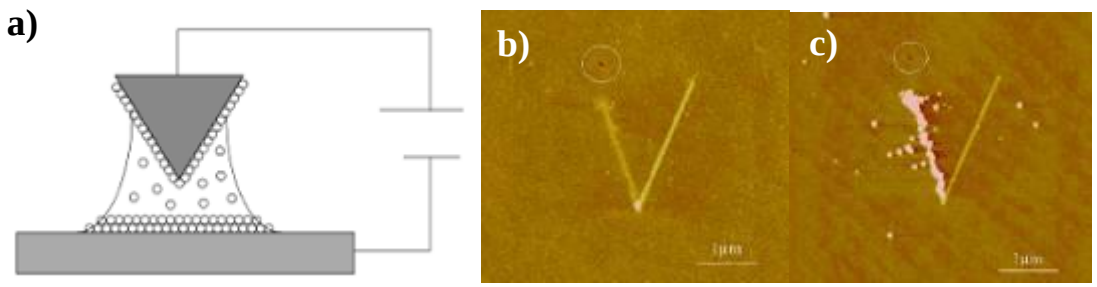


**Figure 5.13** a) A schematic diagram of the E-DPN technique. b) Pt pattern on the left branch of the "V" character generated by applying +4 V to the tip with a 10 nm/s scan speed and silicon oxide ($SiO_2$) on the right side of the "V" character created by a -10 V applied tip voltage at the scan speed of 50 nm/s. c) The same pattern with b) after 500 $^{\circ}$C heating in an ethylene and argon atmosphere for one hour [136].

A study by Bing *et al*. [134] suggested that there were two key factors for successful patterning of metal nanoparticles (NPs) using the DPN method. First of all, they noted how to keep the inks in a liquid form on the AFM tip as long as possible to aid transfer from the tip to a substrate. Another key factor was the development of a novel method called 'scanning-coating' (SC) instead of the conventional dip-coating technique. As shown in Figure 5.14, a general scheme for scanning-coating is first dropping a Co NP solution on a $Si/SiO_x$ substrate. Then the solvent is allowed to evaporate to generate the small condensed droplet of Co NPs as shown in Figure 5.14 a). After that the AFM tip was dipped into the Co NP droplets and scanned for a couple of minutes before the tip was withdrawn in Figure 5.14 b). These factors were very useful for effectively coating the tip with ink.

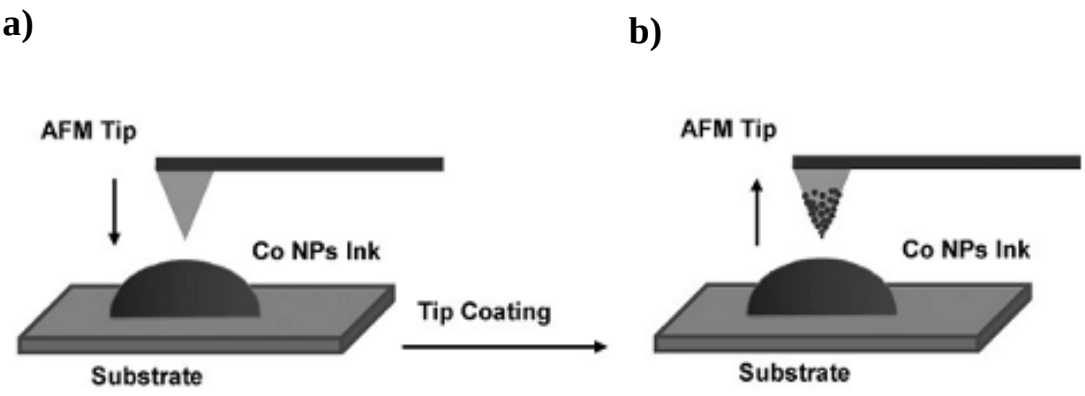


**Figure 5.14** Schematic diagrams of the scanning-coating process: a) dropping of Co NP on $Si/SiO_x$ substrate and moving the tip down before b) coating of the AFM tip by scanning for 1-2 min and retracting the tip [134].

In Figure 5.15, the dot and line features were obtained by DPN on a $Si/SiO_x$ surface [134]. The smallest dot diameter was 68 nm (see Figure 5.15 b)), while the average diameter of dots was 381 nm. The average height of dots was 11 nm. Figure 5.15 c) displays a zigzag line of Co NPs with 880 nm width. Bing and co-workers [134] described how the patterning of Co NPs with controlled sizes, shapes, and spacing can be successfully obtained using the scanning-coating approach for coating and DPN for deposition.

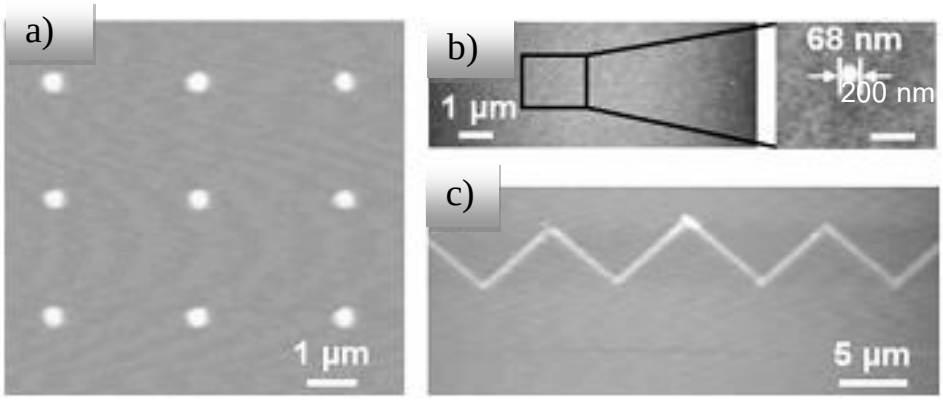


**Figure 5.15** AFM images of dot and line patterns of Co NPs fabricated by employing DPN on a Si/$SiO_x$ substrate. a) Dot patterns of Co NPs produced by bringing the Co-NP-coated tip into contact with the surface for 0.8 s. b) The smallest diameter of a Co NP dot was 68 nm. c) A zigzag line of Co NPs [134].

### 5.1.4 Overview of fountain-pen nanolithography

Even though, there are a number of advantages of using DPN for nano-scale patterning, as already discussed in earlier sections, the DPN technique is still limited by having to repeatedly dip the AFM tip into the ink when patterning of complicated structures or large areas is required [137]. This leads to a limited throughput and unavoidable realignment which cause time-consuming steps during such patterning processes [137]. In order to resolve this difficulty, a new approach known as fountain-pen nanolithography (FPN) was created for continuous feeding of molecular inks by using a micropipette [137-139].

The first report of FPN was by Lewis *et al.* [138] in 1999 shortly after the first report of DPN [103]. Lewis and colleagues [138] demonstrated the delivery of a chrome etchant through a quartz cantilevered micropipette for etching of a chrome film surface using contact mode AFM. They used a combination of a force-sensing cantilevered micropipette with an AFM/near-field optical microscope system known as the Nanonics (AFM)/NSOM-100 (Nanonics, Ltd., Jerusalem, Israel) and this system was integrated with a conventional optical microscope as shown in Figure

5.16. Considering their experiments, the authors noted that when the micropipette was brought into contact with the surface the etchant flowed by capillary forces along with formed drops at the end of the pipette and was strongly influenced by the surface tension more than by the viscosity. Lewis *et al.* [138] found that the etchant formed globules after leaving the micropipette and then solidified on the surface causing hindrance during the writing process. The solution to this problem was suggested by keeping the pipette and surface surrounded at absolute humidity (fully saturated water vapour). In addition, the authors also suggested increasing the writing time while changing relevant parameters such as the chemical concentration in the pipette, the surrounding temperature and the pressure of the tip on the surface. In their final results, etched lines could be achieved with a line width of *ca.* 0.1 μm and a depth of 120 nm. However, the authors [138] believed that they could achieve better resolution and suggested improvements, for example, using an intermittent contact-mode AFM (tapping-mode AFM) instead of a contact-mode AFM, altering the chemical properties (e.g., the hydrophobicity or hydrophilicity) of the surface and the tip, optimising the geometry of the pipette tip and considering how the nature of the liquid influenced the flow (e.g., capillary osmosis, lubrication and wetting properties).

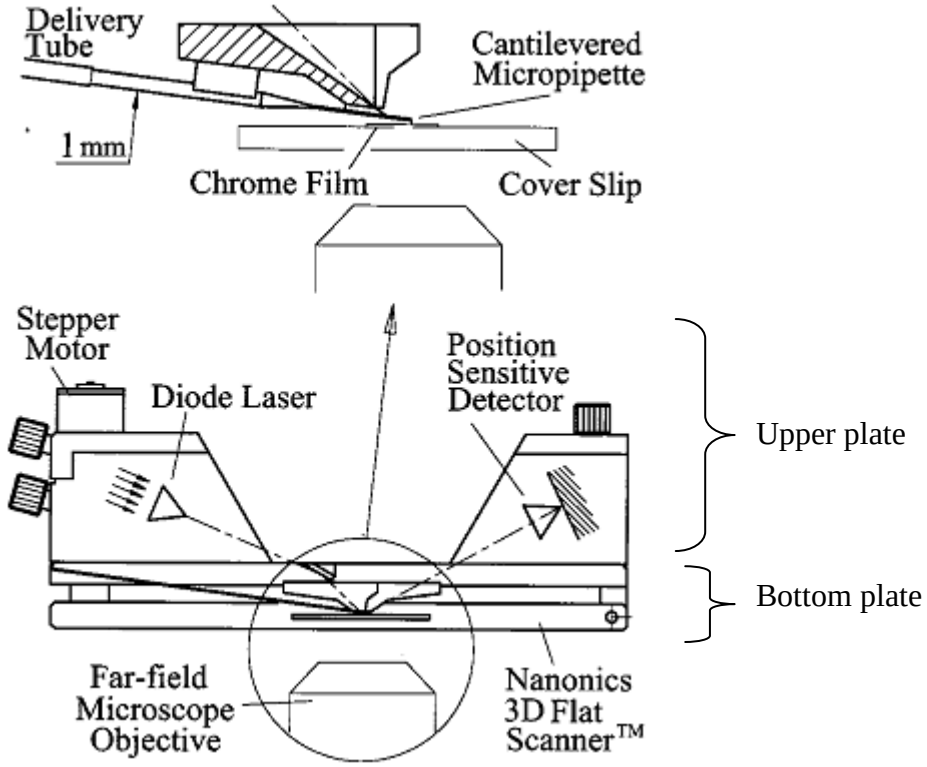


**Figure 5.16** A schematic model representation (bottom of the figure) of the Nanonics SPM system mounted on a microscope stage of a conventional inverted optical microscope. The upper plate consists of the diode laser and a position-sensitive detector for conventional force sensing when the tip is mounted. The bottom plate that is hinged on the right to the upper plate is a flat scanning stage with an opening in the middle on which a sample is placed. The top half of this figure shows the region for mounting the cantilevered micropipette and the related liquid delivery system [138].

Subsequently, Taha *et al.* [139] used the FPN technique with a Nanonics system similar to the work of Lewis *et al.* [138] for the direct printing of proteins on various surfaces. Taha and colleagues [139] showed that ~ 100-nm aperture of the cantilevered nanopipettes could achieve the printing of protein features as small as ~200 nm without the need of external electric field and environmental control. Moreover, they also emphasised that this technique did not require any specific treatments on the substrate for the protein printing.

Another work of Taha and colleagues [140] demonstrated the nanowriting of gold nanocolloids on semiconducting and non-conducting surfaces using FPN [138, 139] under ambient conditions. Taha *et al.* [140] showed that they were freely able to create Au nanowires written by FPN on a semiconductor surface in comparison with the Au lines fabricated by the electron beam lithography (EBL) technique as shown in Figure 5.17. The authors prepared a suspension of 0.1 nmol/mL gold colloids by using 1.2 nm gold nanoparticles which were attached to an amino group suspended in methanol. Au lines fabricated by FPN with a 100 nm aperture nanopipette and a writing speed of 0.1 µm/s could be achieved with a width of 100 nm and a height of ~ 15 nm (see Figure 5.17 c)). In addition, Figure 5.17 d) clearly showed evidence of the electron induced X-ray fluorescence spectrum of the FPN fabricated nanowire that was composed of gold particles.

Taha *et al.* [140] noted that the dimensions of gold nanowires written by FPN could depend on a number of factors such as the aperture size of the nanopipette, writing speed and applied pressure on the nanopipette probe. Taha and colleagues [140] also presented an example of the effect of different apertures of nanopipettes on the nanowires in Figure 5.18. The gold nanowires were fabricated on a glass substrate functionalised with an aldehyde group using 200 nm and 100 nm pipettes as shown in Figure 5.18 a) and b), respectively. The contact mode AFM with 10 % set-point of the maximum set-point of the system and a writing speed of 5 µm/s was used. The average line width and height of gold nanowires written by 200 nm pipette were 550 nm and 60 nm, whereas the size of nanowires obtained by 100 nm pipette were 350 nm wide and 30 nm high. The authors noted that the line width, height and continuity could be improved by optimising the writing parameters. More importantly, Taha *et al.* [140] also pointed out that the advantage of using FPN was the ability to freely fabricate nanowires under ambient conditions.

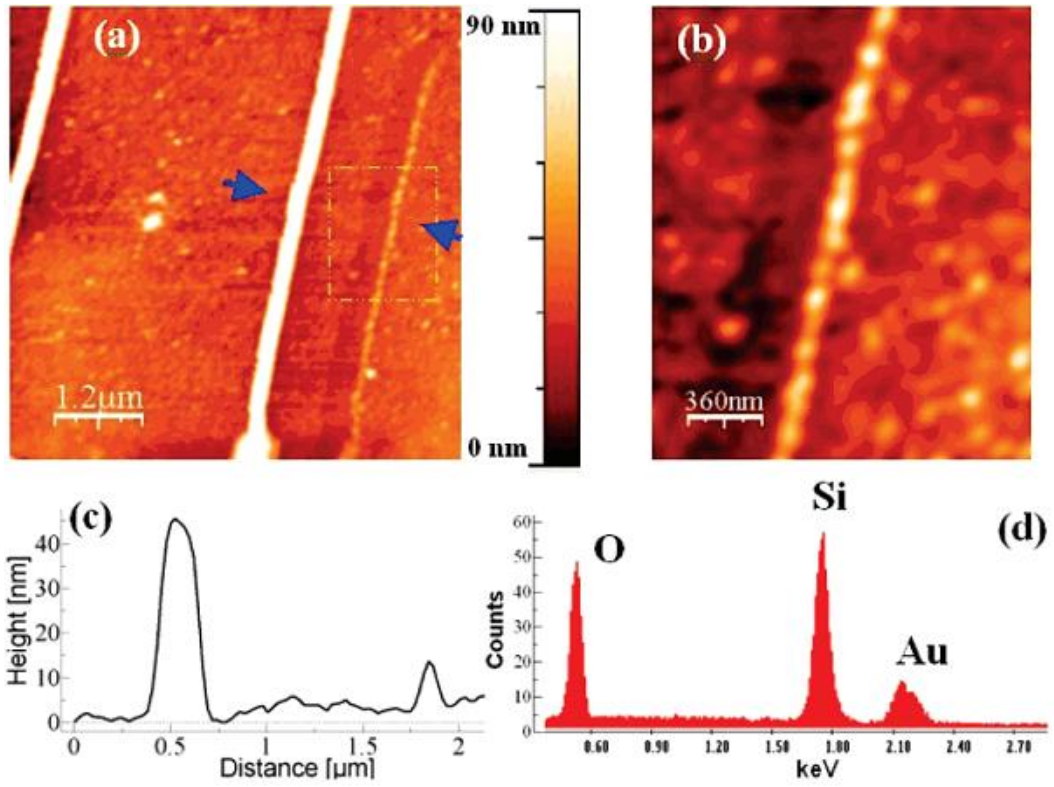


**Figure 5.17** a) AFM image of gold nanoparticle lines fabricated by electron beam lithography (EBL) (two bigger lines on the left side of the image) and a gold colloid line printed by FPN is on the right side of the image (a smaller line). These gold lines were deposited on a semiconductor surface. b) Expanded image of the marked area as shown on a) to highlight the gold deposited line from the FPN technique. c) The height profile of lines between the marked arrows on a) shows the gold line fabricated by EBL on the left with a 250 nm width and 45 nm height. The far right profile shows the FPN deposited line with a 100 nm width and 15 nm height. d) Electron induced X-ray fluorescence spectrum of the FPN deposited line show the Au composition on the right peak [140].

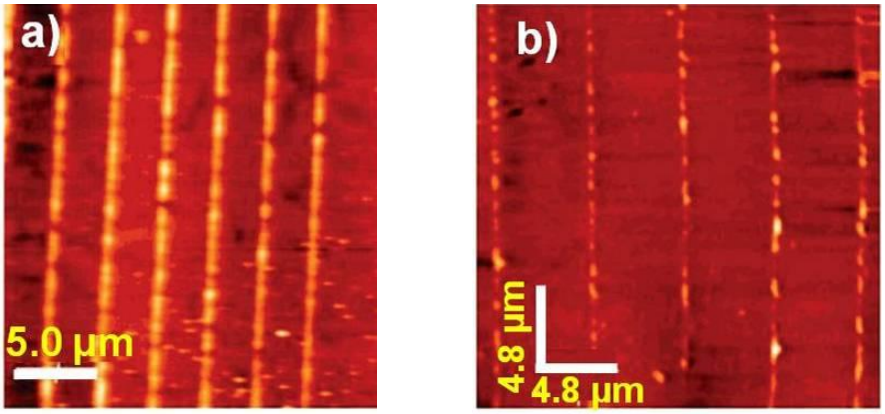


**Figure 5.18** Gold nanowires created using FPN on a modified glass substrate with an aldehyde group and different nanopipette apertures; a) Gold nanowires fabricated by using a 200 nm aperture of a nanopipette and b) gold nanowires fabricated from a 100 nm aperture of a nanopipette [140].

Omrane and Papadopoulos [141] also employed a Nanonics AFM (Nanonics MV-1000, Jerusalem, Israel) to perform nanowriting with directly patterned catalyst solutions (i.e., $Al_2O_3$-FeMo suspension and cationised ferritin) which are commonly used for carbon nanotube (CNT) growth on predefined surfaces. Figure 5.19 a) demonstrates a schematic diagram of the nanowriting process with a nanopipette using a contact mode AFM. Figure 5.19 b) shows an SEM image of a borosilicate glass nanopipette with *ca.* 100 nm aperture. Furthermore, the effect of the tip velocity on catalyst morphology was studied. Figure 5.20 a) and 5.21 a) display AFM images of line patterns drawn with $Al_2O_3$-FeMo suspension on a native-oxide-layer-coated Si substrate and line patterns drawn with cationised ferritin on a 1-µm-thermal-oxide-layer-coated Si substrate, respectively, at various tip velocities as indicated above each pattern. The authors [139] noted that it was clearly seen from the images that the amount of catalyst deposited increased when the tip velocity decreased. The cross-sectional profiles of the written lines of $Al_2O_3$-FeMo as shown in Figure 5.20 b) and c) indicate that the line height increases from 1.5 nm to 3.5 nm as the tip velocity decreases from 50 µm/s to 5 µm/s. In the case of ferritin catalyst as illustrated in Figure 5.21 b) and c), similar results were obtained with an increase of the line height from 9 nm (about one monolayer) to 20 nm when the tip velocity was decreased from 50 µm/s to 5 µm/s. The authors [141] also found that under similar

conditions the width of $Al_2O_3$-FeMo lines was normally larger than that of ferritin lines. The authors [141] believed that this behaviour was related to the larger contact angle of the aqueous ferritin solution on $SiO_2$ surface. This led to the amount of liquid spreading on the surface being reduced and causing the fabrication of narrower lines.

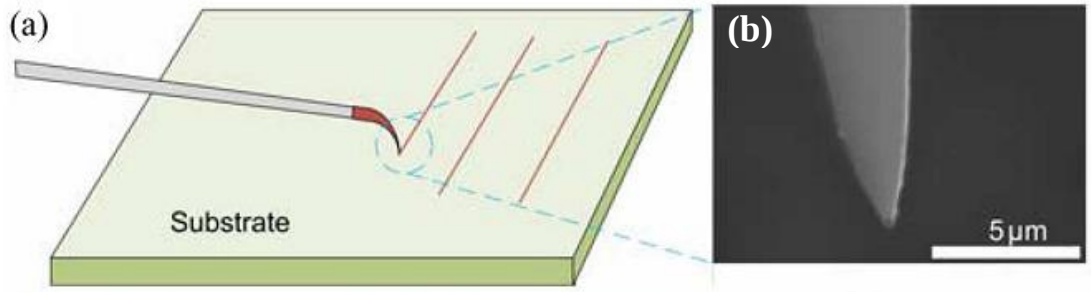


**Figure 5.19** a) A schematic representation of FPN process using nanopipette tip filled with catalyst solution. The pipette is brought into contact with a surface and scanned using contact-mode AFM to write desired patterns. b) Expanded SEM image shows a borosilicate glass nanopipette with ~100 nm aperture [141].

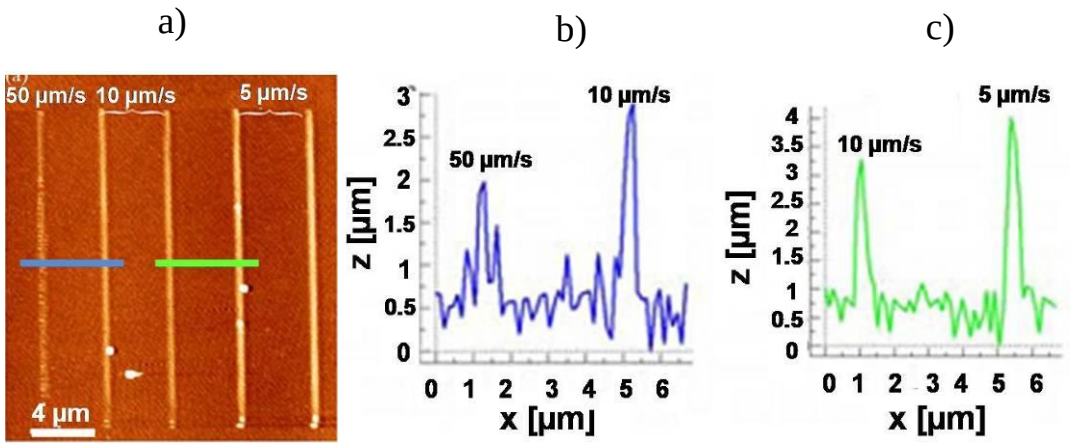


**Figure 5.20** a) An AFM image of parallel $Al_2O_3$-FeMo lines written by using a borosilicate glass nanopipette on a native-oxide-layer-coated Si (100) at various tip velocities of 5, 10 and 50 µm/s. b) The cross-sectional profile of 50 µm/s and 10 µm/s $Al_2O_3$-FeMo lines demonstrates the heights of 1.5 nm and 2.5 nm, respectively. c) The cross-sectional profile of 10 µm/s and 5 µm/s $Al_2O_3$-FeMo lines shows the heights of 2.5 nm and 3.5 nm, respectively [141].

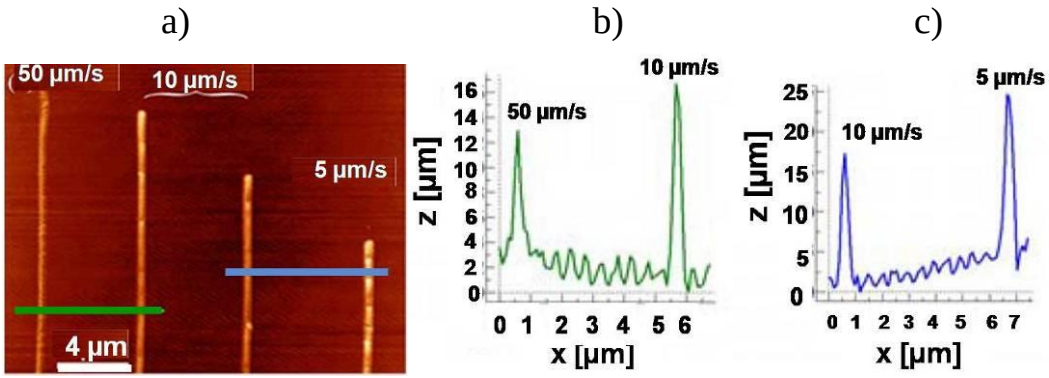


**Figure 5.21** a) An AFM image of parallel lines written on a 1 µm-thermal-oxide-layer-coated Si (100) by using a quartz nanopipette filled with a 1:50 dilution ferritin. The tip velocities were varied as 5, 10 and 50 µm/s. b) The cross-sectional profiles of 50 µm/s and 10 µm/s ferritin lines displays the heights of 9 nm and 15 nm, respectively. c) The cross-sectional profile of 10 µm/s and 5 µm/s ferritin lines shows the heights of 14 nm and 20 nm, respectively [141].

There are other reports which have demonstrated alternative ways for fabrication of fountain pens. The publications by Kim and co-workers [137, 142] introduced a new micro-fluidic AFM probe, called the "Nanofoutain probe" (NFP), which is composed of a "volcano" tip, integrated microchannels and an on-chip reservoir as shown in Figure 5.22 a). An ink solution is extruded by capillary force from the reservoir and transported via the microchannel to the "volcano" tip. Subsequently, a liquid-air interface is formed around the core tip in Figure 5.22 b) [137]. Ink molecules are then transported by diffusion from this interface to a surface via a water meniscus. In a preliminary test shown in Figure 5.23 it was found that Kim *et al.* [142] could achieve a minimum feature size of *ca.* 200 nm for a line of MHA solution in acetonitrile. The line was written with a scan speed of 0.03 µm/s and a relative humidity of 50 %. In the later paper, Kim *et al*. (2005) [137] showed that they could successfully generate patterns of MHA with the smallest line width around 40 nm on a Au surface as shown in Figure 5.24 d). They used a 1 mM solution of MHA in ethanol. The pattern of MHA shown in Figure 5.24 d) was fabricated with a 0.05 µm/s sweeping rate at 60 % RH. In their experiments, both writing and imaging were performed by the same tip. Considering their result, the

patterned line width was smaller than the tip radius by about a factor of 3. The authors supposed that this was related to the tip roughness caused by the microfabrication step leading to a much smaller contact area compared to the smooth tip [137]. They also showed that the same NFP was able to fabricate with the same solution of nanopatterns with multiple ink feeds and without cleaning over a day. As a consequence, the nanofeatures could be obtained with consistency and reproducibility.

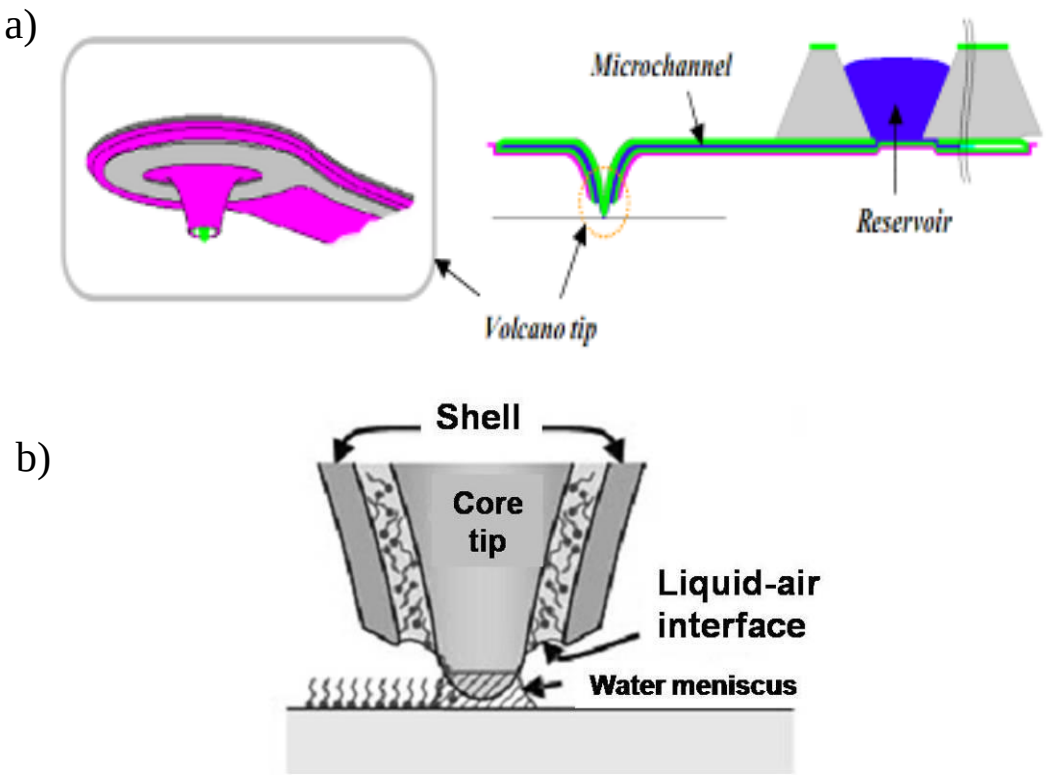


**Figure 5.22** a) A schematic model of the nanofountain probe device consisting of a reservoir, microchannel and volcano tip. An ink molecule was fed from the reservoir to the volcano tip by capillary force [142]. b) The writing mechanism of the NFP device shows an ink solution from the reservoir forming a liquid-air interface at an annular aperture [137].

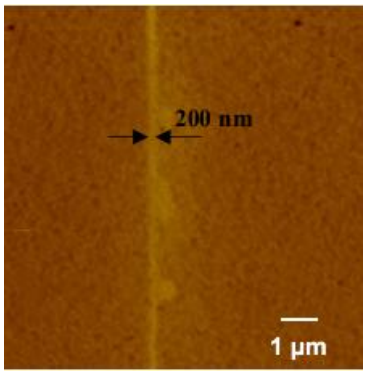


**Figure 5.23** A lateral force image of a line and dots from a saturated solution of MHA in acetonitrile written by a nanofountain probe with a 0.03 µm/s scan rate and a relative humidity of 50 % [142].

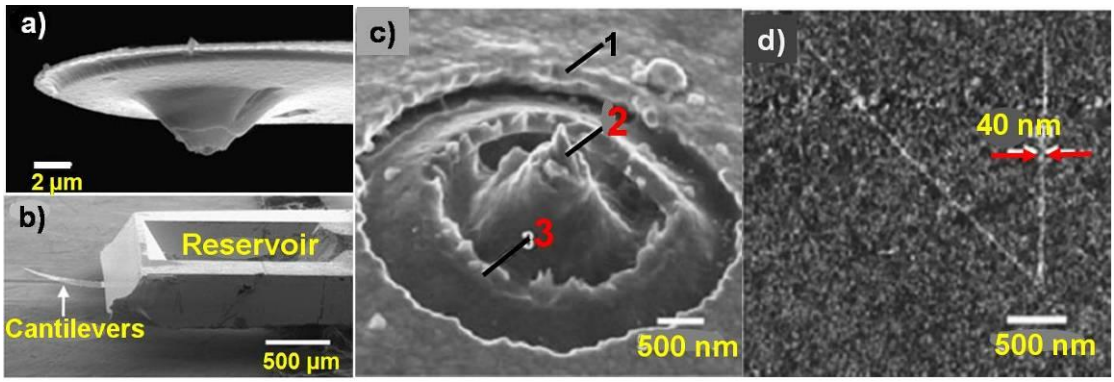


**Figure 5.24** a) Scanning electron micrograph (SEM) of a volcano tip. b) SEM of an on-chip reservoir. c) SEM of a volcano tip used for the experiment: 1) Au sealing layer, 2) writing tip and 3) top nitride layer (volcano shell). d) Lateral force image shows the deposition of MHA on a Au surface [137].

By employing a nanofountain probe (NFP), Wu *et.al*. [143] demonstrated the direct deposition of Au nanoparticles onto an amino-terminated oxidised Si surface. Figure 5.25 displays a schematic presentation of how a Au colloidal solution was transported from the NFP reservoir to the tip by capillary force and deposited on a functionalised Si surface. As shown in Figure 5.26 a), arrays of Au nanodots were fabricated with a 2 s contact time and the corresponding height profile demonstrates 600-700 nm diameter and 150-180 nm height dots. This is due to the fact that a non-volatile residue existed with the Au particles. However, after rinsing the sample with

deionised water, a well-defined Au particle pattern was found with an average height of 15-30 nm (see Figure 5.26 b)). The authors suggested that Au nanodots were probably composed of two monolayers. Furthermore, they also investigated other parameters which can influence the dot size and revealed that the deposition mechanism and resolution depend on the NFP tip dimensions, wetting characteristics and evaporation rate.

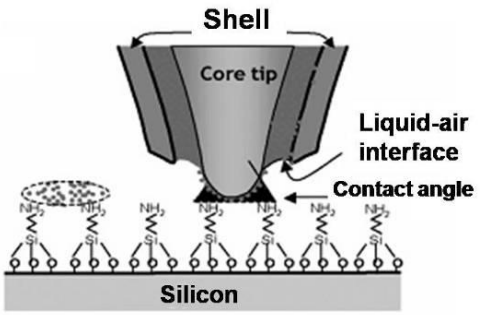


**Figure 5.25** A schematic diagram of Au nanoparticles transported to a modified Si substrate by the NFP with a 2 s contact time [143].

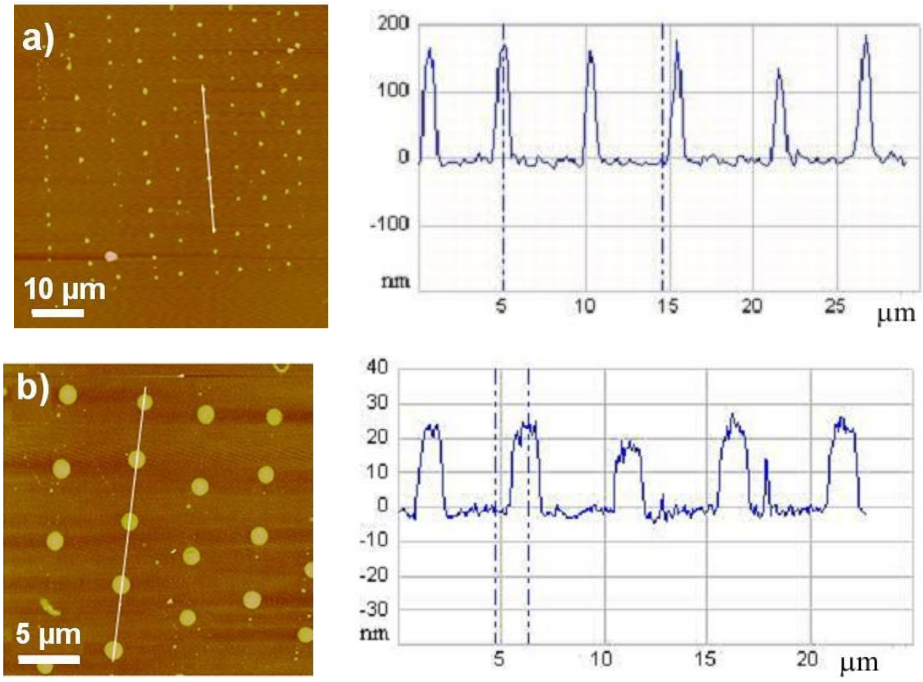


**Figure 5.26** a) AFM image of patterned Au nanoparticles before rinsing with deionised (DI) water (left) and the corresponding height profile along the white-line (right). b) AFM image of Au nanodots after rinsing with DI water (left) and the corresponding height profile show an average height of dots around 15-30 nm [143].

## 5.2 Motivation

The development of selective syntheses for gold nanoparticles over the last few decades has been an area of intense interest due to the dependence of their properties (e.g., electronic, magnetic and optical properties) on both shape and size [144-147]. In particular, there has been strong interest in prospective applications involving gold nanoparticles for surface-enhanced Raman scattering (SERS) [148, 149] to enable single-molecule detection. The ultimate aim of this chapter was to explore a state-of-the-art method to fabricate Au nanostructures on a patterned $SiO_2$ substrate with a low-cost, simple and effective technique. There were also several other requirements. For example, the technique should directly deposit Au metals on native-oxide-layer-coated Si substrates without the need of a functionalised or pre-treated surface. In addition, the technique should have the possibility to controllably pattern nanostructures at desired locations.

Taking these requirements into consideration, the DPN technique was the first option which may fulfill our goal due to a number of its advantages as already mentioned in Section 5.1.1 and 5.1.2. The possibility of using $HAuCl_4$ as the ink and then depositing the ink onto insulating substrates by using a similar DPN strategy as the study of Sung *et al.* [29] is reported in the following section. There were some differences in our methods, for example, we did not immerse the whole AFM tip into ink solution to avoid attenuation of the AFM feedback signal from the backside of the AFM tip [134]. The 'scanning-coating' (SC) of AFM tips as demonstrated by Bing *et al.* [134] was used instead of the dip-coating technique. To the best of our knowledge, a study of SC time of AFM tips with $HAuCl_4$ ink in particular has not yet been reported. Therefore, the study of time for scanning-coating process of $HAuCl_4$ ink has been performed to optimise the SC time for the suitable loading of $HAuCl_4$ ink onto AFM tips and to investigate the uniformity of the ink coating on the tip. Moreover, we did not use a tip-heater to increase the tip temperature but we still controlled the chamber temperature and chamber humidity. Since thermal treatment is necessary to reduce the Au (III) to Au (0) after depositing Au (III) ink on such substrates as reported by Sung and colleagues [29], the effect of annealing temperature on the Au ink reduction has also been investigated by using a stereo

microscope for imaging and an SEM energy-dispersive X-ray spectroscopy (EDS) for elemental content analysis.

However, as already mentioned since the DPN technique still has limitations for patterning large areas and causing low throughput due to the depletion of ink, a second option would be to use FPN technique with the benefit of continuous feeding of ink. A cantilevered nanopipette was used to deliver $HAuCl_4$ ink and a variety of solvents onto a substrate at the predefined positions. Even though, the resolution of patterning features was ultimately limited by the aperture of the nanopipette, the benefit of free writing of Au structures on any patterned semiconducting surface makes the FPN technique worth consideration.

## 5.3 Results and discussion

### 5.3.1 Gold deposition using dip-pen nanolithography

#### 5.3.1.1 Effect of the annealing temperature on the gold deposition

In order to test how the annealing temperature influences the reduction of $HAuCl_4$ (Au (III)) solution to gold (Au (0)) after depositing Au (III) ink on substrates, we investigated on the macroscale using a stereo microscope for imaging and SEM-EDS for elemental content analysis. A small amount (*ca.* 2 µL) of the 20 mM $HAuCl_4$ ink solution in acetonitrile was dropped on native-oxide-layer-coated Si substrates and followed by annealing each substrate at different temperatures of 250 °C, 300 °C and 350 °C. Subsequently, images were taken under a stereo microscope (Nikon SMZ 1500) with an attached microscope camera (Leica DFC425 C). The optical microscope images of various native-oxide-layer-coated Si wafers at different steps of the treatment are shown in Figure 5.27.

The results in Figure 5.27 step 1 demonstrate the substrates after dropping the $HAuCl_4$ ink solution onto the substrate and evaporating solvent overnight prior to annealing treatment. After that, the substrates were annealed in Ar for 5 mins at different temperatures: 250 °C, 300 °C and 350 °C for sample S2, sample S3 and sample S4, respectively, and then cooled to room temperature before imaging. The results in Figure 5.27 step 2 illustrate that, when the annealing temperature was increased from 250 °C to 350 °C, a gold-like-yellow colouration was noticeably observed to form on the sample, together with a reduction in the intensity of the white colour compared to the substrates before annealing (see step 1). The colour change was clearly seen in sample S4 with 350 °C of annealing temperature. This phenomenon was assumed to be the reduction of Au (III) salt to Au (0) metal by thermal annealing since in our experiment there was no reducing agent present. Therefore, in order to prove this assumption, a water treatment was applied since only the Au (III) salt is water-soluble, whereas the Au (0) metal is water-insoluble. The solubility of $HAuCl_4.4H_2O$ and Au metal can be found from the *CRC* Handbook of Chemistry and Physics [126]. As a result, after the wafers were immersed in deionised (DI) water to remove the Au (III) salt as shown in Figure 5.27 step 3, no

remaining salt on the wafer S1 (without annealing) was observed but the wafer S2 which was annealed at 250 °C showed some remaining particles at the corner. In contrast, on the wafers S3 and S4 which were annealed at 300 °C and 350 °C, respectively, there was a noticeable presence of the remaining particles which were certainly not the Au (III) salt because the Au (III) should be completely removed by water. Subsequently, the substrates were immersed in a Au etchant to confirm that it is Au (0) remaining after water treatment. As we can see in Figure 5.27 step 4, no remaining particles were observed on all substrates. Thus, it can be deduced that only Au particles left on the substrate after washing with water. Moreover, at high annealing temperature (300 °C and 350 °C), the visual observation suggested that there were large amounts of the reduction of Au (III) to Au (0). However, to further confirm the decomposition of $HAuCl_4$ to Au, we employed SEM-EDS analysis (a Philips XL30CP with Princeton Gamma-Tech (PGT) Instruments, Inc Spirit EDS X-ray analysis) to study the elemental content of deposited particles on the substrates after the annealing process (step 2 in Figure 5.27).

Figure 5.28 demonstrates the EDS spectral results of the effect of different annealing temperatures on $HAuCl_4$ salt on native-oxide-layer-coated Si substrates. It can be seen that the EDS spectral results of the molecular layer before the annealing process (see Figure 5.28 a) and b)) and after annealing at 250 °C (see Figure 5.28 c) and d)) showed a significant amount of Au and Cl. This means that the $HAuCl_4$ salt still remained on the substrate. However, after annealing at 300 °C (see Figure 5.28 e) and f)), the Cl peaks were considerably reduced and were very small compared to the Au peak. Then, after annealing at 350 °C, only Au peaks were present on the substrates as shown in Figure 5.28 g) and h). This evidence confirms that, after increasing the annealing temperature to 350 °C, no $HAuCl_4$ salt remained on the substrate. Our results were similar to the previous studies of Murphy *et al.* [150] and Sung *et al.* [29]. Murphy and co-workers [150] reported that the Au (III) complex of $[AuCl_4]^-$ broke down and precipitates as Au (0) at high temperature above 250 °C. Murphy *et al.* [150] noted that the exact temperature of their observation seemed to be involved with oxygen fugacity. Considering the study of Sung *et al.* [29] using EDS and X-ray photoelectron spectroscopy (XPS) analysis, they also found that after

annealing above 300 °C all of the Au (III) was reduced to Au (0). Our observations confirm a strong temperature dependence of the $HAuCl_4$ reduction and the $HAuCl_4$ was reduced to Au metal at the annealing temperature above 300 °C.

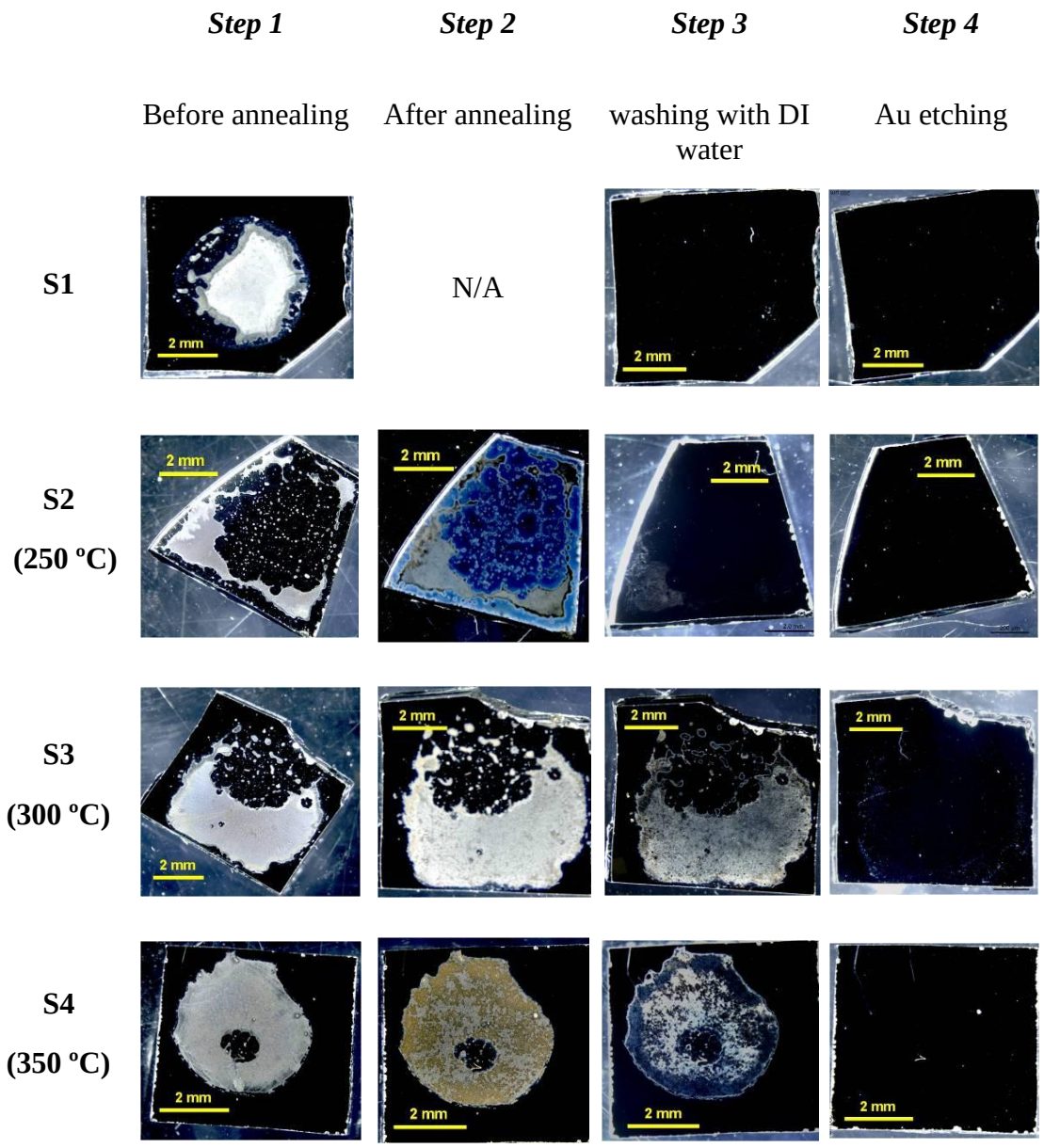


**Figure 5.27** Optical microscope images of $HAuCl_4$ solution dropped on 4 native-oxide-layer-coated Si wafers (row S1-S4) and treated with 4 steps including before annealing (step 1), after annealing (step 2) at 250 °C , 300 °C and 350 °C of sample S2, sample S3 and sample S4, respectively, after washing with DI water (step 3) and after Au etching (step 4). Note that S1 is a control experiment without annealing.

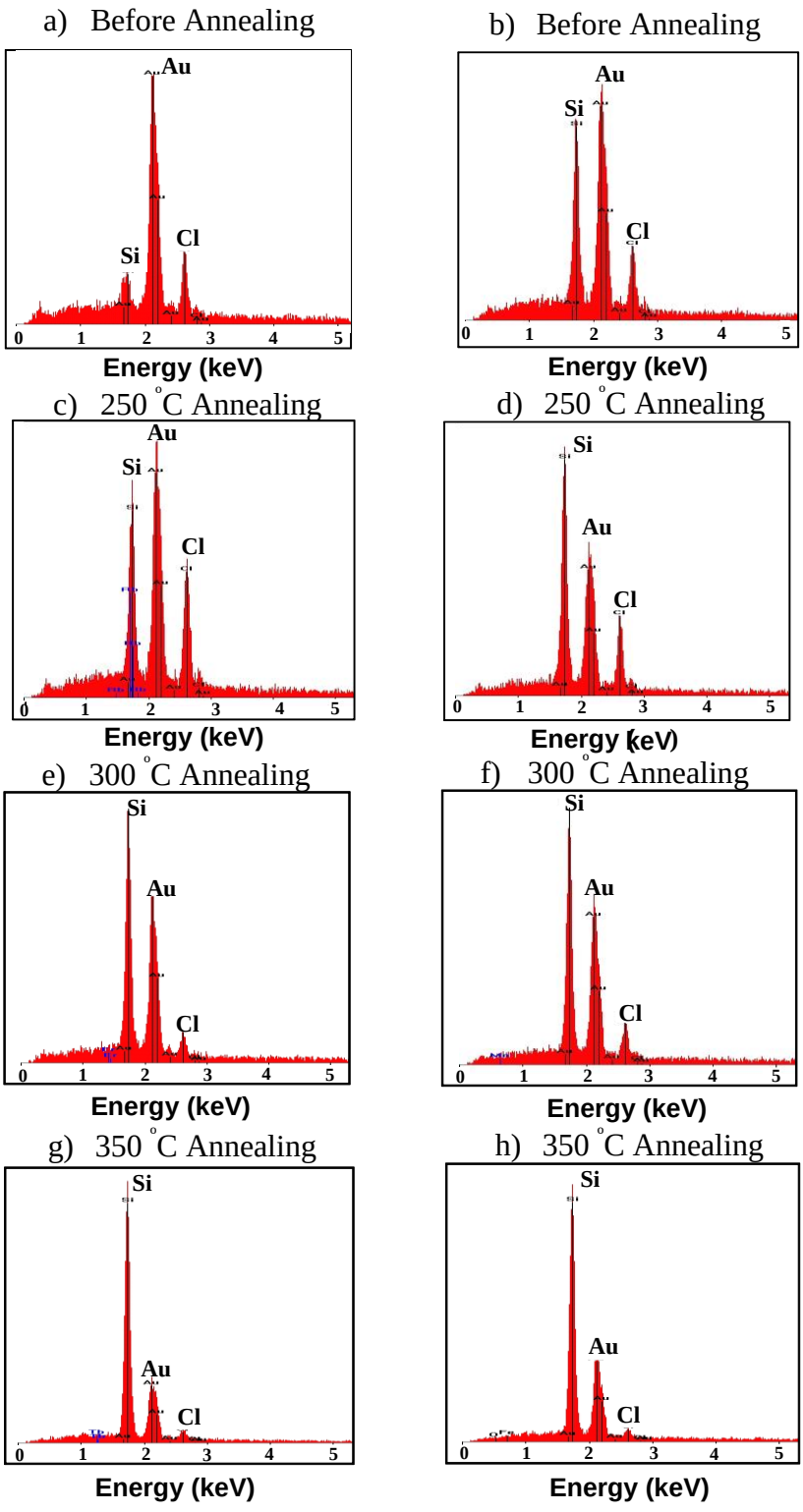


**Figure 5.28** EDS analysis showing the effect of annealing temperature on the elemental contents of particles on native-oxide-layer-coated Si surfaces: before the annealing process in Ar (a, b) and after the annealing process in Ar at (c, d) 250 °C, (e, f) 300 °C and (g, h) 350 °C.

#### 5.3.1.2 Effect of the scanning-coating time on the ink coating on the gold-coated AFM tip

By using the scanning-coating (SC) strategy as developed by Bing *et al.* [134], we studied how the $HAuCl_4$ ink molecule coated onto the AFM tips with varying the SC time. A Au-coated tip (NSG01/Au, see Table 5.1) with a tip radius *ca.* 35 nm, a normal force constant of 5.1 N/m and a resonance frequency of 150 kHz [28] was used in this section. The primary consideration for choosing this tip was its coating material to improve the adhesion of the molecular ink to the tip surface. As previously studied by Sung *et al.* [29], the Au surface has a good adhesion with the $HAuCl_4$ ink. Four AFM tips were SC in a small droplet of $HAuCl_4$ ink for four different durations of 1, 2, 3 and 4 minutes. SEM measurement was employed to characterise the adhesion of the $HAuCl_4$ ink on the Au-coated AFM tip after the SC process. Figure 5.29 shows a brand new Au-coated AFM tip prior to ink coating. Figure 5.30 a), c), e) and g) show SEM images of the AFM tips after $HAuCl_4$ ink coating for 1, 2, 3 and 4 minutes, respectively. Considering the uniformity of the ink coating, the results of 2 min, 3 min and 4 min showed a non-uniform coating of the ink molecule on the AFM tip surface. In Figure 5.30 a), e) and g), the images show that the amount of ink molecules coated on the tip surface increased with increasing the SC time. However, Figure 5.30 c) of 2 min SC time of a $HAuCl_4$-ink-coated tip shows a larger amount of ink molecules on the tip surface compared to that of 3 and 4 min SC time of $HAuCl_4$-ink-coated tips in Figure 5.30 e) and g). Plausible reasons would be due to the different height of the $HAuCl_4$ ink droplet in each area as well as the influence of the capillary force of the ink solution on the adhesion and coating of ink molecule to the AFM tip.

.

#### 5.3.1.3 Effect of the scanning-coating time of the gold-coated AFM tip on the deposition of gold nanodots

In order to study gold deposition using the DPN technique, the $HAuCl_4$-ink-coated AFM tips with different SC time from previous section were used to deposit $HAuCl_4$ ink molecules on a native-oxide-layer-coated Si substrate. Experiments were

performed in contact mode. The temperature and humidity were monitored and controlled during the experiments and the values were shown in Table 5.3. After the deposition, the samples were annealed at 350 °C in Ar for 5 min.

The results of the Au depositions after annealing process were characterised using AFM. To give some idea about the effect of different AFM tips on the Au patterning, Figure 5.31 shows the overall AFM imaging results of Au dots deposited on the native-oxide-layer-coated Si substrates after annealing with different AFM tips between 1-min-ink SC and 4-min-ink SC. It was found to be very difficult to achieve with arrays of nanodots, as the real attempts were designed for deposition due to the number of variables that might affect. Although, parameters such as chamber temperature, relative humidity and deposition time were monitored and controlled as consistent as possible, the exact amount of ink diffusion to the substrate was impossible to control.

Figure 5.32–5.35 shows the AFM images at a higher magnification of Au dots with different coated AFM tips from 1 min SC to 4 min SC, respectively as well as the cross-sectional profile of a Au dot is also displayed at the bottom of each AFM image. As shown in Figure 5.33 a), 5.34 a) and 5.35 a), it could be seen that there were some small particles surrounding the large central dots. This phenomenon could potentially be the result of a number of factors. Firstly, since the diffusion of the ink on the substrate is faster than the deposition rate of the ink molecule as previously discussed by Jang *et al.* [127] (see section 5.1.2), this can lead to the diffusion of ink molecules, which are not chemisorbed, to the perimeter of the chemisorbed structure to continue to growth. Secondly, it could be related to the meniscus size effect. As already discussed in section 5.1.2, the meniscus size was dependent on many factors, such as temperature, humidity and deposition conditions (rate, surface hydrophobicity and tip hydrophobicity) [151]. In our case, the meniscus size should be large due to the high humidity condition (61-78 ºC), hydrophilic surface ($SiO_2$) and hydrophilic ink ($HAuCl_4$) use. The large size of the meniscus results in a large number of ink molecules being transported. Moreover, ink contamination with residual co-solvents can affect the ink solubility [151] and co-deposition [152]. As the study of Wang *et al.* [152], at high humidity of 70 %, the solvent matrix could be

simultaneously deposited with ink molecules. As a result, in our case both $HAuCl_4$ ink molecules and solvent (acetronitrile) could be deposited onto the substrate. Subsequently, after annealing, the solvent matrix evaporated and only the pure Au dots were left on the substrate. To further confirm, Table 5.4 indicates that the number of observed results of Au dots was higher than that of real attempts for Au deposition for all experiments.

Figure 5.36 shows log-normal size distributions of Au dots obtained from all SC AFM tips as a function of height in the left panel and half-width on the right panel. The data in Figure 5.36 were extracted from Figure 5.31 with measurements of all observed dots. Subsequently, the data from Figure 5.36 were used to create plots of the average dot height and half-width as a function of the SC time of each AFM tip as shown in Figure 5.37 a) and b), respectively. Considering the average height as shown in Figure 5.37 a), when the SC time of AFM tip was increased from 1 min to 4 min, the height follows a linear dependence with a gradient of $-1.3 \pm 0.5$ nm/min and decreasing from $6.5 \pm 2.3$ nm to $1.2 \pm 0.5$ nm. As illustrated in Figure 5.37 b), the average half-width of Au dots linearly decreases from $23.0 \pm 4.5$ nm to $19.6 \pm 5.5$ nm with increasing SC time of AFM tip from 1 min to 3 min; however, in the case of 4 min SC time, the average half-width shows the anomalous result with the greatest value of $57.8 \pm 9.5$ nm. From these two plots, it can be assumed that low SC time of AFM tip tended to give high aspect ratio features. However, no conclusion could be drawn from this investigation yet, since all of the observed dots were not from individual deposition attempts.

Figure 5.30 right panel shows SEM images of the $HAuCl_4$-ink-coated AFM tips after Au deposition. In comparison with the $HAuCl_4$-ink-coated AFM tips before Au deposition as shown in Figure 5.30 left panel, the ink molecules coated on the AFM tips after patterning (see Figure 5.30 right panel) did not show a significant depletion of the amount of ink. However, we can only observe the tips blunting occurred.

Additionally, several studies suggested that the cantilever resonance frequency can be used to detect mass change onto cantilevers [153-157]. The resonance frequency (ν) of a cantilever can be expressed as following;

$$\nu = (1/2\pi)\,(K/m^*)^{1/2} \quad (1)$$

Where $m^*$ is the effective mass of a rectangular cantilever and $K$ is the spring constant. The $HAuCl_4$ ink depletion is assumed to be uniform on the AFM cantilever and then $K$ is constant. The mass change ($\Delta m$) due to depletion of ink is

$$\Delta m = (K/4\pi^2)\,(1/\nu_1^2 - 1/\nu_0^2) \quad (2)$$

Where $\nu_0$ and $\nu_1$ are the resonance frequencies before and after ink deposition, respectively. To verify if the ink molecule was efficiently deposited onto the substrate, the resonance frequencies and the mass change values of the $HAuCl_4$ ink before and after the deposition process of all AFM tips were calculated and summarised in Table 5.2. In the case of mass of deposited dots, this was calculated from the volume of dot obtained from measurement of the height and the half-width data from Figure 5.37. From the AFM image results in Figure 5.31 and the size measurement in Figure 5.36-5.37, it was assumed that the geometry of nanodots is close to a cylindrical shape. The volume was then calculated by the following equation:

$$V_{dot} = \pi\,(HW)^2 h \quad (3)$$

Where HW is the half-width and h is the height of nanodots. Then, the mass of nanodots (m) was calculated from the following equation:

$$m = \rho V_{dot} \quad (4)$$

Where ρ is the density of Au (19.3 $g \cdot cm^3$ from ref [126] ) since the size was measured after the annealing process in which the $HAuCl_4$ ink was reduced to Au (0). In order to avoid the residual solvent affecting the overestimation of the mass reduction from the tip, we measured the resonance frequency of the tip 7 months after the deposition as shown in Table 5.2. To demonstrate the calculation of 3 min

SC ink-coated tip (*K*= 5.1 N/m) after deposition by using equation (2) as an example, the resonance frequency changed from 148.213 kHz to 153.459 kHz resulting in a reduction of mass of -0.3953 *p*g (see Table 5.2). This means the $HAuCl_4$ ink from the AFM tip deposited onto the substrate should *ca.* 0.3953 *p*g. However, it was found that the mass of Au which was estimated from the volume of dots was 1.706 x $10^{-5}$ *p*g in the case of 3 min SC ink-coated tip. This indicated that a much smaller amount of Au was actually deposited on the substrate compared to the mass depletion from the tip. Many factors may affect this such as the estimation of the dot geometry as a cylindrical shape or tip damage causing a greater reduction of mass from the AFM tip. Considering the 1 min SC and 4 min SC AFM tips, the results also showed similar trends as 3 min SC AFM tip. Apart from the 2 min SC tip, the calculated mass from the resonance frequency did not decrease as we expected. In contrast, after deposition, the SEM images of 2 min SC tip (see Figure 5.30 d)) clearly showed the decrease of the ink from the AFM tip compared to the tip before deposition (see Figure 5.30 c)). Taking into account the mass changes of 7-month-later measurements after deposition ($\Delta m_{3-1}$) (see Table5.2) of 1 min, 3 min and 4 min SC, they were consistent with the number of observed dots but were not consistent with the volume measurements as illustrated in Table 5.4. The number of dots observed in 1 min, 4 min and 3 min were 120, 180 and 206 dots, respectively, while the mass changes measured 7-month-later after deposition process were -5.305 x $10^{-3}$ *p*g, -0.3261 *p*g and -0.3953 *p*g, respectively. However, either the mass of observed dots (see Table 5.2) or the volume of dots (see Table 5.4) showed the opposite trends with the number of the observed dots. It was worth to note that in the case of 1 min SC tip, the mass change of immediate measurements after deposition ($\Delta m_{2-1}$) showed an increase in mass of +5.228 x $10^{-3}$ *p*g, but after 7-month-later measurements of the resonance frequency of the AFM tip the mass change showed a reduction of the mass of -5.305 x $10^{-3}$ *p*g as expected.

To verify that the deposited material after annealing was indeed composed of Au dots, the substrates were immersed into gold etchant (a mixture of $I_2$ + KI + $(NH_4)_2KPO_4$ + $H_2O$) for 20 min. Subsequent AFM imaging (see Figure 5.38) revealed that almost all of the Au dots were removed from the substrate.

**Table 5.1:** Specifications of an AFM tip used for investigation in this section.

| ***Type*** | ***Coating*** | ***Tip radius (nm)*** | ***Force constant (N/m)*** | ***Resonance frequency (kHz)*** |
|---|---|---|---|---|
| NSG01-Au | Au(Ti)[a] | ~ 35 | 5.1 (1.45 - 15.1) | 150 (87 - 230) |

**[a] Ti is an adhesion layer as provided by the manufacturer [28].

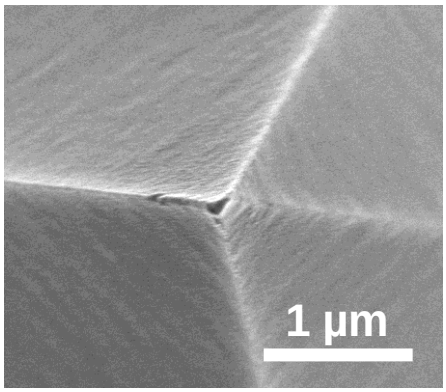


**Figure 5.29** SEM image of a new Au-coated tip (NSG01/Au) with a tip radius *ca.* 35 nm, a normal force constant of 5.1 N/m and a resonance frequency of 150 kHz.

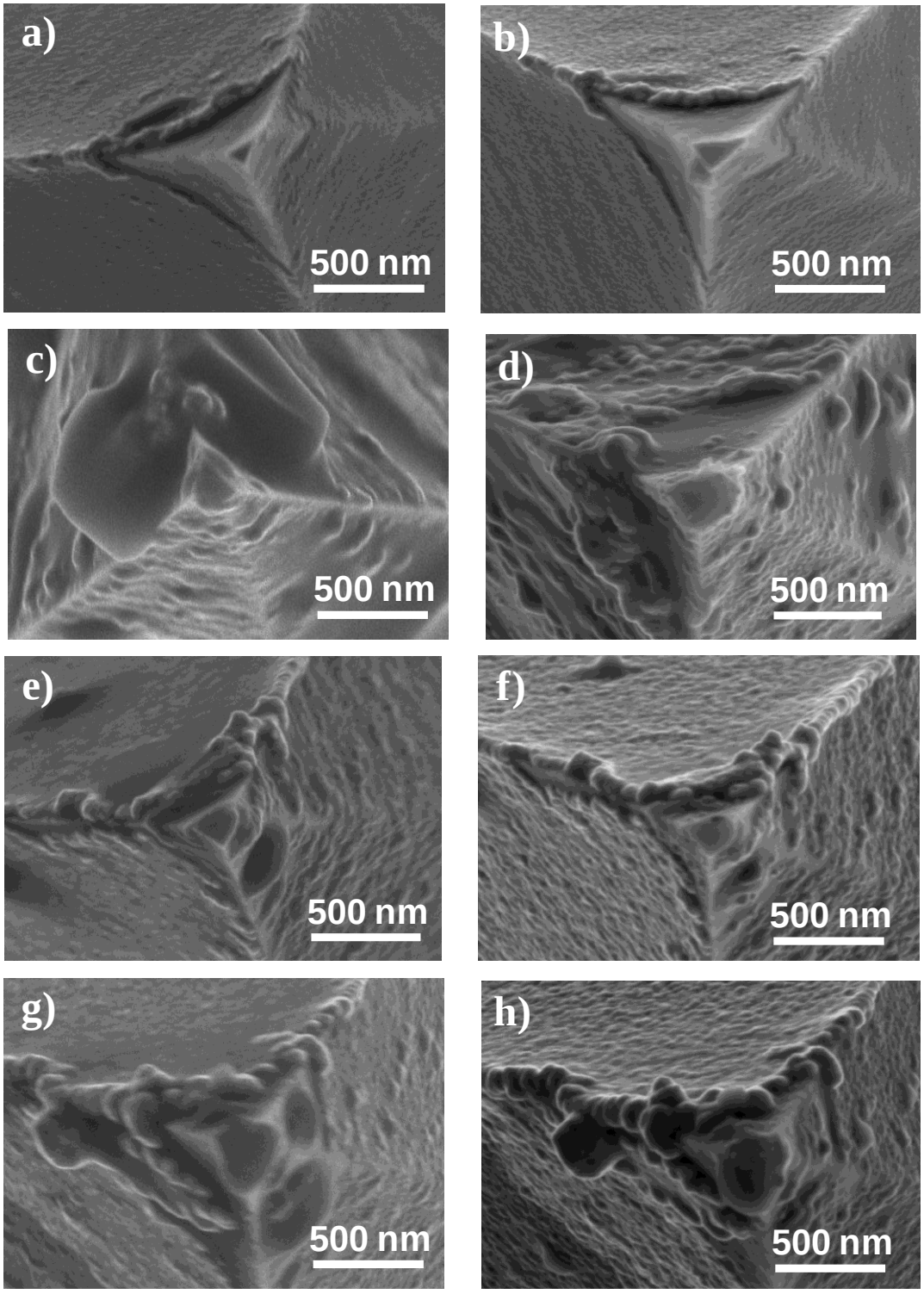


**Figure 5.30** SEM images of $HAuCl_4$-ink-coated AFM tips before (left panel) and after (right panel) performing Au deposition by DPN with different scanning-coating times of (a, b) 1 min, (c, d) 2 min, (e, f) 3 min and (g, h) 4 min in a 20 mM $HAuCl_4$ ink solution.

**Table 5.2:** Cantilever resonance frequencies of ink-coated AFM tips before and after deposition and the calculated mass change after SC as well as after Au deposition.

| ***Tip No. (NSG01-Au)*** | ***SC time (min)*** | ***After SC and before deposition*** | ***After deposition*** | | | | |
|---|---|---|---|---|---|---|---|
| | | | ***Measured immediately*** | | ***Measured after 7 months later*** | | ***Mass[(a)] obtained from dot volume (pg)*** |
| | | ***$RF_1$ (kHz)*** | ***$RF_2$ (kHz)*** | ***$\Delta m_{2-1}$ (pg)*** | ***$RF_3$ (kHz)*** | ***$\Delta m_{3-1}$ (pg)*** | |
| 1 | 1 | 146.051 | 145.988 | $+5.228 \times 10^{-3}$ | 146.115 | $-5.305 \times 10^{-3}$ | $3.038 \times 10^{-5}$ |
| 2 | 2 | 159.449 | 159.401 | $+3.061 \times 10^{-3}$ | 139.764 | 1.532 | $1.662 \times 10^{-5}$ |
| 3 | 3 | 148.213 | 148.393 | $-1.426 \times 10^{-2}$ | 153.459 | -0.3953 | $1.706 \times 10^{-5}$ |
| 4 | 4 | 137.203 | 137.228 | $-2.500 \times 10^{-3}$ | 140.583 | -0.3261 | $2.136 \times 10^{-4}$ |

.

**[(a)] Mass was assumed to be Au mass obtained from $m = \rho V_{dot}$ .

Where m is Au mass (g), ρ is density of gold (19.3 $g \cdot cm^{-3}$) and $V_{dot}$ is volume of nanodots ($cm^{-3}$).

Where RF is a resonance frequency and Δm is a mass change of $HAuCl_4$ ink.

**Table 5.3:** Conditions during Au DPN of each AFM tip.

| *Tip number (NSG01-Au)* | *Scanning-coating (SC) time* | *Temperature (ºC)* | *Relative humidity (%)* |
|---|---|---|---|
| 1 | 1 | 25.2 – 27.0 | 70 - 78 |
| 2 | 2 | 23.8 ± 0.5 | 67 - 78 |
| 3 | 3 | 23.8 ± 0.5 | 64 - 78 |
| 4 | 4 | 24.0 – 25.4 | 61 - 74 |

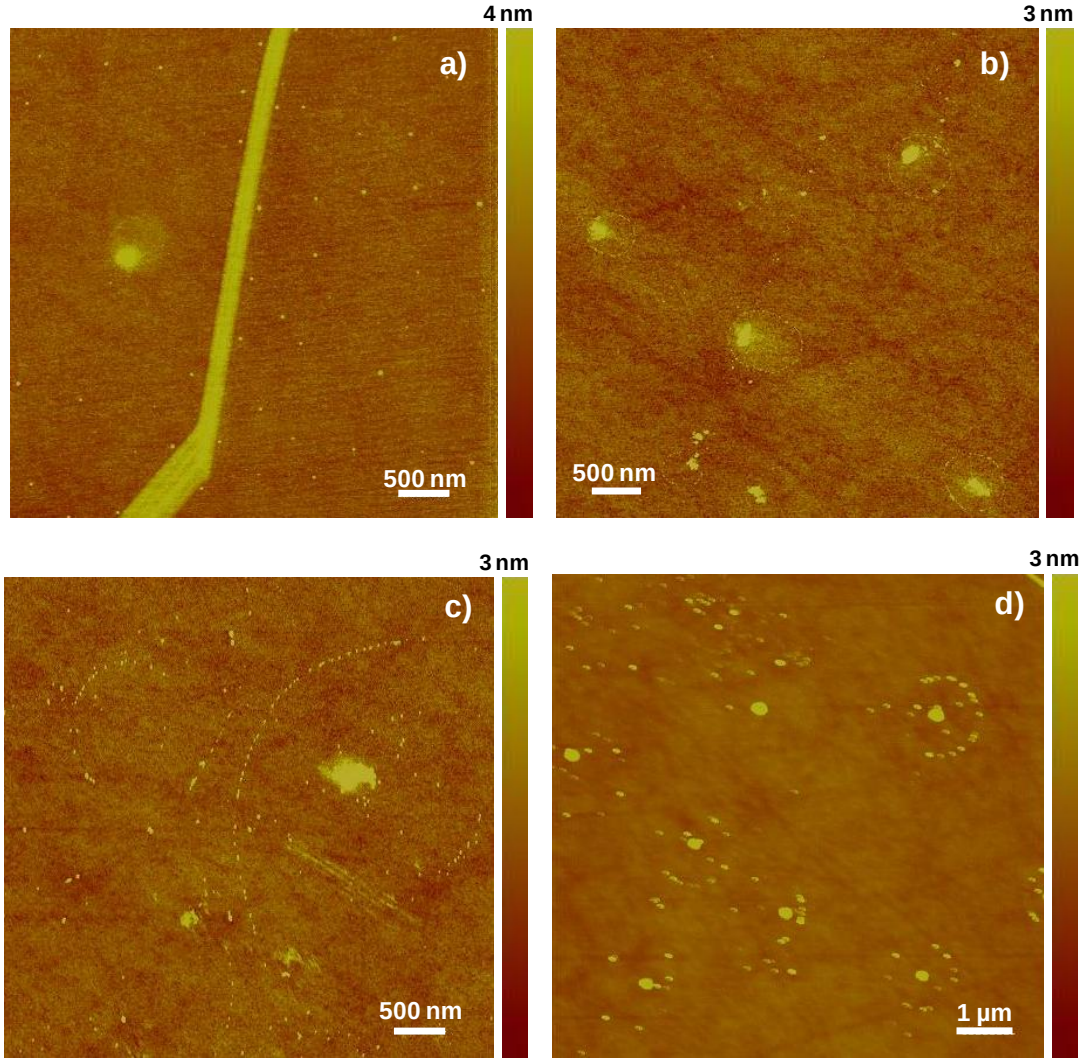


**Figure 5.31** AFM images of Au dots grown with different SC AFM tips of a) 1 min, b) 2 min, c) 3 min and d) 4 min on native-oxide-layer-coated Si substrates after annealing process at 350 ºC in Ar for 5 min.

**Table 5.4** Comparison of the number of Au dots from the real attempt during Au deposition and the observed results in AFM images as well as the volume measured from all of the observed dots in each AFM tip.

| *NSG01-Au* | *Scanning-coating (SC) time (min)* | *Real attempts (dots)* | *Observed results (dots)* | *Volume of dots ($nm^3$)* |
|---|---|---|---|---|
| 1 | 1 | 42 | 120 | $1.574 \times 10^6$ |
| 2 | 2 | 50 | 130 | $8.611 \times 10^5$ |
| 3 | 3 | 48 | 206 | $8.841 \times 10^5$ |
| 4 | 4 | 30 | 180 | $1.107 \times 10^7$ |

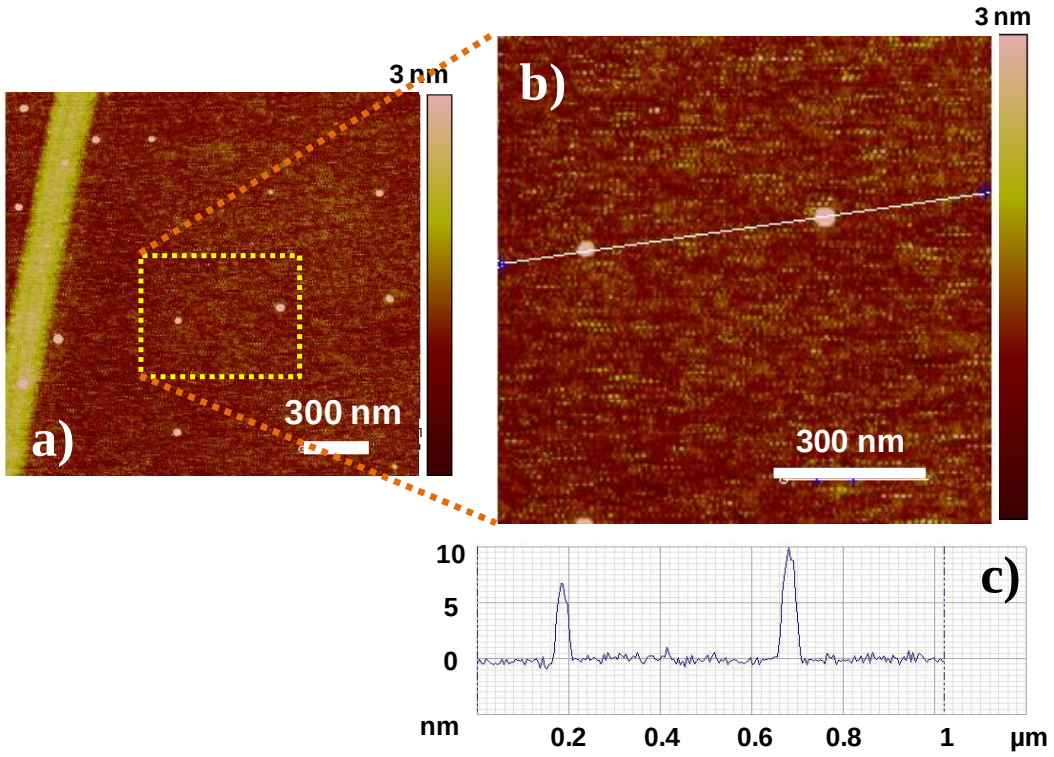


**Figure 5.32** a) An AFM image of Au dots grown with 1-min-ink-SC AFM tips on a native-oxide-layer-coated Si substrate after annealing process at 350 ºC in Ar for 5 min. The chamber temperature was 25.2-27.0 ºC and the relative humidity was 70-78 %. b) Expanded image of the marked area of dots as shown on a). c) The cross-sectional profile of dots in b).

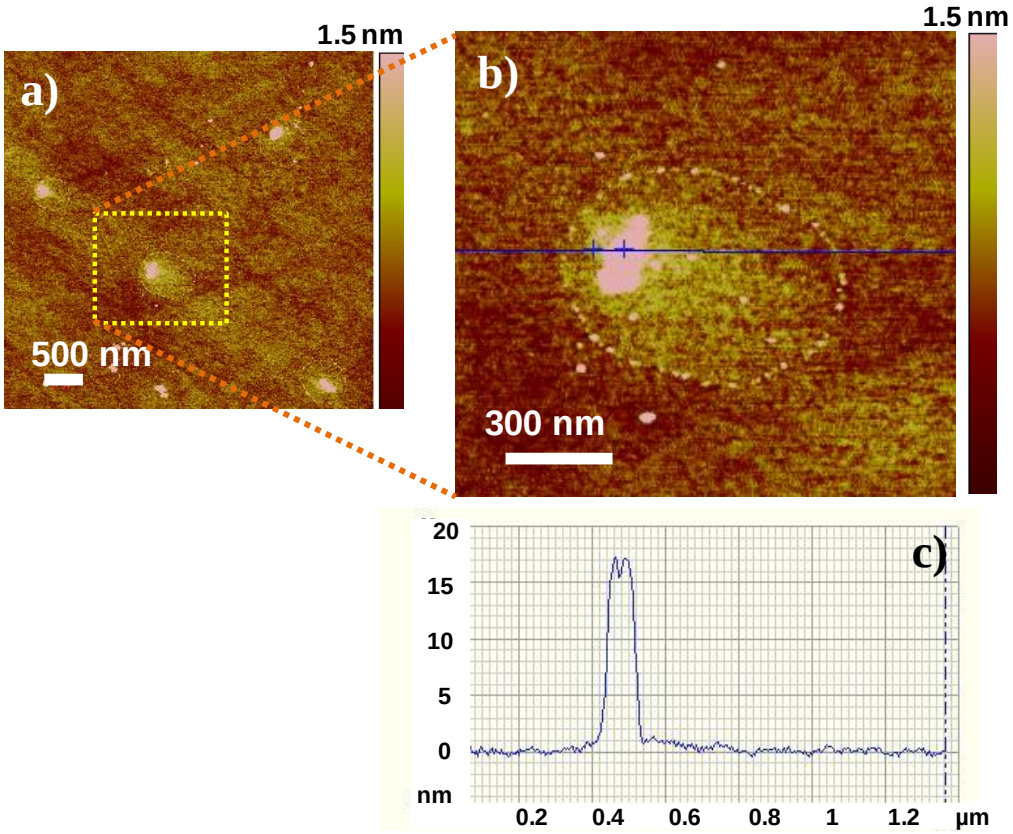


**Figure 5.33** a) An AFM image of Au dots grown with 2-min-ink-SC AFM tips on a native-oxide-layer-coated Si substrate after annealing process at 350 ºC in Ar for 5 min. The chamber temperature was 23.8 ± 0.5 ºC and the relative humidity was 67-78 %. b) Expanded image of the marked area of dot as shown on a). c) The cross-sectional profile of dots in b).

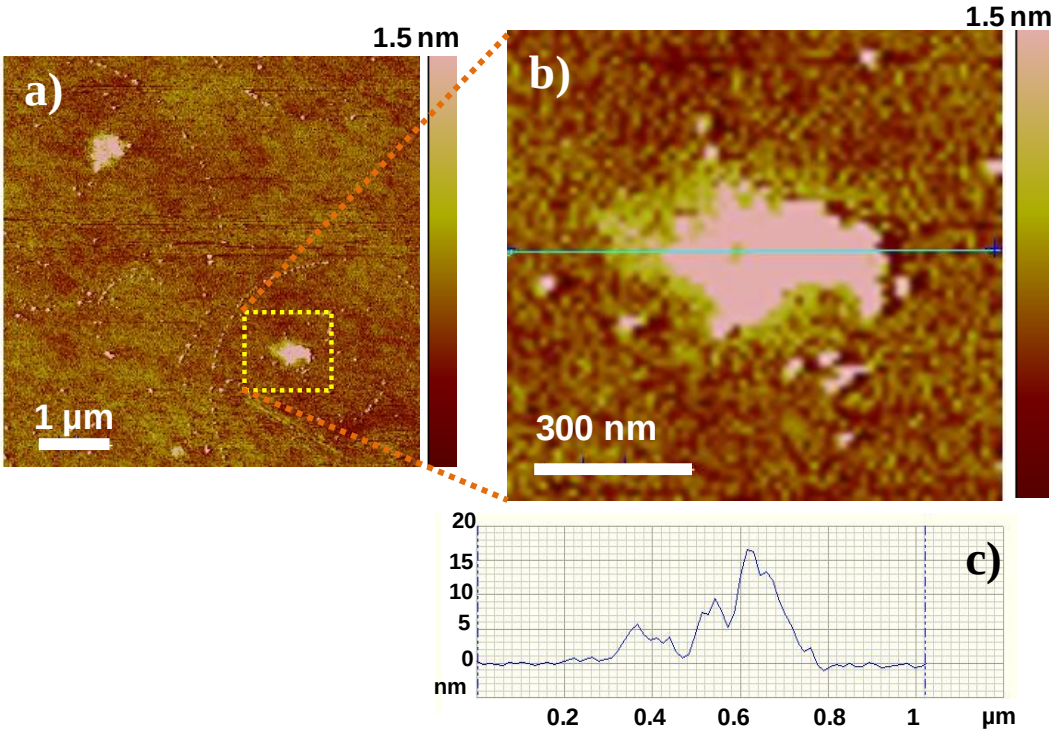


**Figure 5.34** a) An AFM image of Au dots grown with 3-min-ink-SC AFM tips on a native-oxide-layer-coated Si substrate after annealing process at 350 ºC in Ar for 5 min. The chamber temperature was 23.8 ± 0.5 ºC and the relative humidity was 64-78 %. b) Expanded image of the marked area of dot as shown on a). c) The cross-sectional profile of dot in b).

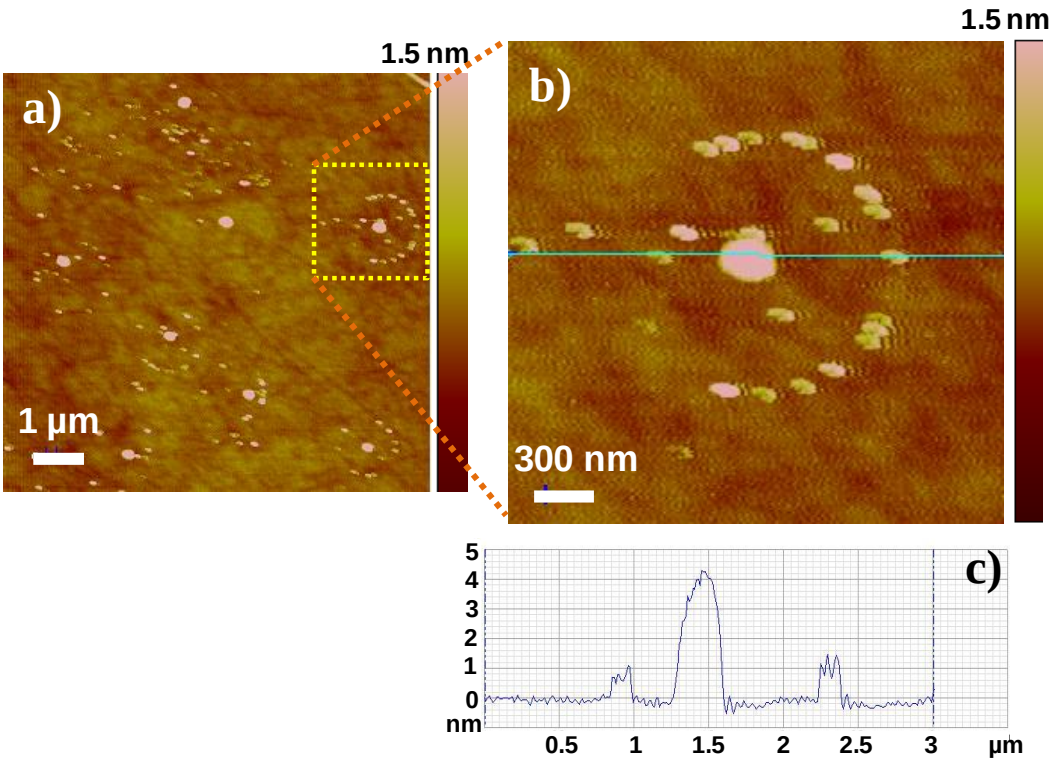


**Figure 5.35** a) An AFM image of Au dots grown with 4-min-ink-SC AFM tips on a native-oxide-layer-coated Si substrate after annealing process at 350 ºC in Ar for 5 min. The chamber temperature was 24.0-25.5 ºC and the relative humidity was 61-74 %. b) Expanded image of the marked area as shown on a). c) The cross-sectional profile of dot in b).

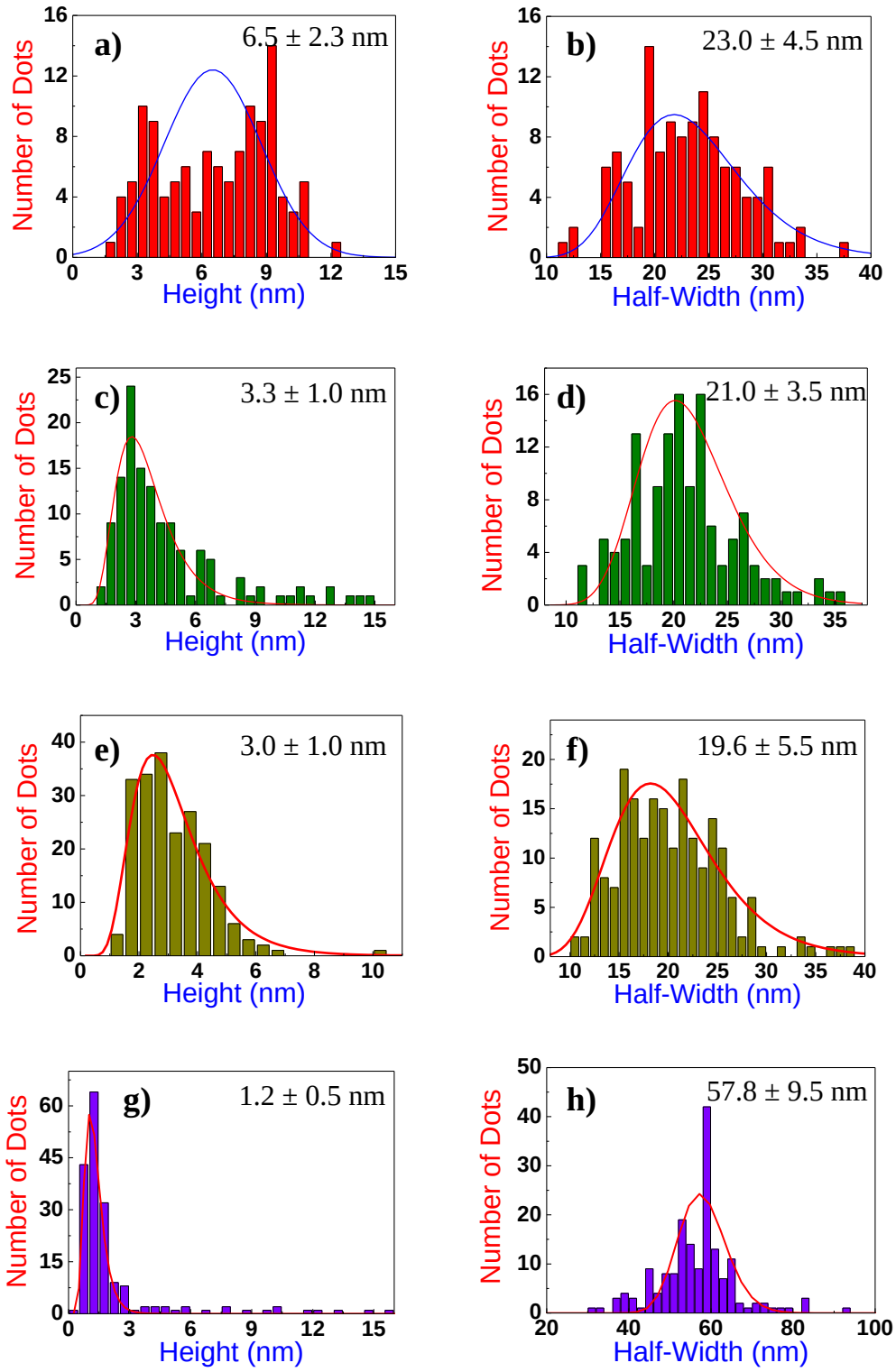


**Figure 5.36** Size distributions of Au dot height (left panel) and half-width (right panel) with different SC times of AFM tip (a, b) 1 min, (c, d) 2 min, (e, f) 3 min, (g, h) 4 min. The data were extracted from Figure 5.31.

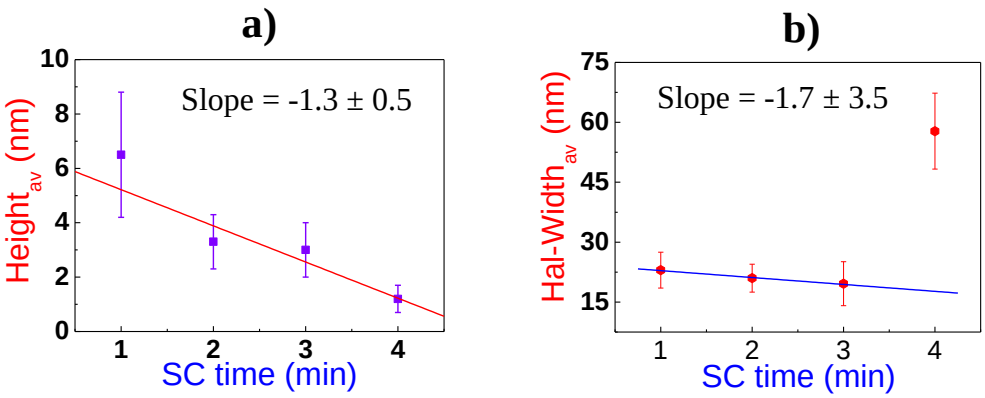


**Figure 5.37** Dependence of the height and half-width of the Au dots as a function of the SC time of AFM tips. The data were obtained from Figure 5.36. (a) The average height of Au dots with different coated time of AFM tip (b) The average half-width of Au dots with different coated time of AFM tip.

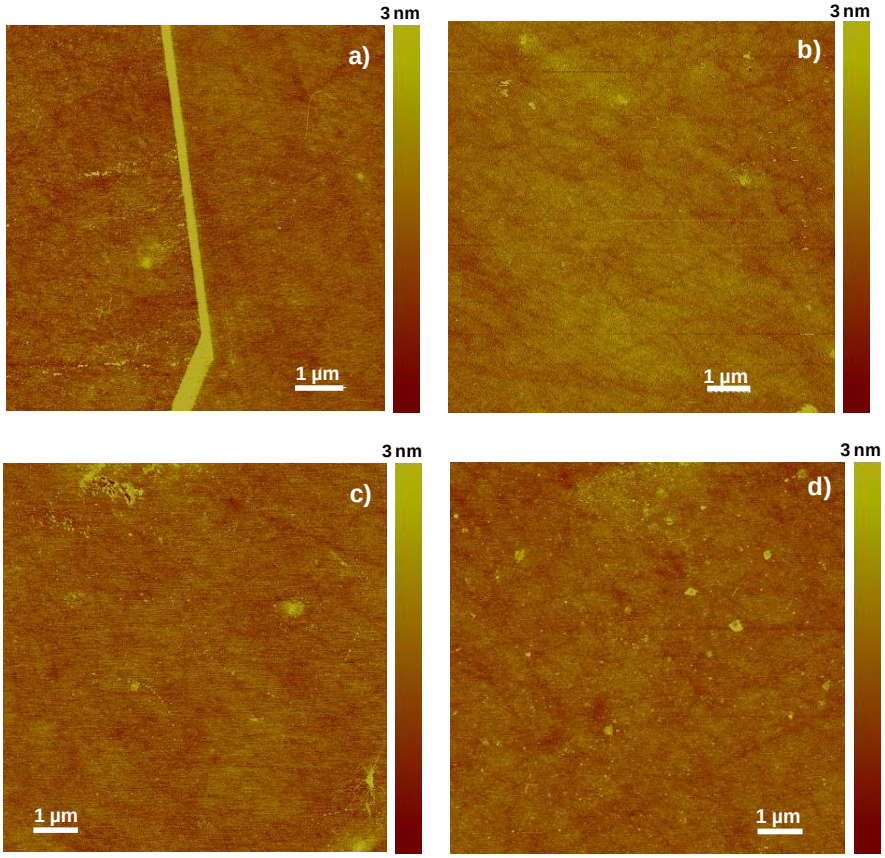


**Figure 5.38** AFM images of $Si/SiO_2$ substrate after Au etching by iodine tincture for different scanning-coated AFM tips of a) 1 min, b) 2 min, c) 3 min and d) 4 min SC time.

### 5.3.2 Gold deposition using fountain-pen nanolithography

#### 5.3.2.1 Effect of the ink-solvent systems on nanowriting

Preliminary experiments with different ink-solvent systems were carried out to investigate their influence on nanowriting with the FPN technique. A 20 mM $HAuCl_4$ solution in acetonitrile and an aqueous solution of 0.6 mM $HAuCl_4$ were primarily used to study in this section. The former solution was chosen since it was used in the previous section using the DPN technique. Consequently, it was easy to begin with this ink first. The latter solution was considered to be a simple solution system to initially test for investigation in the FPN technique.

Firstly, patterning of a 20 mM $HAuCl_4$ solution in acetonitrile was performed using 150-nm-aperture pipettes. Both contact mode and tapping mode were used to draw patterns on a native-oxide-layer-coated Si substrate. Figure 5.39 a) – c) show optical microscope images of large asymmetrical dots created by the FPN technique in contact mode with different scan speed values of 5 µm/s, 10 µm/s and 50 µm/s, respectively. The setpoint[10] for contact mode was controlled at 0.12. The pre-written script was designed with a pipette travelling along lines back and forth in the y direction while incrementally increasing the x direction as illustrated in Figure 5.39 e). Drawing start point was the top left and end point was bottom right at the pattern. This simple script will be mostly used in this section for patterning using the FPN technique. It was found that large amounts of ink pass through the pipette and rapidly deposited onto the substrate with inhomogeneous distribution and end up as a large-asymmetrical-shape dot. An example of an AFM image of the dot obtained from Figure 5.39 a) is shown in Figure 5.39 d) with the height and half-width of approximately 570 nm and 13 µm, respectively. The small dots around the big dot were assumed to be residuals after evaporating of some solvents. Plausible reasons for obtaining these results could be explained with the low viscosity of acetonitrile which is about 0.369 mPa.s at 25 ºC [126] causing a rapid flow of the ink.

[10] A setpoint is a reference force which is used to control the force between the tip and the sample when bringing the probe into contact with the sample.

Furthermore, it was considered that the native-oxide-layer-coated Si substrate is quite hydrophilic and the contact angle of the surface was less than 10 degrees for acetonitrile. This means that the ink solution with acetonitrile as the solvent has a very high wettability on $SiO_2$ substrate. This could produce a rapid flow and asymmetrical dispersion of the ink. In addition, the large aperture (150 nm) of the used pipette could influence the size of the structures. Subsequently, the same pipette was used in tapping mode for writing; however, no evidence for deposition was found. We supposed that either the pipette was possibly run out of ink or the pipette was already blocked. These investigations of using the 20 mM $HAuCl_4$ solution in acetonitrile as the ink indicated that this ink was not suitable to achieve our aim for the FPN patterning of gold ink solution on a native-oxide-layer-coated Si substrate.

Subsequently, the aqueous solution of 0.6 mM $HAuCl_4$ was used to create patterns on the native-oxide-layer-coated Si substrate. 150-nm-aperture pipettes were used in the first attempt. The experiments were performed in both contact mode and tapping mode with varying scan speed values as shown in Figure 5.40 and 5.41, respectively. Although, different scan speed values were applied, the patterning was still not achieved with the required script; in contrast, round shape dots were obtained instead. The tapping mode AFM was then employed to measure the size of dots obtained from nanowriting with the FPN technique. The height of dots obtained by tapping mode FPN seems to be smaller than that by contact mode FPN. The height decreased with increasing scan speed in the case of tapping mode as shown in Figure 5.41. However, these results could not draw any good correlation between the structure size and the scan speed since the obtained structures did not represent the real attempt of drawn patterning. It is worth to mention that this ink in aqueous solution flowed slower than the ink in acetonitrile solution. The possible explanation could be related to the higher viscosity of water (0.89 mPa.s at 25 ºC) compared to the viscosity of acetonitrile (0.369 mPa.s at 25 ºC). Moreover, the surface tension could play an essential role in ink flow. In comparison with the surface tension of acetonitrile (28.66 mN/m at 25 ºC), the surface tension value of water (71.99 mN/m at 25 ºC) is much greater by about a factor of 2.5 causing a slower flow of the ink when the pipette was in contact on the substrate.

As the study of Taha *et al.* [140] showed that the aperture size of pipettes could strongly influence on fabricated nanostructure, we decided to use 100-nm-aperture pipettes in this section to compare with above results obtained from 150-nm-aperture pipettes. The same aqueous solution of 0.6 mM $HAuCl_4$ was used to create patterns on the native-oxide-layer-coated Si substrate with both contact mode and tapping mode as illustrated in Figure 5.42 and Figure 5.43, respectively. The scan speed values were varied as 1 µm/s, 2.5 µm/s, 5 µm/s and 10 µm/s for both operating modes. In comparison with the results of 150-nm-aperture pipettes, the patterns created by 100-nm-aperture pipettes were much better; however, the problems with the discontinuity and a variety of widths of the line pattern still existed. This phenomenon was similar to the problem with hand writing as discussed by Taha *et al.* [140]. In order to see the pattern size in more detail, samples of AFM measurements of the size of patterns obtained from Figure 5.42 are shown in Figure 5.44 and Figure 5.45 for a scan speed of 1 µm/s and 10 µm/s, respectively. The patterns were created by contact mode. Taking the height profile of the obtained data into consideration, the line width, height and continuity of the patterns were still variable and it was not possible to find any correlation.

The height and half-width of the patterns were measured and shown as a function of the scan speed in Figure 5.46 and Figure 5.47 for contact mode and tapping mode, respectively. Based on data from Figure 5.46, the height at each scan speed for contact mode was found to be 23.8 ± 24.2 nm, 22.2 ± 7.5 nm and 26.9 ± 10.2 nm for 1 µm/s, 2.5 µm/s and 10 µm/s, respectively. The half-width at each scan speed for contact mode was found to be 254.0 ± 75.0 nm, 238.7 ± 69.4 nm and 287.2 ± 96.5 nm, respectively. In the case of tapping mode as shown in Figure 5.47, the height at each scan speed was found to be 45.8 ± 30.0 nm, 58.3 ± 86.0 nm, 29.6 ± 28.7 nm and 26.9 ± 59.3 nm for 1 µm/s, 2.5 µm/s, 5 µm/s and 10 µm/s, respectively. The half-width at each scan speed for tapping mode was 383.0 ± 211.7 nm, 406.8 ± 174.7 nm, 403.6 ± 245.3 nm and 269.9 ± 147.7 nm for 1 µm/s, 2.5 µm/s, 5 µm/s and 10 µm/s, respectively. Taking these results into consideration, it was found that no dependence of both the height and the width on the scan speed was shown since the huge error bars and fluctuation of the average values were obtained.

One noticeable difference was that with the same scan speed the average sizes of the patterns obtained by contact mode FPN were smaller than that obtained by tapping mode FPN. In the case of contact mode, the maximum values of height and half-width obtained from a scan speed of 10 μm/s were approximately 26.9 ± 10.2 nm and 287.2 ± 96.5 nm, respectively. In the case of tapping mode, the maximum values of height and half-width obtained from a scan speed of 2.5 μm/s were around 58.3 ± 86.0 nm and 406.8 ± 174.7 nm, respectively. Considering the continuity, patterns created by tapping mode gave better continuity than contact mode.

Additionally, it was found difficult to achieve reproducible results and no evidence of deposition was found at all from the second attempt. Although, parameters such as scan speed, pipette aperture size and ink concentration (an aqueous solution of 0.6 mM $HAuCl_4$) could be consistent, the deposition of the ink was impossible to control. Other parameters such as temperature and humidity may also affect the writing; however, for the above experiments these parameters were not controlled. It was believed that the resolution of nanowriting was possible to improve with other ink-solvent systems. As proposed by Lewis *et al.* [138], the solvent nature could be a critical factor for ink flow, capillary osmosis, lubrication and wettability in the FPN technique, the study of solvents alone will be discussed in the following section.

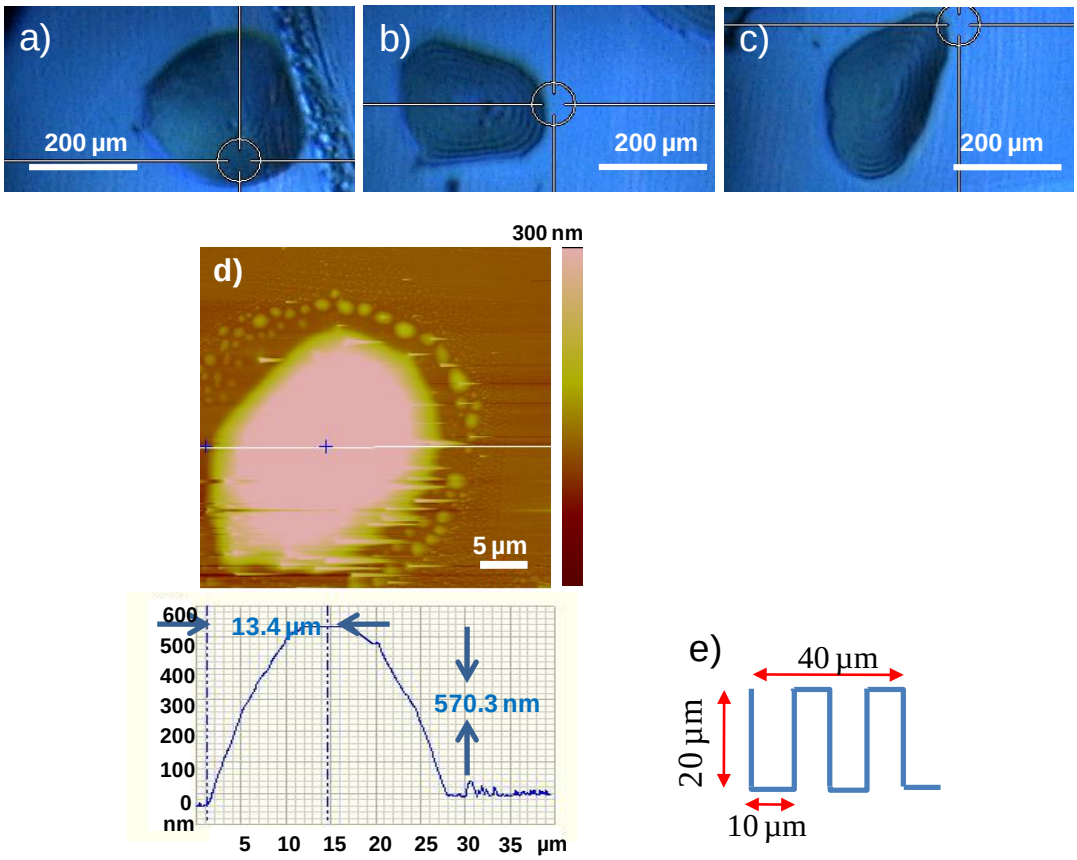


**Figure 5.39** a) - c) Optical microscope images and d) AFM image and corresponding height profile of the asymmetrical dot in a). Three sample dots of 20 mM $HAuCl_4$ in acetonitrile were written by the FPN technique on a native-oxide-layer-coated Si substrate using 150-nm-aperture micropipettes in contact mode with different scan speed values of a) 5 µm/s, b) 10 µm/s and c) 50 µm/s with a setpoint of 0.12. e) A sample design of a pre-written script used in these experiments. The script is started at the top left of the image and finished at the bottom right of the image.

| ***Parameter settings*** | | | | ***Results after patterning*** | |
|---|---|---|---|---|---|
| ***Scan speed (μm/s)*** | ***mode*** | ***Setpoint*** | ***Pre-written script*** | ***Optical microscope image*** | ***AFM image*** |
| 5 | Contact | 0.12 | 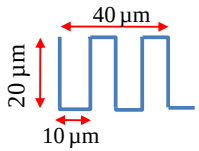 | 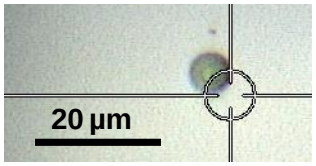 | **N/A** |
| 10 | Contact | 0.12 | 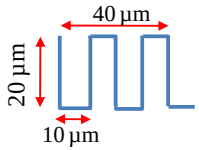 | 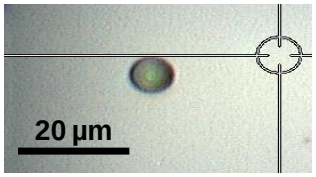 | 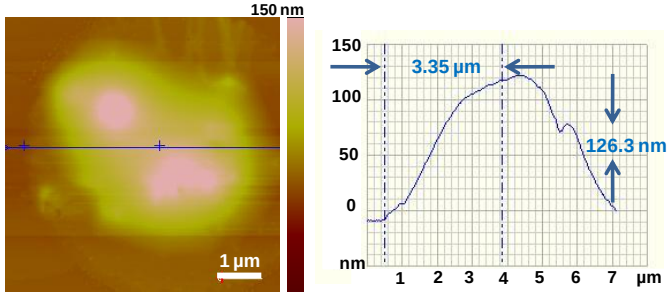 |

**Figure 5.40** Summary of various parameter settings during experiments along with optical microscope image and AFM image results of an aqueous solution of 0.6 mM $HAuCl_4$ created by FPN technique with 150-nm-aperture micropipettes in contact mode with different scan speed values on a native-oxide-layer-coated Si substrate.

| ***Parameter settings*** | | | | ***Results after patterning*** | |
|---|---|---|---|---|---|
| ***Scan speed (μm/s)*** | ***mode*** | ***Setpoint*** | ***Pre-written script*** | ***Optical microscope image*** | ***AFM image*** |
| 1 | Tapping | 20% | 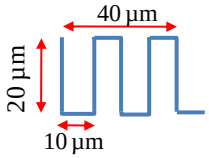  | 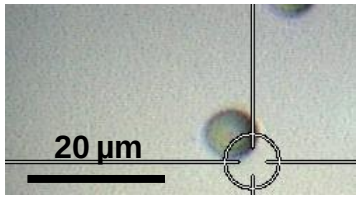  | 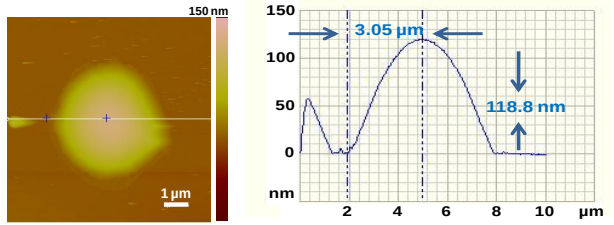  |
| 5 | Tapping | 20% | 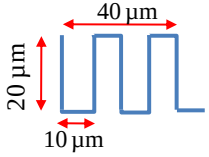  | 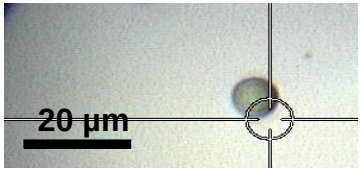  | 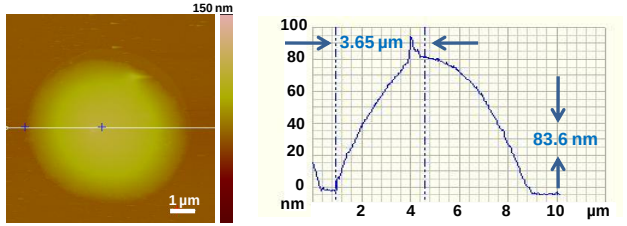  |
| 5 | Tapping | 20% |  | 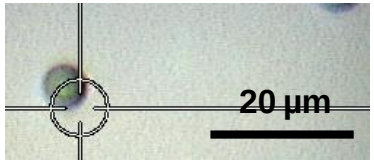  | 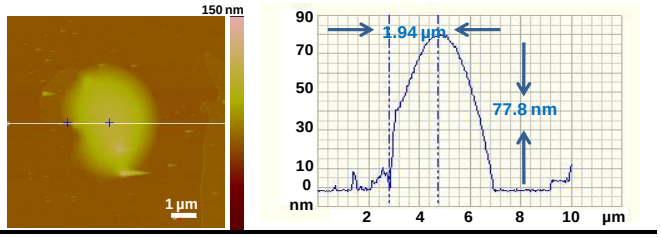  |

**Figure 5.41** Summary of various parameter settings during experiments along with optical microscope image and AFM image results of an aqueous solution of 0.6 mM $HAuCl_4$ created by FPN technique with 150-nm-aperture micropipettes in tapping mode with different scan speed values on a native-oxide-layer-coated Si substrate.

| ***Parameters settings*** | | | | ***Results after patterning*** | |
|---|---|---|---|---|---|
| ***Scan speed (μm/s)*** | ***mode*** | ***Setpoint*** | ***Pre-written script*** | ***Optical microscope image*** | ***AFM image*** |
| 1 | Contact | 0.12 | 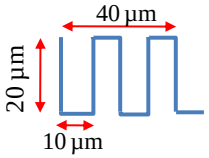 | 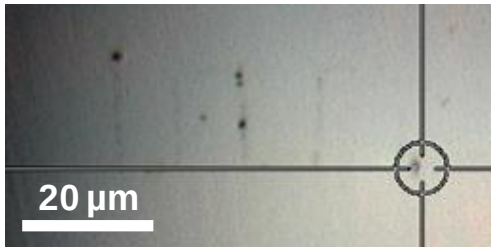 | 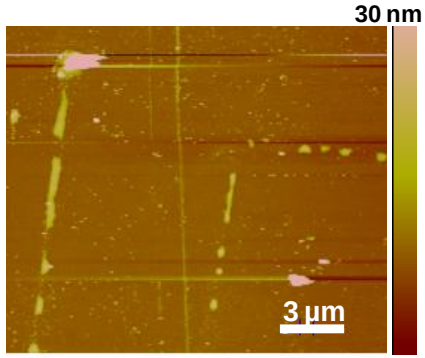 |
| 2.5 | Contact | 0.12 | 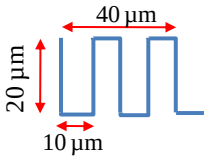 | 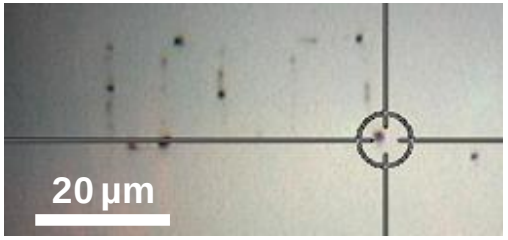 | 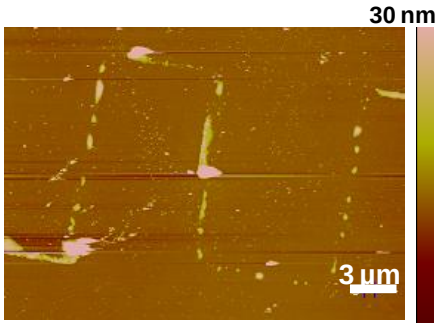 |

| ***Parameter settings*** | | | | ***Results after patterning*** | |
|---|---|---|---|---|---|
| ***Scan speed (μm/s)*** | ***mode*** | ***Setpoint*** | ***Pre-written script*** | ***Optical microscope image*** | ***AFM image*** |
| 5 | Contact | 0.12 | 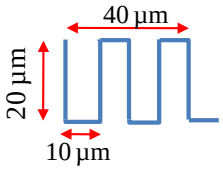 |  | 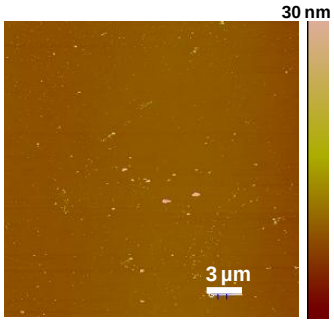 |
| 10 | Contact | 0.12 | 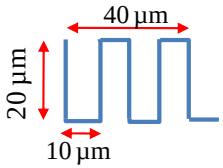 | 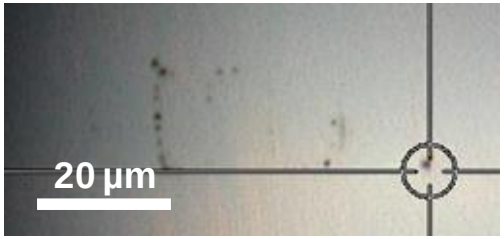 | 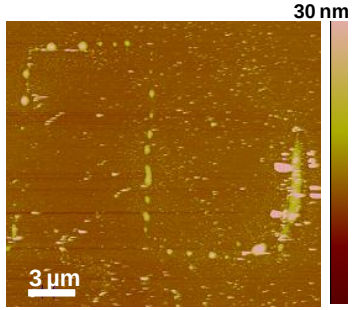 |

**Figure 5.42** Summary of various parameter settings during experiments along with optical microscope image and AFM image results of an aqueous solution of 0.6 mM $HAuCl_4$ created by FPN technique with 100-nm-aperture nanopipettes in contact mode with different scan speed values on a native-oxide-layer-coated Si substrate.

| ***Parameter settings*** | | | | ***Results after patterning*** | |
|---|---|---|---|---|---|
| ***Scan speed (μm/s)*** | ***mode*** | ***Setpoint*** | ***Pre-written script*** | ***Optical microscope image*** | ***AFM image*** |
| 1 | Tapping | 20% | 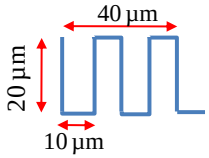 | 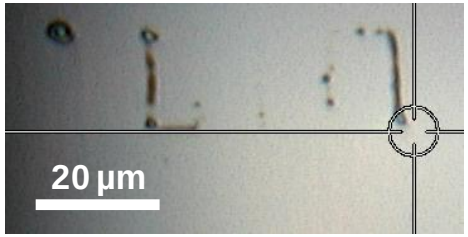 | 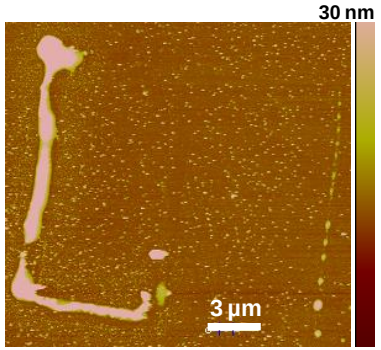 |
| 2.5 | Tapping | 20% | 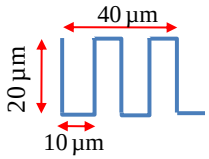 | 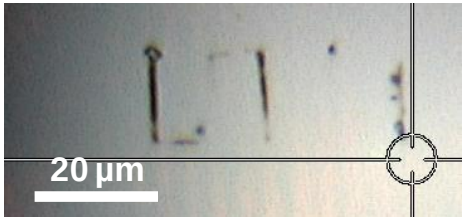 | 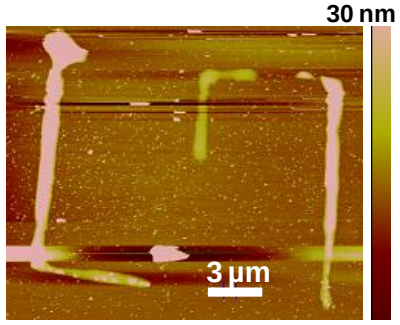 |

| ***Parameter settings*** | | | | ***Results after patterning*** | |
|---|---|---|---|---|---|
| ***Scan speed (μm/s)*** | ***mode*** | ***Setpoint*** | ***Pre-written script*** | ***Optical microscope image*** | ***AFM image*** |
| 5 | Tapping | 20% | 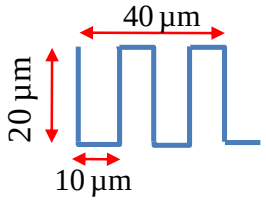 | 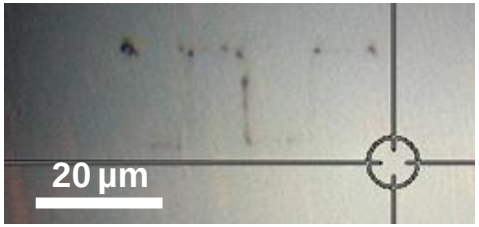 | 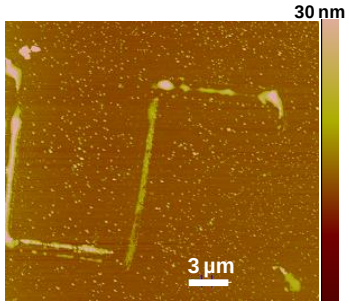 |
| 10 | Tapping | 20% | 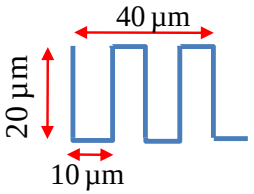 | 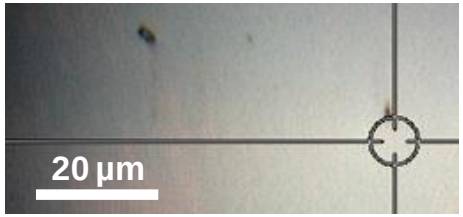 | 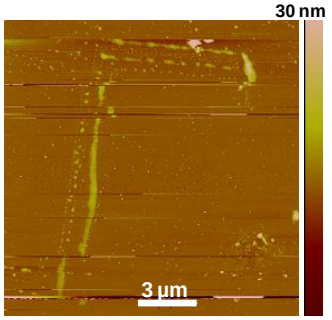 |

**Figure 5.43** Summary of various parameter settings during experiments as well as optical microscope image and AFM image results of an aqueous solution of 0.6 mM $HAuCl_4$ written by FPN technique with 100-nm-aperture nanopipettes in tapping mode with different scan speed values on a native-oxide-layer-coated Si substrate.

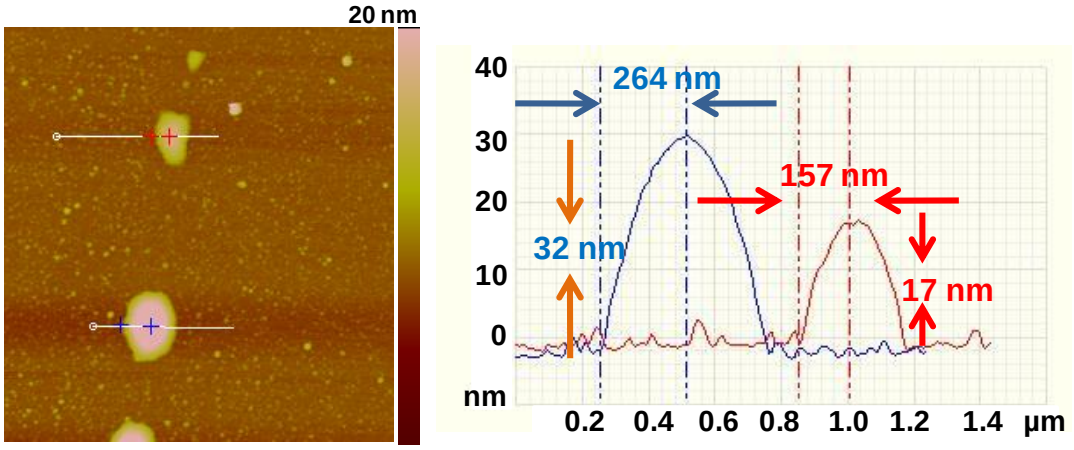


**Figure 5.44** Expanded AFM image from Figure 5.42 (row 1) and corresponding height profile of the pattern of an aqueous solution of 0.6 mM $HAuCl_4$ written by the FPN technique with 100-nm-aperture nanopipette in contact mode with a scan speed of 1 μm/s on a native-oxide-layer-coated Si substrate.

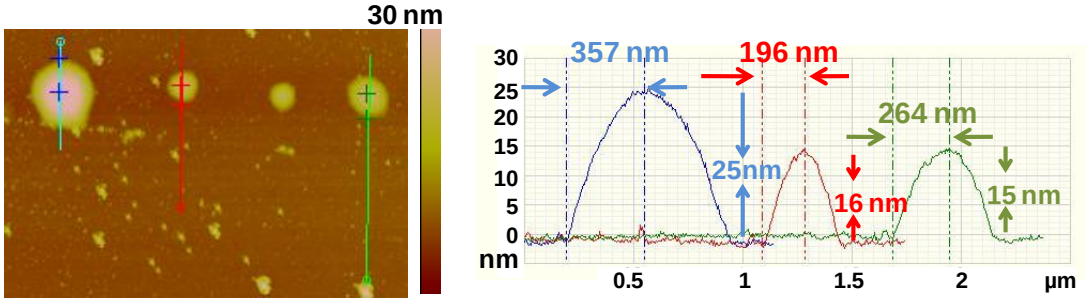


**Figure 5.45** Expanded AFM image from Figure 5.42 (row 4) and corresponding height profile of the pattern of an aqueous solution of 0.6 mM $HAuCl_4$ written by the FPN technique with 100-nm-aperture nanopipette in contact mode with a scan speed of 10 μm/s on a native-oxide-layer-coated Si substrate.

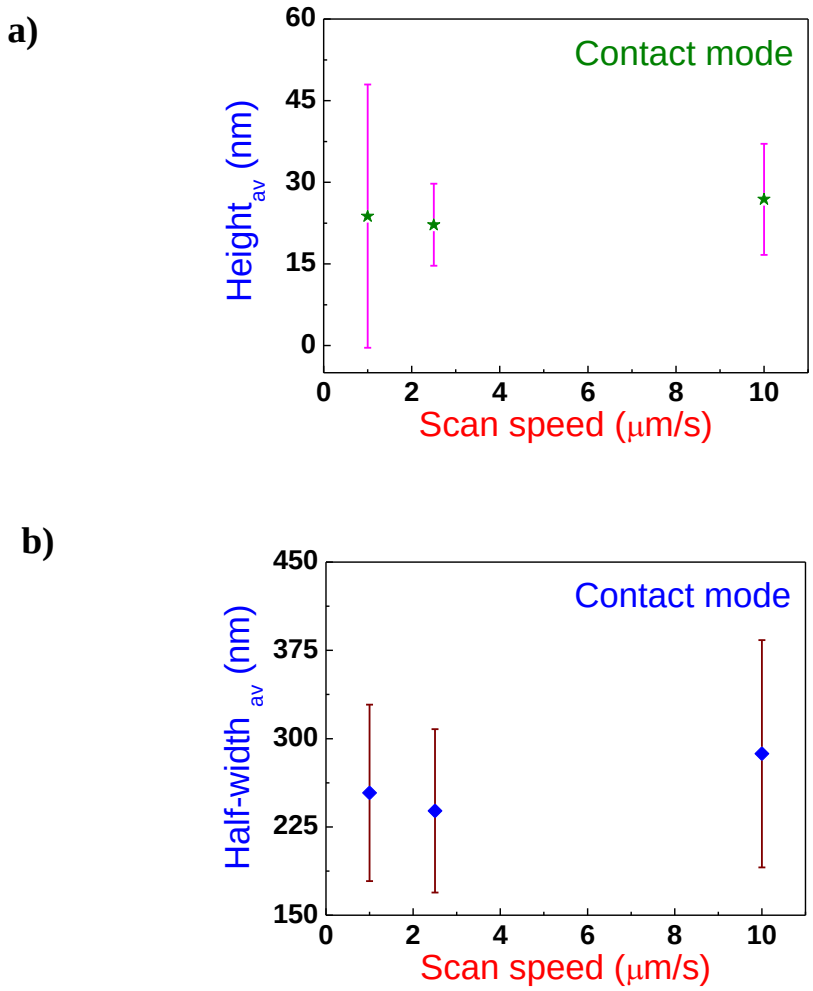


**Figure 5.46** Dependence of the structure height and half-width as a function of the scan speed based on over 30 point measurements along the patterns extracted from the data in Figure 5.42 using contact mode FPN technique. The error bars represent the standard deviation of the mean value of each pattern. a) The average height of patterns at different scan speeds. b) The average half-width of patterns at different scan speeds.

**a)**

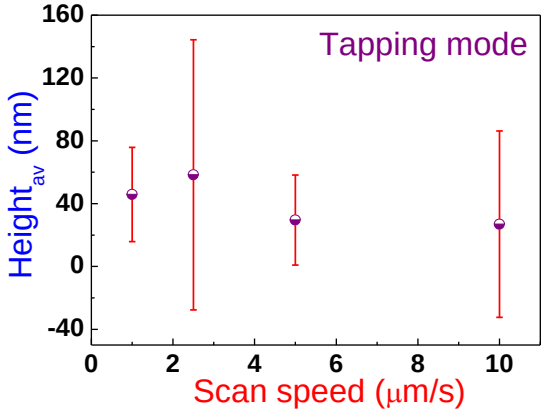


**b)**

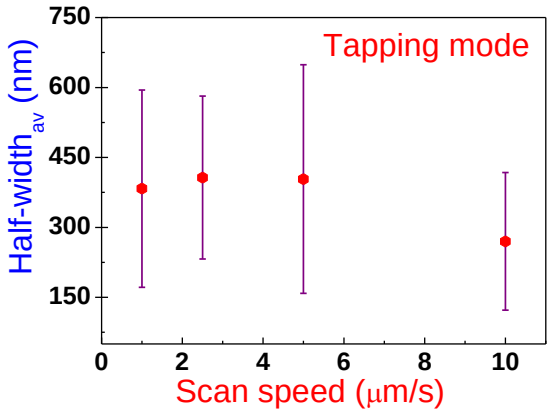


**Figure 5.47** Dependence of the structure height and half-width as a function of the scan speed based on over 30 point measurements along the patterns extracted from the data in Figure 5.43 using tapping mode FPN technique. The error bars represent the standard deviation of the mean value of each pattern. a) The average height of patterns at different scan speeds. b) The average half-width of patterns at different scan speeds.

### 5.3.2.2 Effect of the solvent alone on nanowriting

In order to understand the behaviour of solvents in the FPN technique, preliminary experiments with different solvents alone were conducted to investigate their effect on nanowriting with cantilever nanopipettes. The wide range of solvents which were used in this section are tabulated in Table 5.5. The principle for choosing these solvents was their common use in the laboratory as solvents or chemical

reagents. Moreover, their physical properties, for example, surface tension, viscosity, contact angle (wettability) [158] and boiling point were also taken into consideration as detailed in Table 5.5.

It was found that only 2 solvents, namely ethanol and toluene, were successfully deposited onto a native-oxide-layer-coated Si substrate. 100-nm apertures of cantilevered nanopipette were used in these investigations. In the case of ethanol alone as shown in Figure 5.48, a large amount of liquid was deposited on the substrate using contact mode with a scan speed of 50 µm/s (a left blob) and 1 µm/s (a right blob). In the case of toluene alone as shown in Figure 5.49, only a small amount of liquid was discontinuously deposited onto the substrate as a pattern using contact mode with a scan speed of 1 µm/s. However, it was found to be difficult to achieve repeatable results in the case of ethanol alone after the repeated experiments.

On the other hand, other remaining solvents including diethylene glycol, isopropanol, methanol, N-methyl-2-pyrrolidone (NMP), water and ethanol:Toluene (1:1) were not successfully deposited on the substrate. No evidence of deposition was found at all. In the case of water, it was expected to see a positive result because in the previous section the aqueous solution of $HAuCl_4$ was successfully deposited onto the substrate; however, it was still not achieved with writing water alone on the substrate. Although, various parameters such as scan speed and nanopipette aperture size could be consistent and selected, it was still difficult to achieve with a good result so far. Temperature and humidity were investigated during the experiments but were not controlled. These parameters could also play a critical role for the results. Considering the physical properties of all solvents, no conclusion could be drawn about which properties were the most effective for nanowriting.

**Table 5.5:** Physical quantities of solvents used in solvent alone testing with NFP experiments and the obtained results.

| ***Solvent*** | ***Viscosity[(a)] (mPa s) at 25 $^{o}$C*** | ***Surface tension[(a)] (mN/m) at 25 $^{o}$C*** | ***Boiling point[(a)] ($^{o}$C)*** | ***Contact angle[(b)] on $SiO_2$*** | ***Observed results after FPN*** |
|---|---|---|---|---|---|
| Ethanol | 1.074 | 21.97 | 78.2 | N/A | Big blobs |
| Toluene | 0.560 | 27.73 | 110.6 | 5.3 ± 0.4 | Discontinuous pattern |
| Diethylene glycol | 30.200 | 44.77 | 245.8 | N/A | Negative |
| Isopropanol (2-Propanol) | 2.038 | 20.93 | 82.3 | <10 | Negative |
| Methanol | 0.544 | 22.07 | 64.6 | <10 | Negative |
| N-Methyl-2-pyrrolidone (NMP) | 1.660 | 40.21 | 202 | N/A | Negative |
| Water | 0.890 | 71.99 | 100.0 | <10 | Negative |
| ethanol : Toluene (1:1) | N/A | N/A | N/A | N/A | Negative |

[(a)]The data were obtained from the CRC Handbook of Chemistry and Physics [126].

[(b)] The data were obtained from the report of Janssen *et al.* [158].

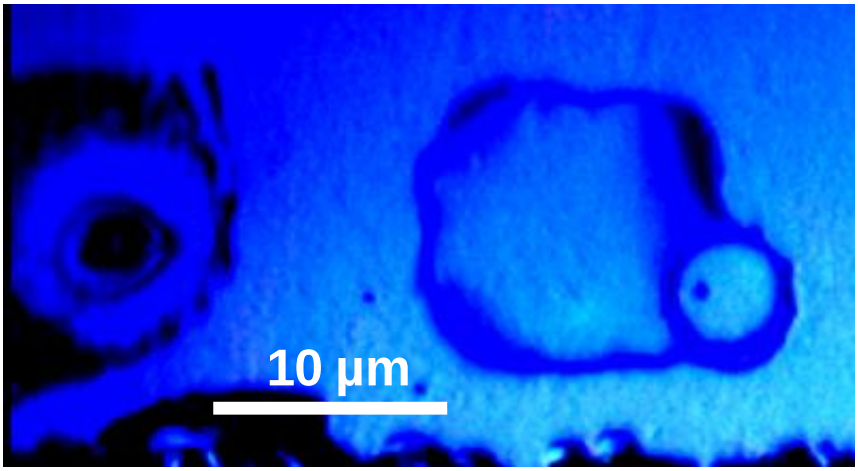


**Figure 5.48** Optical microscope image of 2 big blobs of ethanol alone created by FPN technique with 100-nm-aperture nanopipette in contact mode with a tip speed of 50 µm/s (a left blob) and 1 µm/s (a right blob) on a native-oxide-layer-coated Si substrate.

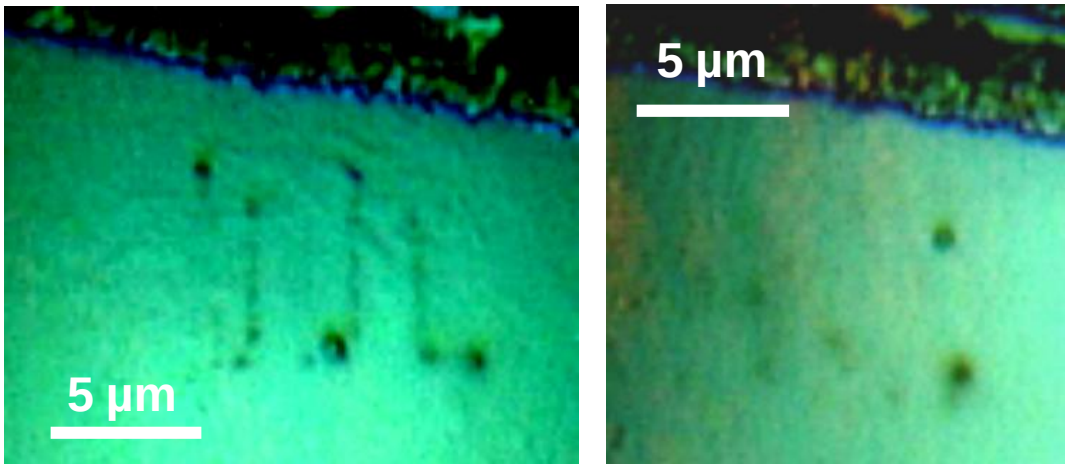


**Figure 5.49** Optical microscope images of line pattern of toluene alone created by FPN technique with 100-nm-aperture nanopipette in contact mode with a tip speed of 1 µm/s on a native-oxide-layer-coated Si substrate.

## 5.4 Conclusions

In the case of DPN, the study of a thermal annealing process to decompose the $HAuCl_4$ dots to leave Au (0) dots using a stereo microscope and SEM–EDS analysis for characterisation found the optimal annealing temperature to be above 300 $^{\circ}$C in Ar. This investigation was in good agreement with the studies of Murphy *et al.* who found the optimal temperature above 250 $^{\circ}$C [150] and Sung *et al.* who reported the annealing temperature above 300 $^{\circ}$C [29]. The study of the optimal time for scanning-coating (SC) of $HAuCl_4$ ink showed a non-uniform coating for all experiments from 1 min SC to 4 min SC. The SEM images showed that the amount of ink molecules coated on the tip surface increased with increasing the SC time (ranging from 1 min to 4 min SC). For the DPN experiments, it was found difficult to achieve the desired arrays of nanodots for all AFM tips used. Although, many parameters such as chamber temperature, relative humidity and deposition time were controlled, the precise control of the amount of ink diffusion to the substrate was impossible. It was found that the phenomenon of small particles surrounding the large central dots could be the result of a number of factors such as the faster diffusion rate of ink compared to the deposition rate, the large meniscus size causing a large number of inks being transport or the solvent matrix co-deposition with ink molecule. This observation was in agreement with the number of observed Au dots which was higher than the number of attempts for deposition.

In the case of the study of the size of nanodots, the height of nanodots showed a linear dependence on the SC time of AFM tips from 1 min to 4 min with a gradient of -1.3 ± 0.5 nm/min and the size decreased from 6.5 ± 2.3 nm to 1.2 ± 0.5 nm. The average half-width also showed a linear dependence on the SC time between 1 min and 3 min with the dot size decreased from 23.0 ± 4.5 nm to 19.6 ± 5.5 nm. Since the SEM images of before and after deposition did not show a significant depletion of the amount of ink, the calculation of the resonance frequency change was employed to confirm the efficiency of Au deposition. Comparison between the mass changes of the ink reduction from the AFM tips and the mass of deposited dots did not show a good agreement. It was found a much smaller mass of nanodots deposited on the substrates compared to the mass depletion from the AFM

tips. This could be the results of many factors. In addition, the mass changes of the ink depletion were in good agreement with the number of observed dots but were not in good agreement with the volume of deposited dots.

In the case of the FPN experiments, the study of the ink-solvent system showed that an aqueous solution of $HAuCl_4$ salt gave better results for Au nanowriting than the ink solution in acetonitrile. The possible reasons could be from the lower viscosity and lower surface tension of acetonitrile compared to those of water. A smaller size of a nanopipette with a 100 nm aperture was found to give better results than a bigger size of a micropipette with a 150 nm aperture. This was in good agreement with the study of Taha *et al.* [140] reporting the dependence of the fabricated nanostructures on the aperture size of pipettes. However, the problem with the discontinuity and a variety of widths of the line patterns still existed. No dependence of either the height or the width on the scan speed values ranging from 1 μm/s to 10 μm/s was found. Comparison between the contact mode FPN and the tapping mode FPN for nanowriting showed that with the same scan speed the average sizes of the patterns obtained by contact mode FPN were smaller than those obtained by tapping mode FPN. In the case of contact mode, the maximum values of height and half-width obtained from a scan speed of 10 μm/s were 26 ± 10 nm and 287 ± 96 nm, respectively. In the case of tapping mode, the maximum values of height and half-width obtained from a scan speed of 2.5 μm/s were 58 ± 86 nm and 407 ± 175 nm, respectively. The patterns created by tapping mode showed better continuity of the lines than contact mode. However, it was still found difficult to achieve repeatable results, although the parameters such as scan speed, pipette aperture size and ink concentrations were controlled. It was supposed that other factors, for example, temperature and humidity may play critical roles in the nanowriting. In the study of solvents alone, it was found that only 2 solvents, namely ethanol and toluene, were successfully deposited onto a native-oxide-layer-coated Si substrate. The deposition of big blobs was found in the case of ethanol alone and the discontinuous deposition in the case of toluene alone. Although, a number of parameters such as scan speed and pipette aperture size could be consistent, it was still difficult to achieve positive results with other solvents. It was

difficult to draw any conclusions about which properties were the most effective for nanowriting.

# Chapter 6 Conclusions and Outlook

In this thesis, the possibility of using scanning probe microscopy (SPM) nanolithography to controllably deposit nanoparticles on patterned Si substrates with high positional control has been explored. These nanoparticles have a range of interesting properties and have been characterised by electron microscopy and scanning probe microscopy. The influences of different deposition parameters on the properties of the resulting nanoparticles were studied.

AFM-based LON in contact mode was used to oxidise substrates under the apex of an AFM tip biased with a negative voltage with respect to the sample. A number of parameters that can influence the AFM-based LON process were investigated on either a native-oxide-layer-coated Si substrate or a Mo substrate. It was found that the height and width of the oxide patterns fabricated on the native-oxide-layer-coated *n*-type Si (100) substrate strongly depended on the applied voltage and scan speed. The height and width grew linearly as a function of applied tip voltage. The dependence of the height and the width on the scan speed was found. For fast scan speeds, oxidation occurred in the lateral dimension due to ionic diffusion until it reached a limit related to the water meniscus diameter which was determined by the humidity and the applied electric field. Subsequently, the oxidation was able to grow only in the vertical direction with a slower scan speed. Consequently, after the width was saturated, the oxide height linearly depended on the scan speed.

The TUNA technique provided the ability to measure ultralow currents flowing through the sample to the tip during the oxidation process. For our experiments, the threshold voltage was found to be -4.0 ± 1.6 V applied to the tip when fabricating geometric patterns as well as 2.9 ± 1.6 V and 2.8 ± 2.2 V applied to the substrate for nanodot fabrication. The nanodot fabrication showed a clear dependence on the applied voltage, type of sample, relative humidity and ramping time but did not show a clear dependence on type of AFM tip. The height and width of the nanodots generated on the native-oxide-layer-coated Si wafer were also seen

to linearly increase with increasing bias voltage. With a fixed hydrophobic AFM tip, the height and width of oxide dots on the native hydrophilic $SiO_2$ surface are less than those on the hydrophobic Mo surface. The fabricated oxide dots on the Mo surface increased in size with increasing relative humidity. It was found that the height increased by a factor of 2.3 and the width increased by a factor of 1.48 when the humidity was increased about 23 % from 43 ± 2 % to 66 ± 2 %. The effect of ramping time was investigated on the Mo surface. The results showed that the oxidation efficiency decreased with increasing ramping time. The oxidation process on the Mo surface depends on the ramping time but only for short ramping times.

Dip-pen nanolithography (DPN) was used to study a direct deposition strategy for gold (Au) nanodot fabrication on a native-oxide-layer-coated Si substrate. In this process, hydrogen tetrachloroaurate ($HAuCl_4$) molecules were deposited onto the substrate via a molecular diffusion process, in the absence of electrochemical reactions. This approach allowed for the generation of Au dots on the $SiO_2$ substrate without the need for surface modification or additional electrode structures. A thermal annealing process was used to decompose the generated $HAuCl_4$ molecular dots to leave Au (0) metal dots. A stereomicroscope has been used for preliminary observation of different steps of Au deposition treatments. SEM energy-dispersive X-ray spectroscopy (EDS) has provided information about the elemental content of deposited particles for different annealing temperatures. It was confirmed from the SEM-EDS analysis that there was a strong temperature dependence on the $HAuCl_4$ reduction. The $HAuCl_4$ was reduced to Au metal at annealing temperatures above 300 $^{\circ}$C. The study of the optimum time for scanning-coating (SC) AFM tips with $HAuCl_4$ ink was performed. It was found that the amount of ink molecules coated on the tip surface generally increased with increasing the SC time (ranging from 1 min to 4 min SC). The dependence of the size of the Au dots obtained with different SC times of AFM tips was studied. A scanning electron microscope (SEM) was used to characterise the SC AFM tips both before and after the DPN process. For the DPN experiments, it was found difficult to achieve the desired arrays of nanodots for all AFM tips used. It was found that the phenomenon of small particles surrounding the large central dots could be the result

of a number of factors. This observation was in agreement with the number of observed Au dots which was higher than the number of attempts for deposition. The height of nanodots showed a linear dependence on the SC time of AFM tips from 1 min to 4 min with the size decreased from 6.5 ± 2.3 nm to 1.2 ± 0.5 nm. The average half-width also showed a linear dependence on the SC time between 1 min and 3 min with the dot size decreased from 23.0 ± 4.5 nm to 19.6 ± 5.5 nm. It was found a much smaller mass of nanodots deposited on the substrates compared to the mass depletion from the AFM tips. In addition, the mass changes of the ink depletion were in good agreement with the number of observed dots but were not in good agreement with the volume of deposited dots.

Fountain-pen nanolithography (FPN) has also been used to study nanowriting of $HAuCl_4$ salt and a variety of solvents on a native-oxide-layer-coated Si surface. In this technique, a nanopipette was mounted within an AFM to deliver appropriate solutions to the silica substrate. It was found that an aqueous Au salt solution was the most suitable ink for depositing gold using the FPN technique. A nanopipette with a 100 nm aperture was found to give better results than a micropipette with a 150 nm aperture. No dependence of either the height or the width on the scan speed was found. With the same scan speed the average sizes of the patterns obtained by contact mode FPN were smaller than those obtained by tapping mode FPN. In the case of contact mode, the maximum values of height and half-width obtained from a scan speed of 10 μm/s were 26 ± 10 nm and 287 ± 96 nm, respectively. In the case of tapping mode, the maximum values of height and half-width obtained from a scan speed of 2.5 μm/s were 58 ± 86 nm and 407 ± 175 nm, respectively. The patterns created by tapping mode showed better continuity than contact mode. In the case of solvents alone, it was found that only 2 solvents, namely ethanol and toluene, were successfully deposited onto a native-oxide-layer-coated Si substrate. No conclusion could be drawn about which properties were the most effective for nanowriting.

## 6.1 Outlook

For the DPN experiment in Chapter 5, in order to achieve the nanofabrication requirement with high positional control, a more systematic study of the parameters such as temperature, humidity and deposition time is necessary. Moreover, better control of the conditions during deposition such as higher tip temperatures and longer deposition times are considered to be essential factors that are directly related to the controlled deposition of ink molecules.

For the FPN experiment, a greater variety of solvents still needs to be tested in order to get a suitable solvent for FPN deposition. Control of the conditions such as temperature and humidity during the nanowriting may be necessary in order to achieve a better resolution.

# References


1. Feynman, R.P., *There's plenty of room at the bottom [data storage]*. Microelectromechanical Systems, 1992. **1**(1): p. 60-66.

2. Binnig, G., et al., *Surface studies by scanning tunneling microscopy.* Physical Review Letters, 1982. **49**(1): p. 57-61.

3. Binnig, G., C.F. Quate, and C. Gerber, *Atomic force microscope.* Physical Review Letters, 1986. **56**(9): p. 930.

4. *Nanoscience and Nanotechnologies: opportunities and uncertenties*. 2004, The Royal Society & The Royal Academy of Engineering.

5. Gates, B.D., et al., *New approaches to nanofabrication: molding, printing, and other techniques.* Chemical Reviews, 2005. **105**(4): p. 1171-1196.

6. Quate, C.F., *Scanning probes as a lithography tool for nanostructures.* Surface Science, 1997. **386**(1-3): p. 259-264.

7. Tseng, A.A., A. Notargiacomo, and T.P. Chen, *Nanofabrication by scanning probe microscope lithography: A review.* Journal of Vacuum Science & Technology B, 2005. **23**(3): p. 877-894.

8. Wiesendanger, R., *Scanning probe microscopy and spectroscopy: methods and applications*. 1994, Cambridge: Cambridge University Press. 637.

9. Bonnell, D., *Scanning probe microscopy and spectroscopy: theory, techniques, and applications*. 2nd ed, ed. D. Bonnell. 2001, New York: John Wiley & Sons, Inc. 493.

10. *Basic SPM Training Course*. 2000, Digital Instruments Veeco, Inc.

11. Moore, A.M. and P.S. Weiss, *Functional and spectroscopic measurements with scanning tunneling microscopy.* Annual review of analytical chemistry (Palo Alto, Calif.), 2008. **1**: p. 857-882.

12. Tersoff, J. and D.R. Hamann, *Theory of the scanning tunneling microscope.* Physical Review B, 1985. **31**(2): p. 805-813.

13. Bowen, W.R. and N. Hilal, *Atomic force microscopy in process engineering: Introduction to AFM for improved process and products*. 1st ed. 2009: Elsevier Ltd. 300.

14. Babicz, S. and J. Smulko, *Enhancing capabilities of atomic force microscopy by tip motion harmonics analysis*, in *XI National Conference on Electronics*. 2012: Eastern Darłówko. p. 1-8.

15. Pishkenari, H.N., M. Behzad, and A. Meghdari, *Nonlinear dynamic analysis of atomic force microscopy under deterministic and random excitation.* Chaos, Solitons & Fractals, 2008. **37**(3): p. 748-762.

16. Eaton, P. and P. West, *Atomic force microscopy*. 1st ed. 2010, Oxford: Oxford University Press Inc., New York. 248.

17. Schaffer, T.E., et al., *Studies of vibrating atomic force microscope cantilevers in liquid.* Journal of Applied Physics, 1996. **80**(7): p. 3622-3627.

18. De Wolf, P., E. Brazel, and A. Erickson, *Electrical characterization of semiconductor materials and devices using scanning probe microscopy.* Materials Science in Semiconductor Processing, 2001. **4**(1-3): p. 71-76.

19. *Application Modules: NanoScope Software v7*. 2007, Veeco Instruments Inc.

20. Egerton, R.F., *Physical principles of plectron microscopy: an Introduction to TEM, SEM, and AEM*. 2005, New York: Springer Science+Business Media, Inc.

21. Reimer, L., *Scanning electron microscopy: physics of image formation and microanalysis*. Measurement Science and Technology. Vol. 11. 2000. 1826.

22. *Budget Sensors: Technical information and dimensions for budgetSensor AFM holder, cantilever and tip*. [Online] 2012 [cited 2012 16 July]; Available from: http://www.tedpella.com/probes_html/holderchip.jpg.

23. *Bruker AFM probes*. [Online] 2012 [cited 2012 16 July]; Available from: http://www.brukerafmprobes.com/Product.aspx?ProductID=3388.

24. *Budget Sensors AFM Probes: Tap 300 Al-G*. [Online] 2012 [cited 2012 16 July]; Available from: http://www.tedpella.com/probes_html/budgetsensors-1.htm.

25. *NT-MDT Co: NSG01-DLC*. [Online] 2012 [cited 2012 16 July]; Available from: http://www.ntmdt-tips.com/text/about.

26. *Bruker AFM Probes*. [Online] 2012 [cited 2012 16 July ]; Available from: http://www.brukerafmprobes.com/Product.aspx?ProductID=3309.

27. *Budget Sensors AFM Probes*. [Online] 2012 [cited 2012 16 July]; Available from: http://www.tedpella.com/probes_html/budgetsensors-1.htm#TAP300GD.

28. *NT-MDT Tips*. [Online] 2012 [cited 2012 16 July]; Available from: http://www.ntmdttips.com/usa/fmg01-co-15.html.

29. Sung, M.G., et al., *Uniform Patterning of Sub-50-nm-Scale Au Nanostructures on Insulating Solid Substrate via Dip-Pen Nanolithography.* Langmuir, 2009. **26**(3): p. 1507-1511.

30. Shojiro, M., et al., *Nanofabrication by mechanical and electrical processes using electrically conductive diamond tip.* Journal of Vacuum Science & Technology B: Microelectronics and Nanometer Structures, 2008. **26**(5): p. 1660-1665.

31. *diDimension V:Instruction Manual*. 2006, Veeco Instrument Inc. p. 368.

32. Kabir, M.S., et al., *Fabrication of individual vertically aligned carbon nanofibres on metal substrates from prefabricated catalyst dots.* Nanotechnology, 2006. **17**(3): p. 790.

33. Dagata, J.A., et al., *Modification of hydrogen-passivated silicon by a scanning tunneling microscope operating in air.* Applied Physics Letters, 1990. **56**(20): p. 2001-2003.

34. Nagahara, L.A., T. Thundat, and S.M. Lindsay, *Nanolithography on semiconductor surfaces under an etching solution.* Applied Physics Letters, 1990. **57**(3): p. 270-272.

35. Fontaine, P.A., E. Dubois, and D. Stievenard, *Characterization of scanning tunneling microscopy and atomic force microscopy-based techniques for nanolithography on hydrogen-passivated silicon.* Journal of Applied Physics, 1998. **84**(4): p. 1776-1781.

36. Snow, E.S., P.M. Campbell, and P.J. McMarr, *Fabrication of silicon nanostructures with a scanning tunneling microscope.* Applied Physics Letters, 1993. **63**(6): p. 749-751.

37. Lyding, J.W., et al., *Nanometer scale patterning and oxidation of silicon surfaces with an ultrahigh vacuum scanning tunneling microscope.* Journal of Vacuum Science & Technology B: Microelectronics and Nanometer Structures, 1994. **12**(6): p. 3735-3740.

38. Thundat, T., et al., *Modification of tantalum surfaces by scanning tunneling microscopy in an electrochemical cell.* Journal of Vacuum Science & Technology A: Vacuum, Surfaces, and Films, 1990. **8**(4): p. 3537-3541.

39. Song, H.J., et al., *25 nm chromium oxide lines by scanning tunneling lithography in air.* Journal of Vacuum Science & Technology B: Microelectronics and Nanometer Structures, 1994. **12**(6): p. 3720-3724.

40. Sugimura, H., et al., *Nanofabrication of titanium surface by tip-induced anodization in scanning tunneling microscopy.* Japanese Journal of Applied Physics, 1993. **32**: p. L553.

41. Sugimura, H., et al., *Scanning tunneling microscope tip-Induced anodization for nanofabrication of titanium.* The Journal of Physical Chemistry, 1994. **98**(16): p. 4352-4357.

42. Day, H.C. and D.R. Allee, *Selective area oxidation of silicon with a scanning force microscope.* Applied Physics Letters, 1993. **62**(21): p. 2691-2693.

43. Campbell, P.M., E.S. Snow, and P.J. McMarr, *AFM-based fabrication of Si nanostructures.* Physica B: Condensed Matter, 1996. **227**(1-4): p. 315-317.

44. Yasutake, M., Y. Ejiri, and T. Hattori, *Modification of silicon surface using atomic force microscope with conducting probe.* Japanese Journal of Applied Physics, 1993. **32**: p. L1021-L1023.

45. Dagata, J.A., et al., *Understanding scanned probe oxidation of silicon.* Applied Physics Letters, 1998. **73**(2): p. 271-273.

46. Dawen, W., T. Liming, and K.L. Wang, *Nanometer-structure writing on Si(100) surfaces using a non-contact-mode atomic force microscope.* Applied Physics Letters, 1994. **65**(11): p. 1415-1417.

47. Martinez, R.V. and R. Garcia, *Nanolithography based on the formation and manipulation of nanometer-size organic liquid menisci.* Nano Letters, 2005. **5**(6): p. 1161-1164.

48. Kuramochi, H., K. Ando, and H. Yokoyama, *Effect of humidity on nano-oxidation of p-Si(001) surface.* Surface Science, 2003. **542**(1-2): p. 56-63.

49. Campbell, P.M., E.S. Snow, and P.J. McMarr, *Fabrication of nanometer-scale side-gated silicon field effect transistors with an atomic force microscope.* Applied Physics Letters, 1995. **66**(11): p. 1388-1390.

50. Snow, E.S., et al., *Si nanostructures fabricated by anodic oxidation with an atomic force microscope and etching with an electron cyclotron resonance source.* Applied Physics Letters, 1995. **66**(14): p. 1729-1731.

51. Snow, E.S. and P.M. Campbell, *Fabrication of Si nanostructures with an atomic force microscope.* Applied Physics Letters, 1994. **64**(15): p. 1932-1934.

52. Snow, E.S., et al., *Ultrathin PtSi layers patterned by scanned probe lithography.* Applied Physics Letters, 2001. **79**(8): p. 1109-1111.

53. Snow, E.S., G.G. Jernigan, and P.M. Campbell, *The kinetics and mechanism of scanned probe oxidation of Si.* Applied Physics Letters, 2000. **76**(13): p. 1782-1784.

54. Kuramochi, H., et al., *Faradaic current detection during anodic oxidation of the H-passivated p-Si(001) surface with controlled relative humidity.* Nanotechnology, 2004. **15**(3): p. 297.

55. Snow, E.S., D. Park, and P.M. Campbell, *Single-atom point contact devices fabricated with an atomic force microscope.* Applied Physics Letters, 1996. **69**(2): p. 269-271.

56. Dawen, W., et al., *Nanofabrication of thin chromium film deposited on Si(100) surfaces by tip induced anodization in atomic force microscopy.* Applied Physics Letters, 1995. **67**(9): p. 1295-1297.

57. Snow, E.S., et al., *A metal/oxide tunneling transistor.* Applied Physics Letters, 1998. **72**(23): p. 3071-3073.

58. Bouchiat, V., et al., *Josephson junctions and superconducting quantum interference devices made by local oxidation of niobium ultrathin films.* Applied Physics Letters, 2001. **79**(1): p. 123-125.

59. Thomas, S., et al., *Current-induced local oxidation of metal films: mechanism and quantum-size effects.* Applied Physics Letters, 1998. **73**(15): p. 2173-2175.

60. Kazuhiko, M., et al., *Room-temperature single-electron memory made by pulse-mode atomic force microscopy nano oxidation process on atomically flat alpha-alumina substrate.* Applied Physics Letters, 2000. **76**(2): p. 239-241.

61. Lopour, F., et al., *Application of AFM in microscopy and fabrication of micro/nanostructures.* Surface and Interface Analysis, 2002. **34**(1): p. 352-355.

62. Vullers, R.J.M., et al., *Field induced local oxidation of Ti and Ti/Au structures by an atomic force microscope with diamond coated tips.* Journal of Vacuum Science & Technology B: Microelectronics and Nanometer Structures, 1999. **17**(6): p. 2417-2422.

63. Bloeß, H., G. Staikov, and J.W. Schultze, *AFM induced formation of $SiO_2$ structures in the electrochemical nanocell.* Electrochimica Acta, 2001. **47**(1): p. 335-344.

64. Dagata, J.A., et al., *Role of space charge in scanned probe oxidation.* Journal of Applied Physics, 1998. **84**(12): p. 6891-6900.

65. Gordon, A.E., et al., *Mechanisms of surface anodization produced by scanning probe microscopes.* Journal of Vacuum Science & Technology B: Microelectronics and Nanometer Structures, 1995. **13**(6): p. 2805-2808.

66. Sugimura, H. and N. Nakagiri, *Chemical approach to nanofabrication: modifications of silicon surfaces patterned by scanning probe anodization.* Japanese Journal of Applied Physics, 1995. **34**(Part 1, No. 6B): p. 3406-3411.

67. Avouris, P., T. Hertel, and R. Martel, *Atomic force microscope tip-induced local oxidation of silicon: kinetics, mechanism, and nanofabrication.* Applied Physics Letters, 1997. **71**(2): p. 285-287.

68. Gwo, S., *Scanning probe oxidation of Si3N4 masks for nanoscale lithography, micromachining, and selective epitaxial growth on silicon.* Journal of Physics and Chemistry of Solids, 2001. **62**(9-10): p. 1673-1687.

69. Mo, Y., et al., *Fabrication and adhesion measurement of a nanotextured surface with ionic liquid monolayers.* The Journal of Physical Chemistry C, 2011. **115**(20): p. 10125-10130.

70. Jungblut, H., D. Wille, and H.J. Lewerenz, *Nano-oxidation of H-terminated p-Si(100): Influence of the humidity on growth and surface properties of oxide islands.* Applied Physics Letters, 2001. **78**(2): p. 168-170.

71. Held, R., et al., *Nanolithography by local anodic oxidation of metal films using an atomic force microscope.* Physica E: Low-dimensional Systems and Nanostructures, 1998. **2**(1-4): p. 748-752.

72. Farkas, N., et al., *Nanoscale oxidation of zirconium surfaces: kinetics and mechanisms.* Journal of Vacuum Science & Technology A: Vacuum, Surfaces, and Films, 2003. **21**(4): p. 1188-1193.

73. Tseng, A.A. and A. Notargiacomo, *Nanoscale fabrication by nonconventional approaches.* Journal of Nanoscience and Nanotechnology, 2005. **5**(5): p. 683-702.

74. Perez-Murano, F., et al., *Nanometer-scale oxidation of Si(100) surfaces by tapping mode atomic force microscopy.* Journal of Applied Physics, 1995. **78**(11): p. 6797-6801.

75. Ma, Y.R., et al., *Tip-induced local anodic oxidation on the native $SiO_2$ layer of Si(111) using an atomic force microscope.* Physical Review B, 2001. **64**(19): p. 195324.

76. Tello, M. and R. Garcia, *Nano-oxidation of silicon surfaces: Comparison of noncontact and contact atomic-force microscopy methods.* Applied Physics Letters, 2001. **79**(3): p. 424-426.

77. Avouris, P., et al., *AFM-tip-induced and current-induced local oxidation of silicon and metals.* Applied Physics A: Materials Science & Processing, 1998. **66**(0): p. S659-S667.

78. Fang, T.-H., T.H. Wang, and K.-T. Wu, *Local oxidation of titanium films by non-contact atomic force microscopy.* Microelectronic Engineering, 2008. **85**(7): p. 1616-1623.

79. Kim, J.O., et al., *Effect of contact potential barrier of organic resists on atomic force microscope anodization lithography.* Colloids and Surfaces A: Physicochemical and Engineering Aspects, 2005. **257-258**(0): p. 251-254.

80. Rolandi, M., C.F. Quate, and H. Dai, *A New Scanning Probe Lithography Scheme with a Novel Metal Resist.* Advanced Materials, 2002. **14**(3): p. 191-194.

81. *Physical Constants of Inorganic Compounds*, in *CRC Handbook of Chemistry and Physics, 89th Edition (Internet Version 2009)*, D.R. Lide, Editor. 2009, CRC press/Taylor and Francis, Boca Raton, FL.

82. Kazuya, G., T. Hidekazu, and K. Tomoji, *Fabrication of $(Fe,Mn)_3O_4$ ferromagnetic oxide nanostructure using molybdenum nanomask atomic force microscope lithography.* Journal of Applied Physics, 2009. **105**(6): p. 064301.

83. Pellegrino, L., et al., *$(Fe,Mn)_3O_4$ Nanochannels fabricated by AFM local-oxidation nanolithography using Mo/poly(methyl methacrylate) nanomasks.* Advanced Materials, 2006. **18**(23): p. 3099-3104.

84. Hattori, T., et al., *Fabrication of nanometer-scale structures using atomic force microscope with conducting probe.* Journal of Vacuum Science & Technology A: Vacuum, Surfaces, and Films, 1994. **12**(4): p. 2586-2590.

85. Perez-Murano, F., et al., *Voltage modulation scanned probe oxidation.* Applied Physics Letters, 1999. **75**(2): p. 199-201.

86. Park, C.H., S. Bae, and H. Lee, *Nano-oxidation of Si using ac modulation in atomic force microscope lithography.* Colloids and Surfaces A: Physicochemical and Engineering Aspects, 2006. **284-285**(0): p. 552-555.

87. Stievenard, D., P.A. Fontaine, and E. Dubois, *Nanooxidation using a scanning probe microscope: an analytical model based on field induced oxidation.* Applied Physics Letters, 1997. **70**(24): p. 3272-3274.

88. Nemes-Incze, P., et al., *Anomalies in thickness measurements of graphene and few layer graphite crystals by tapping mode atomic force microscopy.* Carbon, 2008. **46**(11): p. 1435-1442.

89. Mechler, ร.d., et al., *Anomalies in nanostructure size measurements by AFM.* Physical Review B, 2005. **72**(12): p. 125407.

90. Calleja, M., M. Tello, and R. Garcia, *Size determination of field-induced water menisci in noncontact atomic force microscopy.* Journal of Applied Physics, 2002. **92**(9): p. 5539-5542.

91. Cabrera, N. and N.F. Mott, *Theory of the oxidation of metals.* Reports on Progress in Physics, 1949. **12**(1): p. 163.

92. Djurkovic, S., et al., *Effects of the electric field shape on nano-scale oxidation.* Surface Science, 2007. **601**(23): p. 5340-5358.

93. Kremmer, S., et al., *Modification and characterization of thin silicon gate oxides using conducting atomic force microscopy.* Materials Science and Engineering: B, 2003. **102**(1-3): p. 88-93.

94. Takemura, Y., et al., *Applied voltage dependence of nano-oxidation of ferromagnetic thin films using atomic force microscope.* Journal of Applied Physics, 2003. **93**(10): p. 7346-7348.

95. Lin, J.F., C.K. Tai, and S.L. Lin, *Theoretical and experimental studies for nano-oxidation of silicon wafer by ac atomic force microscopy.* Journal of Applied Physics, 2006. **99**(5): p. 054312-11.

96. Vladimir, C. and S. Jan, *The influence of sample conductivity on local anodic oxidation by the tip of atomic force microscope.* Journal of Applied Physics, 2007. **102**(7): p. 074315.

97. Schenk, M., M. Futing, and R. Reichelt, *Direct visualization of the dynamic behavior of a water meniscus by scanning electron microscopy.* Journal of Applied Physics, 1998. **84**(9): p. 4880-4884.

98. Grosse, I. and K. Estel, *Thin surfactant layers at the solid interface.* Colloid & Polymer Science, 2000. **278**(10): p. 1000-1006.

99. Kaibara, Y., et al., *Control wettability of the hydrogen-terminated diamond surface and the oxidized diamond surface using an atomic force microscope.* Diamond and Related Materials, 2003. **12**(3-7): p. 560-564.

100. Cramer, T., F. Zerbetto, and R. Garcia, *Molecular mechanism of water bridge buildup: field-induced formation of nanoscale menisci.* Langmuir, 2008. **24**(12): p. 6116-6120.

101. Yasushi, T., et al., *Measurement of faradaic current during AFM local oxidation of magnetic metal thin films.* Journal of Physics: Conference Series, 2007. **61**(1): p. 1147.

102. Shimada, Y., et al., *Measurement of reaction current during atomic force microscope local oxidation of conductive surfaces capped with insulating layers.* Japanese Journal of Applied Physics, 2008. **47**(1): p. 768-770.

103. Piner, R.D., et al., *"Dip-Pen" Nanolithography.* Science, 1999. **283**(5402): p. 661-663.

104. Zhang, H., Z. Li, and C.A. Mirkin, *Dip-pen nanolithography-based methodology for preparing arrays of nanostructures functionalized with oligonucleotides.* Advanced Materials, 2002. **14**(20): p. 1472-1474.

105. Zhou, H., et al., *Direct patterning of rhodamine 6G molecules on mica by dip-pen nanolithography.* Applied Surface Science, 2004. **236**(1-4): p. 18-24.

106. Hong, S. and C.A. Mirkin, *A nanoplotter with both parallel and serial writing capabilities.* Science, 2000. **288**(5472): p. 1808-1811.

107. Demers, L.M., et al., *Direct patterning of modified oligonucleotides on metals and insulators by dip-pen nanolithography.* Science, 2002. **296**(5574): p. 1836-1838.

108. Wilson, D.L., et al., *Surface organization and nanopatterning of collagen by dip-pen nanolithography.* Proceedings of the National Academy of Sciences, 2001. **98**(24): p. 13660-13664.

109. Nyamjav, D. and A. Ivanisevic, *Properties of polyelectrolyte templates generated by dip-pen nanolithography and microcontact printing.* Chemistry of Materials, 2004. **16**(25): p. 5216-5219.

110. Lim, J.H. and C.A. Mirkin, *Electrostatically driven dip-pen nanolithography of conducting polymers.* Advanced Materials, 2002. **14**(20): p. 1474-1477.

111. Noy, A., et al., *Fabrication of luminescent nanostructures and polymer nanowires using dip-pen nanolithography.* Nano Letters, 2001. **2**(2): p. 109-112.

112. Ben Ali, M., et al., *Atomic force microscope tip nanoprinting of gold nanoclusters.* Langmuir, 2002. **18**(3): p. 872-876.

113. Liao, J.-H., L. Huang, and N. Gu, *Fabrication of nanoparticle pattern through atomic force microscopy tip-induced deposition on modified silicon surfaces.* Chinese Physics Letters, 2002. **19**(1): p. 134.

114. Maynor, B.W., Y. Li, and J. Liu, *Au "ink" for AFM "dip-pen" nanolithography.* Langmuir, 2001. **17**(9): p. 2575-2578.

115. Li, Y., B.W. Maynor, and J. Liu, *Electrochemical AFM "Dip-Pen" Nanolithography.* Journal of the American Chemical Society, 2001. **123**(9): p. 2105-2106.

116. Porter, L.A., et al., *Electroless nanoparticle film deposition compatible with photolithography, microcontact printing, and dip-pen nanolithography patterning technologies.* Nano Letters, 2002. **2**(12): p. 1369-1372.

117. Xie, X.N., et al., *Nanoscale materials patterning and engineering by atomic force microscopy nanolithography.* Materials Science and Engineering: R: Reports, 2006. **54**(1-2): p. 1-48.

118. Piner, R.D. and C.A. Mirkin, *Effect of water on lateral force microscopy in air.* Langmuir, 1997. **13**(26): p. 6864-6868.

119. Basnar, B. and I. Willner, *Dip-pen-nanolithographic patterning of metallic, semiconductor, and metal oxide nanostructures on surfaces.* Small, 2009. **5**(1): p. 28-44.

120. Jang, J., G.C. Schatz, and M.A. Ratner, *Liquid meniscus condensation in dip-pen nanolithography.* The Journal of Chemical Physics, 2002. **116**(9): p. 3875-3886.

121. Weeks, B.L., M.W. Vaughn, and J.J. DeYoreo, *Direct imaging of meniscus formation in atomic force microscopy using environmental scanning electron microscopy.* Langmuir, 2005. **21**(18): p. 8096-8098.

122. Weeks, B.L. and J.J. DeYoreo, *Dynamic meniscus growth at a scanning probe tip in contact with a gold substrate.* The Journal of Physical Chemistry B, 2006. **110**(21): p. 10231-10233.

123. Chung, S., et al., *Temperature-dependence of ink transport during thermal dip-pen nanolithography.* Applied Physics Letters, 2011. **99**(19): p. 193101-3.

124. Schwartz, P.V., *Molecular transport from an atomic force microscope tip: a comparative study of dip-pen nanolithography.* Langmuir, 2002. **18**: p. 4041.

125. Hampton, J.R., A.A. Dameron, and P.S. Weiss, *Double-Ink Dip-Pen Nanolithography Studies Elucidate Molecular Transport.* Journal of the American Chemical Society, 2006. **128**(5): p. 1648-1653.

126. *Handbook of Physical Properties of Organic Chemicals*, ed. P.H. Howard and W.M. Meylan. 1997, Boca Raton, FL: CRC Press.

127. Jang, J., et al., *Self-assembly of ink molecules in dip-pen nanolithography: A diffusion model.* The Journal of Chemical Physics, 2001. **115**(6): p. 2721-2729.

128. Manandhar, P., et al., *Anomalous surface diffusion in nanoscale direct deposition processes.* Physical Review Letters, 2003. **90**(11): p. 115505.

129. Lee, N.-K. and S. Hong, *Modeling collective behavior of molecules in nanoscale direct deposition processes.* The Journal of Chemical Physics, 2006. **124**(11): p. 114711-5.

130. Garno, J.C., et al., *Precise positioning of nanoparticles on surfaces using scanning probe lithography.* Nano Letters, 2003. **3**(3): p. 389-395.

131. Thomas, P.J., G.U. Kulkarni, and C.N.R. Rao, *Dip-pen lithography using aqueous metal nanocrystal dispersions.* Journal of Materials Chemistry, 2004. **14**(4): p. 625-628.

132. Prime, D., et al., *Nanoscale patterning of gold nanoparticles using an atomic force microscope.* Materials Science and Engineering: C, 2005. **25**(1): p. 33-38.

133. Wiechmann, M., et al., *Nanoscale lines of supported nanogold particles and lysozyme–nanogold conjugates generated by atomic force microscopy in aqueous solution.* Surface and Interface Analysis, 2006. **38**(6): p. 1004-1009.

134. Bing, L., et al., *Patterning Colloidal Metal Nanoparticles for Controlled Growth of Carbon Nanotubes.* Advanced Materials, 2008. **20**(24): p. 4873-4878.

135. Su, M., et al., *Moving beyond molecules: patterning solid-state features via dip-pen nanolithography with sol-based inks.* Journal of the American Chemical Society, 2002. **124**(8): p. 1560-1561.

136. Li, Y., B.W. Maynor, and J. Liu, *Electrochemical AFM "dip-pen" nanolithography.* Journal of the American Chemical Society, 2001. **123**(9): p. 2105-2106.

137. Kim, K.H., N. Moldovan, and H.D. Espinosa, *A Nanofountain probe with sub-100 nm molecular writing resolution.* Small, 2005. **1**(6): p. 632-635.

138. Lewis, A., et al., *Fountain pen nanochemistry: atomic force control of chrome etching.* Applied Physics Letters, 1999. **75**(17): p. 2689-2691.

139. Taha, H., et al., *Protein printing with an atomic force sensing nanofountainpen.* Applied Physics Letters, 2003. **83**(5): p. 1041-1043.

140. Taha, H., A. Lewis, and C. Sukenik, *Controlled deposition of gold nanowires on semiconducting and nonconducting surfaces.* Nano Letters, 2007. **7**(7): p. 1883-1887.

141. Omrane, B. and C. Papadopoulos, *A direct-write approach for carbon nanotube catalyst deposition.* Nanotechnology, IEEE Transactions on, 2010. **9**(3): p. 375-380.

142. Kim, K.H., et al., *A novel AFM chip for fountain pen nanolithography - Design and Microfabrication.* Materials Research. Society Symposium Proceedings, 2004. **782**: p. A5.56.1-6.

143. Wu, B., et al., *Direct deposition and assembly of gold colloidal particles using a nanofountain probe.* Langmuir, 2007. **23**(17): p. 9120-9123.

144. Sau, T.K. and C.J. Murphy, *Room temperature, high-yield synthesis of multiple shapes of gold nanoparticles in aqueous solution.* Journal of the American Chemical Society, 2004. **126**(28): p. 8648-8649.

145. Kim, F., et al., *Platonic gold nanocrystals.* Angewandte Chemie International Edition, 2004. **43**(28): p. 3673-3677.

146. Zhang, J., et al., *Synthesis and SERS properties of nanocrystalline gold octahedra generated from thermal decomposition of $HAuCl_4$ in block copolymers.* Advanced Materials, 2006. **18**(24): p. 3233-3237.

147. Chen, Y., et al., *Shape controlled growth of gold nanoparticles by a solution synthesis.* Chemical Communications, 2005(33): p. 4181-4183.

148. Zhou, Q., et al., *Charge transfer between metal nanoparticles interconnected with a functionalized molecule probed by surface-enhanced Raman spectroscopy.* Angewandte Chemie International Edition, 2006. **45**(24): p. 3970-3973.

149. Orendorff, C.J., et al., *Surface-enhanced Raman spectroscopy of self-assembled monolayers: sandwich architecture and nanoparticle shape dependence.* Analytical Chemistry, 2005. **77**(10): p. 3261-3266.

150. Murphy, P.J., G. Stevens, and M.S. LaGrange, *The effects of temperature and pressure on gold-chloride speciation in hydrothermal fluids: a Raman spectroscopic study.* Geochimica et Cosmochimica Acta, 2000. **64**(3): p. 479-494.

151. Rozhok, S., R. Piner, and C.A. Mirkin, *Dip-pen nanolithography: what controls ink transport?* The Journal of Physical Chemistry B, 2002. **107**(3): p. 751-757.

152. Wang, W.M., et al., *Direct patterning of gold nanoparticles using dip-pen nanolithography.* ACS Nano, 2008. **2**(10): p. 2135-2142.

153. Battiston, F.M., et al., *A chemical sensor based on a microfabricated cantilever array with simultaneous resonance-frequency and bending readout.* Sensors and Actuators B: Chemical, 2001. **77**(1-2): p. 122-131.

154. Raiteri, R., et al., *Micromechanical cantilever-based biosensors.* Sensors and Actuators B: Chemical, 2001. **79**(2-3): p. 115-126.

155. Cleveland, J.P., et al., *A nondestructive method for determining the spring constant of cantilevers for scanning force microscopy.* Review of Scientific Instruments, 1993. **64**(2): p. 403-405.

156. Thundat, T., et al., *Detection of mercury vapor using resonating microcantilevers.* Applied Physics Letters, 1995. **66**(13): p. 1695-1697.

157. Thundat, T., et al., *Thermal and ambient-induced deflections of scanning force microscope cantilevers.* Applied Physics Letters, 1994. **64**(21): p. 2894-2896.

158. Janssen, D., et al., *Static solvent contact angle measurements, surface free energy and wettability determination of various self-assembled monolayers on silicon dioxide.* Thin Solid Films, 2006. **515**: p. 1433-1438.